An Investigation of the Stability of Viscous Channel Flow

Shi Zhao
St Hilda's College
University of Oxford

A thesis submitted for the degree of
Doctor of Philosophy

Michaelmas 2014

This thesis is dedicated to
Ying
for her love and support

Acknowledgements

First and foremost, I must express my deepest gratitude to my supervisor Prof. Stephen Duncan. It has been a fruitful and joyful experience to work with Steve and his constant guidance and encouragement during the past three years make this thesis possible. I am also grateful to Steve for being a great friend and giving me so much freedom.

I would like to thank Prof. Antonis Papachristodoulou for many interesting and enlightening discussions. In that respect I must also thank many of my fellow members of the Control Group: James Anderson, Bing Chu , Sandira Gayadeen, Edward Hancock, Giorgio Valmorbida, Hao Wang, Xuan Zhang and Xiaowei Zhao.

Helpful advice from my thesis examiners Prof. Paul Goulart and Dr. Bryn Jones is greatly appreciated. I am obliged to Dr. Ati Sharma and Prof. Colin Macdonald for answering many of my questions.

I am indebted to the China Scholarship Council (CSC). Without their generous financial support, I would not have been able to pursue my D.Phil studies and spend three fantastic years in Oxford.

I would like to acknowledge the use of the University of Oxford Advanced Research Computing (ARC) in carrying out this work.

However wonderful my Oxford experience has been, I often feel depressed for one reason: not being able to be with Ying, who is now three hundred miles away. I would like to express my deepest love to her, for everything she has done for me. To her this thesis is dedicated.

Abstract

This thesis focuses on the use of systems theory to study the stability of viscous channel flow. In the first part of the thesis, the flow is modelled as a feedback connection between a linear dynamical subsystem and a memoryless nonlinear subsystem. After discretisation, the system is approximated by a finite-dimensional model and its global stability is analysed using the passivity theorems, which are extended from finite-dimensional Euclidean spaces to finite-dimensional Hilbert spaces. The passivity analysis leads to the Reynolds number below which the flow is globally stable and the flow can be unstable above this number because of possible energy amplification. The thesis then addresses inaccuracy of the numerical methods that are typically used in the literature to calculate the energy amplification in the flow. It is identified that the inaccuracy is caused by the presence of spurious eigenvalues with negative real parts of large magnitude and numerical integration errors. A remedy to this problem is given in the thesis.

In the second part of the thesis, the effects of riblets on the linear stability and the energy amplification in channel flow are investigated numerically. Riblets are small protrusions aligned with the direction of the flow and it is known that the use of riblets on an aerodynamic body can result in significant reduction in drag, although the mechanism of drag reduction by riblets is not yet clear. Three types of riblets (sinusoidal, triangular and semi-circular ones) are considered and in order to use spectral methods to discretise the governing equations, the complex geometry associated with the riblets is transformed to a standard domain by a change of coordinates. The differential equations also have to be transformed into the new coordinate system and the presence of riblets poses a serious difficulty in representing the fluid flow by a state space model. To circumvent this difficulty, a novel formulation of the Navier-Stokes equations is derived.

Contents

List of Figures

List of Abbreviations

BMI	bilinear matrix inequality
CFD	computational fluid dynamics
DNS	direct numerical simulation
FDM	finite difference method
FEM	finite element method
IBM	immersed boundary method
IIM	immersed interface method
KYP	Kalman-Yakubovich-Popov
NSEs	Navier-Stokes equations
ODE	ordinary differential equation
PDE	partial differential equation
ROA	region of attraction
SDP	semidefinite programming
SOS	sum of squares
SVD	singular value decomposition

Chapter 1

Introduction

1.1 Background

Instabilities of viscous flow and the transition from laminar flow to turbulent flow are widely observed in nature and are important in engineering [49]. Laminar flow occurs when a fluid flows orderly in parallel layers and it is associated with less drag or skin friction at boundaries, compared to turbulent flow, which is characterised by chaotic, rapid mixing between layers. A laminar flow subject to a disturbance is described as being stable if it returns to its original laminar state and it is called unstable if it changes into a different state due to growth of the disturbance [133]. Instability of a flow is often a precursor to turbulence, although strictly speaking it does not always lead to laminar-turbulent transition [100], which is an extremely complicated process and remains an unsolved problem. Hydrodynamic stability theory, which studies the stability and instability of fluid flows, is of fundamental importance in understanding the laminar-turbulent transition. The theory has a long history, beginning in the late 19th century with the theoretical work of Helmholtz, Kelvin and Rayleigh and the experimental investigations of Reynolds [50]. It is concerned with how and why a laminar flow becomes unstable when a disturbance of small or moderate amplitude is present. Despite numerous efforts of scientists in over a century, the mechanism of instability of some presumably simple prototype flows, such as plane Poiseuille flow and plane Couette flow, is still not fully understood [157].

A foundation of hydrodynamic stability theory is linear stability analysis, which is the first method used to analyse the stability of a given flow [49]. Typically the method consists of the following four steps:

1. The partial differential equations (PDEs) that govern the evolution of the flow are perturbed about a steady state.

2. The equations of motion are linearised by neglecting the products of the perturbations.
3. The resulting equations are discretised so that all the operators are replaced by appropriate matrices.
4. The linear stability of the flow is determined by examining the eigenvalues of the discretised, linearised system.

The flow is said to be linearly stable if all the eigenvalues have negative real parts and it is linearly unstable if there is at least one eigenvalue with positive real part.

This approach has achieved success in analysing the stabilities of some flows such as Taylor-Couette flow and Rayleigh-Bénard convection, whose instabilities are driven by thermal or centrifugal forces, in the sense that the predicted critical Reynolds numbers match experimental results [157]. However, the predictions from eigenvalue analysis agree poorly with experiments for many other flows, such as plane Poiseuille flow and plane Couette flow. In 1971, Orszag found the critical Reynolds number for plane Poiseuille flow predicted by eigenvalue analysis of the Orr-Sommerfeld stability equation is $\mathrm{Re}_c = 5772.22$ [112]. But experiments show that the Reynolds number at which the transition occurs can be as low as $\mathrm{Re} \approx 1000$ [117] [27]. Plane Couette flow is expected to be stable for any Reynolds number by linear stability analysis [80] [133], but the transition is observed when the Reynolds number is as low as $\mathrm{Re} \approx 350$ [101].

Linearisation about a steady state flow is justified only when the perturbations are of small magnitude such that the nonlinear effects can be ignored. Indeed, it is expected that when the disturbance grows and reaches a certain threshold, the nonlinearity comes into play and its effects cannot be neglected. The invalidity of the linearised model has long been believed to be one of the reasons for the discrepancy between theoretical predictions and experimental results [157].

Starting from the early 1990s, along with the study of pseudospectra of matrices and operators, the failure of linear stability analysis was also attributed to the nonnormality of the linearised operators [134]. It is found that linear operators arising in Taylor-Couette flow and Rayleigh-Bénard convection are normal [157], whereas the operators in Poiseuille and Couette flows are far from normal [123]. This fact suggests that nonnormality is a possible explanation for the discrepancy between theoretical analysis and what is observed in the laboratory. For a normal linear operator, all its eigenfunctions are orthogonal to each other. By contrast, the eigenfunctions of a nonnormal linear operator are not orthogonal, even if they form a complete set. It is therefore believed that for nonnormal linear operators, the eigenvalues do not tell the whole story and sometimes are even misleading [151][152][156]. Instead, pseudospectra, which describe the sensitivity of eigenvalues of linear operators to perturbations, are a better tool to study the behaviour of nonnormal linear operators [156].

Transient energy growth, which is a direct consequence of nonnormality, is recognised as a possible explanation for the subcritical transition [157]. If the eigenfunctions are not orthogonal, the inputs of a system can be amplified, even though all the eigenvalues have strictly negative real parts. For example, the eigenvalues of the Orr-Sommerfeld operator are very sensitive to perturbations at high Reynolds number and due to the nonorthogonality of the eigenfunctions, the energy of perturbations may still grow temporarily even if all the eigenvalues lie in the open left half of the complex plane [123].

Another standard tool of analysing the stability of a fluid flow is the energy approach [131] [111], which is based on variational calculus and aims to find the Reynolds number below which there is no energy growth for perturbations of arbitrary magnitudes. Using this approach, Serrin proved that an incompressible flow in a bounded domain is globally stable when the Reynolds number is smaller than $\mathrm{Re} < 5.71$ [135]. This result was sharpened by Joseph and it was shown that the energy Reynolds number for plane Poiseuille flow is $\mathrm{Re}_E \approx 49.6$ and the number for plane Couette flow is $\mathrm{Re}_E \approx 20.7$ [80] [133]. It is not surprising that the results are quite conservative compared to the experimentally observed transition values of $\mathrm{Re} \approx 1000$ and $\mathrm{Re} \approx 350$ respectively, given that the monotonic decay requirement is likely to be unnecessarily restrictive. In fact, studying the stability of a fluid flow using the energy approach is essentially Lyapunov analysis in which the kinetic energy of the flow is used as the Lyapunov function.

Turbulence is often undesirable (but not always so) as it is associated with more drag or skin friction at interfaces between walls and fluids. Considerable efforts have been made to study how to relaminarise transitional and turbulent flows or delay laminar-turbulent transition. One of the early studies used blowing and suction so that the normal velocity on the walls is opposite to the normal velocity at a specified location and this strategy is known as “opposition control” [36]. Joshi *et al.* applied classical control theory to control 2-dimensional plane Poiseuille flow and the role of control feedback is to place the poles of the system in the left of the complex plane [81] [82]. Cortelezzi *et al.* used modern control theory to design optimal controllers and robust controllers to stabilise 2-dimensional plane Poiseuille flow and it was found that the skin friction can be reduced by 10% in direct numerical simulation (DNS) of a turbulent channel flow when a robust reduced-order controller is applied [39] [92] [93]. Stabilisation of 3-dimensional channel flow using optimal and robust control strategies has been considered by Bewley and Liu [18] and the effectiveness of these controllers was investigated in [73]. Model predictive control [19] and gain scheduling [72] have also been used to relaminarise turbulent flows. Understanding the mechanism of instability of fluid flows can be useful for designing effective controllers. For example, the performance of a controller in model predictive control of turbulence depends on the choice of cost functions and it was found that the cost functions that aims to reduce the effects of the coupling term of the Orr-Sommerfeld/Squire operator can result in an effective controller [19]. The coupling term is mainly responsible for the enhancement of the nonnormality of the operator and the nonnormality is a critical factor in the onset of turbulence. In [99], it was found that without the coupling term, the near wall turbulence cannot be sustained. In [136] and [103], feedback controllers were designed to suppress transient growth in supercritical and subcritical plane Poiseuille flow.

Apart from active control strategies, there are also many passive techniques to control fluid flows such that the skin friction is reduced. One of the passive techniques is the use of riblets, which are small protrusions that are aligned in the direction of flow. Riblet structures are widely observed in nature, for example on shark skin, seal fur and scallop shells. Oil channel experiments conducted by Bechert *et al.* showed that riblets inspired by shark skin can reduce the shear stress by up to 10% [17] [16], while a 12% drag reduction was achieved in the experimental study by Itoh *et al.* in channel flow over seal fur surface [77]. Riblet structures of scallop shells were also studied in [7].

The drag reduction benefits of riblets on aircrafts were confirmed by many wind tunnel experiments and flight tests [159]. For example, in 1988, experiments on a 1/11th scale Airbus 320 model cruising at Mach 0.7 in a wind tunnel showed that skin friction was reduced by 4.85%, with two thirds of the wetted area fitted with riblets [40]. A flight test on an Airbus 320 with 75% wetted area covered by riblet films showed that approximately 2% reduction in overall drag was achieved [128]. Skin friction and lift induced drag are two of the largest sources of the overall drag of an aircraft [40]. Since even a small reduction in skin friction can result in significant economy in fuel and reduced emissions, riblets have been under extensive study during the last few decades.

The effects of riblets on sails were studied experimentally in [4] and it was found that although no drag reduction was obtained, the lift of a sail was increased by 3% by riblets. There have also been some applications of riblets to sports events, although it is hard to tell whether riblets played an effective role. For example, riblets have been used on the Stars and Stripes America's Cup racing yacht and on the swimsuits used by the USA Olympic swimming team [40].

Apart from experimental studies, there have also been considerable numerical investigations on the effects of riblets in turbulent flows. In order to gain better understandings of the mechanisms of drag reduction over riblets, DNS has been frequently carried out such that near wall flow structures can be analysed in detail [37][35] [58] [54]. Although the mechanism of drag reduction over riblets is not yet fully understood, it is now generally believed that riblets reduce the drag by impeding the cross-flow motion induced by streamwise vortices [84].

As drag reduction by riblets is usually associated with the turbulent regime, most studies in the literature focus on the effects of riblets in turbulent flows [78]. The impact of riblets on the stability of laminar flow is less studied and there have been some contradictory results in the literature. In the numerical study by Launder and Li [90], it was reported that in the case where the lower wall of a channel flow is fitted with "blade" riblets, no drag reduction is achieved in laminar flow. Similarly, the numerical study of Choi *et al.* [34] concluded that when the triangular riblets are present on both walls, the net drag is increased in fully developed laminar channel flows. However, in the experimental study of Djenidi *et al.* [45], the skin friction of laminar boundary layer over triangular riblets is not increased. Furthermore, the experimental study in [66] has shown that triangular riblets can delay laminar-turbulent transition and shift the transition downstream.

The primary purpose of this thesis is to study the stability of viscous flows from the systems theory point of view. The focus is mainly on plane Poiseuille flow, which is one of the most popular prototype flows in the literature of hydrodynamic stability and flow control. The approach here is to transform infinite-dimensional fluid flow systems into finite-dimensional ones by discretising the governing equations in the spatial domain, as is typically done in the literature. The dependence of the results of stability analysis of fluid flows on the choice of spatial discretisation methods is also discussed. We then investigate how the presence of riblets on one wall changes the stability of plane Poiseuille flow, in an attempt to provide a possible explanation for the transition delay by riblets.

1.2 The Navier-Stokes equations

In 3-dimensional Cartesian coordinates (x, y, z), the motion of an isothermal, incompressible viscous fluid is governed by the following equations

$$\rho\left(\frac{\partial u}{\partial t}+u\frac{\partial u}{\partial x}+v\frac{\partial u}{\partial y}+w\frac{\partial u}{\partial z}\right)=-\frac{\partial p}{\partial x}+\mu\left(\frac{\partial^2 u}{\partial x^2}+\frac{\partial^2 u}{\partial y^2}+\frac{\partial^2 u}{\partial z^2}\right)+f_x \tag{1.1a}$$

$$\rho\left(\frac{\partial v}{\partial t}+u\frac{\partial v}{\partial x}+v\frac{\partial v}{\partial y}+w\frac{\partial v}{\partial z}\right)=-\frac{\partial p}{\partial y}+\mu\left(\frac{\partial^2 v}{\partial x^2}+\frac{\partial^2 v}{\partial y^2}+\frac{\partial^2 v}{\partial z^2}\right)+f_y \tag{1.1b}$$

$$\rho\left(\frac{\partial w}{\partial t}+u\frac{\partial w}{\partial x}+v\frac{\partial w}{\partial y}+w\frac{\partial w}{\partial z}\right)=-\frac{\partial p}{\partial z}+\mu\left(\frac{\partial^2 w}{\partial x^2}+\frac{\partial^2 w}{\partial y^2}+\frac{\partial^2 w}{\partial z^2}\right)+f_z \tag{1.1c}$$

together with the continuity equation

$$\frac{\partial u}{\partial x}+\frac{\partial v}{\partial y}+\frac{\partial w}{\partial z}=0 \tag{1.1d}$$

where $u(x, y, z, t)$, $v(x, y, z, t)$ and $w(x, y, z, t)$ are the components of the velocity of the fluid in the x, y and z directions, respectively, $f_x(x, y, z, t)$, $f_y(x, y, z, t)$ and $f_z(x, y, z, t)$ are the components of the external force in each of these directions, $p(x, y, z, t)$ is the pressure, ρ is the fluid density, which is a constant as the flow is incompressible, and μ is the fluid viscosity, which is also a constant for the flows considered in this thesis.

The first three equations (1.1a)-(1.1c) are based on the conservation of momentum (or Newton's second law) and for this reason, they are referred to as the momentum equations. The continuity equation (1.1d) is derived from the principle of conservation of mass and such a velocity field is said to be divergence free. These equations are known as the Navier-Stokes equations (NSEs) and their derivation can be found in many standard fluid mechanics textbooks, for example, [14] [64] [48].

The NSEs can be written in the compact form

$$\begin{aligned}\rho\left(\frac{\partial \mathbf{u}}{\partial t}+\mathbf{u}\cdot\nabla\mathbf{u}\right) &= -\nabla p+\mu\nabla^2\mathbf{u}+\mathbf{f} && (1.2a)\\ \nabla\cdot\mathbf{u} &= 0 && (1.2b)\end{aligned}$$

where $\mathbf{u} = (u, v, w)$, $\mathbf{f} = (f_x, f_y, f_z)$, ∇ is the gradient operator

$$\nabla=\left(\frac{\partial}{\partial x},\frac{\partial}{\partial y},\frac{\partial}{\partial z}\right) \tag{1.3}$$

and ∇^2 is the Laplace operator

$$\nabla^2=\frac{\partial^2}{\partial x^2}+\frac{\partial^2}{\partial y^2}+\frac{\partial^2}{\partial z^2} \tag{1.4}$$

Nondimensionlising the equations (1.1) by defining a characteristic length L_c, a characteristic velocity U_c and performing the following change of variables

$$\begin{aligned}
(\tilde{x}, \tilde{y}, \tilde{z}) &= \left(\frac{x}{L_c}, \frac{y}{L_c}, \frac{z}{L_c}\right), \quad \tilde{t} = \frac{U_c}{L_c} t \\
(\tilde{u}, \tilde{v}, \tilde{w}) &= \left(\frac{u}{U_c}, \frac{v}{U_c}, \frac{w}{U_c}\right), \quad \tilde{p} = \frac{p}{\rho U_c^2} \\
\left(\tilde{f}_x, \tilde{f}_y, \tilde{f}_z\right) &= \left(\frac{L_c}{\rho U_c^2} f_x, \frac{L_c}{\rho U_c^2} f_y, \frac{L_c}{\rho U_c^2} f_z\right)
\end{aligned}$$

gives the dimensionless NSEs

$$\frac{\partial u}{\partial t} + u\frac{\partial u}{\partial x} + v\frac{\partial u}{\partial y} + w\frac{\partial u}{\partial z} = -\frac{\partial p}{\partial x} + \frac{1}{\mathrm{Re}}\left(\frac{\partial^2 u}{\partial x^2} + \frac{\partial^2 u}{\partial y^2} + \frac{\partial^2 u}{\partial z^2}\right) + f_x \tag{1.5a}$$

$$\frac{\partial v}{\partial t} + u\frac{\partial v}{\partial x} + v\frac{\partial v}{\partial y} + w\frac{\partial v}{\partial z} = -\frac{\partial p}{\partial y} + \frac{1}{\mathrm{Re}}\left(\frac{\partial^2 v}{\partial x^2} + \frac{\partial^2 v}{\partial y^2} + \frac{\partial^2 v}{\partial z^2}\right) + f_y \tag{1.5b}$$

$$\frac{\partial w}{\partial t} + u\frac{\partial w}{\partial x} + v\frac{\partial w}{\partial y} + w\frac{\partial w}{\partial z} = -\frac{\partial p}{\partial z} + \frac{1}{\mathrm{Re}}\left(\frac{\partial^2 w}{\partial x^2} + \frac{\partial^2 w}{\partial y^2} + \frac{\partial^2 w}{\partial z^2}\right) + f_z \tag{1.5c}$$

$$\frac{\partial u}{\partial x} + \frac{\partial v}{\partial y} + \frac{\partial w}{\partial z} = 0 \tag{1.5d}$$

where the tilde has been neglected for notational convenience and the Reynolds number Re is

$$\mathrm{Re} = \frac{\rho U_c L_c}{\mu} \tag{1.6}$$

Defined as the ratio of inertial forces to viscous forces, the Reynolds number characterises the relative importance of these two types of forces. Reynolds discovered in his famous transition experiment that the stability of viscous flows is closely related to the Reynolds number [130].

In the dimensionless NSEs (1.5), the variables include the velocity components (u, v, w) and the pressure term p, which are referred to as the primitive variables. For this reason, this formulation is called the primitive variable formulation. There are other formulations of the NSEs and although mathematically they are equivalent, depending on the circumstances, one formulation may be preferred to others [67]. As we will see later in this thesis, the choice of the formulation does matter in the study of stability of fluid flows.

The presence of the pressure term p in the primitive variable form often causes difficulties due to the lack of a time-dependent governing equation for p. The treatment of pressure is an important topic in computational fluid dynamics (CFD) [26]. It is therefore sometimes desirable to eliminate the pressure term from the NSEs. The vorticity-stream function formulation and the velocity-vorticity formulation are two forms of the NSEs in which pressure p is eliminated. The velocity-vorticity formulation is more often used in the literature of hydrodynamic stability and flow control and its derivation will be given in Chapter 2.

1.3 Prototype flows

In this thesis, we restrict our attention to plane channel flow, which is a fluid flow between two parallel plates of infinite extents. The geometry of channel flow is shown in Figure 1.1, where x is the direction the fluid flows and it is called the streamwise direction, y is normal to the two walls and it is called the wall-normal direction, whereas z is called the spanwise direction. The spatial domain is normalised such that $y \in [-1, 1]$. The flow is called plane Poiseuille flow when the two plates are stationary or there is no relative movement between them. It is known as plane Couette flow when one plate is moving at a constant velocity relative to the other one.

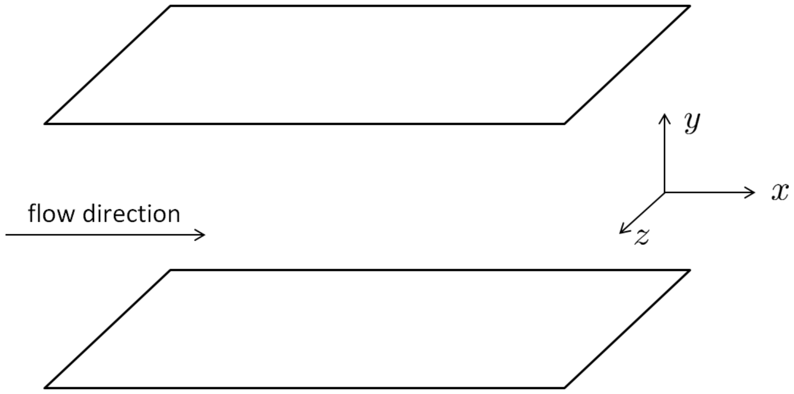

Figure 1.1: Geometry of plane channel flow.

It is standard practice to assume that there is no external force and that no-slip boundary conditions are satisfied on the walls, which means that the relative velocity of the fluid to the wall at any point of the boundaries is zero. Consider plane Poiseuille flow in which both walls are stationary. The steady state solution $(U, 0, 0)$ satisfies the dimensionless NSEs (1.5) together with the boundary conditions

$$U(y = 1) = U(y = -1) = 0 \tag{1.7}$$

Defining the characteristic velocity as the velocity of the steady state at the centreline of the channel, which means that

$$U(y = 0) = 1 \tag{1.8}$$

it is straightforward to obtain

$$U(y) = 1 - y^2 \tag{1.9}$$

which gives the parabolic velocity profile in Figure 1.2. This steady state is often used as the base flow in the study of laminar channel flow.

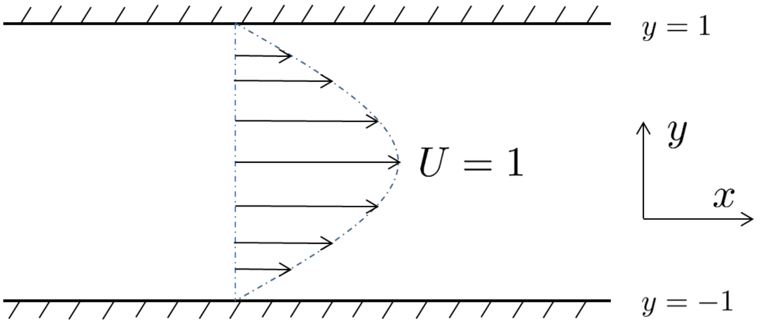

Figure 1.2: 2-dimensional view of steady state velocity profile of plane Poiseuille flow.

As a comparison, consider plane Couette flow in which the two walls are moving towards opposite directions at the same speed. Still, the steady state takes the form $(U, 0, 0)$. Defining the velocity of the upper wall as the characteristic velocity, then we have

$$U(y = 1) = 1 \tag{1.10}$$

$$U(y = -1) = -1 \tag{1.11}$$

The steady state solution can be obtained

$$U(y) = y \tag{1.12}$$

and it gives the velocity profile shown in Figure 1.3.

Plane channel flow, especially plane Poiseuille flow, is a standard prototype flow that has been studied extensively in the literature of hydrodynamic stability and flow control. Plane poiseuille flow is a simplification of Hagen-Poiseuille flow, which is a fluid flow in a circular pipe of constant cross section with the length of the pipe substantially longer than its diameter. Hagen-Poiseuille flow was studied in Reynolds' transition experiment [130]. Plane Couette flow, on the other hand, is a simplification of Taylor-Couette flow, which is a flow between two rotating cylinders. The stability of Taylor-Couette flow was studied by Taylor in his famous paper [147]. It should be pointed out that the term plane channel flow is often used to refer to plane Poiseuille flow in the literature without extra clarification.

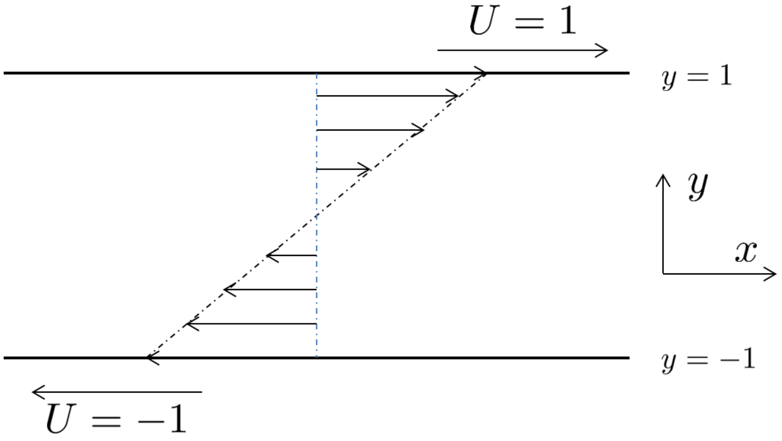

Figure 1.3: 2-dimensional view of steady state velocity profile of plane Couette flow.

In many studies, the spanwise direction z is omitted such that the fluid flow is further simplified. In both plane Poiseuille flow and plane Couette flow, such a simplification does not have any effect on the steady states as they are independent of the spanwise direction. However, the order of the finite-dimensional models obtained through discretisation can be significantly reduced. In 2-dimensional channel flow, a stream function formulation of the NSEs is often used and this will be discussed in Chapter 4.

1.4 Outline and contributions of the thesis

The rest of the thesis is organised as follows.

In Chapter 2, plane channel flow is modelled as a feedback connection of a linear time-invariant dynamical system and a memoryless nonlinear system. The stability of the fluid flow is then studied using the passivity theorems from systems theory. Before the analysis, definitions of dynamical system stability and spectral methods that are often used to discretise the NSEs are briefly introduced. Part of the work in this chapter has been published in [165].

Chapter 3 addresses the accuracy of numerical discretisation methods in the calculation of transient growth in plane channel flow. Numerical experiments are conducted to show that the Chebyshev collocation method, which is typically used in the literature, is not sufficiently accurate to calculate the transient growth at low Reynolds number and the reason for the lack of accuracy is explained. Furthermore, it is shown that using a Chebyshev Galerkin method can avoid such a problem. This chapter is based on the publication [168].

Chapter 4 is mainly concerned with numerical issues in the stability analysis of fluid flows using finite-dimensional models. A numerical discretisation of the 2-dimensional NSEs is proposed in which the nonlinear terms of different forms remain equivalent and energy-preserving after discretisation. Methods of searching for general Lyapunov functions and determining the estimated region of attraction (ROA) are briefly reviewed. Some low order models for qualitative study are also discussed.

From Chapter 5 onwards, the focus of the thesis is shifted to the stability of channel flow over riblets. Since the computational domain is now irregular, it is difficult to use spectral methods directly to discretise the governing equations. Chapter 5 reviews some methods that can circumvent this difficulty. As a preparation for the study of the linear stability of the flow, some of the most commonly used eigenvalue algorithms are also introduced. After that, the NSEs governing the motion of channel flow over riblets are presented and the steady state is solved numerically.

Chapter 6 studies the effects of riblets on the linear stability of plane Poiseuille flow. Due to the presence of riblets on the lower wall, the steady state flow is now a function of the spanwise direction. As a result, the velocity-vorticity formulation of the NSEs that has been used in the previous chapters is no longer a suitable choice. A novel velocity-velocity formulation and corresponding boundary conditions are derived, without making extra assumptions. Sinusoidal, triangular and semi-circular riblets are considered in the study.

In Chapter 7, the impact of riblets on the energy amplification in channel flow is investigated. Two scenarios in which the flow can experience energy amplification are considered. In the first scenario, the kinetic energy has a transient growth in the presence of an initial perturbation, while in the second one, the flow is subject to stochastic noise. The attention is restricted to streamwise-constant flow as it is identified as the flow modes that have the largest possible energy amplification. A 2-dimensional/3-component (2D/3C) formulation of the NSEs is used and the same types of riblets as in Chapter 6 are considered. Part of the work in this chapter has been published in [167]. The analysis can also be extended to pipe flow [166].

Chapter 8 summarises the conclusions of the thesis and points out possible directions for future research.

The main contributions of the thesis are:

- Extending the passivity theorems from finite-dimensional Euclidean spaces to Hilbert spaces;
- Providing an alternative method to find the critical energy Reynolds number of plane channel flow;
- Identifying the sources of the inaccuracy of calculating the transient growth using the Chebyshev collocation method;

- Giving a Chebyshev Galerkin method that is more accurate when calculating the transient growth;
- Presenting a numerical discretisation of the 2-dimensional NSEs in which the nonlinearity of different forms remain equivalent and lossless;
- Deriving a novel velocity-velocity formulation of the NSEs that is suitable for the linear stability analysis of channel flow over riblets;
- Analysing the effects of sinusoidal, triangular and semi-circular riblets on the linear stability of channel flow using two different formulations of the NSEs;
- Confirming that the energy amplification in channel flow can be reduced significantly by riblets.

Chapter 2

Passivity of Plane Channel Flow

2.1 Introduction

This chapter uses the passivity theorems from systems theory to study the stability of plane channel flow. Passivity is a concept closely related to the stability and the energy of a system. The nonlinearity of plane channel flow is lossless in the sense that the nonlinearity does not create or consume energy and is responsible for the interaction between different modes [133]. Although it is pointed out by Sharma *et al.* [137] [138] that introducing feedback control to remove the nonnormality and make the linear part passive can stabilise the flow, little attention has been paid to the passivity of the uncontrolled flow.

In this chapter, plane channel flow is modelled as the interconnection of a linear time-invariant dynamical system and a memoryless, lossless nonlinear system. Discretisation of the linear part of the governing equations leads to a set of decoupled finite-dimensional subsystems and the passivity of each is examined. According to the passivity theorems [86], the feedback connection of two passive systems is passive, and if the dynamical linear part is strictly passive and the memoryless nonlinear part is passive, the origin of the closed-loop system is asymptotically stable. In addition, the origin is globally asymptotically stable if the storage function of the dynamical linear system is radially unbounded. Therefore, the Reynolds number below which all the linear subsystems are always strictly passive is the lower bound below which the flow is globally stable.

Before going to the details of the analysis, we first introduce various stability definitions of a given nonlinear dynamical systems. Since there are many different ways of describing the stability of a system, it is necessary to distinguish them by giving precise mathematical definitions. In order to approximate an infinite-dimensional system with a finite-dimensional model, the governing equations of the system have to be discretised spatially and the numerical methods that are commonly used to discretise PDEs are also briefly introduced.

2.2 Stability of dynamical systems

Consider a finite-dimensional dynamical system which is modelled by the following coupled ordinary differential equations (ODEs)

$$\begin{aligned} \dot{x}_1 &= f_1(t, x_1, x_2, \ldots, x_n, u_1, u_2, \ldots, u_p) \\ \dot{x}_2 &= f_2(t, x_1, x_2, \ldots, x_n, u_1, u_2, \ldots, u_p) \\ \vdots\ &\quad \vdots \\ \dot{x}_n &= f_n(t, x_1, x_2, \ldots, x_n, u_1, u_2, \ldots, u_p) \end{aligned}$$

where the dot denotes time derivative $\frac{\mathrm{d}}{\mathrm{d}t}$, while $x_1, x_2, \ldots, x_n \in \mathbb{R}$ are the state variables and $u_1, u_2, \ldots, u_p \in \mathbb{R}$ are the input variables. The system is n_{th}-order since there are n state variables.

The model is usually written in the compact form

$$\dot{x} = f(t, x, u) \tag{2.1a}$$

where

$$\begin{aligned} x &= [x_1, x_2, \ldots, x_n]^T \\ u &= [u_1, u_2, \ldots, u_p]^T \\ f(t, x, u) &= [f_1(t, x, u), f_2(t, x, u), \ldots, f_n(t, x, u)]^T \end{aligned}$$

The output of the system is usually a function of time t, the state x and the input u

$$y = h(t, x, u) \tag{2.1b}$$

where $y \in \mathbb{R}^q$ is q dimensional output variable. Equation (2.1a) is called the state equation and equation (2.1b) is called the output equation. These two equations form the state space model of the system.

In the case that the functions f and h do not explicitly depend on the time variable t, the system is called time-invariant or autonomous. When the input u of an autonomous system is zero or can be written as a function of the state x, the state equation can be further simplified as

$$\dot{x} = f(x) \tag{2.2}$$

We assume the the function $f(x)$ is continuously differentiable.

When considering the stability of a dynamical system, we are usually referring to the stability of a particular equilibrium of the system, which is a special case of the stability of a solution. A point $x = x_0$ is said to be an equilibrium of a dynamical system if the system state remains at x_0 whenever it starts with x_0. It is straightforward to see that for the autonomous system (2.2), an equilibrium x_0 satisfies

$$f(x_0) = 0 \tag{2.3}$$

Note that there might be multiple equilibria for a system, which reflects the fact that there might exist multiple solutions to the equation

$$f(x) = 0 \tag{2.4}$$

Without loss of generality, we can always assume that the equilibrium of interest is the origin, which can be easily justified by a change of variables. As a result, we assume that $f(0) = 0$. In practice, we often call a system stable when its origin is stable whenever there is no risk of confusion. The following stability definitions and theorems can be found in standard textbooks, for example, [86].

2.2.1 Stability definitions

Definition 1. ***(Lyapunov stability)*** *The equilibrium point $x = 0$ of system (2.2) is stable if for each $\epsilon > 0$, there exists a $\delta = \delta(\epsilon) > 0$ such that*

$$\|x(0)\| < \delta \Rightarrow \|x(t)\| < \epsilon \;\; \forall t \geq 0$$

The initial state $x(0)$ can be regarded as a perturbation of the equilibrium $x = 0$. Loosely speaking, Lyapunov stability means that if the perturbation is small (the perturbation is within the norm ball centred at the origin with the radius δ), the state will remain small (the trajectory will not leave the ϵ neighbourhood). Notice that under this definition, the perturbation does not necessarily decay to zero even when the origin is Lyapunov stable.

Definition 2. ***(Local asymptotical stability)*** *The equilibrium point $x = 0$ of system (2.2) is (locally) asymptotically stable if it is stable and there exists a $\delta > 0$ such that*

$$\|x(0)\| < \delta \Rightarrow \lim_{t \to \infty} x(t) = 0$$

We are often interested in δ when the origin is asymptotically stable. Roughly speaking, the larger δ, the more likely the system will return to the equilibrium point when it is subject to a disturbance. In other words, δ indicates the largest amplitude of the perturbation that the system can recover from, and as a result, δ is closely related to the region of attraction (ROA).

Definition 3. ***(Region of attraction)*** *The ROA is the set of all initial conditions for which the solution of the system $x(t) \to 0$ when t approaches ∞.*

Definition 4. ***(Global asymptotical stability)*** *The equilibrium point $x = 0$ of system (2.2) is globally asymptotically stable if it is asymptotically stable and*

$$\delta = \infty$$

This amounts to requiring that the ROA is the entire domain $\mathbb{R}^n$. Being globally asymptotically stable means that no matter how large the perturbation $x(0)$, the trajectory of the system will eventually return to the origin. The origin of a globally asymptotically stable system must be the unique equilibrium point. If there was another equilibrium x_0, then the trajectory would remain at x_0 when it starts at x_0. This contradicts the statement that the state of the system will converge to the origin.

These definitions say nothing about the convergence rate of the state variable to a point of equilibrium.

Definition 5. ***(Exponential stability)*** *The equilibrium point $x = 0$ of system (2.2) is exponentially stable if there exists $K > 0, \beta > 0$ and $\delta > 0$ such that*

$$\|x(0)\| < \delta \Rightarrow \|x(t)\| \leq K\|x(0)\|\mathrm{e}^{-\beta t} \quad \forall t > 0$$

Exponential stability implies asymptotical stability. In the case that $\delta = \infty$, the system is said to be globally exponentially stable.

A nonlinear system is often approximated by the linearisation about the origin, as is typically done in the study of hydrodynamic stability. Denote the Jacobian matrix

$$A = \left.\begin{bmatrix} \frac{\partial f_1}{\partial x_1} & \frac{\partial f_1}{\partial x_2} & \cdots & \frac{\partial f_1}{\partial x_n} \\ \frac{\partial f_2}{\partial x_1} & \frac{\partial f_2}{\partial x_2} & \cdots & \frac{\partial f_2}{\partial x_n} \\ \vdots & \vdots & \ddots & \vdots \\ \frac{\partial f_n}{\partial x_1} & \frac{\partial f_n}{\partial x_2} & \cdots & \frac{\partial f_n}{\partial x_n} \end{bmatrix}\right|_{x=0} \tag{2.5}$$

the linearised system takes the form

$$\dot{x} = Ax \tag{2.6}$$

Definition 6. ***(Linear stability)*** *The equilibrium point $x = 0$ of system (2.2) is linearly stable when all the eigenvalues of the Jacobian matrix A have negative real parts. The system is linearly unstable when A has eigenvalues with positive real parts.*

The linear stability of the system can be determined by examining the eigenvalue of A with largest real part. Therefore this particular eigenvalue is often called the most unstable eigenvalue. In the complex plane, the eigenvalue is the one in the rightmost position. For this reason, it is also called the rightmost eigenvalue. A square matrix A is called Hurwitz if all its eigenvalues have strictly negative real parts. It is also called a stability matrix for apparent reasons. Note that the above definition does not address the stability of the origin when the rightmost eigenvalue has zero real part. In that case, the stability can be analysed by using the centre manifold theorem [86], which will not be discussed in this thesis.

2.2.2 Stability theorems

Stability of a nonlinear dynamical system can rarely be determined by checking whether it satisfies a stability definition. In practice, a more frequently used approach is to carry out Lyapunov analysis. The analysis is based on stability theorems, which are standard results in systems theory.

Theorem 1. ***(Lyapunov stability theorem)*** *Let $D \subset \mathbb{R}^n$ be a domain containing the origin. The equilibrium point $x = 0$ of system (2.2) is stable if there exists a continuously differentiable function $V(x)$ such that*

$$\begin{aligned} V(0) &= 0 && \text{(2.7a)} \\ V(x) &> 0 \ \ \forall x \in D - \{0\} && \text{(2.7b)} \\ \dot{V}(x) &\leq 0 \ \ \forall x \in D && \text{(2.7c)} \end{aligned}$$

The function $V(x)$ is called Lyapunov function and $\dot{V}(x)$ is the derivative of $V(x)$ along the system trajectory. More precisely,

$$\dot{V}(x) = \frac{\partial V}{\partial x} f(x) = \begin{bmatrix} \frac{\partial V}{\partial x_1} & \frac{\partial V}{\partial x_2} & \cdots & \frac{\partial V}{\partial x_n} \end{bmatrix} \begin{bmatrix} f_1(x) \\ f_2(x) \\ \vdots \\ f_n(x) \end{bmatrix}$$

The origin is asymptotically stable if

$$\dot{V}(x) < 0 \ \ \forall x \in D - \{0\} \tag{2.8}$$

To establish the global asymptotical stability, extra conditions need to be satisfied.

Theorem 2. ***(Barbashin-Krasovskii theorem)*** *The equilibrium point $x = 0$ of system (2.2) is globally asymptotically stable if there exists a continuously differentiable function $V(x)$ such that*

$$\begin{aligned} V(0) &= 0 && \text{(2.9a)} \\ V(x) &> 0 \;\; \forall x \neq 0 && \text{(2.9b)} \\ \|x\| \to \infty &\Rightarrow V(x) \to \infty && \text{(2.9c)} \\ \dot{V}(x) &< 0 \;\; \forall x \neq 0 && \text{(2.9d)} \end{aligned}$$

The function $V(x)$ is said to be positive definite if it satisfies the first two conditions. It is said to be radially unbounded if the third condition is satisfied. The theorem then states that the equilibrium point is globally asymptotically stable if there exists a positive definite, radially unbounded Lyapunov function whose derivative along the trajectory is negative definite.

It should be noted that these stability theorems only give sufficient conditions. Failure to satisfy the conditions does not mean that the origin is not stable/asymptotically stable/globally asymptotically stable. For example, for the origin to be globally asymptotically stable, the condition that $\dot{V}(x)$ is negative definite is not always necessary.

The stability of the origin of system (2.2) is related to its linear stability by Lyapunov's indirect method.

Theorem 3. ***(Lyapunov's indirect method)*** *The origin of system (2.2) is asymptotically exponentially stable if it is linearly stable, i.e., all the eigenvalues of the Jacobian matrix A, as defined in (2.5), have negative real parts. The origin is unstable if it is linearly unstable, i.e., A has eigenvalues with positive real parts.*

2.2.3 Passivity definitions

The primary aim of this chapter is to study the stability of plane channel flow using the passivity theorems. To do this, we need to give the standard definitions of the passivity of a system. These definitions can be found in standard textbooks such as [86]. We start with memoryless systems.

Consider a memoryless function

$$y = h(t, u) \tag{2.10}$$

where $h : [0, \infty) \times \mathbb{R}^p \to \mathbb{R}^p$. It is clear that the output y does not depend on the past input, which is why the function is called memoryless.

Definition 7. ***(Passivity of memoryless systems)*** *The memoryless system (2.10) is said to be passive if*

$$u^T y \geq 0 \quad \forall (t, u) \in [0, \infty) \times \mathbb{R}^p$$

It is said to be lossless if

$$u^T y = 0 \quad \forall (t, u) \in [0, \infty) \times \mathbb{R}^p$$

The definition originates from electrical circuit theory. For example, a linear resistor satisfying Ohm's law can be described by the equation (2.10).

Now consider a dynamical system represented by the state model

$$\dot{x} = f(x, u) \tag{2.11a}$$

$$y = h(x, u) \tag{2.11b}$$

where $f : \mathbb{R}^n \times \mathbb{R}^p \to \mathbb{R}^n$ is locally Lipschitz, $h : \mathbb{R}^n \times \mathbb{R}^p \to \mathbb{R}^p$ is continuous, $f(0, 0) = 0$ and $h(0, 0) = 0$.

Definition 8. ***(Passivity of dynamical systems)*** *The dynamical system (2.11) is called passive if there exists a positive semidefinite storage function $V(x)$ such that*

$$u^T y \geq \dot{V}(x) \quad \forall (x, u) \in \mathbb{R}^n \times \mathbb{R}^p$$

It is lossless if

$$u^T y = \dot{V}(x) \quad \forall (x, u) \in \mathbb{R}^n \times \mathbb{R}^p$$

and it is strictly passive if it is passive and for some positive definite function $\phi(x)$

$$u^T y \geq \dot{V}(x) + \phi(x) \quad \forall (x, u) \in \mathbb{R}^n \times \mathbb{R}^p$$

For a linear time-invariant system with a minimal realisation [51]

$$\dot{x} = Ax + Bu \tag{2.12a}$$

$$y = Cx + Du \tag{2.12b}$$

where $A \in \mathbb{R}^{n \times n}, B \in \mathbb{R}^{n \times p}, C \in \mathbb{R}^{p \times n}$ and $D \in \mathbb{R}^{p \times p}$, the passivity of the system is closely related to the positive realness of the transfer function $G(s) = C(sI - A)^{-1}B + D$ where $G(s)$ has $p \times p$ elements. A pole of any element of $G(s)$ is called a pole of $G(s)$.

Definition 9. ***(Positive realness)*** *The transfer function $G(s)$ is said to be positive real if all the following three conditions are satisfied*

1. *$G(s)$ has no poles with positive real part. Equivalently, A has no eigenvalue with positive real part.*
2. *The matrix $G(j\omega) + G^T(-j\omega)$ is positive semidefinite for all real w for which $j\omega$ is not a pole of $G(s)$.*
3. *The order of any pure imaginary pole $j\omega$ of $G(s)$ is 1 and $\lim_{s\to j\omega}(s - j\omega)G(s)$ is positive semidefinite.*

The transfer function $G(s)$ is strictly passive if there exists a constant ε such that $G(s-\varepsilon)$ is positive real.

We can now relate the positive realness of the transfer function to the passivity of the system.

Lemma 1. *A linear time-invariant system with a minimal realisation (2.12) is passive if its transfer function $G(s)$ is positive real. The system is strictly passive if $G(s)$ is strictly positive real.*

It is usually difficult to determine the positive realness of a transfer function by checking whether it satisfies the definition. A more straightforward method is given by the positive real lemma.

Lemma 2. ***(Positive real lemma)*** *The transfer function $G(s)$ is positive real if and only if there exist matrices $P = P^T > 0$, L and W such that*

$$PA + A^TP = -L^TL \tag{2.13a}$$

$$PB = C^T - L^TW \tag{2.13b}$$

$$W^TW = D + D^T \tag{2.13c}$$

For strict positive realness, the following lemma holds.

Lemma 3. ***(Kalman-Yakubovich-Popov (KYP) lemma)*** *[70] The transfer function $G(s)$ is strictly positive real if and only if there exist matrices $P = P^T > 0$, L and W, and a constant $\varepsilon > 0$ such that*

$$PA + A^TP = -L^TL - \varepsilon P \tag{2.14a}$$

$$PB = C^T - L^TW \tag{2.14b}$$

$$W^TW = D + D^T \tag{2.14c}$$

2.2.4 Passivity theorems

We now consider the feedback connection of two systems H_1 and H_2, as shown in Figure 2.1. Each of the subsystems H_1 and H_2 is either a time-invariant dynamical system described by

$$\begin{aligned} \dot{x}_i &= f_i(x_i, e_i) && \text{(2.15a)} \\ y_i &= h_i(x_i, e_i) && \text{(2.15b)} \end{aligned}$$

or a memoryless system described by

$$y_i = h_i(t_i, e_i) \tag{2.16}$$

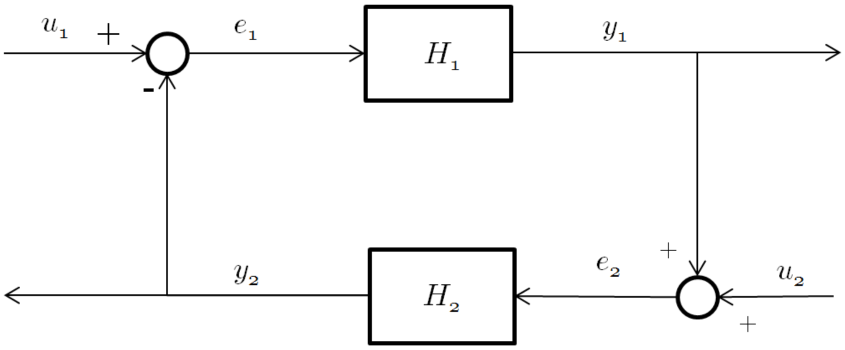

Figure 2.1: Diagram of feedback connection.

The feedback connection can be regarded as a closed-loop system and the following theorem can be easily proved [86].

Theorem 4. ***(Passivity theorem 1)*** *The feedback connection of Figure 2.1 is passive if both H_1 and H_2 are passive.*

The stability of such a feedback connection is addressed in the following theorem [86].

Theorem 5. ***(Passivity theorem 2)*** *Consider the feedback connection of Figure 2.1. Let H_1 be a strictly passive, time-invariant dynamical system and H_2 be a passive, memoryless system. The origin of the closed-loop system without input is asymptotically stable. Moreover, if the storage function for H_1 is radially unbounded, the origin is globally asymptotically stable.*

The state variables considered so far are real-valued, i.e., $x \in \mathbb{R}^n$. It should be noted that the definitions and theorems discussed in this section can be readily extended to the complex space such that $x \in \mathbb{C}^n$ with only slight modifications.

2.3 Spatial discretisation

In the previous section, all the systems under consideration were finite-dimensional, which means that they were governed by a finite number of ODEs. However, the motion of plane channel flow is described by the NSEs, which are nonlinear PDEs. Therefore the fluid flow system of interest is infinite-dimensional. Systems governed by PDEs can be studied in the framework of infinite-dimensional system theory [41], but generally it is difficult to show the well-posedness of the systems [143]. Moreover, only under rare circumstances can the linear stability of an infinite-dimensional system be determined analytically. In practice, infinite-dimensional systems are usually approximated by finite-dimensional models. To achieve this, the governing equations need to be discretised spatially. Among the most commonly used methods are the finite difference methods (FDM) [96], the finite element methods (FEM) [124] and spectral methods [20]. In the past few decades, especially in CFD, spectral methods have gained increasing popularity due to their high-order accuracy. In fact, the critical Reynolds number $\mathrm{Re}_c = 5772.22$ for plane Poiseuille flow was first accurately calculated by Orszag using spectral methods [112]. In this thesis, we will use spectral methods for spatial discretisation and in this section we give a brief introduction to spectral methods. More details can be found in [20] [153] [25] [85].

Using an infinite sequence of orthogonal functions $\phi_k(x)$ to represent a continuous function $u(x)$ is an old idea that can at least be traced back to Fourier's approach to solve the heat equation and it is now a standard technique to use trigonometric series to approximate a periodic function. When the function u is sufficiently smooth, in the sense that it is infinitely differentiable with periodic derivatives, the k_{th} coefficient of the approximation $u(x) = \sum_{k=0}^{\infty} \hat{u}_k \phi_k(x)$ decays faster than any algebraic power of k. As a result, the infinite series can be truncated to finite series and the function can still be approximated with great accuracy, which is referred to as spectral accuracy in the literature.

However, while spectral accuracy is always desirable, in practice not all functions are periodic. When it comes to nonperiodic functions, it turns out that similar results also hold true, as shown by the Weierstrass approximation theorem [154].

Theorem 6. ***(Weierstrass approximation theorem)*** *Let $u(x)$ be a continuous function in $x \in [-1, 1]$. For any $\epsilon > 0$, there exists a polynomial p such that*

$$\|u - p\|_\infty < \epsilon$$

Weierstrass approximation theorem established the fact that a continuous function on a bounded domain can be approximated arbitrarily accurate by polynomials. Generally, the function $u(x)$ does not even have to be smooth, but in order to achieve spectral accuracy, not only the function $u(x)$ is required to be smooth, but also the basis functions $\phi_k(x)$ have to be carefully chosen.

We note that it is also possible to expand nonperiodic functions into Fourier series. The basic idea is simple and natural: extending the nonperiodic function $u(x)$ in $x \in [-1, 1]$ to a periodic function on a larger interval. Such an extension is a fascinating subject itself and more details can be found in [76].

2.3.1 Method of weighted residual

Consider a differential equation in a domain $\Omega : (x, t) \in [-1, 1] \times [0, \infty]$

$$\mathcal{L}(u(x,t)) = 0 \tag{2.17}$$

with boundary conditions

$$\mathcal{B}(u(x,t)) = 0 \quad \text{at } x = \pm 1 \tag{2.18}$$

where $\mathcal{L}$ and $\mathcal{B}$ are some well defined operators. Except in some simple cases, it is generally not possible to solve the equation analytically. To solve the problem numerically, the solution $u(x, t)$ is approximated by $u^\delta(x, t)$, which is formed by truncating an infinite series

$$u^\delta(x,t) = \sum_{k=0}^{N} \hat{u}_k(t)\phi_k(x) \tag{2.19}$$

where $\phi_k(x)$ are called trial functions or basis functions and $\hat{u}_k(t)$ are the coefficients of the trial functions at time t.

Due to the error introduced by the truncation, the following equation

$$\mathcal{L}(u^\delta(x,t)) = 0 \tag{2.20}$$

usually cannot be satisfied everywhere in the domain Ω (otherwise $u^\delta(x, t)$ is an exact solution to the original problem (2.17), which means we find the analytical solution), and we define the residual as

$$R(u^\delta) = \mathcal{L}(u^\delta) \tag{2.21}$$

The $N + 1$ unknown coefficients $\hat{u}_k$ can be determined by solving $N + 1$ equations. The weighted residual method places $N + 1$ constraints on the residual in the following form

$$\langle R, v_k \rangle = 0, \quad k = 0, 1, \cdots, N \tag{2.22}$$

where $v_k(x)$ are called test functions and the inner product $\langle , \rangle$ is defined by

$$\langle f, g\rangle = \int_{x=-1}^{x=1} f(x)g(x)^* w(x)\mathrm{d}x \tag{2.23}$$

with $*$ denoting complex conjugate and $w(x)$ being the weight function, which is usually constructed to make the trial functions orthogonal and in many cases has the simple form $w(x) = 1$. By choosing different trial functions and test functions, we arrive at different spectral methods.

Collocation method: In the case that the test function is the Dirac function $v_k(x) = \delta(x - x_k)$ and $w(x) = 1$, where x_k are a set of collocation points, the method is called spectral collocation method. Essentially, it means that the residual is only required to be zero at the collocation points instead of being zero everywhere. Since we should also impose the boundary conditions, we have $N + 3$ equations with only $N + 1$ unknowns. It is straightforward to get around this difficulty: we simply delete the two equations obtained using the test function $v_0(x)$ and $v_N(x)$. It should also be noted that the spectral coefficients $\hat{u}_k$ are usually not calculated explicitly in the collocation method.

Galerkin method: When the trial functions $\phi_k(x)$ satisfy the boundary conditions, i.e.,

$$\mathcal{B}(\phi_k(1)) = \mathcal{B}(\phi_k(-1)) = 0 \tag{2.24}$$

and the test functions are chosen to be the same as the trial functions $v_k(x) = \phi_k(x)$, the method is called spectral Galerkin method. Once appropriate trial functions are found, there is no extra need to impose the boundary conditions. However, in practice it is not always possible to find such trial functions. For the same reason, it is usually not applicable to problems with time dependent boundary conditions. We note that usually in this method the trial functions are no longer orthogonal because of its requirement to satisfy the boundary conditions.

Spectral tau method: If it is difficult to find suitable trial functions that satisfy the boundary conditions, it is reasonable to relax this requirement. In spectral tau method, the test functions are once again chosen to be the same as the trial functions, but the trial functions do not have to satisfy the boundary conditions. The imposition of the boundary conditions now is different from that in the collocation method. We have to replace the two equations obtained using the test functions $v_{N-1}(x)$ and $v_N(x)$ with the two equations obtained from the boundary conditions. As a result, the tau method enjoys far more flexibility than the Galerkin method.

The methods described above are not the only weighted residual methods, but this thesis will only use these three methods, which are the most widely used spectral methods. The name of a particular spectral method is often associated with the basis functions. For example, when the Chebyshev polynomials are used as the trial functions, the spectral methods are frequently referred to as Chebyshev collocation method, Chebyshev Galerkin method and Chebyshev tau method. We note in some references, the tau method is also called the Galerkin method [20], but in this thesis we emphasise the difference between these two methods by using different terms, as in [163].

2.3.2 Periodic functions

A periodic function $u(x)$ in $x \in [0, 2\pi]$ can be expanded as the Fourier series

$$u(x) = \sum_{k=-\infty}^{\infty} \hat{u}_k \phi_k(x) \tag{2.25}$$

where the trial functions

$$\phi_k(x) = \mathrm{e}^{\mathrm{i}kx} \tag{2.26}$$

are periodic and satisfy the orthogonal condition

$$\int_{x=0}^{x=2\pi} \phi_i^*(x)\phi_j(x)\mathrm{d}x = 2\pi\delta_{ij} \tag{2.27}$$

with δ_{ij} denoting the Kronecker delta function

$$\delta_{ij} = \begin{cases} 1, & i = j, \\ 0, & i \neq j. \end{cases} \tag{2.28}$$

To determine the coefficients $\hat{u}_k$, we apply the weighted residual method with test functions $v_k(x) = \mathrm{e}^{\mathrm{i}kx}$, then

$$\hat{u}_k = \frac{1}{2\pi}\int_{x=0}^{x=2\pi} u(x)\mathrm{e}^{-\mathrm{i}kx}\mathrm{d}x \tag{2.29}$$

Suppose that $u(x)$ is infinitely differentiable with all the derivatives periodic in $x \in [0, 2\pi]$, then it follows from integration by parts that

$$\hat{u}_k = \frac{1}{2\pi}\frac{1}{(\mathrm{i}k)^p}\int_{x=0}^{x=2\pi} u^{(p)}(x)\mathrm{e}^{-\mathrm{i}kx}\mathrm{d}x \tag{2.30}$$

where p is any positive integer and $u^{(p)}(x)$ is the p_{th} derivative of $u(x)$. As a result, $\hat{u}_k$ decays faster than any algebraic power due to the presence of the term $\frac{1}{(\mathrm{i}k)^p}$. When the function is not infinitely differentiable, the integration by parts has to stop at some point, which means that the coefficients can only decay in algebraic rate. An example is the triangular wave function, which is continuous but not differentiable.

In practice, we usually have to approximate the function $u(x)$ by the truncation of the Fourier series

$$P_N u(x) = \sum_{k=-N/2}^{k=N/2} \hat{u}_k \mathrm{e}^{\mathrm{i}kx} \tag{2.31}$$

where P_N is seen as a projection onto a continuous domain.

In many problems encountered, the exact calculation of the coefficients $\hat{u}_k$ by equation (2.29) is either not possible or very inefficient. To overcome this difficulty, the Fourier coefficients can be calculated by numerical integration

$$\tilde{u}_k = \frac{1}{N} \sum_{j=0}^{N-1} u(x_j) \mathrm{e}^{\mathrm{i}kx_j}, \quad k = -N/2, \cdots, N/2-1 \tag{2.32}$$

where the Fourier collocation points are defined by

$$x_j = \frac{2\pi j}{N}, \quad j = 0, 1, \cdots, N-1 \tag{2.33}$$

Equation (2.32) gives the formula of discrete Fourier transform (DFT), which can be computed efficiently by fast Fourier transform (FFT) algorithms [38]. As a consequence, the function $u(x)$ can be approximated by

$$I_N u(x) = \sum_{k=-N/2}^{k=N/2} \tilde{u}_k \mathrm{e}^{\mathrm{i}kx} \tag{2.34}$$

which is known as the discrete Fourier series of u. It can be shown that $I_N u(x_j) = u(x_j)$ where x_j are the Fourier collocation points and $I_N u(x)$ is an interpolation at the collocation points x_j.

The use of discrete Fourier transform can introduce aliasing errors due to the following relation

$$\tilde{u}_k = \hat{u}_k + \sum_{m=-\infty, m\neq 0}^{\infty} \hat{u}_{k+Nm}, \quad k = -N/2, \cdots, N/2-1 \tag{2.35}$$

and increasing N can reduce the error. For more details about aliasing errors, see [153] [25]. The complexity of calculating the Fourier series of a nonlinear function $u(x)v(x)$ in a naive way is $\mathrm{O}(N^2)$, which is expensive. In fact, the cost of dealing with nonlinearity used to be a serious barrier to applying spectral methods to nonlinear differential equations. A method to overcome this difficulty is now known as the 3/2 rule [25] and will be discussed in Chapter 4.

2.3.3 Nonperiodic functions

The Chebyshev polynomials of the first kind $T_k(x)$ are the most frequently used basis functions to approximate nonperiodic functions in the domain $x \in [-1, 1]$. The polynomial is defined by

$$T_k(x) = \cos(k\theta), \quad \theta = \arccos(x) \tag{2.36}$$

The fact that after a change of variable the Chebyshev polynomials are cosine functions is the reason for their popularity. From the trigonometric identities, it is easy to derive the following iterative relation

$$T_{k+1}(x) = 2xT_k(x) - T_{k-1}(x), \quad k = 1, \cdots, N \tag{2.37}$$

The first few Chebyshev polynomials are

$$\begin{aligned} T_0(x) &= 1 \\ T_1(x) &= x \\ T_2(x) &= 2x^2 - 1 \\ T_3(x) &= 4x^3 - 3x \end{aligned}$$

The Chebyshev polynomials are orthogonal in the sense that

$$\int_{x=-1}^{x=1} \frac{1}{\sqrt{1-x^2}} T_i(x) T_j(x) \mathrm{d}x = \frac{\pi}{2} c_i \delta_{ij} \tag{2.38}$$

where again δ_{ij} is the Kronecker delta function and c_i is defined by

$$c_i = \begin{cases} 2, & i = 0, \\ 1, & i > 0. \end{cases} \tag{2.39}$$

$u(x)$ now can be approximated by the projection

$$P_N u(x) = \sum_{k=0}^{N} \hat{u}_k T_k(x) \tag{2.40}$$

Similar to the case of Fourier approximation, the Chebyshev coefficients $\hat{u}_k$ can be determined by applying the weighted residual method, with test functions $T_k(x)$ and weight function $w(x) = \frac{1}{\sqrt{1-x^2}}$, so that

$$\hat{u}_k = \frac{2}{\pi c_k} \int_{x=-1}^{x=1} u(x) T_k(x) w(x) \mathrm{d}x \tag{2.41}$$

By the same argument, the Chebyshev coefficients of a sufficiently smooth function decays faster than algebraically. Once again, the coefficients can be more conveniently calculated by numerical integration. When $p(x)$ is a polynomial of order less than $2N-1$, the following integration can be calculated exactly by

$$\int_{x=-1}^{x=1} p(x)\mathrm{d}x = \sum_{j=0}^{N} p(x_j)q(x_j) \tag{2.42}$$

where the Chebyshev Gauss-Lobatto points x_j are defined by

$$x_j = \cos\frac{\pi j}{N}, \quad j = 0, 1, \cdots, N \tag{2.43}$$

and $q(x_j)$ are carefully chosen quadrature weight [153]. The discrete Chebyshev coefficients can then be calculated by

$$\tilde{u}_k = \frac{1}{\gamma_k}\sum_{j=0}^{N} u(x_j)T_k(x_j)q(x_j) \tag{2.44}$$

where

$$\gamma_k = \begin{cases} \frac{\pi}{2}c_k, & k < N, \\ \pi, & k = N. \end{cases} \tag{2.45}$$

This is an analogue to the discrete Fourier transform and is called the discrete polynomial transform.

The polynomial of degree N that interpolates at x_j to approximate $u(x)$ is given by

$$I_N u(x) = \sum_{k=0}^{N} \tilde{u}_k T_k(x) \tag{2.46}$$

It turns out that the Chebyshev polynomials are only one special kind of Jacobi polynomials [25], which are the eigenfunctions of the singular Sturm-Liouville eigenvalue problem in $x \in [-1, 1]$

$$-((1-x)^{1+\alpha}(1+x)^{1+\beta}u')' = \lambda(1-x)^{\alpha}(1+x)^{\beta} \tag{2.47}$$

where the prime denotes first derivative and $-1 \leq \alpha, \beta \leq 1$. The Chebyshev polynomials are Jacobi polynomials with $\alpha = \beta = 0.5$. Like the Chebyshev polynomials, other Jacobi polynomials can be used to approximate nonperiodic functions. The flexibility of choosing α and β means that the collocation points can be chosen with more degrees of freedom, which sometimes can lead to advantages [148]. Another special kind of Jacobi polynomials are the Legendre polynomials with $\alpha = \beta = 0$. The use of the Legendre polynomials as the basis functions in spectral methods is common in the literature. For example, Legendre Galerkin method was used in [146] to calculate the eigenvalues of a flow in a duct. In [139], basis functions based on the Legendre polynomials were proposed to efficiently solve some second and fourth order PDEs. Note that the existence of the fast cosine transform algorithm gives the Chebyshev polynomials a decisive advantage over other Jacobi polynomials.

2.3.4 Differentiation

Once the function $u(x)$ is approximated by a finite series (either a projection or an interpolation), it is straightforward to calculate the derivatives. In the case that $u(x)$ is periodic, we have

$$(P_N u(x))' = \sum_{k=-N/2}^{k=N/2} \mathrm{i}k\hat{u}_k \mathrm{e}^{\mathrm{i}kx} \tag{2.48}$$

$$(I_N u(x))' = \sum_{k=-N/2}^{k=N/2} \mathrm{i}k\tilde{u}_k \mathrm{e}^{\mathrm{i}kx} \tag{2.49}$$

It is worth noting that while $(P_N u(x))' = P_N u'(x)$, generally $(I_N u(x))' \neq I_N u'(x)$.

In the case that $u(x)$ is nonperiodic,

$$(P_N u(x))' = \sum_{k=0}^{k=N} \hat{u}_k T_k'(x) \tag{2.50}$$

$$P_N u'(x) = \sum_{k=0}^{k=N} \hat{u}_k^{(1)} T_k(x) \tag{2.51}$$

where

$$\hat{u}_k^{(1)} = \frac{2}{c_k} + \sum_{p=k+1, p+k \text{ odd}} p\hat{u}_p, \quad k \geq 0 \tag{2.52}$$

which can be derived from the trigonometric identities. Note that $(P_N u(x))' \neq P_N u'(x)$.

As mentioned previously, the discrete spectral coefficients $\tilde{u}_k$ are rarely computed explicitly in the collocation method. Instead, the differentiation is simply obtained by the matrix multiplication $\mathbf{u}' = \mathbf{D}\mathbf{u}$ where $\mathbf{u}$ is the vector obtained by evaluating $u(x)$ at the collocation points and $\mathbf{D}$ is the differentiation matrix. We use a simple example to illustrate the reason that the differentiation can be computed in this way. Suppose $u(x)$ is interpolated by

$$I_N u(x) = \sum_{k=0}^{N} \tilde{u}_k \phi_k(x) \tag{2.53}$$

Since it is an interpolation, we have $\mathbf{u} = \mathbf{T}\tilde{\mathbf{u}}$ where

$$\underset{\mathbf{u}}{\begin{bmatrix} u(x_0) \\ \vdots \\ u(x_N) \end{bmatrix}} = \underset{\mathbf{T}}{\begin{bmatrix} \phi_0(x_0) & \cdots & \phi_N(x_0) \\ \vdots & \ddots & \vdots \\ \phi_0(x_N) & \cdots & \phi_N(x_N) \end{bmatrix}} \underset{\tilde{\mathbf{u}}}{\begin{bmatrix} \tilde{u}_0 \\ \vdots \\ \tilde{u}_N \end{bmatrix}} \tag{2.54}$$

The matrix $\mathbf{T}$ is guaranteed to be nonsingular because the basis functions $\phi_k(x)$ form a complete set, provided the collocation points are distinct. Therefore $\tilde{\mathbf{u}} = \mathbf{T}^{-1}\mathbf{u}$. Similarly,

$$\underbrace{\begin{bmatrix} (I_N u)'(x_0) \\ \vdots \\ (I_N u)'(x_N) \end{bmatrix}}_{\mathbf{u}'} = \underbrace{\begin{bmatrix} \phi_0'(x_0) & \cdots & \phi_N'(x_0) \\ \vdots & \ddots & \vdots \\ \phi_0'(x_N) & \cdots & \phi_N'(x_N) \end{bmatrix}}_{\mathbf{T}'} \underbrace{\begin{bmatrix} \tilde{u}_0 \\ \vdots \\ \tilde{u}_N \end{bmatrix}}_{\tilde{\mathbf{u}}} \tag{2.55}$$

where $\phi'(x)$ is the first derivative of $\phi(x)$. Now

$$\mathbf{u}' = \mathbf{T}'\tilde{\mathbf{u}} = \mathbf{T}'\mathbf{T}^{-1}\mathbf{u} = \mathbf{D}\mathbf{u} \tag{2.56}$$

Higher order differentiation matrices can be obtained in a similar manner. We stress that this is only served as an example to show the principle of differentiation in the collocation method. In practice, in order to improve both the accuracy and efficiency, the differentiation matrices are not computed in the way described above. Precise formulas of each elements of the matrices are usually derived by using the properties of the basis functions. Fourier and Chebyshev differentiation matrices can be accurately generated by the matrix suite provided by Weideman and Reddy [161]. The MATLAB code in [141] can be used to calculate Legendre and Jacobi differentiation matrices.

2.3.5 Higher dimensions

So far only the approximation of functions with one spatial dimension has been discussed. Now consider a nonperiodic function $u(x, y)$ in the standard domain Ω: $(x, y) \in [-1, 1] \times [-1, 1]$. It is evident that the function can be approximated by the truncation

$$P_N u(x, y) = \sum_{i=0}^{N_x} \sum_{j=0}^{N_y} \hat{u}_{ij} T_i(x) T_j(y) \tag{2.57}$$

or the corresponding interpolation $I_N u(x, y)$. Differentiation matrices in 2-dimensional space can be readily obtained by Kronecker product. For example, $\frac{\partial^2 u}{\partial x \partial y}$ can be numerically calculated by $\mathbf{D}_x \bigotimes \mathbf{D}_y \mathbf{u}$ where $\bigotimes$ denotes Kronecker product, $\mathbf{D}_x$ and $\mathbf{D}_y$ are first order differentiation matrices in x and y directions, respectively and $\mathbf{u}$ is the vector stacking the values of $u(x, y)$ at all the collocation points. See [153] for a more detailed illustration.

2.4 Equations of motion of channel flow

As stated in Chapter 1, in 3-dimensional Cartesian coordinates (x, y, z), the flow of an isothermal, incompressible viscous fluid can be described by the dimensionless NSEs

(1.5). Here we rewrite the equations for ease of reference

$$\frac{\partial u}{\partial t}+u\frac{\partial u}{\partial x}+v\frac{\partial u}{\partial y}+w\frac{\partial u}{\partial z}=-\frac{\partial p}{\partial x}+\frac{1}{\mathrm{Re}}\nabla^2 u+f_x \tag{2.58a}$$

$$\frac{\partial v}{\partial t}+u\frac{\partial v}{\partial x}+v\frac{\partial v}{\partial y}+w\frac{\partial v}{\partial z}=-\frac{\partial p}{\partial y}+\frac{1}{\mathrm{Re}}\nabla^2 v+f_y \tag{2.58b}$$

$$\frac{\partial w}{\partial t}+u\frac{\partial w}{\partial x}+v\frac{\partial w}{\partial y}+w\frac{\partial w}{\partial z}=-\frac{\partial p}{\partial z}+\frac{1}{\mathrm{Re}}\nabla^2 w+f_z \tag{2.58c}$$

$$\frac{\partial u}{\partial x}+\frac{\partial v}{\partial y}+\frac{\partial w}{\partial z}=0 \tag{2.58d}$$

where $u(x,y,z,t)$, $v(x,y,z,t)$ and $w(x,y,z,t)$ are the components of the velocity of the fluid in the x, y and z directions, respectively, $f_x(x,y,z,t)$, $f_y(x,y,z,t)$ and $f_z(x,y,z,t)$ are the components of the external force in each of these directions, $p(x,y,z,t)$ is the pressure, and ∇^2 is the Laplace operator

$$\nabla^2=\frac{\partial^2}{\partial x^2}+\frac{\partial^2}{\partial y^2}+\frac{\partial^2}{\partial z^2} \tag{2.59}$$

Re is the Reynolds number, which is defined by

$$\mathrm{Re}=\frac{\rho U_{\mathrm{c}} L_{\mathrm{c}}}{\mu} \tag{2.60}$$

with U_c being the velocity of the steady state flow at the centreline for plane Poiseuille flow and the velocity of the upper plate for plane Couette flow, L_c being the half width of the channel, ρ being the fluid density and μ being the dynamic viscosity.

Taking the steady state $(U,0,0,P)$ as the base flow, a perturbed state can be described by $(U+u,v,w,P+p)$ together with an external force (f_x,f_y,f_z). As mentioned in Chapter 1, the steady state velocity has the form $U=1-y^2$ for plane Poiseuille flow and $U=y$ for plane Couette flow. Both the steady state and the perturbed state satisfy the NSEs. Subtracting the equations for the steady state and the perturbed state leads to the nonlinear disturbance equations

$$\frac{\partial u}{\partial t}+U\frac{\partial u}{\partial x}+vU'+S_1=-\frac{\partial p}{\partial x}+\frac{1}{\mathrm{Re}}\nabla^2 u+f_x \tag{2.61a}$$

$$\frac{\partial v}{\partial t}+U\frac{\partial v}{\partial x}+S_2=-\frac{\partial p}{\partial y}+\frac{1}{\mathrm{Re}}\nabla^2 v+f_y \tag{2.61b}$$

$$\frac{\partial w}{\partial t}+U\frac{\partial w}{\partial x}+S_3=-\frac{\partial p}{\partial z}+\frac{1}{\mathrm{Re}}\nabla^2 w+f_z \tag{2.61c}$$

$$\frac{\partial u}{\partial x}+\frac{\partial v}{\partial y}+\frac{\partial w}{\partial z}=0 \tag{2.61d}$$

where U' denotes $\frac{\mathrm{d}U}{\mathrm{d}y}$ and

$$S_1 = u\frac{\partial u}{\partial x} + v\frac{\partial u}{\partial y} + w\frac{\partial u}{\partial z} \tag{2.62a}$$

$$S_2 = u\frac{\partial v}{\partial x} + v\frac{\partial v}{\partial y} + w\frac{\partial v}{\partial z} \tag{2.62b}$$

$$S_3 = u\frac{\partial w}{\partial x} + v\frac{\partial w}{\partial y} + w\frac{\partial w}{\partial z} \tag{2.62c}$$

No-slip boundary conditions are assumed on the walls

$$u(y = \pm 1) = v(y = \pm 1) = w(y = \pm 1) = 0 \tag{2.63}$$

It follows from the continuity equation (2.61d) that

$$\frac{\partial v}{\partial y}(y = \pm 1) = 0 \tag{2.64}$$

To study the evolution of the flow system subject to an initial perturbation, it is desirable to quantify the size of the disturbance at given time t. One natural choice is to define the kinetic energy of the disturbance in a volume Ω as

$$E(t) = \frac{1}{2}\int_{\Omega} (u^2 + v^2 + w^2)\,\mathrm{d}\Omega \tag{2.65}$$

then $E(t)$ gives a description how the disturbance develops over time [133].

2.4.1 State space model

As mentioned in Chapter 1, the velocity-vorticity formulation is more commonly used than the primitive variable formulation in the literature of hydrodynamic stability and flow control. One advantage of the velocity-vorticity formulation is that the number of state variables is reduced to two. By contrast, there are four state variables in the primitive variable formulation. Additionally, the model in the primitive variable formulation is differential-algebraic, while the difficulties associated with differential-algebraic models can be avoided in the velocity-vorticity form. As a tradeoff, higher spatial derivatives have to be calculated in the velocity-vorticity form, which could potentially cause numerical issues when the solutions are not sufficiently smooth.

The derivation of the velocity-vorticity formulation is standard practice and can be found in many references, for example, [133]. For completeness, we now briefly describe how to write the disturbance equations into the form. Taking the divergence of the momentum equations (2.61a)-(2.61c) and using the continuity equation (2.61d) gives

$$-\nabla^2 p = 2U'\frac{\partial v}{\partial x} + \left(\frac{\partial S_1}{\partial x} + \frac{\partial S_2}{\partial y} + \frac{\partial S_3}{\partial z}\right) - \left(\frac{\partial f_x}{\partial x} + \frac{\partial f_y}{\partial y} + \frac{\partial f_z}{\partial z}\right) \tag{2.66}$$

This equation and (2.61b) can be used to eliminate p so that

$$\begin{aligned}\left(\frac{\partial}{\partial t}+U\frac{\partial}{\partial x}\right)\nabla^2 v-U''\frac{\partial v}{\partial x}-\frac{1}{\mathrm{Re}}\nabla^4 v=&\frac{\partial^2 S_1}{\partial y\partial x}-\left(\frac{\partial^2 S_2}{\partial x^2}+\frac{\partial^2 S_2}{\partial z^2}\right)+\frac{\partial^2 S_3}{\partial y\partial z}\\ &-\frac{\partial^2 f_x}{\partial y\partial x}+\left(\frac{\partial^2 f_y}{\partial x^2}+\frac{\partial^2 f_y}{\partial z^2}\right)-\frac{\partial^2 f_z}{\partial y\partial z}\end{aligned} \tag{2.67}$$

Defining the normal vorticity as

$$\eta=\frac{\partial u}{\partial z}-\frac{\partial w}{\partial x} \tag{2.68}$$

an expression for the evolution of the vorticity can be obtained by taking $\frac{\partial}{\partial z}$ of (2.61a) and $\frac{\partial}{\partial x}$ of (2.61c) and then subtracting the two resulting equations to give

$$\frac{\partial \eta}{\partial t}+U\frac{\partial \eta}{\partial x}+U'\frac{\partial v}{\partial z}-\frac{1}{\mathrm{Re}}\nabla^2\eta=\frac{\partial(f_x-S_1)}{\partial z}-\frac{\partial(f_z-S_2)}{\partial x} \tag{2.69}$$

The evolution of the flow is described in terms of v and η, and for this reason, this form of NSEs is known as the velocity-vorticity formulation. The description of the system is completed by expressions for u and w in terms of v and η. From (2.61d) and (2.68),

$$\left(\frac{\partial^2}{\partial x^2}+\frac{\partial^2}{\partial z^2}\right)u=-\frac{\partial^2 v}{\partial x\partial y}+\frac{\partial \eta}{\partial z} \tag{2.70}$$

$$\left(\frac{\partial^2}{\partial x^2}+\frac{\partial^2}{\partial z^2}\right)w=-\frac{\partial^2 v}{\partial z\partial y}-\frac{\partial \eta}{\partial x} \tag{2.71}$$

Equations (2.67) and (2.69)-(2.71) can be combined to give

$$\dot{\mathbf{x}} = \mathcal{A}\mathbf{x}+\mathcal{B}\mathbf{f}-\mathcal{B}\mathbf{S} \tag{2.72a}$$

$$\mathbf{y} = \mathcal{C}\mathbf{x} \tag{2.72b}$$

where $\mathbf{x}=\begin{bmatrix}v & \eta\end{bmatrix}^{\mathrm{T}}$, $\mathbf{f}=\begin{bmatrix}f_x & f_y & f_z\end{bmatrix}^{\mathrm{T}}$, $\mathbf{S}=\begin{bmatrix}S_1 & S_2 & S_3\end{bmatrix}^{\mathrm{T}}$, $\mathbf{y}=\begin{bmatrix}u & v & w\end{bmatrix}^{\mathrm{T}}$ and $\mathcal{A},\mathcal{B},\mathcal{C}$ and $\mathcal{E}$ are the operators

$$\mathcal{A}=\mathcal{E}^{-1}\begin{bmatrix}-U\frac{\partial}{\partial x}\nabla^2+U''\frac{\partial}{\partial x}+\frac{1}{\mathrm{Re}}\nabla^4 & 0\\ -U'\frac{\partial}{\partial z} & -U\frac{\partial}{\partial x}+\frac{1}{\mathrm{Re}}\nabla^2\end{bmatrix} \tag{2.73}$$

$$\mathcal{B}=\mathcal{E}^{-1}\begin{bmatrix}-\frac{\partial^2}{\partial x\partial y} & \frac{\partial^2}{\partial x^2}+\frac{\partial^2}{\partial z^2} & -\frac{\partial^2}{\partial y\partial z}\\ \frac{\partial}{\partial z} & 0 & -\frac{\partial}{\partial x}\end{bmatrix} \tag{2.74}$$

$$\mathcal{E}=\begin{bmatrix}\nabla^2 & 0\\ 0 & 1\end{bmatrix} \tag{2.75}$$

$$\mathcal{C} = \begin{bmatrix} \dfrac{\partial^2}{\partial x^2} + \dfrac{\partial^2}{\partial z^2} & 0 & 0 \\ 0 & 1 & 0 \\ 0 & 0 & \dfrac{\partial^2}{\partial x^2} + \dfrac{\partial^2}{\partial z^2} \end{bmatrix}^{-1} \begin{bmatrix} -\dfrac{\partial^2}{\partial x \partial y} & \dfrac{\partial}{\partial z} \\ 1 & 0 \\ -\dfrac{\partial^2}{\partial z \partial y} & -\dfrac{\partial}{\partial x} \end{bmatrix} \tag{2.76}$$

The mapping from $\mathbf{y}$ to $\mathbf{S}$ can be viewed as a memoryless nonlinearity of the form $\mathbf{S} = \Delta(\mathbf{y})$. As shown in Figure 2.2, the system can be regarded as the feedback connection between the linear time-invariant system $(\mathcal{A}, \mathcal{B}, \mathcal{C})$, and a memoryless nonlinearity $\Delta(.)$, with $\mathbf{f}$ acting as an external input to the system. The input to the linear system is thus $\mathbf{e} = \mathbf{f} - \mathbf{S}$.

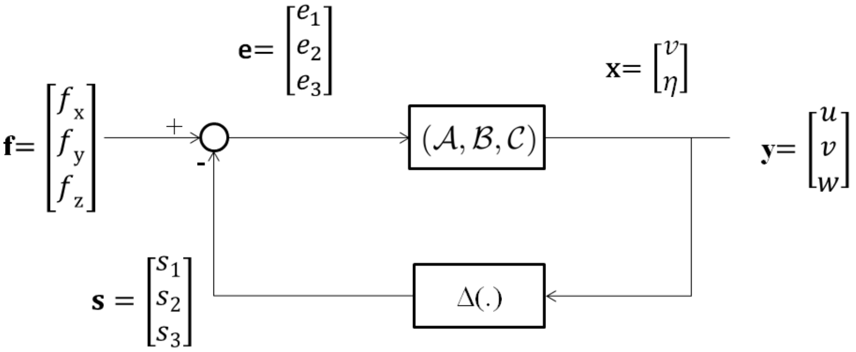

Figure 2.2: Block diagram of the fluid flow system.

2.4.2 Semi-discrete formulation

Assuming that the flow (together with the external force) is periodic in the x and z directions with periods L_x and L_z respectively, then $v(x,y,z,t)$ can be expressed in the form

$$v(x,y,z,t) = \sum_{m=-\infty}^{\infty} \sum_{n=-\infty}^{\infty} \tilde{v}_{mn}(y,t)\, \mathrm{e}^{\mathrm{i}\alpha_m x} \mathrm{e}^{\mathrm{i}\beta_n z} \tag{2.77}$$

where $\alpha_m = \frac{2\pi m}{L_x}$ and $\beta_n = \frac{2\pi n}{L_z}$ are the streamwise and spanwise wavenumbers. Similarly, $\eta(x,y,z,t)$, $u(x,y,z,t)$, $w(x,y,z,t)$, $f_x(x,y,z,t)$, $f_y(x,y,z,t)$ and $f_z(x,y,z,t)$ can also be written in the form of a Fourier series. It follows from (2.62) that the nonlinearities $S_1(x,y,z,t)$, $S_2(x,y,z,t)$ and $S_3(x,y,z,t)$ are also periodic in the x and z directions and can be expressed in terms of Fourier series.

The linear system can now be reduced to a set of decoupled systems

$$\dot{\tilde{\mathbf{x}}}_{mn} = \mathcal{A}_{mn}\tilde{\mathbf{x}}_{mn} + \mathcal{B}_{mn}\tilde{\mathbf{e}}_{mn} \tag{2.78a}$$

$$\tilde{\mathbf{y}}_{mn} = \mathcal{C}_{mn}\tilde{\mathbf{x}}_{mn} \tag{2.78b}$$

with state $\tilde{\mathbf{x}}_{mn} = \begin{bmatrix}\tilde{v}_{mn} & \tilde{\eta}_{mn}\end{bmatrix}^{\mathrm{T}}$, input $\tilde{\mathbf{e}}_{mn} = \begin{bmatrix}\tilde{e}^{(1)}_{mn} & \tilde{e}^{(2)}_{mn} & \tilde{e}^{(3)}_{mn}\end{bmatrix}^{\mathrm{T}}$, output $\tilde{\mathbf{y}}_{mn} = \begin{bmatrix}\tilde{u}_{mn} & \tilde{v}_{mn} & \tilde{w}_{mn}\end{bmatrix}^{\mathrm{T}}$ and

$$\mathcal{A}_{mn} = \begin{bmatrix}\mathcal{D}^2 - k^2_{mn} & 0\\ 0 & 1\end{bmatrix}^{-1}\begin{bmatrix}\mathcal{L}_{OS} & 0\\ -\mathrm{i}\beta_n U' & \mathcal{L}_{SQ}\end{bmatrix} \tag{2.79}$$

$$\mathcal{B}_{mn} = \begin{bmatrix}\mathcal{D}^2 - k^2_{mn} & 0\\ 0 & 1\end{bmatrix}^{-1}\begin{bmatrix}-\mathrm{i}\alpha_m\mathcal{D} & -k^2_{mn} & -\mathrm{i}\beta_n\mathcal{D}\\ \mathrm{i}\beta_n & 0 & -\mathrm{i}\alpha_m\end{bmatrix} \tag{2.80}$$

$$\mathcal{C}_{mn} = \begin{bmatrix}-k^2_{mn} & 0 & 0\\ 0 & 1 & 0\\ 0 & 0 & -k^2_{mn}\end{bmatrix}^{-1}\begin{bmatrix}-\mathrm{i}\alpha_m\mathcal{D} & \mathrm{i}\beta_n\\ 1 & 0\\ -\mathrm{i}\beta_n\mathcal{D} & -\mathrm{i}\alpha_m\end{bmatrix} \tag{2.81}$$

where $k^2_{mn} = \alpha^2_m + \beta^2_n$, $\mathcal{D}$ denotes differentiation in the y direction, and

$$\mathcal{L}_{OS} = -\mathrm{i}\alpha_m U(\mathcal{D}^2 - k^2_{mn}) + \mathrm{i}\alpha_m U'' + \frac{1}{\mathrm{Re}}(\mathcal{D}^2 - k^2_{mn})^2 \tag{2.82}$$

$$\mathcal{L}_{SQ} = -\mathrm{i}\alpha_m U + \frac{1}{\mathrm{Re}}(\mathcal{D}^2 - k^2_{mn}) \tag{2.83}$$

The operator $(\mathcal{D}^2 - k^2_{mn})^{-1}\mathcal{L}_{OS}$ is called the Orr-Sommerfeld operator and $\mathcal{L}_{SQ}$ is called the Squire operator, thus the operator $\mathcal{A}_{mn}$ is known as the Orr-Sommerfeld/Squire operator. The eigenvalues of $\mathcal{A}_{mn}$ consist of the eigenvalues of the Orr-Sommerfeld operator and the eigenvalues of the Squire operator. According to the Squire theorem, all the eigenvalues of the Squire operator have negative real parts [133], therefore the linear stability of the system is determined by the Orr-Sommerfeld operator. It is clear that the effects of the coupling term $-\mathrm{i}\beta_n U'$ cannot be reflected from eigenvalue analysis.

These state space representations are not valid when $m = n = 0$, since $\tilde{v}_{00}(y,t) = \tilde{\eta}_{00}(y,t) = 0$, so that $\tilde{u}_{00}(y,t)$ and $\tilde{w}_{00}(y,t)$ cannot be calculated in the model (2.78). In [133], the state in this mode is defined by $\tilde{\mathbf{x}}_{00} = \begin{bmatrix}\tilde{u}_{00} & \tilde{w}_{00}\end{bmatrix}^{\mathrm{T}}$, the output is the same as the input so that $\tilde{\mathbf{y}}_{00} = \tilde{\mathbf{x}}_{00}$, and the operators are

$$\mathcal{A}_{00} = \begin{bmatrix}\frac{1}{\mathrm{Re}}\mathcal{D}^2 & 0\\ 0 & \frac{1}{\mathrm{Re}}\mathcal{D}^2\end{bmatrix} \tag{2.84}$$

$$\mathcal{B}_{00} = \begin{bmatrix}1 & 0\\ 0 & 1\end{bmatrix} \tag{2.85}$$

$$\mathcal{C}_{00} = \begin{bmatrix}1 & 0\\ 0 & 1\end{bmatrix} \tag{2.86}$$

The decoupled system for each (m,n) varies continuously in the x, y and z directions and as a result, has infinite dimensions. As standard practice, a finite-dimensional approximation can be obtained by

1. replacing the Fourier series with finite sums by choosing $(m\,n) \in [-M, \dots, 0, \dots, M] \times [-N, \dots, 0, \dots, N]$, for sufficiently large M and N, and then
2. applying the Chebyshev collocation method with $K+1$ Gauss-Lobatto points in the y direction so that the differential operators $\mathcal{D}, \mathcal{D}^2$ and $\mathcal{D}^4$ are replaced by the Chebyshev differentiation matrices $\mathbf{D}_1, \mathbf{D}_2$ and $\mathbf{D}_4$, respectively, on which the boundary conditions are implicitly imposed.

This gives a finite set of $(2M+1)(2N+1)$ decoupled state space models

$$\dot{\hat{\mathbf{x}}}_{mn} = \mathbf{A}_{mn}\hat{\mathbf{x}}_{mn} + \mathbf{B}_{mn}\hat{\mathbf{e}}_{mn} \tag{2.87a}$$

$$\hat{\mathbf{y}}_{mn} = \mathbf{C}_{mn}\hat{\mathbf{x}}_{mn} \tag{2.87b}$$

where $\hat{\mathbf{x}}_{mn} \in \mathbb{C}^{2(K-1)}$, $\hat{\mathbf{e}}_{mn} \in \mathbb{C}^{3(K-1)}$, $\hat{\mathbf{y}}_{mn} \in \mathbb{C}^{3(K-1)}$ are vectors which stack the values of $\tilde{\mathbf{x}}_{mn}, \tilde{\mathbf{e}}_{mn}$ and $\tilde{\mathbf{y}}_{mn}$ at all the $K-1$ collocation points between the two end points in the y direction, $\mathbf{A}_{mn}, \mathbf{B}_{mn}$ and $\mathbf{C}_{mn}$ are discretised versions of $\mathcal{A}_{mn}, \mathcal{B}_{mn}$ and $\mathcal{C}_{mn}$, respectively

$$\mathbf{A}_{mn} = \begin{bmatrix} \mathbf{D}_2 - k_{mn}^2\mathbf{I} & \mathbf{0} \\ \mathbf{0} & \mathbf{I} \end{bmatrix}^{-1} \begin{bmatrix} \mathbf{L}_{OS} & \mathbf{0} \\ -\mathrm{i}\beta_n\mathbf{U}' & \mathbf{L}_{SQ} \end{bmatrix} \tag{2.88}$$

$$\mathbf{B}_{mn} = \begin{bmatrix} \mathbf{D}_2 - k_{mn}^2\mathbf{I} & \mathbf{0} \\ \mathbf{0} & \mathbf{I} \end{bmatrix}^{-1} \begin{bmatrix} -\mathrm{i}\alpha_m\mathbf{D}_1 & -k_{mn}^2\mathbf{I} & -\mathrm{i}\beta_n\mathbf{D}_1 \\ \mathrm{i}\beta_n\mathbf{I} & \mathbf{0} & -\mathrm{i}\alpha_m\mathbf{I} \end{bmatrix} \tag{2.89}$$

$$\mathbf{C}_{mn} = \begin{bmatrix} -k_{mn}^2\mathbf{I} & \mathbf{0} & \mathbf{0} \\ \mathbf{0} & \mathbf{I} & \mathbf{0} \\ \mathbf{0} & \mathbf{0} & -k_{mn}^2\mathbf{I} \end{bmatrix}^{-1} \begin{bmatrix} -\mathrm{i}\alpha_m\mathbf{D}_1 & \mathrm{i}\beta_n\mathbf{I} \\ \mathbf{I} & \mathbf{0} \\ -\mathrm{i}\beta_n\mathbf{D}_1 & -\mathrm{i}\alpha_m\mathbf{I} \end{bmatrix} \tag{2.90}$$

with $\mathbf{U} \in \mathbb{C}^{(K-1)\times(K-1)}$, $\mathbf{U}' \in \mathbb{C}^{(K-1)\times(K-1)}$ and $\mathbf{U}'' \in \mathbb{C}^{(K-1)\times(K-1)}$ being the diagonal matrices formed from the values of the steady state velocity and its derivatives with respect to y, at each of the sample points, $\mathbf{I}$ being the identity matrix of appropriate size, and

$$\mathbf{L}_{OS} = -\mathrm{i}\alpha_m\mathbf{U}(\mathbf{D}_2 - k_{mn}^2\mathbf{I}) + \mathrm{i}\alpha_m\mathbf{U}'' + \frac{1}{\mathrm{Re}}(\mathbf{D}_4 - 2k_{mn}^2\mathbf{D}_2 + k_{mn}^4\mathbf{I}) \tag{2.91}$$

and

$$\mathbf{L}_{SQ} = -\mathrm{i}\alpha_m\mathbf{U} + \frac{1}{\mathrm{Re}}(\mathbf{D}_2 - k_{mn}^2\mathbf{I}) \tag{2.92}$$

These models are valid for both plane Poiseuille flow and plane Couette flow. For simplicity, for the moment we only consider plane Poiseuille flow, which means that $U(y) = 1 - y^2$.

2.5 Passivity and stability

2.5.1 Passivity of the nonlinearity

The nonlinear part of the plane Poiseuille flow preserves energy in the sense that it does not contribute to the overall increase or decrease of the kinetic energy of the disturbance, which is defined by (2.65). This remarkable fact reflects the following equation

$$\int_{\Omega} (uS_1 + vS_2 + wS_3)\,\mathrm{d}\Omega = 0 \tag{2.93}$$

which can be readily proved by using integration by parts together with the divergence free condition, the periodic conditions and boundary conditions. This feature of the nonlinearity is extensively used in many energy and energy-like approaches [80] [63] [62].

Replacing all the vectors in (2.93) by the corresponding Fourier series, the memoryless nonlinear system $\Delta(.)$ can be said to be passive (or lossless, to be more precise) in the sense that

$$\langle \tilde{\mathfrak{u}}, \tilde{\mathfrak{s}} \rangle = \int_{-1}^{1} \tilde{\mathfrak{u}}^{*} \tilde{\mathfrak{s}} \mathrm{d}y = 0 \tag{2.94}$$

where

$$\tilde{\mathfrak{u}} = \left[\ldots \tilde{u}_{mn} \; \tilde{v}_{mn} \; \tilde{w}_{mn} \ldots \right]^T \tag{2.95}$$

$$\tilde{\mathfrak{s}} = \left[\ldots \tilde{S}^{(1)}_{mn} \; \tilde{S}^{(2)}_{mn} \; \tilde{S}^{(3)}_{mn} \ldots \right]^T \tag{2.96}$$

2.5.2 Passivity of the linearised flow

Since the nonlinear system is memoryless, it is relatively easy to study its passivity within the framework of infinite-dimensional theory. For dynamical systems, the situation becomes far more involved. For this reason, we choose to reduce all the infinite-dimensional decoupled linear systems (2.78) to finite-dimensional ones (2.87) by discretisation.

Given that the nonlinear part of the flow system is lossless, then using ideas from finite-dimensional systems theory, it is expected that the closed-loop flow system without external forcing is stable when the dynamical linear system $(\mathcal{A}, \mathcal{B}, \mathcal{C})$ is strictly passive. Furthermore, the linear system is expected to be strictly passive if all the linearised decoupled systems (2.87) are strictly passive.

It now remains to check the passivity of these systems. The standard definition of passive dynamical systems is given in Section 2.2. However, this definition does not apply to the flow system under consideration because the nonlinearity is lossless with respect to the inner product (2.94) rather than the standard scalar product. Consequently, there is a need to extend the definition.

Let $\mathcal{H}_1 \subset \mathbb{C}^n$ and $\mathcal{H}_2 \subset \mathbb{C}^p$ be two Hilbert spaces with inner product defined as $\langle \cdot, \cdot \rangle_{\mathcal{H}_1} : \mathcal{H}_1 \times \mathcal{H}_1 \to \mathbb{C}$ and $\langle \cdot, \cdot \rangle_{\mathcal{H}_2} : \mathcal{H}_2 \times \mathcal{H}_2 \to \mathbb{C}$, respectively. We denote an operator A from $\mathcal{H}_1$ to $\mathcal{H}_2$ as $A : \mathcal{H}_1 \to \mathcal{H}_2$.

Definition 10. ***(Adjoint)*** *For a linear operator $A : \mathcal{H}_1 \to \mathcal{H}_2$, the unique linear operator $A^\dagger : \mathcal{H}_2 \to \mathcal{H}_1$ satisfying*

$$\langle Au_1, u_2 \rangle_{\mathcal{H}_2} = \left\langle u_1, A^\dagger u_2 \right\rangle_{\mathcal{H}_1}, \qquad \forall\ u_1 \in \mathcal{H}_1, u_2 \in \mathcal{H}_2$$

is called the adjoint of A.

In the case that $\mathcal{H}_1 = \mathcal{H}_2$, A is said to be a linear operator on the Hilbert space $\mathcal{H}_1$ (or $\mathcal{H}_2$). A is called self-adjoint if $A = A^\dagger$. It is called strictly positive and denoted as $A > 0$ if it is self-adjoint and

$$\langle Au_1, u_1 \rangle_{\mathcal{H}_1} > 0, \qquad \forall\ u_1 \in \mathcal{H}_1 - \{0\}$$

Consider a finite-dimensional dynamical system

$$\dot{x}_1 = f(x_1, u_1) \tag{2.97a}$$

$$y_1 = h(x_1, u_1) \tag{2.97b}$$

where $f : \mathcal{H}_1 \times \mathcal{H}_2 \to \mathcal{H}_1$ is locally Lipschitz, $h : \mathcal{H}_1 \times \mathcal{H}_2 \to \mathcal{H}_2$ is continuous, $f(0,0) = 0$ and $h(0,0) = 0$.

Definition 11. ***(Generalised passivity)*** *The system (2.97) is called passive if there exists a continuously differentiable positive semidefinite storage function $V(x_1)$ such that*

$$\texttt{real}\, \langle u_1, y_1 \rangle_{\mathcal{H}_2} \geq \dot{V} = \frac{\partial V}{\partial x_1} f(x_1, u_1), \qquad \forall\ (x_1, u_1) \in \mathcal{H}_1 \times \mathcal{H}_2 \tag{2.98}$$

where `real` denotes the real part. The system is called strictly passive if

$$\texttt{real}\, \langle u_1, y_1 \rangle_{\mathcal{H}_2} \geq \dot{V} + \phi(x_1), \qquad \forall\ (x_1, u_1) \in \mathcal{H}_1 \times \mathcal{H}_2 \tag{2.99}$$

where $\phi(x_1)$ is a positive definite function. In the case that the system is memoryless, the convention that $V = 0$ is adopted.

If $\mathcal{H}_2 = \mathbb{C}^p$ and the inner product is defined as the standard scalar product $\langle y_1, u_1 \rangle = y_1^* u_1$, then a finite-dimensional linear time-invariant system G is passive if and only if its transfer function $G(s)$ is positive real [22]. The test for positive real transfer functions is given by the positive real lemma [6]. Moreover, the system G is strictly passive if its transfer function $G(s)$ is strictly positive real and the KYP lemma gives a test of strictly positive real transfer functions.

If $\mathcal{H}_2$ is not a Euclidean space, the positive real lemma and KYP lemma cannot be used directly because on $\mathcal{H}_2$ the adjoint of a matrix is not its conjugate transpose. However, we are able to extend the positive real lemma and KYP lemma to general finite-dimensional Hilbert spaces.

Proposition 1. *Consider the finite-dimensional linear time-invariant system*

$$\dot{x}_1 = Ax_1 + Bu_1 \tag{2.100a}$$

$$y_1 = Cx_1 \tag{2.100b}$$

where $x_1 \in \mathcal{H}_1$,$u_1, y_1 \in \mathcal{H}_2$, $A : \mathcal{H}_1 \to \mathcal{H}_1$, $B : \mathcal{H}_2 \to \mathcal{H}_1$ *and* $C : \mathcal{H}_1 \to \mathcal{H}_2$*. It is passive in the sense of Definition 11 if there exists a strictly positive* $P : \mathcal{H}_1 \to \mathcal{H}_1$ *such that*

$$PA + (PA)^\dagger \leq 0 \tag{2.101a}$$

$$PB = C^\dagger \tag{2.101b}$$

The system is strictly passive in the sense of Definition 11 if there exist a strictly positive $P : \mathcal{H}_1 \to \mathcal{H}_1$ *and a positive constant* ε *such that*

$$PA + (PA)^\dagger \leq -\varepsilon P \tag{2.102a}$$

$$PB = C^\dagger \tag{2.102b}$$

Proof. Use $V(x_1) = \frac{1}{2} \langle x_1, Px_1 \rangle_{\mathcal{H}_1}$ as the storage function,

$$\begin{aligned}
\texttt{real} \, \langle u_1, y_1 \rangle_{\mathcal{H}_2} - \dot{V} &= \texttt{real} \, \langle u_1, Cx_1 \rangle_{\mathcal{H}_2} - \frac{1}{2} \frac{\mathrm{d} \langle x_1, Px_1 \rangle_{\mathcal{H}_1}}{\mathrm{dt}} \\
&= \texttt{real} \, \langle u_1, Cx_1 \rangle_{\mathcal{H}_2} - \frac{1}{2} (\langle \dot{x}_1, Px_1 \rangle_{\mathcal{H}_1} + \langle x_1, P\dot{x}_1 \rangle_{\mathcal{H}_1}) \\
&= \texttt{real} \left(\left\langle x_1, C^\dagger u_1 \right\rangle_{\mathcal{H}_1} - \langle x_1, P(Ax_1 + Bu_1) \rangle_{\mathcal{H}_1} \right) \\
&= \texttt{real} \left(\left\langle x_1, (C^\dagger - PB) u_1 \right\rangle_{\mathcal{H}_1} - \langle x_1, PAx_1 \rangle_{\mathcal{H}_1} \right) \\
&\geq \frac{1}{2} \varepsilon \langle x_1, Px_1 \rangle_{\mathcal{H}_1}
\end{aligned}$$

In the case of $\varepsilon = 0$, the system is passive, while when $\varepsilon > 0$, the system is strictly passive. □

Theorem 5 can be extended for general inner products in a similar manner.

Proposition 2. *Consider the feedback connection of Figure 2.1 where* H_1 *is a linear time-invariant system described by*

$$\begin{aligned} \dot{x}_1 &= Ax_1 + Be_1 && (2.103) \\ y_1 &= Cx_1 && (2.104) \end{aligned}$$

and H_2 *is a memoryless system represented by*

$$y_2 = H_2(e_2) \tag{2.105}$$

with $x_1 \in \mathcal{H}_1$, $e_1, e_2, y_1, y_2 \in \mathcal{H}_2$, $A : \mathcal{H}_1 \to \mathcal{H}_1$, $B : \mathcal{H}_2 \to \mathcal{H}_1$ *and* $C : \mathcal{H}_1 \to \mathcal{H}_2$.

Suppose that the memoryless system is passive, that is,

$$\boldsymbol{\mathtt{real}}\, \langle e_2, y_2 \rangle_{\mathcal{H}_2} \geq 0 \tag{2.106}$$

then the origin of the closed-looped system (when $u_1 = u_2 = 0$*) is globally uniformly asymptotically stable if there exist a strictly positive* P *and a positive constant* ε *satisfying the conditions (2.102).*

Proof. Choose $V = V_1(x_1) = \frac{1}{2}\langle x_1, Px_1 \rangle_{\mathcal{H}_1}$ as the Lyapunov function candidate. $e_1 = -y_2$ and $e_2 = y_1$ since $u_1 = u_2 = 0$, then

$$\begin{aligned} \dot{V} &= \dot{V}_1 \\ &\leq \mathtt{real}\, \langle e_1, y_1 \rangle_{\mathcal{H}_2} - \frac{1}{2}\varepsilon \langle x_1, Px_1 \rangle_{\mathcal{H}_1} \\ &= -\mathtt{real}\, \langle y_2, e_2 \rangle_{\mathcal{H}_2} - \frac{1}{2}\varepsilon \langle x_1, Px_1 \rangle_{\mathcal{H}_1} \\ &\leq -\frac{1}{2}\varepsilon \langle x_1, Px_1 \rangle_{\mathcal{H}_1} \end{aligned}$$

Thus it is evident that V is positive definite and $\dot{V}$ is negative definite. Moreover, V is radially unbounded. Then the conclusion follows. □

Applying this result to Definition 11, the system described by (2.87) is said to be strictly passive if there exists a positive semidefinite storage function $V(\hat{\mathbf{x}}_{mn})$ such that

$$\mathtt{real}\, \langle \hat{\mathbf{y}}_{mn}, \hat{\mathbf{e}}_{mn} \rangle \geq \dot{V} + \phi(\hat{\mathbf{x}}_{mn}) \tag{2.107}$$

$\forall\ (\hat{\mathbf{y}}_{mn}, \hat{\mathbf{e}}_{mn}) \in \mathbb{C}^{2(K-1)} \times \mathbb{C}^{3(K-1)}$ where $\phi(\hat{\mathbf{x}}_{mn})$ is a positive definite function and

$$\langle \hat{\mathbf{y}}_{mn}, \hat{\mathbf{e}}_{mn} \rangle = \int_{-1}^{1} \tilde{\mathbf{y}}_{mn}^{*} \tilde{\mathbf{e}}_{mn} \mathrm{d}y \tag{2.108}$$

In accordance with Proposition 1, system (2.87) is strictly passive if there exist a $\mathbf{P}_{mn} = \mathbf{P}_{mn}^{\dagger} > 0$ such that

$$\begin{aligned} \mathbf{P}_{mn}\mathbf{A}_{mn} + (\mathbf{P}_{mn}\mathbf{A}_{mn})^{\dagger} &< 0 \qquad (2.109a) \\ \mathbf{P}_{mn}\mathbf{B}_{mn} &= \mathbf{C}_{mn}^{\dagger} \qquad (2.109b) \end{aligned}$$

With respect to the inner product

$$\langle \gamma, \xi \rangle = \int_{-1}^{1} \gamma^* \xi \mathrm{d}y \tag{2.110}$$

it can be proved that [41]

$$\mathcal{D}^{\dagger} = -\mathcal{D} \tag{2.111}$$

when the boundary condition

$$\gamma(y = \pm 1) = \xi(y = \pm 1) = 0 \tag{2.112}$$

is assumed, thus the adjoint of $\mathcal{C}_{mn}$ given in (2.81) is

$$\mathcal{C}_{mn}^{\dagger} = \frac{1}{k_{mn}^2} \begin{bmatrix} \mathrm{i}\alpha_m \mathcal{D} & k_{mn}^2 & \mathrm{i}\beta_n \mathcal{D} \\ \mathrm{i}\beta_n & 0 & -\mathrm{i}\alpha_m \end{bmatrix} \tag{2.113}$$

It follows that

$$\mathbf{D}_1^{\dagger} = -\mathbf{D}_1 \tag{2.114}$$

and naturally $\mathbf{C}_{mn}^{\dagger}$ can be obtained by discretising $\mathcal{C}_{mn}^{\dagger}$ in the y direction

$$\mathbf{C}_{mn}^{\dagger} = \frac{1}{k_{mn}^2} \begin{bmatrix} \mathrm{i}\alpha_m \mathbf{D}_1 & k_{mn}^2 \mathbf{I} & \mathrm{i}\beta_n \mathbf{D}_1 \\ \mathrm{i}\beta_n \mathbf{I} & \mathbf{0} & -\mathrm{i}\alpha_m \mathbf{I} \end{bmatrix} \tag{2.115}$$

We therefore find that the only solution to (2.109b) is

$$\mathbf{P}_{mn} = \frac{1}{k_{mn}^2} \begin{bmatrix} k_{mn}^2 \mathbf{I} - \mathbf{D}_2 & \mathbf{0} \\ \mathbf{0} & \mathbf{I} \end{bmatrix} \tag{2.116}$$

which is self-adjoint and positive definite.

Similarly, using integration by parts, it can be shown [133]

$$\mathcal{L}_{OS}^{\dagger} = \mathrm{i}\alpha_m U(\mathcal{D}^2 - k_{mn}^2) + 2\mathrm{i}\alpha_m U' \mathcal{D} + \frac{1}{\mathrm{Re}}(\mathcal{D}^2 - k_{mn}^2)^2 \tag{2.117}$$

$$\mathcal{L}_{SQ}^{\dagger} = \mathrm{i}\alpha_m U + \frac{1}{\mathrm{Re}}(\mathcal{D}^2 - k_{mn}^2) \tag{2.118}$$

discretisation in the y direction yields

$$\mathbf{L}_{OS}^{\dagger} = \mathrm{i}\alpha_m \mathbf{U}(\mathbf{D}_2 - k_{mn}^2 \mathbf{I}) + 2\mathrm{i}\alpha_m \mathbf{U}' \mathbf{D}_1 + \frac{1}{\mathrm{Re}}(\mathbf{D}_4 - 2k_{mn}^2 \mathbf{D}_2 + k_{mn}^4 \mathbf{I}) \tag{2.119}$$

$$\mathbf{L}_{SQ}^{\dagger} = \mathrm{i}\alpha_m \mathbf{U} + \frac{1}{\mathrm{Re}}(\mathbf{D}_2 - k_{mn}^2 \mathbf{I}) \tag{2.120}$$

Then we have

$$\mathbf{P}_{mn}\mathbf{A}_{mn} + (\mathbf{P}_{mn}\mathbf{A}_{mn})^{\dagger} = \frac{1}{k_{mn}^2}\begin{bmatrix} -\mathbf{L}_{OS} - \mathbf{L}_{OS}^{\dagger} & \mathrm{i}\beta_n \mathbf{U}' \\ -\mathrm{i}\beta_n \mathbf{U}' & \mathbf{L}_{SQ} + \mathbf{L}_{SQ}^{\dagger} \end{bmatrix} \tag{2.121}$$

and when it is negative definite for all wavenumber pairs (m, n), the linear part of the flow system is strictly passive and moreover, the entire flow system without external forcing is globally uniformly asymptotically stable.

2.5.3 Results

Numerical computation shows that $\mathbf{P}_{mn}\mathbf{A}_{mn} + (\mathbf{P}_{mn}\mathbf{A}_{mn})^{\dagger} < 0$ for all wavenumber pairs (m, n) when the Reynolds number does not exceed $\mathrm{Re} \approx 49.6$, which is the same as the energy Reynolds number derived by the classical energy approach [80]. The lowest subcritical Reynolds number is obtained at $\alpha_m = 0, \beta_n \approx 2.05$. Figure 2.3 plots the upper bound of the Reynolds number Re so that $\mathbf{P}_{mn}\mathbf{A}_{mn} + (\mathbf{P}_{mn}\mathbf{A}_{mn})^{\dagger} < 0$ as a function of the wavenumber pairs (α_m, β_n). Note that the sharp peak at the centre of the figure reflects the fact that the flow mode at $\alpha_m = 0, \beta_n = 0$ is strictly passive for any Reynolds number.

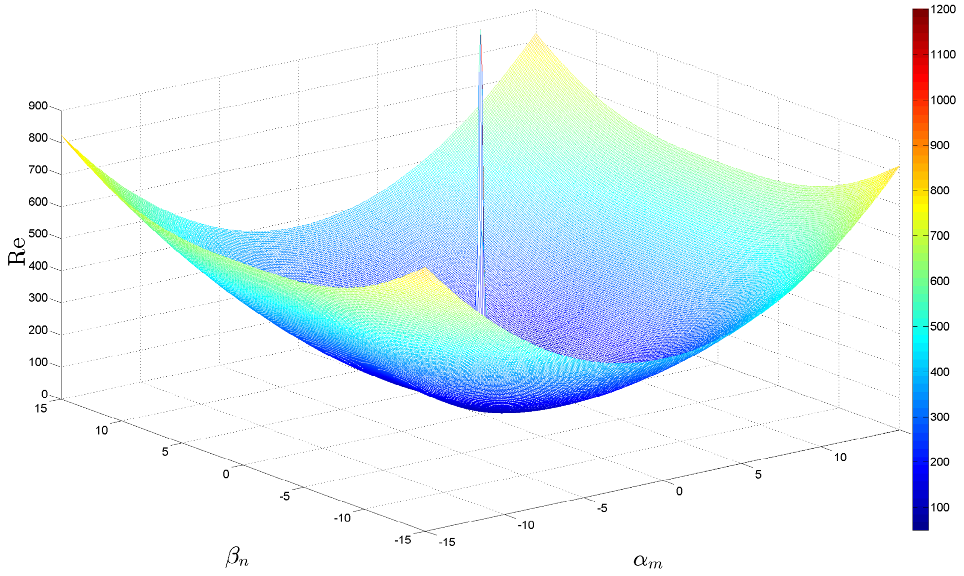

Figure 2.3: Subcritical Reynolds number plotted against wavenumbers.

So far the plane Poiseuille flow has been considered is 3-dimensional, but the result for 2-dimensional flow can also be obtained by using the same approach. The result shows that in the case of 2-dimensional plane Poiseuille flow, the subscritical Reynolds number is Re ≈ 87.7, which is equal to the energy Reynolds number obtained by Orr [111]. In addition, the passivity approach can be readily applied to plane Couette flow. The results agree with the energy Reynolds numbers derived by energy approach for both 2-dimensional and 3-dimensional cases.

2.5.4 Generalised passivity and loop transformation

We now establish a connection between generalised passivity and loop transformation. Specifically, it can be shown that if system (2.97) can be proved stable by using extended passivity theorems on Hilbert spaces, its stability can also be determined by using standard passivity theorems on Euclidean spaces after applying a loop transformation.

Let E_2 be the Euclidean space that has the same vector space as $\mathcal{H}_2$, which means that

$$u_1 \in \mathcal{H}_2 \Leftrightarrow u_1 \in E_2 \tag{2.122}$$

and the difference between E_2 and $\mathcal{H}_2$ is that the inner products are defined differently on these two spaces. Denote the inner product on E_2 as $\langle \cdot, \cdot \rangle_{E_2}$ and the inner product on $\mathcal{H}_2$ as $\langle \cdot, \cdot \rangle_{\mathcal{H}_2}$. It follows from the definitions of inner products and bilinear functions that $\langle \cdot, \cdot \rangle_{\mathcal{H}_2}$ is a bilinear function on E_2 [43].

Define $\|u_1\|_{\mathcal{H}_2} = \sqrt{\langle u_1, u_1 \rangle_{\mathcal{H}_2}}$ and $\|u_1\|_{E_2} = \sqrt{\langle u_1, u_1 \rangle_{E_2}}$ where $u_1 \in E_2$. It is a standard result that any two norms on finite-dimensional normed spaces are equivalent [43]. As a result, there exist positive numbers ψ and φ such that

$$\psi \|u_1\|_{E_2} \leq \|u_1\|_{\mathcal{H}_2} \leq \varphi \|u_1\|_{E_2}, \qquad \forall u_1 \in E_2 \tag{2.123}$$

It follows from Schwarz's inequality that

$$| \langle u_1, u_2 \rangle_{\mathcal{H}_2} | \leq \|u_1\|_{\mathcal{H}_2} \|u_2\|_{\mathcal{H}_2} \leq \varphi^2 \|u_1\|_{E_2} \|u_2\|_{E_2}, \qquad \forall u_1, u_2 \in E_2 \tag{2.124}$$

which means that the bilinear functional $\langle \cdot, \cdot \rangle_{\mathcal{H}_2}$ is bounded on E_2 [43]. Then according to Theorem 4.3.13 in [43], there exists a unique operator Q on E_2 such that

$$\langle u_1, u_2 \rangle_{\mathcal{H}_2} = \langle u_1, Q u_2 \rangle_{E_2}, \qquad \forall u_1, u_2 \in E_2 \tag{2.125}$$

It means that the system (2.97) is passive with respect to $\langle \cdot, \cdot \rangle_{\mathcal{H}_2}$ if and only if the system

$$\dot{x_1} = f(x_1, u_1) \tag{2.126a}$$

$$\check{y}_1 = Q y_1 = Q h(x_1, u_1) \tag{2.126b}$$

is passive with respect to $\langle\cdot,\cdot\rangle_{E_2}$. System (2.126) can be obtained by a loop transformation of system (2.97). Therefore if the closed-loop system in Figure 2.4(a) can be proved stable using passivity theorems on $\mathcal{H}_2$, the stability can also be shown by applying standard passivity theorems on Euclidean spaces to the system in Figure 2.4(b), which is obtained by a loop transformation.

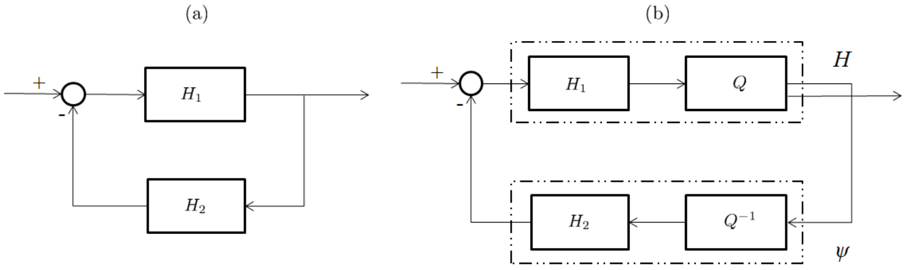

Figure 2.4: Loop transformation.

Note that Q^{-1} always exists as Q is nonsingular. This can be easily proved from the properties of inner products. For if Q is singular, there exists $u_1 \neq 0$ so that

$$\langle u_1, Qu_1\rangle_{E_2} = \langle u_1, u_1\rangle_{\mathcal{H}_2} = 0 \tag{2.127}$$

but from the definition of inner products $\langle u_1, u_1\rangle_{\mathcal{H}_2} = 0$ implies $u_1 = 0$, which contradicts $u_1 \neq 0$. It should also be noted that although the existence and uniqueness of such a Q are guaranteed, it may not be straightforward to find.

2.6 Conclusion

In this chapter, we have used passivity theorems to study the global stability of plane channel flow. The Reynolds number below which 3-dimensional plane Poiseuille flow is globally stable is Re $\approx$ 49.6, which is the same as the energy Reynolds number obtained using the classical energy approach. This result is expected as essentially in the passivity approach, the kinetic energy of the system is used as the Lyapunov function. The same method can be applied to plane Couette flow. In the process of finding the subcritical Reynolds number, we have extended the definition of passive systems and KYP lemma, as well as the passivity theorems, from finite-dimensional Euclidean spaces to finite-dimensional Hilbert spaces. A connection between generalised passivity and loop transformation is also established.

Chapter 3

Calculation of Transient Growth in Channel Flow

3.1 Introduction

In the last chapter, we have used the generalised passivity approach to show that the kinetic energy of plane Poiseuille flow cannot grow when the Reynolds number is lower than $\mathrm{Re}_E \approx 49.6$. This result indicates that the energy of the disturbances in the flow may experience growth when $\mathrm{Re} > \mathrm{Re}_E$ even when the flow is linearly stable, i.e., $\mathrm{Re} < \mathrm{Re}_c = 5772.22$. This is indeed the case and such a phenomenon is called transient energy growth, or sometimes transient growth for short, in the literature [129] [133].

Transient growth has been widely recognised as one explanation for subcritical transition in plane Poiseuille flow [129] [157]. It has been pointed out that due to the nonnormality of the Orr-Sommerfeld/Squire operator, the kinetic energy of the fluid flow may grow rapidly before it decays, even when all the eigenvalues of the operator have negative real parts [157] [152]. Using a finite difference method, Butler and Farrell [24] (hereafter referred to as BF) have shown that the disturbance energy of the flow can be up to $\mathcal{O}(1000)$ times the initial energy at $\mathrm{Re} = 5000$. Reddy and Henningson [125] (hereafter referred to as RH) used a Chebyshev collocation method to compute the energy growth of the flow, and their results agree with those of BF. In the literature of flow control, the disturbance energy of plane channel flow plays an important role [18][134] and control laws have been designed to remove transient growth so that the flow system is stabilised [138] [103]. Thus the accuracy of numerical methods to compute the transient growth is important.

As shown in the last chapter using a generalised passivity approach and in the literature using variational calculus [79], for 3-dimensional plane Poiseuille flow, there is no energy growth when $\mathrm{Re} < \mathrm{Re}_E$, which is achieved at $\alpha = 0, \beta \approx 2.05$, where α, β are streamwise and spanwise wavenumbers, respectively. Denoting the greatest possible energy growth function of a single flow mode (α, β) at Reynolds number Re as $G(\alpha, \beta, \mathrm{Re})$. Numerical methods of computing $G(\alpha, \beta, \mathrm{Re})$ are given in BF and RH. As mentioned previously, the primary difference between them is that BF used a finite difference method to discretise the linearised governing equation in the wall-normal direction, while RH used a Chebyshev collocation method. At high Reynolds numbers, these two numerical methods yield very close results, suggesting that both are accurate. However, neither of the articles gives results about the energy growth at low Reynolds numbers. A criterion for evaluating the accuracy of numerical methods to calculate the energy growth is to check if they lead to results that agree with those obtained analytically. The MATLAB implementation of RH's method is given in Appendix A of [133] and it is expected that using the code we will find $G(0, 2.05, \mathrm{Re}) = 1$ for all $\mathrm{Re} < \mathrm{Re}_E$, and $G(0, 2.05, \mathrm{Re}) > 1$ when $\mathrm{Re} > \mathrm{Re}_E$. In addition, the boundary of $G(\alpha, \beta, \mathrm{Re}) = 1$ is determined analytically by applying the Hille-Yosida theorem in §7 of RH. If the numerical methods are sufficiently accurate, they are expected to give the same results as the analytical methods. However, we show that it is not the case and a natural question is, how accurate are the numerical methods?

In this chapter, we show that when computing the energy of the flow system, the Chebyshev collocation method is not sufficiently accurate to discretise the governing equations in the wall-normal direction due to the existence of spurious eigenvalues and errors in numerical integration. By contrast, a Chebyshev Galerkin method in which basis functions satisfying boundary conditions can be used and is shown to give solutions that agree with the results derived by analytical methods.

3.2 Nonnormality and transient growth

Before going to the details of the numerical calculation, we first discuss the reason for the existence of transient growth in a linear system. Consider a linear system described by the differential equation

$$\dot{x} = Ax \tag{3.1}$$

where A can be either a linear operator or a matrix. For convenience, let us assume that A is a matrix, x is a vector of appropriate size and the energy of the system is defined by $E = \|x\|_2^2$. The solution to the differential equation (3.1) is $x(t) = \mathrm{e}^{At}x_0$. Suppose the energy of the system with any initial state x_0 is normalised to unity at $t_0 = 0$, then at time t the largest possible energy the system can achieve is $\|\mathrm{e}^{At}\|_2^2$.

As mentioned in the last chapter, the stability of such a system is straightforward to determine: it is stable if all the eigenvalues of A have negative real parts and it is unstable if A has at least one eigenvalue with positive real part. What the eigenvalue analysis does not tell us is how the energy of the system evolves over time. While it is evident that the energy can grow infinitely when the system is unstable, it is less obvious what will happen when the system is stable. It turns out that in some cases the system energy decays monotonically as expected, while in other cases the system energy can grow for a period even when the system is stable. These observations may not agree with one's intuition. As a simple example, let us consider the following two matrices

$$A_1 = \begin{bmatrix} -1 & -10 \\ 0 & -2 \end{bmatrix} \qquad A_2 = \begin{bmatrix} -1 & 0 \\ 0 & -2 \end{bmatrix}$$

Although A_1 and A_2 have the same eigenvalues, the behaviours of $\|e^{A_1 t}\|_2^2$ and $\|e^{A_2 t}\|_2^2$ are quite different, as can be seen from Figure 3.1.

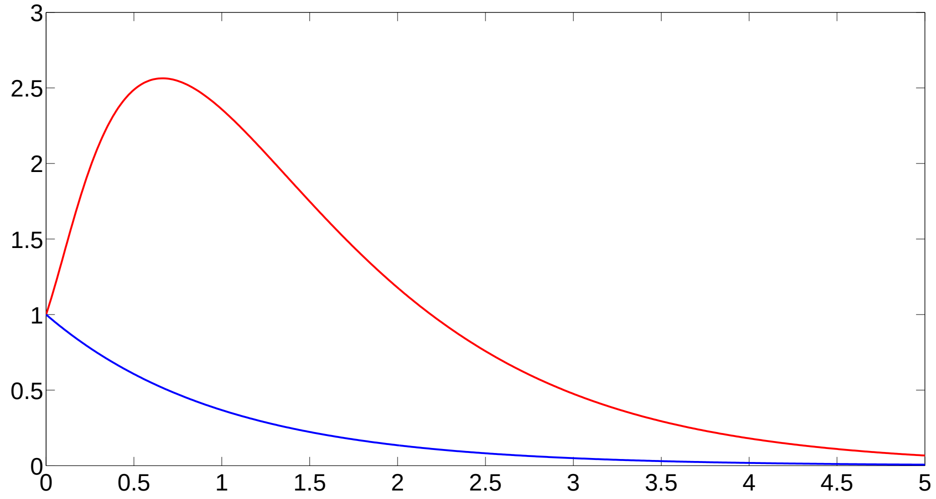

Figure 3.1: $\|e^{A_1 t}\|_2^2$ (red) and $\|e^{A_2 t}\|_2^2$ (blue) versus time t.

The reason for such a difference is that the eigenvectors of A_1 are not orthogonal, while the eigenvectors of A_2 are. The solution $x(t) = e^{At}x_0$ can be seen as a linear combination of the two eigenvectors of A from a linear algebra point of view. Denoting the two eigenvectors as v_1 and v_2, we have

$$x(t) = a(t)v_1 + b(t)v_2 \tag{3.2}$$

where $a(t)$ and $b(t)$ are the coefficients at t. Since the system is stable, the magnitudes of $a(t)$ and $b(t)$ decay monotonically over time. However, $\|x(t)\|_2$ does not necessarily decay. For example, the two eigenvectors of A_1 are $v_1 = \begin{bmatrix}1 & 0\end{bmatrix}^T$ and $v_2 = \begin{bmatrix}10 & 1\end{bmatrix}^T$. An initial condition $x_0 = \begin{bmatrix}0.1558 & -0.9878\end{bmatrix}^T$ can be written as $x_0 = 10.0337v_1 - 0.9878v_2$.

At time $t = 1$, the system solution is $x(t = 1) = \mathrm{e}^{A_1 t}x_0 = \begin{bmatrix}2.3544 & -0.1337\end{bmatrix}^T$, which can be written as $x(t = 1) = 3.6912v_1 - 0.1337v_2$. As we can see, the magnitudes of the coefficients decrease since both the eigenvalues of A_1 are negative. However, $\|x(t = 1)\|_2 > \|x_0\|_2$, which means the energy of the system is increased.

It is clear from Figure 3.1 why the phenomenon is called transient growth. The system energy will eventually decay to zero as long as the system matrix A is Hurwitz. It is not difficult to see that the non-orthogonality of the eigenvectors is a necessary condition for a system to have transient growth. If the eigenvectors are orthogonal, the 2-norm of a linear combination of eigenvectors will necessarily decay when the coefficients decrease over time. A matrix with a complete set of orthogonal eigenvectors is referred to as a normal matrix [152]. It is a standard result that a matrix A is normal is equivalent to the condition $AA^* = A^*A$. It should be noted that nonnormality of the system matrix A is only a necessary condition for transient growth to occur in a system.

In the case that A is a linear operator, the arguments above are still valid, although the details are more technical. A is normal if $AA^\dagger = A^\dagger A$, where $A^\dagger$ is a well defined adjoint operator of A. Similarly, a normal linear operator has a complete set of orthogonal eigenfunctions. If the eigenfunctions are not orthogonal, there is a possibility for the system to experience transient growth even if all of the eigenvalues are located in the open left half of the complex plane.

Although the eigenfunctions of the Orr-Sommerfeld operator in plane Poiseuille flow form a complete set [68], they are not orthogonal [125], and the nonnormality of the Orr-Sommerfeld operator makes transient growth possible. Furthermore, the coupling term in the Orr-Sommerfled/Squire operator enhances the nonnormality. Therefore it is not surprising that the eigenvalue analysis does not tell the whole story about the fluid flow system. The so-called pseudospectra are a more appropriate tool than the spectra (eigenvalues) to study the behaviour of a system governed by a nonnormal operator or matrix [157]. The reader is referred to [156] for details about pseudospectra.

3.3 Model of the fluid flow

The state space representation of plane Poiseuille flow has been derived in Section 2.4. For ease of reference, we now briefly review the model of the system. In 3-dimensional Cartesian coordinates (x, y, z) where x, y and z are streamwise, wall-normal and spanwise directions, respectively, plane Poiseuille flow at a particular flow mode (α, β) is described by

$$\dot{\tilde{\mathbf{x}}} = \mathcal{A}\tilde{\mathbf{x}} + \mathcal{B}\tilde{\mathbf{e}} \tag{3.3a}$$

$$\tilde{\mathbf{y}} = \mathcal{C}\tilde{\mathbf{x}} \tag{3.3b}$$

with state $\tilde{\mathbf{x}} = \begin{bmatrix}\tilde{v} & \tilde{\eta}\end{bmatrix}^{\mathrm{T}}$, input $\tilde{\mathbf{e}} = \begin{bmatrix}\tilde{e}^{(1)} & \tilde{e}^{(2)} & \tilde{e}^{(3)}\end{bmatrix}^{\mathrm{T}}$, output $\tilde{\mathbf{y}} = \begin{bmatrix}\tilde{u} & \tilde{v} & \tilde{w}\end{bmatrix}^{\mathrm{T}}$ and

$$\mathcal{A} = \begin{bmatrix}\mathcal{D}^2 - k^2 & 0 \\ 0 & 1\end{bmatrix}^{-1} \begin{bmatrix}\mathcal{L}_{OS} & 0 \\ -\mathrm{i}\beta_n U' & \mathcal{L}_{SQ}\end{bmatrix} \tag{3.4}$$

$$\mathcal{B} = \begin{bmatrix}\mathcal{D}^2 - k^2 & 0 \\ 0 & 1\end{bmatrix}^{-1} \begin{bmatrix}-\mathrm{i}\alpha\mathcal{D} & -k^2 & -\mathrm{i}\beta\mathcal{D} \\ \mathrm{i}\beta_n & 0 & -\mathrm{i}\alpha\end{bmatrix} \tag{3.5}$$

$$\mathcal{C} = \begin{bmatrix}-k^2 & 0 & 0 \\ 0 & 1 & 0 \\ 0 & 0 & -k^2\end{bmatrix}^{-1} \begin{bmatrix}-\mathrm{i}\alpha\mathcal{D} & \mathrm{i}\beta_n \\ 1 & 0 \\ -\mathrm{i}\beta\mathcal{D} & -\mathrm{i}\alpha\end{bmatrix} \tag{3.6}$$

where $k^2 = \alpha^2 + \beta^2$, the prime denotes $\frac{\mathrm{d}}{\mathrm{d}y}$, $\mathcal{D}$ denotes $\frac{\partial}{\partial y}$, and

$$\mathcal{L}_{OS} = -\mathrm{i}\alpha U(\mathcal{D}^2 - k^2) + \mathrm{i}\alpha_m U'' + \frac{1}{\mathrm{Re}}(\mathcal{D}^2 - k^2)^2 \tag{3.7}$$

$$\mathcal{L}_{SQ} = -\mathrm{i}\alpha U + \frac{1}{\mathrm{Re}}(\mathcal{D}^2 - k^2) \tag{3.8}$$

Note that all the subscripts are omitted for notational convenience. By definition, the input to the system $\tilde{\mathbf{e}}$ is a linear combination of the nonlinearity $\tilde{\mathbf{S}}$ and the external force $\tilde{\mathbf{f}}$

$$\tilde{\mathbf{e}} = \tilde{\mathbf{f}} - \tilde{\mathbf{S}} \tag{3.9}$$

Assuming that there is no external force, that is, $\tilde{\mathbf{f}} = 0$, then the input consists only of the nonlinearity of the system. As pointed out in the last chapter, the nonlinearity does not play a role in the increase or decrease in the disturbance kinetic energy, all it does is to move energy from one flow mode to another. Thus it is usually omitted in the study of transient growth in plane channel flow [24] [125], which means that the flow is linearised and the system state is governed by

$$\dot{\tilde{\mathbf{x}}} = \mathcal{A}\tilde{\mathbf{x}} \tag{3.10}$$

The kinetic energy (density) of a single flow mode (α, β) is given by

$$E = \frac{1}{2}\int_{-1}^{1}\left(\tilde{v}^*\tilde{v} + \frac{1}{k^2}((\mathcal{D}\tilde{v})^*\mathcal{D}\tilde{v} + \tilde{\eta}^*\tilde{\eta})\right)\mathrm{d}y \tag{3.11}$$

It should be noted that the nonlinearity does have effects on the development of kinetic energy of the flow, as it moves kinetic energy from one flow mode to another, although no kinetic energy is consumed or absorbed by it. The reason for linearisation is to show that transient growth is a linear mechanism and does not need the involvement of the nonlinearity.

3.4 Calculating transient growth using Chebyshev collocation method

Discretising the linearised governing equations in the wall-normal direction using the Chebyshev collocation method by expanding $\tilde{v}$ and $\tilde{\eta}$ as the Chebyshev series

$$\tilde{v} = \sum_{n=0}^{N} a_{v,n} T_n(y) \tag{3.12}$$

$$\tilde{\eta} = \sum_{n=0}^{N} a_{\eta,n} T_n(y) \tag{3.13}$$

where $T_n(y) = \cos(n \cos^{-1}(y))$ is the Chebyshev polynomial defined on $y \in [-1, 1]$, system (3.10) becomes

$$\dot{\hat{\mathbf{x}}} = \mathbf{A}\hat{\mathbf{x}} \tag{3.14}$$

where $\hat{\mathbf{x}}$ is the state vector of the discretised system. Different ways of implementation of the Chebyshev collocation method can be described by the following two cases:

- Case (i): $\hat{\mathbf{x}}$ is the vector containing the values of $\tilde{\mathbf{x}}$ at each of the Gauss-Lobatto collocation points

  $$y_j = \cos\left(\frac{j\pi}{N}\right), \quad j = 1, ..., N-1 \tag{3.15}$$

  so that

  $$\hat{\mathbf{x}} = \begin{bmatrix} \tilde{v}(y_1) & \dots & \tilde{v}(y_{N-1}) & \tilde{\eta}(y_1) & \dots & \tilde{\eta}(y_{N-1}) \end{bmatrix}^T \tag{3.16}$$

- Case (ii): $\hat{\mathbf{x}}$ is the vector containing the expansion coefficients of the Chebyshev polynomials that are used to approximate $\tilde{\mathbf{x}}$, i.e.,

  $$\hat{\mathbf{x}} = \begin{bmatrix} a_{v,0} & \dots & a_{v,N} & a_{\eta,0} & \dots & a_{\eta,N} \end{bmatrix}^T \tag{3.17}$$

and correspondingly $\mathbf{A}$ is the discretised linear operator on which the boundary conditions are imposed. The energy density for each flow mode can be expressed as

$$E = \hat{\mathbf{x}}^* \mathbf{Q} \hat{\mathbf{x}} \tag{3.18}$$

where $\mathbf{Q}$ is the energy weight matrix and is positive definite in both cases. For case (i), $\mathbf{A}$ can be obtained by using the MATLAB differentiation matrix suite implemented by Weideman and Reddy [161], in which the Neumann boundary condition is imposed by using the clamped boundary technique suggested in [75], and $\mathbf{Q}$ is given in §2.4 of [18]. For case (ii), the procedure of computing $\mathbf{A}$ and $\mathbf{Q}$ is given in Appendix A of [133]. In case (i), the size of $\mathbf{A}$ and $\mathbf{Q}$ is $2(N-1) \times 2(N-1)$, while in case (ii), the size of these matrices is $2(N+1) \times 2(N+1)$.

3.4.1 Conditions for no energy growth

Conditions for no energy growth have been derived analytically by applying the Hille-Yosida theorem and the equivalence between these conditions and those determined by the classical energy approach is shown in [125]. The equation to compute the subcritical Reynolds number below which there is no energy growth at a particular flow mode (α, β) is given in Chapter 5 of [133]. Using the equation, we find that $\mathrm{Re}_E = 49.60392$ at $\alpha = 0, \beta = 2.05$. This result can also be obtained by using the passivity approach discussed in the last chapter.

Numerically, the system has no energy growth if and only if the time derivative of the energy function for all flow modes is negative definite, i.e.,

$$\dot{E} = \hat{\mathbf{x}}^*(\mathbf{A}^*\mathbf{Q} + \mathbf{Q}\mathbf{A})\hat{\mathbf{x}} < 0 \quad \forall\, \hat{\mathbf{x}} \neq \mathbf{0} \tag{3.19}$$

If the discretisation method is sufficiently accurate, this condition is expected to be equivalent to those derived by the Hille-Yosida theorem and the classical energy approach. Therefore we should be able to find the subcritical Reynolds number by solving the inequality

$$\mathbf{A}^*\mathbf{Q} + \mathbf{Q}\mathbf{A} < 0 \tag{3.20}$$

where the inequality should hold for $\mathrm{Re} < \mathrm{Re}_E$ and not hold for $\mathrm{Re} > \mathrm{Re}_E$ at $\alpha = 0, \beta = 2.05$. However, numerical computation shows that inequality (3.20) does not hold for any Reynolds number in either case (i) or case (ii). As mentioned previously, the size of $\mathbf{A}$ and $\mathbf{Q}$ depends on N. It is expected that the least stable eigenvalues of $\mathbf{A}^*\mathbf{Q}+\mathbf{Q}\mathbf{A}$ will remain unchanged for different N when N is sufficiently large. However, as illustrated in Figure 3.2, the largest eigenvalue of the matrix $\mathbf{A}^*\mathbf{Q} + \mathbf{Q}\mathbf{A}$ changes rapidly with increasing N, indicating that there is a numerical problem. Since the collocation method does not enable us to find the subcritical Reynolds number below which there is no energy growth by solving inequality (3.20), the accuracy of using the collocation method to discretise the linear operator $\mathcal{A}$ and then to compute the transient growth is questionable.

3.4.2 Energy amplification factor

The largest possible energy amplification factor for flow mode (α, β) at Reynolds number Re and time t is given by

$$G(\alpha, \beta, \mathrm{Re}, t) = \sup_{E_0 \neq 0} \frac{E(t)}{E_0} = \sup_{\hat{\mathbf{x}}_0 \neq 0} \frac{\hat{\mathbf{x}}^*(t)\mathbf{Q}\hat{\mathbf{x}}(t)}{\hat{\mathbf{x}}_0^*\mathbf{Q}\hat{\mathbf{x}}_0} = \sup_{\hat{\mathbf{x}}_0 \neq 0} \frac{\|\mathbf{F}\hat{\mathbf{x}}(t)\|_2^2}{\|\mathbf{F}\hat{\mathbf{x}}_0\|_2^2} = \|\mathbf{F}\mathrm{e}^{\mathbf{A}t}\mathbf{F}^{-1}\|_2^2 \tag{3.21}$$

where $\mathbf{F}$ is a nonsingular square matrix satisfying $\mathbf{Q} = \mathbf{F}^*\mathbf{F}$. Such a $\mathbf{F}$ can be obtained by the Cholesky decomposition of $\mathbf{Q}$.

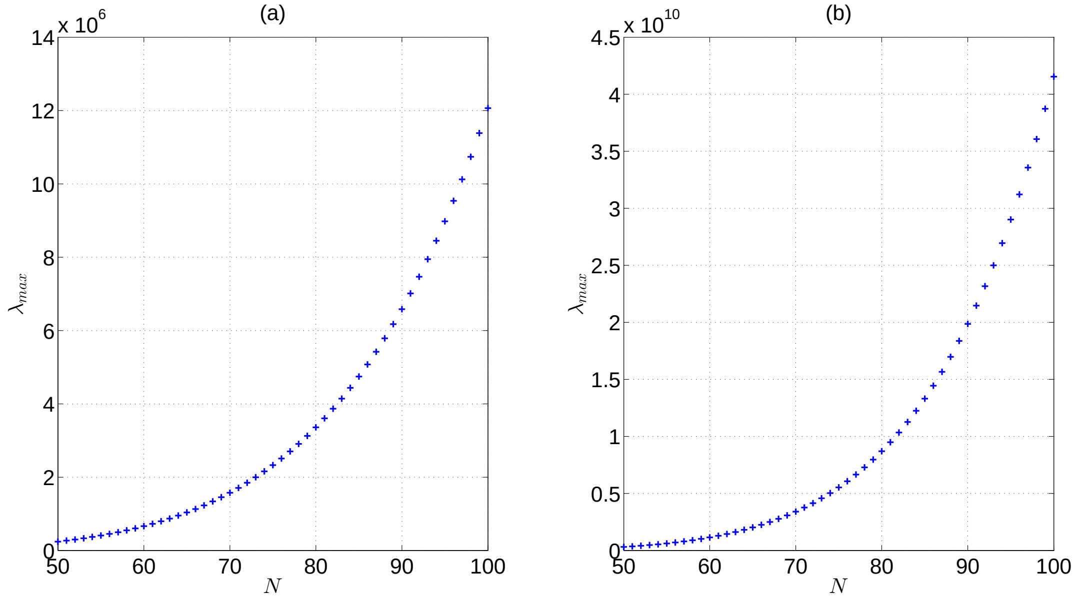

Figure 3.2: The largest eigenvalue of $\mathbf{A}^*\mathbf{Q}+\mathbf{Q}\mathbf{A}$ versus N at $\mathrm{Re}=5, \alpha=0, \beta=2.05$. (a): case (i), (b): case (ii).

Using this expression to determine the evolution of the amplification factor at Reynolds numbers close to Re_E, we can see that the collocation method leads to numerical problems. Figure 3.3 plots the evolution of the energy amplification factor $G(0,2.05,\mathrm{Re},t)$ over the period $t\in[0,0.05]$ for $\mathrm{Re}=49.6$ and $\mathrm{Re}=49.7$ in case (ii), and it can be seen that $G(0,2.05,49.6,t)$ can be as large as 12, which is incorrect since we know the factor should not be larger than 1. Although the only information we know about $G(0,2.05,49.7,t)$ is it is larger than 1 at some time and we do not know when it achieves the largest value and what the largest value is, it is still not difficult to find that plot (b) in Figure 3.3 is unconvincing. Similar plots for case (i) can be obtained and it can be shown that the same problem is also present.

At high Reynolds number $\mathrm{Re}=1000$, the plot of $G(\alpha,\beta,\mathrm{Re},t)$ appears to be quite smooth, as shown in Figure 3.4(a). However, if we restrict our attention to a small time interval $[0,0.25]$, there is a transient peak at the start of the time axis which lasts for typically less than 0.1 dimensionless time unit, see Figure 3.4(b). This is not a special case and there exist transient peaks at all Reynolds numbers and wavenumber pairs.

We note that such transient peaks cannot be found in plots generated by running Schmid and Henningson's code. This is because they use only K least stable eigenvalues and eigenfunctions of $\mathbf{A}$ to compute the amplification factor where $K\ll 2N$ [133]. While it is reasonable to reduce the number of modes to improve the computation time, the accuracy of such an approach is not addressed. Naturally, it is expected that the

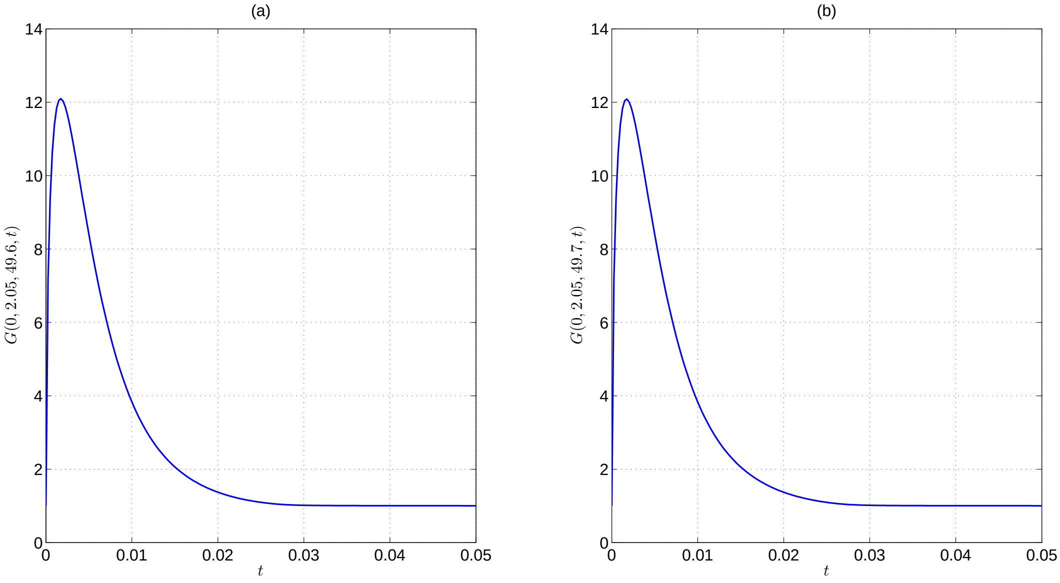

Figure 3.3: (a): $G(0, 2.05, 49.6, t)$, (b): $G(0, 2.05, 49.7, t)$. Both plots are for case (ii) and $N = 100$.

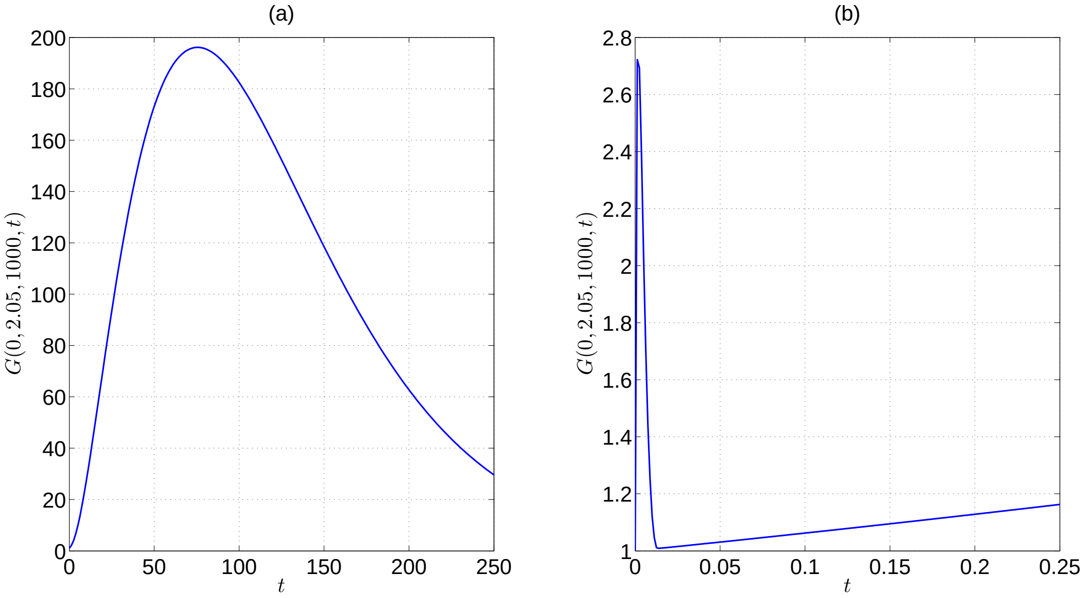

Figure 3.4: $G(0, 2.05, 1000, t)$ at $N = 100$ for case (ii). (a): $t \in [0, 250]$, (b): $t \in [0, 0.25]$.

plots will be more accurate as K becomes larger. However, when all the eigenvalues and eigenfunctions are considered, the transient peaks are present. This suggests that the presence of transient peaks is presumably due to some of the most stable eigenvalues and their corresponding eigenfunctions.

It is not obvious whether transient peaks in Figure 3.4 are physical, since the plots do not change even when N is increased from 100 to 200. As a comparison, it is easier to see that transient peaks in Figure 3.5 are not physical, where the peak becomes even higher when N is increased from 100 to 200, suggesting that the presence of the peak is due to a numerical problem.

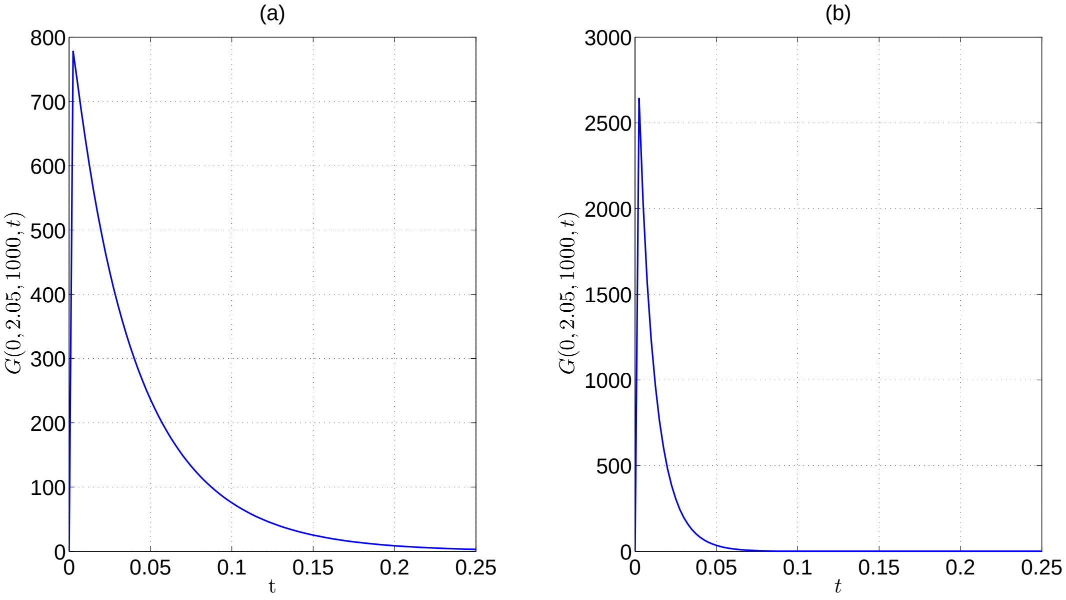

Figure 3.5: $G(0, 2.05, 1000, t)$ for case (i), $N = 100$ in (a) and $N = 200$ in (b).

The existence of unphysical transient peaks in both case (i) and case (ii) makes it impossible to describe the evolution of energy amplification factor accurately at low Reynolds numbers. Furthermore, it raises another question: are the results about energy growth at high Reynolds number accurate if the method used to obtain them suffers from numerical problems?

3.5 Explanation of the numerical issues

The discussion in the previous section has shown that the Chebyshev collocation method is inaccurate when computing the energy evolution of the flow system, no matter whether the collocation point values or the expansion coefficients are used as the state variables. Since there are only two matrices concerned, namely $\mathbf{Q}$ and $\mathbf{A}$, it is natural to conclude that the inaccuracy arises due to the errors in these two matrices. In this section we will show that in case (i), using numerical integration to compute **Q** can introduce large errors. In addition, we will show that the spurious eigenmodes of **A** in both cases are one possible reason for the inaccuracy.

3.5.1 Numerical integration errors

The inner product of two continuous functions $f(y), g(y)$ on the domain $y \in [-1, 1]$ can be computed numerically by

$$\langle f(y), g(y) \rangle = \int_{-1}^{1} f(y)^* g(y) \mathrm{d}y = \hat{\mathbf{f}}^* \mathbf{W} \hat{\mathbf{g}} \tag{3.22}$$

where $\hat{\mathbf{f}}, \hat{\mathbf{g}}$ are vectors obtained by evaluating $f(y), g(y)$ at each of the collocation points and $\mathbf{W}$ can be either the Clenshaw-Curtis quadrature weight (denoted by $\mathbf{W}_1$) [153] or the diagonal matrix specified in §2.4 of [18] (denoted by $\mathbf{W}_2$). In both references, it is stated that the approximation is accurate for smooth functions when the order of the Chebyshev polynomials N is sufficiently large. Indeed, for two particular smooth functions $f(y)$ and $g(y)$, the numerical integration can be very accurate when there are sufficient collocation points. However, when computing the energy weight matrix **Q**, we are not able to reduce the error of numerical integration by increasing N, as illustrated by the following example. Suppose that $\tilde{v}$ is represented by (3.12), then the following inner product can be computed using

$$\begin{aligned} \langle \tilde{v}, \tilde{v} \rangle &= \int_{-1}^{1} \left(\sum_{n=0}^{N} a_{v,n}^* T_n(y) \sum_{n=0}^{N} a_{v,n} T_n(y) \right) \mathrm{d}y \\ &= \begin{bmatrix} a_{v,0} \\ \vdots \\ a_{v,N} \end{bmatrix}^* \begin{bmatrix} \Psi_{0,0} & \dots & \Psi_{0,N} \\ \vdots & \ddots & \vdots \\ \Psi_{N,0} & \dots & \Psi_{N,N} \end{bmatrix} \begin{bmatrix} a_{v,0} \\ \vdots \\ a_{v,N} \end{bmatrix} \end{aligned} \tag{3.23}$$

where

$$\Psi_{i,j} = \int_{y=-1}^{y=1} T_i(y) T_j(y) \mathrm{d}y \tag{3.24}$$

Since both $T_i(y)$ and $T_j(y)$ are known functions and can be written in trigonometric forms, $\Psi_{i,j}$ can be computed exactly using integration by parts and trigonometric identities. On the other hand, $\Psi_{i,j}$ can also be approximated numerically using (3.22). By subtracting the results obtained using these two methods, we are able to calculate the difference. If we are only interested in one particular element $\Psi_{i,j}$, we can always obtain the accurate value numerically by increasing the number N. However, no matter how we increase N, the numerical error of the whole matrix Ψ cannot be reduced since only

$\Psi_{i,j}$ with $i+j \leq 2N-3$ is accurate and the errors of elements close to $\Psi_{N,N}$ are always large. Figure 3.6 shows the errors of Ψ at all the positions i, j when $N = 10$ and the error of $\Psi_{10,10}$ is about 1. When N is increased to 100, the error of $\Psi_{10,10}$ is close to 0, but the error of $\Psi_{100,100}$ is still about 1, as illustrated in Figure 3.7.

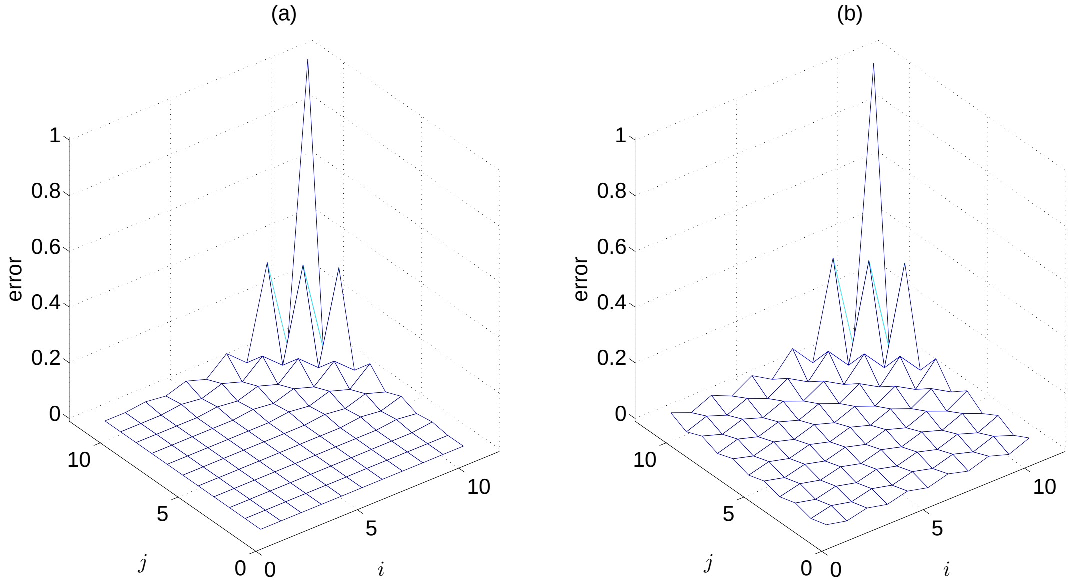

Figure 3.6: Numerical integration error of $\Psi_{i,j}$, $N = 10$. In plot (a) $\mathbf{W}_1$ is used and in plot (b) $\mathbf{W}_2$ is used.

More specifically, when we compute the matrix Ψ, there is a need to calculate

$$\Psi_{N,N} = \int_{y=-1}^{y=1} (T_N(y))^2 \, \mathrm{d}y \tag{3.25}$$

and the order of the integrand $(T_N(y))^2$ is $2N$ while the numerical integration is only accurate for polynomials with order less than $2N-3$. In the case $N = 100$, numerical integration using $\mathbf{W}_1$ yields $\Psi_{N,N} = 2.0000$, and $\Psi_{N,N} = 1.9998$ when $\mathbf{W}_2$ is used. However, the exact value is $\Psi_{N,N} = 1.0000$.

In addition, it follows from (3.11) that we need to compute inner product of the following form

$$\begin{aligned} \left\langle \frac{\partial \tilde{v}}{\partial y}, \frac{\partial \tilde{v}}{\partial y} \right\rangle &= \int_{-1}^{1} \left(\sum_{n=0}^{N} a_{v,n}^{*} \frac{\mathrm{d}\,(T_n(y))}{\mathrm{d}y} \sum_{n=0}^{N} a_{v,n} \frac{\mathrm{d}\,(T_n(y))}{\mathrm{d}y} \right) \mathrm{d}y \\ &= \begin{bmatrix} a_{v,0} \\ \vdots \\ a_{v,N} \end{bmatrix}^{*} \begin{bmatrix} \Xi_{0,0} & \dots & \Xi_{0,N} \\ \vdots & \ddots & \vdots \\ \Xi_{N,0} & \dots & \Xi_{N,N} \end{bmatrix} \begin{bmatrix} a_{v,0} \\ \vdots \\ a_{v,N} \end{bmatrix} \end{aligned} \tag{3.26}$$

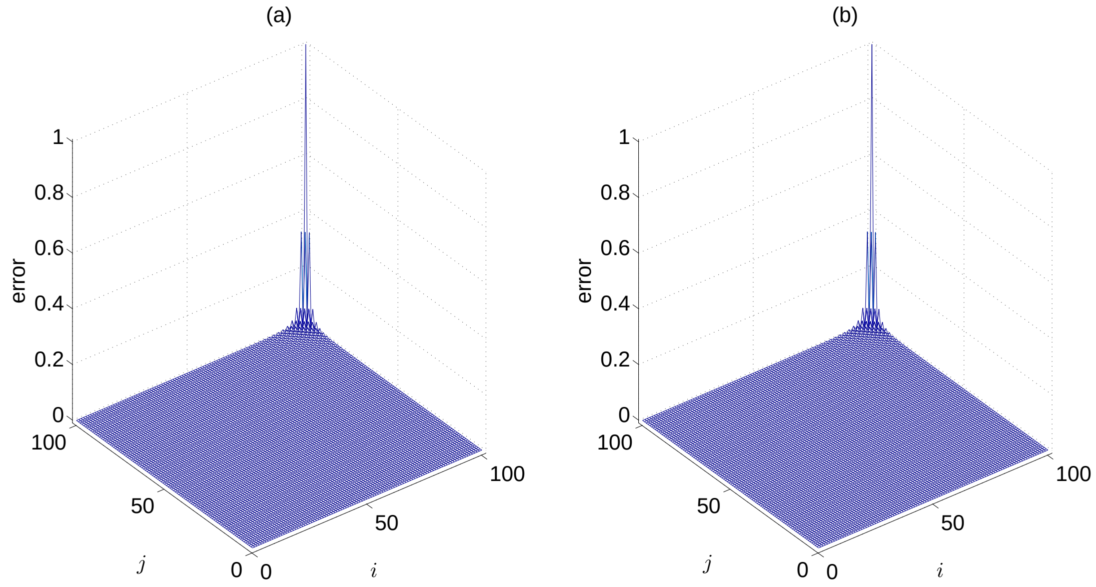

Figure 3.7: Numerical integration error of $\Psi_{i,j}$, $N = 100$. In plot (a) $\mathbf{W}_1$ is used and in plot (b) $\mathbf{W}_2$ is used.

where

$$\Xi_{i,j} = \int_{y=-1}^{y=1} \frac{\mathrm{d}\left(T_i(y)\right)}{\mathrm{d}y} \frac{\mathrm{d}\left(T_j(y)\right)}{\mathrm{d}y} \mathrm{d}y \tag{3.27}$$

Since the function $\frac{\mathrm{d}(T_i(y))}{\mathrm{d}y}$ becomes less smooth as i approaches N, the numerical integration will become less accurate in the process. The values of $\frac{\mathrm{d}(T_i(y))}{\mathrm{d}y}$ and $\frac{\mathrm{d}(T_j(y))}{\mathrm{d}y}$ at each of the collocation points can be computed exactly since analytical expressions can be derived, and $\Xi_{N,N}$ can be calculated either numerically using equation (3.22) or analytically using integration by parts. Table 3.1 shows that the differences between the exact value of $\Xi_{N,N}$ obtained using integration by parts and the values obtained using numerical integration grow rapidly as N increases. The large differences are caused by aliasing, where the product of two highly oscillating functions is approximated by one smooth function, producing large errors [153]. The errors of Ψ and Ξ computed by numerical integration can be very large, although it should be noted that if functions $\tilde{v}$ and $\tilde{\eta}$ are smooth enough, the last coefficients $a_{v,N}$ and $a_{\eta,N}$ should be reasonably small when N is large, which makes the effect of the numerical integration error less extreme.

It is not surprising that for case (i), the energy weight matrix $\mathbf{Q}$ can be very inaccurate since numerical integration can introduce large errors. In Section 3.6 we show that the inaccuracy of $\mathbf{Q}$ is indeed a reason for the numerical problem in case (i). For case (ii), the integration can be computed exactly using integration by parts and the trigonometric identities, thus are free of numerical integration errors. In fact, $\mathbf{Q}$ given in [133] is quite

Table 3.1: Values of $\Xi_{N,N}$ obtained using integration by parts and numerical integration.

	$N = 10$	$N = 100$	$N = 200$
Integration by parts (exact value)	426.6511	6.5687×10^4	2.9047×10^5
Numerical integration using $\mathbf{W}_1$	202.0202	2.0002×10^4	8.0002×10^4
Numerical integration using $\mathbf{W}_2$	5.2742×10^{-28}	3.8127×10^{-22}	6.2443×10^{-21}

accurate, hence the error of $\mathbf{A}$ is the main reason for the discretisation problems in case (ii).

3.5.2 Spurious eigenmodes

Due to its large growth rate with respect to N, the least stable eigenvalue of $\mathbf{A}^*\mathbf{Q} + \mathbf{QA}$ in Figure 3.2 is a spurious eigenvalue. Usually, there are two strategies to deal with spurious eigenvalues. One is to change the discretisation method to avoid the spurious eigenvalues, while the other is to identify and then neglect these spurious eigenvalues in the analysis. In practice, it is not straightforward to implement either of these strategies due to the difficulty of defining and identifying the spurious eigenvalues precisely.

According to Boyd [20], there are two kinds of spurious eigenvalues: numerically spurious eigenvalues and physically spurious eigenvalues. Numerically spurious eigenvalues are due to a lack of resolution and can always be eliminated by increasing N. Physically spurious eigenvalues cannot be avoided using this approach, because they are due to inappropriate application of boundary conditions or incorrect representation of a physical model. Numerically spurious eigenvalues always exist because the Orr-Sommerfeld operator has an infinite number of eigenvalues and no matter how large N is, there are always some eigenvalues that are not well resolved. In this thesis, we will restrict our attention to physically spurious eigenvalues (hereafter referred to as spurious eigenvalues for simplicity).

In many references, only positive eigenvalues that are clearly not physical were considered as spurious eigenvalues. A typical example is the two growing unstable eigenvalues of the Orr-Sommerfeld operator obtained by using the Chebyshev tau method [61]. Numerous modified methods have been proposed to remove the spurious eigenvalues [164] [55] [104] [75]. With sufficient resolution ($N = 100$), for both case (i) and case (ii), the 33 least stable eigenvalues of $\mathbf{A}$ arising from the Orr-Sommerfeld equation at $\alpha = 1, \beta = 0, \mathrm{Re} = 10000$ agree with the 32 values listed in [112] and the additional one given in [46]. When the goal is to decide the linear stability of the flow by examining the eigenvalues of the linear operator, such a matrix $\mathbf{A}$ is sufficiently accurate. Therefore it was believed that $\mathbf{A}$ obtained in both cases is free of spurious eigenvalues.

Usually, eigenvalues with negative real parts of large magnitude are considered unimportant since their temporal effects disappear very rapidly and eigenvalues close to the imaginary axis dominate. However, when the aim is to compute the energy evolution of the flow, then it is these most stable eigenvalues that may be causing problems. As mentioned previously, in case (ii) when only K least stable eigenmodes of $\mathbf{A}$ are considered in the computation where $K \ll 2N$, there is no transient peak in the plot of $G(\alpha, \beta, \mathrm{Re}, t)$ and when all eigenmodes are considered, there are always transient peaks. For ease of reference, denote $G(\alpha, \beta, \mathrm{Re}, t, K)$ as the energy amplification factor computed by using only K least stable eigenmodes of $\mathbf{A}$. To identify the source of transient peaks, we increase K and observe the change of the plot $G(\alpha, \beta, \mathrm{Re}, t, K)$.

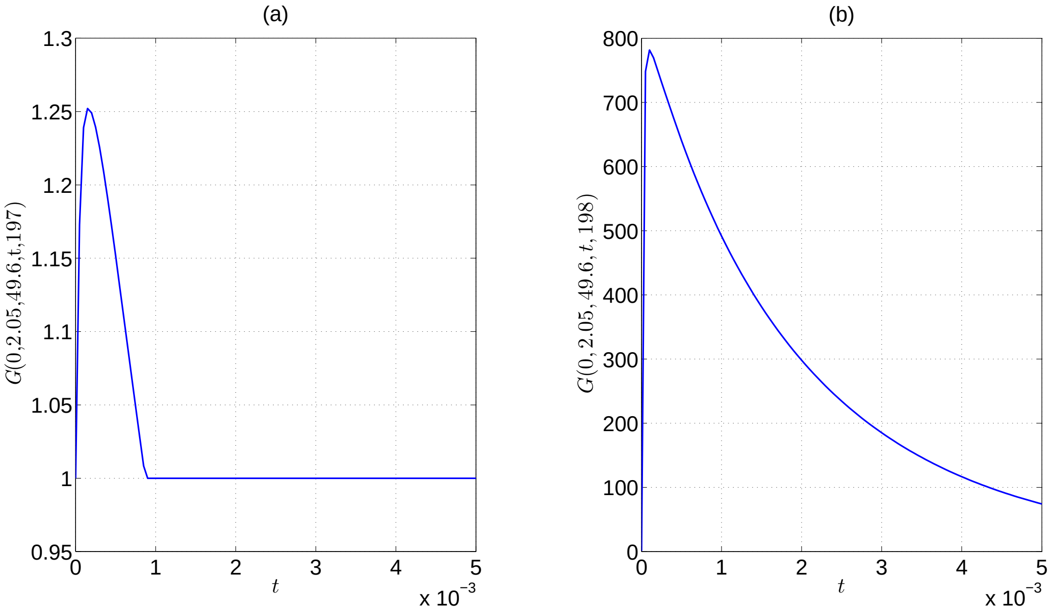

Figure 3.8: (a): $G(0, 2.05, 49.6, t, 197)$, (b): $G(0, 2.05, 49.6, t, 198)$. Both plots are for case (i) and $N = 100$.

Figure 3.8 shows that in case (i), $G(0, 2.05, 49.6, t, 197) < 1.25$ for all time, while the maximal amplification factor is larger than 700 when only one additional eigenmode is included for computation. However, since $\mathbf{Q}$ has large errors, we do not know whether the difference is due to the 198_{th} eigenmode of $\mathbf{A}$, which is the most stable eigenmode, or the inaccuracy of $\mathbf{Q}$, or a combination of both effects. Moreover, we know that the difference between plot (a) and plot (b) of Figure 3.9 for case (ii) is due to the 196_{th} least stable eigenmode, which is the 7_{th} most stable eigenmodes, because the energy weight matrix in this case is accurate. By carrying out numerical experiments in a similar manner, it can be shown that eigenvalues with negative real parts of large magnitude

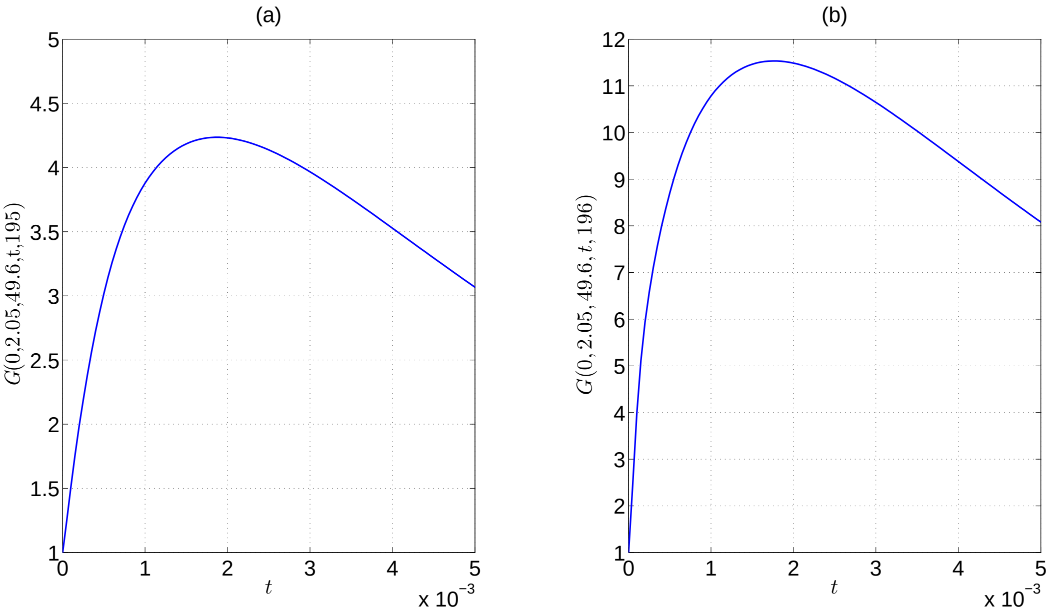

Figure 3.9: (a): $G(0, 2.05, 49.6, t, 195)$, (b): $G(0, 2.05, 49.6, t, 196)$. Both plots are for case (ii) and $N = 100$.

and their corresponding eigenfunctions are one of the reasons for the presence of transient peaks.

It is clear that eigenvalues with negative real parts that are far from the imaginary axis also play an important role when computing the energy evolution. More precisely, it is their corresponding eigenfunctions that are important. The unstable, spurious eigenvalues of $\mathbf{A}^*\mathbf{Q} + \mathbf{Q}\mathbf{A}$ are caused at least partly by the most stable eigenmodes of $\mathbf{A}$ and it can be seen that these eigenmodes are also spurious because the transient peaks in Figure 3.8 and Figure 3.9 are clearly not physical. These eigenmodes were not considered spurious since the eigenvalues are negative instead of positive. In fact, there are at least six more spurious eigenvalues with negative real parts in case (ii) due to the way the boundary conditions are enforced.

Spurious eigenvalues only appear in nonperiodic and generalised eigenvalue problems [20]. Dawkins *et al.* have shown that in the Chebyshev tau method spurious eigenvalues are actually approximations of infinite eigenvalues in generalised eigenvalues problems [42]. Perturbation of generalised eigenvalues can create either negative or positive spurious eigenvalues, which explains why the eigenvalues with negative real parts of large magnitude can also be spurious [20] [42]. Similarly, for the collocation method, eliminating all the positive spurious eigenvalues does not necessarily mean that none of the remaining eigenvalues is spurious.

3.6 Discretisation using Galerkin method

In this section, we show that the spectral Galerkin method can avoid the numerical difficulties that have been encountered. Approximating the wall-normal velocity $\tilde{v}$ using

$$\tilde{v} = \sum_{n=0}^{N} a_{v,n}(1-y^2)^2 T_n(y) \tag{3.28}$$

ensures that the Dirichlet and Neumann boundary conditions are satisfied. Similarly, the wall-normal vorticity $\tilde{\eta}$ can be approximated by

$$\tilde{\eta} = \sum_{n=0}^{N} a_{\eta,n}(1-y^2) T_n(y) \tag{3.29}$$

which satisfies the Dirichlet boundary conditions. This approach was proposed by Moser *et al.* [108] and was used by Jovanovic and Bamieh in [83]. Other basis functions can also be used as long as they are complete and satisfy the boundary conditions. For example, approximating $\tilde{v}$ and $\tilde{\eta}$ with the basis functions

$$\begin{aligned} \psi_n(y) &= T_n(y) - \frac{2(n+2)}{n+3} T_{n+2}(y) + \frac{n+1}{n+3} T_{n+4}(y) && (3.30) \\ \phi_n(y) &= T_n(y) - T_{n+2}(y) && (3.31) \end{aligned}$$

which were proposed by Shen in [140], gives the same result reported here.

When using the Chebyshev collocation method to discretise the system in the wall-normal direction, in order to impose the no-slip boundary conditions, there is always a need to delete two rows and two columns of **A**, which means that two expansion coefficients are neglected. Using the Galerkin method, this problem can be avoided, although its implementation is more difficult [20].

Substituting (3.28) and (3.29) into (3.10), we have

$$(\mathcal{D}^2 - k^2) \sum_{n=0}^{N} \dot{a}_{v,n}(1-y^2)^2 T_n(y) = \mathcal{L}_{OS} \sum_{n=0}^{N} a_{v,n}(1-y^2)^2 T_n(y) \tag{3.32}$$

$$\sum_{n=0}^{N} \dot{a}_{\eta,n}(1-y^2) T_n(y) = -\mathrm{i}\beta U' \sum_{n=0}^{N} a_{v,n}(1-y^2)^2 T_n(y) + \mathcal{L}_{SQ} \sum_{n=0}^{N} a_{\eta,n}(1-y^2) T_n(y) \tag{3.33}$$

Using $(1-y^2)^2 T_n(y)$ as the test functions for (3.32) and $(1-y^2)T_n(y)$ as the test functions for (3.33), the system matrix **A** can be computed.

Substituting (3.28) and (3.29) into (3.11) yields

$$\begin{aligned}
E &= \frac{1}{2}\int_{-1}^{1}\left(\tilde{v}^*\tilde{v}+\frac{1}{k^2}((\mathcal{D}\tilde{v})^*\mathcal{D}\tilde{v}+\tilde{\eta}^*\tilde{\eta})\right)\mathrm{d}y \\
&= \frac{1}{2}\begin{bmatrix} a_{v,0} \\ \vdots \\ a_{v,N}\end{bmatrix}^* \begin{bmatrix} \Upsilon_{0,0} & \dots & \Upsilon_{0,N} \\ \vdots & \ddots & \vdots \\ \Upsilon_{N,0} & \dots & \Upsilon_{N,N}\end{bmatrix} \begin{bmatrix} a_{v,0} \\ \vdots \\ a_{v,N}\end{bmatrix} \\
&+ \frac{1}{2}\begin{bmatrix} a_{\eta,0} \\ \vdots \\ a_{\eta,N}\end{bmatrix}^* \begin{bmatrix} \Theta_{0,0} & \dots & \Theta_{0,N} \\ \vdots & \ddots & \vdots \\ \Theta_{N,0} & \dots & \Theta_{N,N}\end{bmatrix} \begin{bmatrix} a_{\eta,0} \\ \vdots \\ a_{\eta,N}\end{bmatrix}
\end{aligned} \tag{3.34}$$

where

$$\Upsilon_{i,j} = \int_{-1}^{1}\left((1-y^2)^4T_i(y)T_j(y)+\frac{1}{k^2}\frac{\mathrm{d}\left((1-y^2)^2T_i(y)\right)}{\mathrm{d}y}\frac{\mathrm{d}\left((1-y^2)^2T_j(y)\right)}{\mathrm{d}y}\right)\mathrm{d}y \tag{3.35}$$

and

$$\Theta_{i,j} = \frac{1}{k^2}\int_{-1}^{1}\left((1-y^2)^2T_i(y)T_j(y)\right)\mathrm{d}y \tag{3.36}$$

so that the energy weight matrix can be computed exactly

$$\mathbf{Q} = \frac{1}{2}\begin{bmatrix}\Upsilon & \mathbf{0} \\ \mathbf{0} & \Theta\end{bmatrix} \tag{3.37}$$

Before proceeding, we note that at $N = 100$, the 33 least stable eigenvalues of the Orr-Sommerfeld equation obtained in this way agree with the values listed in [112] and [46]. Moreover, as stated in [164], such an approach is free of positive spurious eigenvalues. However, we are not able to determine directly whether there are negative spurious eigenvalues.

The accuracy of the Galerkin approach can be illustrated by the following graphs. From plot (a) of Figure 3.10 we can see that when $N = 100$, by solving inequality (3.20), the subcritical Reynolds number below which there is no energy growth at $\alpha = 0, \beta = 2.05$ is $\mathrm{Re} \approx 49.6039$, which is equivalent to the energy Reynolds number derived by the classical energy approach. Figure 3.10(b) illustrates the relationship between the number N and the subcritical Reynolds number derived by solving inequality (3.20) at $\alpha = 0, \beta = 2.05$. When N is large enough, these plots do not change with N, suggesting that this discretisation method is stable, and these results do not suffer from the problems described in Section 3.1.

The energy evolution of the flow system can now be computed using (3.21). Figure 3.11 plots the evolution of the energy growth function $G(0, 2.05, \mathrm{Re}, t) - 1$ for $\mathrm{Re} = 49.6039$ and $\mathrm{Re} = 49.604$ calculated using the Galerkin method. It can be seen that

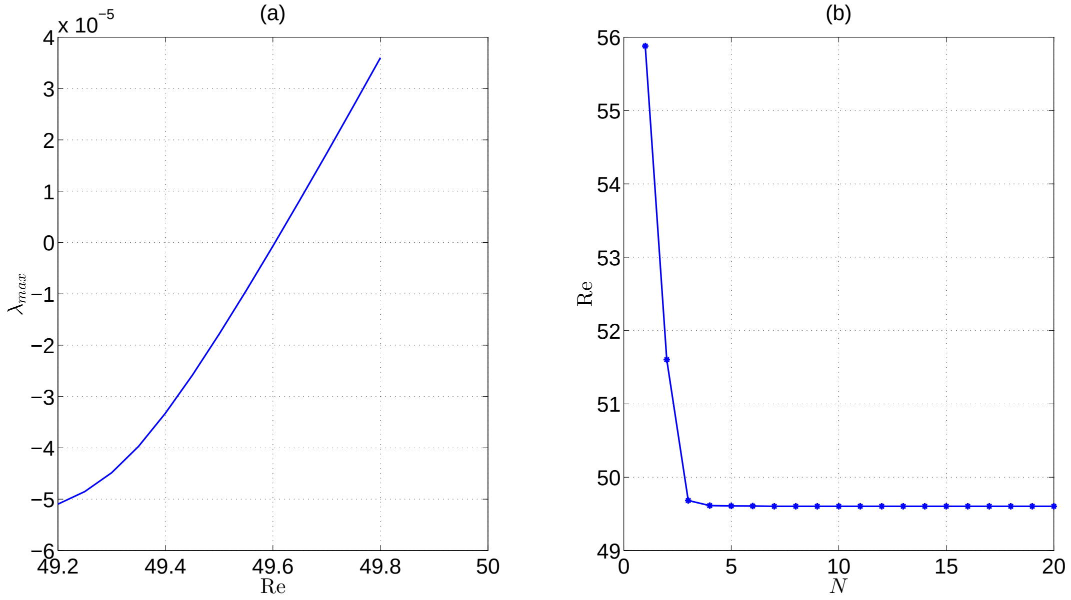

Figure 3.10: (a): The largest eigenvalue of $\mathbf{A}^*\mathbf{Q} + \mathbf{Q}\mathbf{A}$ versus Reynolds number Re at $\alpha = 0, \beta = 2.05, N = 100$. (b): Subcritical Reynolds number Re versus N at $\alpha = 0, \beta = 2.05$.

the perturbation energy decays monotonically at Re = 49.6039, while there is energy growth at Re = 49.604, although the energy amplification factor is extremely small and decays very quickly. When N is increased, these plots do not change, suggesting that the discretisation method converges.

Figure 3.12 reproduces two plots in Figure 3.4, which shows the energy growth at high Reynolds number Re = 1000. There is no transient peak when we use the Galerkin method, which indicates that the transient peak is not physical and it is associated with the spurious eigenmodes of $\mathbf{A}$. When the Reynolds number is large and the time interval is long enough, the plots produced by the collocation method and the Galerkin method are almost identical, suggesting that the collocation method can be used in these situations.

One may think that the superior performance of the Galerkin method over the collocation method is not because of the way the boundary conditions are imposed and the problems associated with the collocation method is due to the ill-conditioning of the discretised Laplace operator $\mathcal{D}^2 - k^2$, which has to be inverted in the calculation. However, the condition number of this operator in the Galerkin method is in fact larger than that in the collocation method. When $N = 100$, this condition number is 8.755×10^7 in the Galerkin method, and it is 4.832×10^6 for case (i) and is 6.275×10^6 for case (ii) in the collocation method. Therefore the conditioning of the Laplace operator cannot

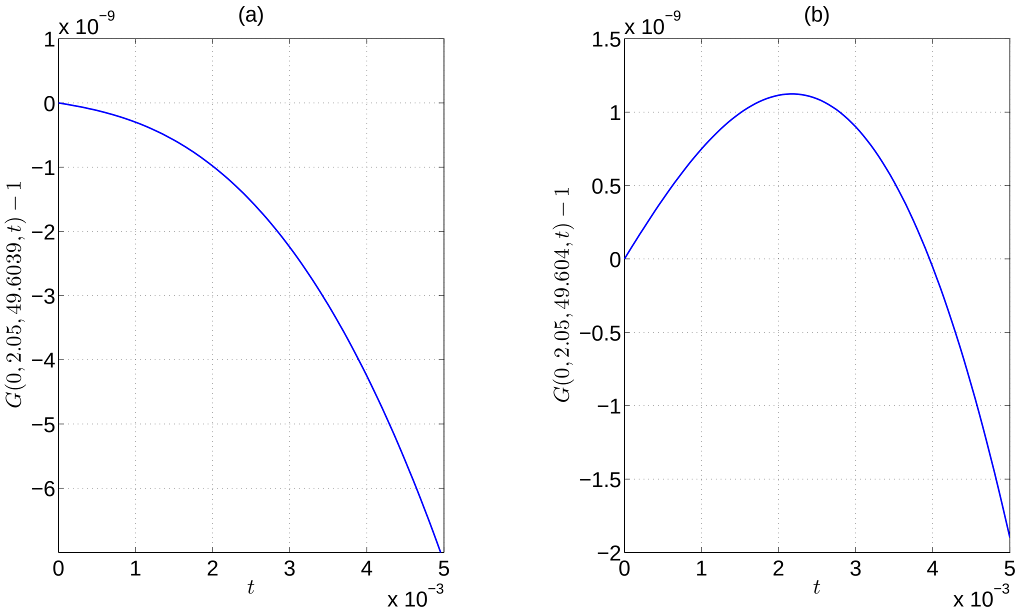

Figure 3.11: (a): $G(0, 2.05, 49.6039, t) - 1$, (b): $G(0, 2.05, 49.604, t) - 1$. $N = 100$ for both plots.

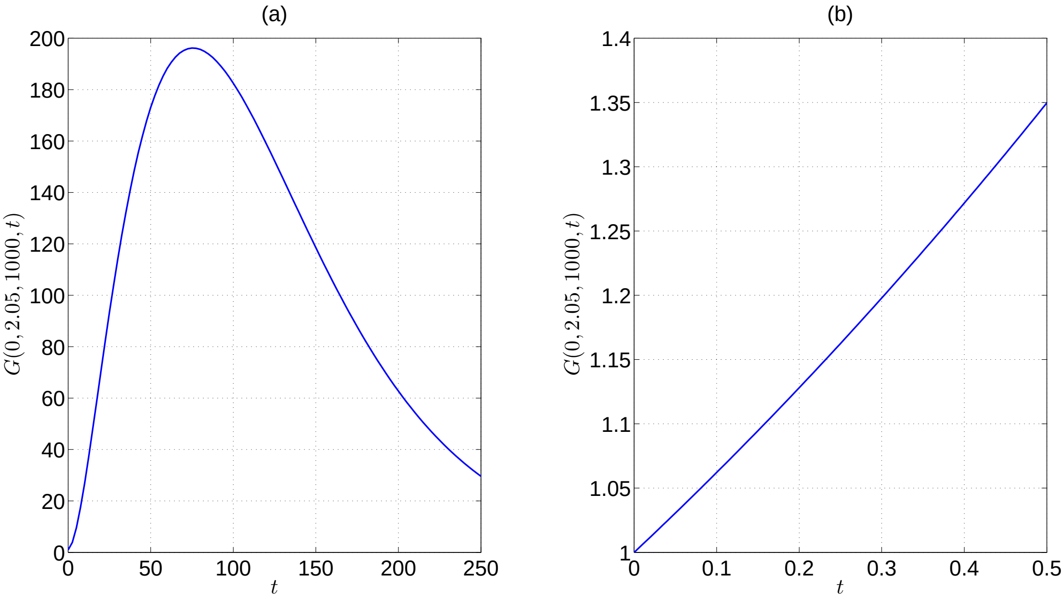

Figure 3.12: $G(0, 2.05, 1000, t)$ by the Galerkin method, $N = 100$. (a): $t \in [0, 250]$, (b): $t \in [0, 0.5]$.

explain the different performances of the Galerkin method and the collocation method. Nevertheless, reducing the condition numbers of the discretised Laplace operator and the Orr-Sommerfeld/Squire operator in the collocation method can still be beneficial to avoiding other numerical problems. A comprehensive investigation of the numerical conditioning of these operators in the collocation method can be found in McKernan's thesis [105].

It still remains to show that the numerical integration error could lead to inaccuracy when computing the energy growth of plane Poiseuille flow. By calculating each $\Upsilon_{i,j}$ and $\Theta_{i,j}$ using numerical integration, we can obtain the energy weight matrix numerically. To avoid confusion, we denote it as $\mathbf{Q}_\epsilon$. Once again, the largest eigenvalue of $\mathbf{A}^*\mathbf{Q}_\epsilon + \mathbf{Q}_\epsilon\mathbf{A}$ moves with changing N and it is always positive, which makes it impossible to find the subcritical Reynolds number with such a $\mathbf{Q}_\epsilon$. In addition, the transient peaks are always present in the energy evolution plots if $\mathbf{Q}_\epsilon$ is used. It means that the inaccuracy of numerical integration is also a source of numerical problems discussed previously.

3.7 Most dangerous initial condition

The function $G(\alpha, \beta, \mathrm{Re}, t)$ gives the largest possible energy amplification factor for a flow mode (α, β) at Re and t, but it does not tell us which initial conditions will lead to such an amplification factor. From (3.21), the kinetic energy of the system subject to any initial condition $\hat{\mathbf{x}}_0$ with unit energy cannot be greater than $G(\alpha, \beta, \mathrm{Re}, t)$ at time t. Therefore $G(\alpha, \beta, \mathrm{Re}, t)$ is an optimisation over all possible initial conditions. The initial condition that leads to the largest possible energy amplification factor is thus called the most dangerous or the optimal initial condition, depending on the perspective of view. It sometimes is also called the most sensitive initial condition.

It is a standard result in numerical linear algebra that the 2-norm of a matrix is its largest singular value [155]. Since

$$G(\alpha, \beta, \mathrm{Re}, t) = \|\mathbf{F}e^{\mathbf{A}t}\mathbf{F}^{-1}\|_2^2 \tag{3.38}$$

we carry out the singular value decomposition (SVD) of the matrix $\mathbf{R} = \mathbf{F}e^{\mathbf{A}t}\mathbf{F}^{-1}$

$$\mathbf{R} = \mathbf{T}\mathbf{\Sigma}\mathbf{V}^* \tag{3.39}$$

where $\mathbf{T}$ and $\mathbf{V}$ are unitary matrices and $\mathbf{\Sigma}$ is the diagonal matrix with all the singular values arranged in descending order in terms of magnitude. Denoting the largest singular value as σ_1, $\mathbf{T}(:,1)$ and $\mathbf{V}(:,1)$ as the first columns of $\mathbf{T}$ and $\mathbf{V}$, respectively, we have

$$\mathbf{R}\mathbf{V}(:,1) = \sigma_1\mathbf{T}(:,1) \tag{3.40}$$

which means that the energy of the input $\mathbf{V}(:,1)$ can be amplified σ_1 times by the system. Taking the energy weight matrix into consideration, it is now straightforward to verify that

$$\hat{\mathbf{x}}_0 = \mathbf{F}^{-1}\mathbf{V}(:,1) \tag{3.41}$$

is the most dangerous initial condition.

The most dangerous initial condition $\hat{\mathbf{x}}_0$ is a function of t as the matrix $\mathbf{R}$ depends on t. For example, at $\alpha = 0, \beta = 2$ and $\text{Re} = 5000$, we calculate the most dangerous initial conditions at three time instants $t_1 = 100, t_2 = 500$ and $t_3 = 1000$ and the development of the system energy over time corresponding to these initial conditions is plotted in Figure 3.13. At t_1, the magenta dashed line achieves the highest value among the three dashed lines. Note that this value is not a maximum over time, but a maximum over initial conditions. While at t_2, the black dashed line reaches the largest value among the three lines. Similarly, the red line achieves the largest value at t_3 among the three lines. As can be seen, the function $G(\alpha, \beta, \text{Re}, t)$ achieves the largest value over all possible initial conditions, therefore it is an optimisation over initial conditions.

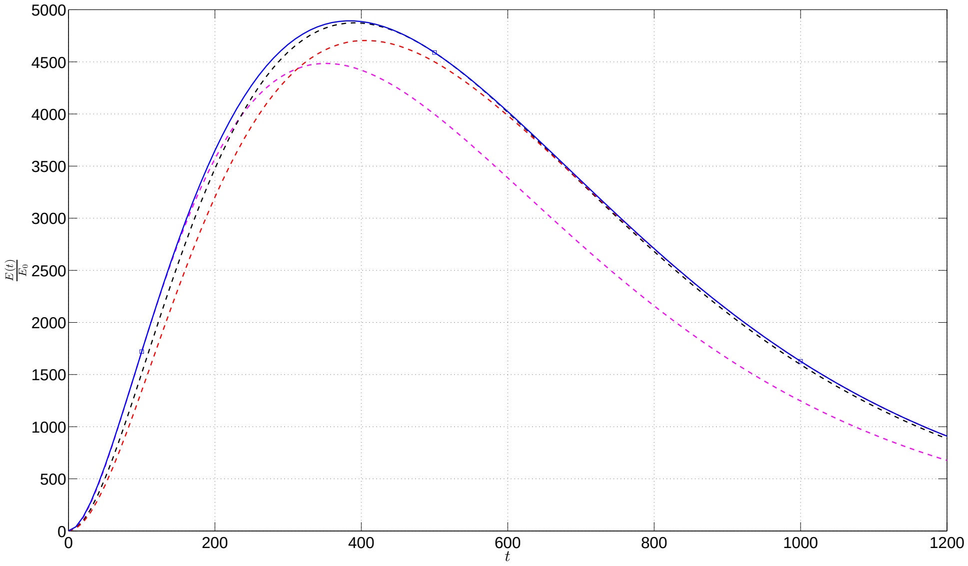

Figure 3.13: Energy amplification factor $\frac{E(t)}{E_0}$ versus time t corresponding to different initial conditions (dashed lines) and $G(0, 2, 5000, t)$ (solid).

The most dangerous initial condition for the flow at $\alpha = 0, \beta = 2$ and $\text{Re} = 5000$ is illustrated in Figure 3.14, where the three velocity components are plotted. With this initial condition, the kinetic energy of the flow will be 4893.18 times of its initial energy at $t = 380$.

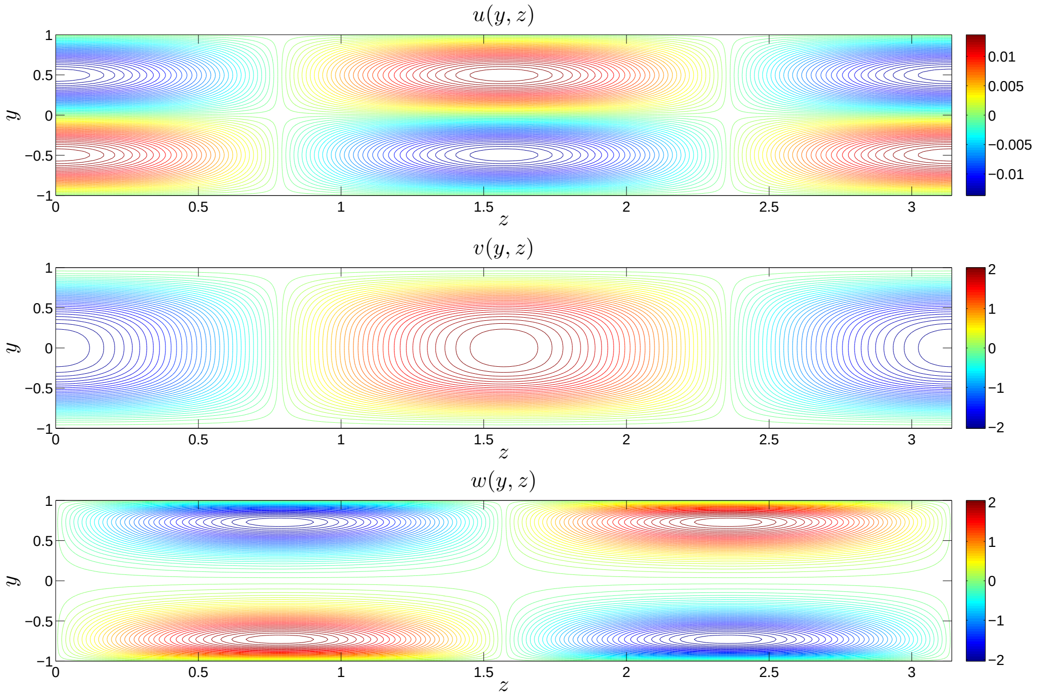

Figure 3.14: Most dangerous initial condition at $\alpha = 0, \beta = 2$ and Re $= 5000$.

However, it should be noted that if the initial condition is completely random, the energy amplification factor is likely to be much smaller, as can be demonstrated by numerical computations. The initial condition in real life may not be as sensitive as the most dangerous one.

3.8 Conclusion

In this chapter, we have shown that the Chebyshev collocation method is not sufficiently accurate to compute the transient growth of plane Poiseuille flow due to the existence of spurious eigenvalues and the errors in numerical integration. While the effect of spurious eigenvalues with positive real parts has been known for some time, this chapter shows that spurious eigenvalues with negative real parts of large magnitude can also affect the calculation of energy growth. We then show that a spectral Galerkin method is sufficiently accurate to allow us to derive the subcritical Reynolds number that matches the energy Reynolds number obtained by the classical energy approach. In addition, it enables us to obtain accurate energy evolution plots that do not exhibit transient peaks.

Chapter 4

Finite-Dimensional Models and Stability Analysis

4.1 Introduction

So far the facts we have understood include:

1. Plane Poiseuille flow is unstable when $\mathrm{Re} > \mathrm{Re}_c = 5772.22$. This is a result of eigenvalue analysis [112] and Lyapunov's indirect method [86];
2. The flow is globally stable when $\mathrm{Re} < \mathrm{Re}_E \approx 49.6$, which has been shown using the classical energy approach in the literature [23] and generalised passivity approach in Chapter 2 of this thesis;
3. The flow can experience transient energy growth when $\mathrm{Re}_E < \mathrm{Re} < \mathrm{Re}_c$, as discussed in Chapter 3.

How about the stability of the flow when $\mathrm{Re}_E < \mathrm{Re} < \mathrm{Re}_c$? This is what we are most interested in. It is not surprising that there is a large gap between Re_E and Re_c, and Re_E is quite conservative compared to the Reynolds number at which the transition is usually observed. Essentially, Re_E is obtained by Lyapunov analysis using the kinetic energy of the disturbance as the Lyapunov function. As mentioned in Chapter 2, conservativeness is fundamental to Lyapunov analysis in the sense that the stability theorems give only sufficient but not necessary conditions for a nonlinear dynamical system to be stable. In addition, the use of a simple quadratic function as the Lyapunov function is likely to be another source of conservativeness. If we could reduce the conservativeness by finding a "better" Lyapunov function, we would be able to raise the lower bound on the Reynolds number below which the flow is globally asymptotically stable. Unfortunately, there is still no systematic way to construct Lyapunov functions for a general nonlinear dynamical system [86].

As mentioned previously, strictly speaking, the flow system under study is infinite-dimensional as it is governed by PDEs. Therefore its stability should be studied within the framework of infinite-dimensional system theory. For example, in the classical energy approach, variational calculus and some optimisation techniques have been used to find the energy Reynolds number Re_E with the kinetic energy used as the Lyapunov functional. However, searching for more general Lyapunov functionals turns out to be very difficult and so far no such a better Lyapunov functional has been found. Nevertheless, it is possible to employ sum of squares (SOS) optimisations to build less conservative Lyapunov functionals for a system described by PDEs [114]. Another route is to first reduce the infinite-dimensional system to a finite-dimensional approximation by spatial discretisation and then search for less conservative Lyapunov functions. After discretisation, the system is described by polynomial vector fields and the construction of Lyapunov functions for such a system is more straightforward compared to that in the infinite-dimensional case. This benefit comes at several costs. First of all, the computational cost of search for general Lyapunov functions becomes significantly higher and this is probably the biggest difficulty. Secondly, the stability result may vary if different spatial discretisation methods are used. We will discuss this later in this chapter. In addition, the physical meaning of the Lyapunov function may be lost, although it is not necessary to associate any physical meaning to a Lyapunov function. Finally, it should be noted that strictly speaking, the stability result for finite-dimensional approximations does not necessarily carry over to the original system. Nevertheless, it would still be encouraging if we could find a higher Reynolds number below which a finite-dimensional model of plane Poiseuille flow is globally asymptotically stable and we might be able to gain more insight to study the stability of the infinite-dimensional system.

Often, we are also interested in the relative stability of dynamical systems. For example, a linear system

$$\dot{x} = A_1 x \tag{4.1}$$

is said to be relatively more stable than another linear system

$$\dot{x} = A_2 x \tag{4.2}$$

if the most unstable eigenvalue of A_1 lies on the left hand side of that of A_2 in the complex plane [47]. Similarly, from the previous chapters we can conclude that plane Poiseuille flow at $\mathrm{Re} < \mathrm{Re}_E$ is relatively more stable than the flow at $\mathrm{Re}_E < \mathrm{Re} < \mathrm{Re}_c$, which in turn is relatively more stable than the flow at at $\mathrm{Re} > \mathrm{Re}_c$. As the flow is a nonlinear dynamical system, its relative stability can not be described by the location of the most unstable eigenvalue alone, although the eigenvalue certainly plays an important part.

The relative stability of a nonlinear system can be more appropriately characterised by its ROA [86]. As mentioned in Chapter 2, the ROA is the set of all initial conditions for which the solution of the system goes to zero when time t approaches ∞. Therefore in essence the ROA includes all the perturbations that the system can recover from. Plane Poiseuille flow at $\mathrm{Re} < \mathrm{Re}_E$ has a ROA of the entire state space as it can recover from any perturbations, while the ROA is expected to become smaller when the Reynolds number is increased. Although it follows from the Lyapunov indirect method that the flow is locally asymptotically stable at $\mathrm{Re} \approx 1000$ as the flow is linearly stable, the ROA of the system might be so small that the state cannot go back to the equilibrium point when it is subject to any perturbation of moderate magnitude. Therefore we might be able to explain the subcritical transition if we could understand how the size of the ROA changes as a function of Re.

Unfortunately, determining the ROA of a nonlinear system is far from trivial and it is usually not possible to find the exact ROA. As a result, the estimated ROA is more often studied in the literature. Once again, reducing the conservativeness as much as possible is important. In this chapter, we will discuss the existing methods of search for the estimated ROA of a nonlinear dynamical system and the difficulties that will be encountered when applying these methods to plane Poiseuille flow.

Throughout this thesis, we have discretised the fluid flow system in space and the dimensionality of the finite-dimensional approximation has to be very high in order to improve the accuracy. So far the largest DNS of channel flow has hundreds of billions of state variables and the simulation has to be carried out on hundreds of thousands of CPU cores [94]. Although in order to study the stability of channel flow quantitatively, an approximation with thousands of state variables might be sufficient, as we will see, the high dimensionality still poses serious difficulties and it remains a barrier we cannot overcome. On the other hand, compared to the original, infinite-dimensional system model, any finite-dimensional approximation is still of low order. Another direction of thinking is to study the stability of the flow system qualitatively using very low order models. We will discuss some low order models that fall into this category in this chapter.

4.2 Numerical considerations

4.2.1 Spatial discretisation methods

As we have shown in the last chapter, the choice of the numerical methods that are used to discretise the NSEs is sometimes crucial to achieve high accuracy when studying the stability of channel flow. Numerical methods that are good for one purpose may not be as good if the aim has changed. For example, the Chebyshev collocation method is sufficiently accurate to calculate the most unstable eigenvalues of the Orr-Sommerfeld operator, but it is less ideal when the transient growth in the flow is calculated. The implication of the results in the last chapter is alarming. If we choose to work directly on the finite-dimensional spaces by discretising the NSEs without calculating any adjoint operators, we can conclude that plane Poiseuille flow is globally asymptotically stable at $\mathrm{Re} < \mathrm{Re}_E$ when the Chebyshev Galerkin method is used, while we could not reach this conclusion if the Chebyshev collocation method is used.

We have seen that the Chebyshev collocation method gives accurate results in the study of the linear stability of the system. It also can be used to calculate the transient growth as long as the Reynolds number is high and the time t is not too small. We note that in both the study of linear stability and transient growth, the governing equations are linearised. If all the nonlinear terms are retained, is it still reasonable to discretise the NSEs using the Chebyshev collocation method?

The answer is it depends. If our purpose is to study the stability by simulating the flow, the Chebyshev collocation method is certainly a valid choice. In fact, it remains one of the most important spectral methods that are widely used in DNS [26]. However, it would be a bad choice if we want to study the stability of the flow through Lyapunov analysis, as shown in the last chapter.

So why do DNS and Lyapunov analysis have such a difference? In other words, why does a model that is good for simulation turn out to be a bad model for Lyapunov analysis and vice versa? Roughly speaking, it is because in DNS the initial condition is chosen to be reasonably well-behaved, while in Lyapunov analysis unphysical initial conditions are usually causing the trouble. We now discuss the reason in more details.

Suppose after discretisation the system state is governed by

$$\dot{\mathbf{x}} = \mathbf{A}\mathbf{x} + \mathbf{A}_2(\mathbf{x} \otimes \mathbf{x}) \tag{4.3}$$

where $\mathbf{A} \in \mathbb{C}^{n\times n}$, $\mathbf{A}_2 \in \mathbb{C}^{n\times n^2}$ and $\otimes$ denotes Kronecker product. The state vector $\mathbf{x} \in \mathbb{C}^n$ can be either the values at the collocation points or the Chebyshev expansion coefficients. Consider the case that $\mathbf{x}$ is a vector obtained by evaluating at the sample points. System (4.3) is globally asymptotically stable if $\mathbf{x} \to 0$ as $t \to \infty$ for any initial perturbation $\mathbf{x}_0 \in \mathbb{C}^n$. But it is important to note that physically plausible perturbations only form a strictly proper subset of $\mathbb{C}^n$. In other words, $\mathbf{x}_0$ cannot be completely random as it is the evaluation of a certain function (velocity and/or vorticity) at the collocation points. In real life, $\mathbf{x}_0$ should be reasonably smooth, which means the values of $\mathbf{x}_0$ at neighbouring points are related instead of independent. For this reason, Lyapunov analysis of system (4.3) is bound to give very conservative results as it also takes unphysical perturbations into consideration. By contrast, in DNS, the initial condition $\mathbf{x}_0$ is never completely random and it is usually obtained by evaluating some particular functions. As shown in Figure 4.1, although both the vectors represented by blue and red asterisks belong to $\mathbb{C}^n$, their behaviours as initial conditions are very different. Requiring system (4.3) to be able to recover from both perturbations is unnecessarily restrictive.

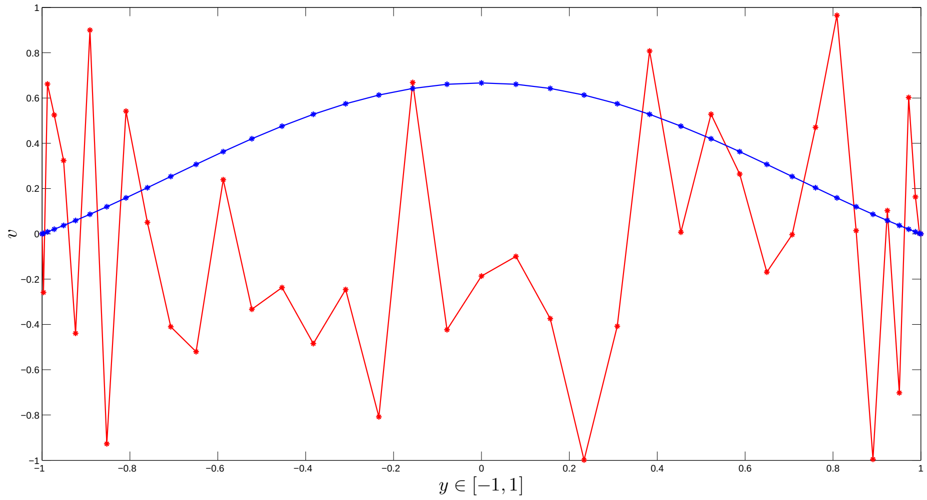

Figure 4.1: Physical (blue) and unphysical (red) initial conditions.

As long as reasonable initial conditions are chosen, DNS using the Chebyshev collocation method can be highly accurate. In fact, due to its ease of implementation and the existence of fast algorithms to calculate the nonlinear terms without aliasing errors, the Chebyshev collocation method has been widely used in DNS of channel flow [26]. By contrast, the implementation of the Chebyshev Galerkin method is more laborious. At every time step, there is a need to transform the variables from spectral spaces (expansion coefficients) to physical spaces (values at sample points). Since in the Galerkin method the basis functions are required to satisfy the boundary conditions, generally there is no fast algorithm to achieve the transform. This poses serious difficulties in calculating the nonlinear terms since the computational burden is too high. For this reason, the Chebyshev Galerkin method is not ideal for DNS of the flow. Instead, the Chebyshev tau method, in which the basis functions do not have to satisfy the boundary conditions, is far more common in DNS as there exist fast cosine transforms so that the calculation of the nonlinear terms is much more efficient.

To illustrate this point, let us consider the product

$$s(y) = u(y)v(y) \tag{4.4}$$

where $y \in [-1, 1]$, and $u(y)$ and $v(y)$ are in the projected space P_N, i.e.,

$$u(y) = \sum_{k=0}^{N} \hat{u}_k \phi_k(y) \tag{4.5}$$

$$v(y) = \sum_{k=0}^{N} \hat{v}_k \phi_k(y) \tag{4.6}$$

The expansion coefficient $\hat{s}_k$ can be determined by applying the weighted residual method, with test function $\phi_k(y)$ and weight function $w(y)$, so that

$$\begin{aligned} \hat{s}_k &= \int_{y=-1}^{y=1} u(y)v(y)\phi_k(y)w(y)\mathrm{d}y \\ &= \begin{bmatrix} \hat{u}_0 \\ \vdots \\ \hat{u}_N \end{bmatrix}^T \begin{bmatrix} \Phi_{0,0} & \cdots & \Phi_{0,N} \\ \vdots & \ddots & \vdots \\ \Phi_{N,0} & \cdots & \Phi_{N,N} \end{bmatrix} \begin{bmatrix} \hat{v}_0 \\ \vdots \\ \hat{v}_N \end{bmatrix} \end{aligned} \tag{4.7}$$

where

$$\Phi_{i,j} = \int_{-1}^{-1} \phi_i(y)\phi_j(y)\phi_k(y)w(y)\mathrm{d}y \tag{4.8}$$

Therefore in a naive way, it takes $\mathcal{O}(N^2)$ operations to calculate the coefficient $\hat{s}_k$. The high computation burden to calculate nonlinear terms used to be the single most important barrier for spectral methods to being used more widely [25].

In the case that the basis functions are the Chebyshev polynomials, it turns out that the computational burden can be significantly reduced by employing the transform methods [25]. The algorithm, also known as the 3/2 rule, can calculate $\hat{s}_k$ without aliasing errors by taking the following steps:

1. Padding the coefficients $\hat{u}_k$ such that

$$\check{u}_k = \begin{cases} \hat{u}_k, & k = 0, 1, \cdots, N, \\ 0, & k = N+1, N+2, \cdots, M. \end{cases}$$

   where $M \geq 3N/2 + 1/2$. $\hat{v}_k$ is padded in the same way;

2. Evaluating $u(y)$ and $v(y)$ at the Gauss-Lobatto points to obtain u_i and v_i with $i = 0, 1, \cdots, M$ by using inverse discrete cosine transform;

3. Calculating s_i at each of the collocation points by direct multiplications $s_i = u_i v_i$;

4. Using discrete cosine transform to obtain $\check{s}_k$, $k = 0, 1, \cdots, M$;

5. $\hat{s}_k = \check{s}_k$, $k = 0, 1, \cdots, N$ is the solution we are seeking.

With this algorithm, it takes only $\mathcal{O}(N \log_2 N)$ operations to calculate $\hat{s}_k$. Fast algorithms to transform between physical spaces (u_i, v_i, s_i) and spectral spaces $(\hat{u}_k, \hat{v}_k, \hat{s}_k)$ play a central part in the process. The connection to cosine functions and the existence of fast cosine algorithms are the main reasons for the popularity of the Chebyshev polynomials in spectral methods.

In the Chebyshev Galerkin method, as the basis functions are required to satisfy the boundary conditions, there are generally no fast algorithms to carry out the second and the fourth steps of the transform methods. For example, in the case that

$$\phi_k(y) = (1+y)^2 T_k(y) \tag{4.9}$$

where $T_k(y)$ is the k_{th} Chebyshev polynomial, it is not trivial to find fast algorithms to transform between u_i and $\hat{u}_k$.

However, if our purpose is to analyse the stability of the system using Lyapunov stability theorems, we do not need to simulate the flow, which means that there is no need to transform between spectral spaces and physical spaces when the Galerkin method is used. As the state vector $\mathbf{x}$ in the Galerkin method contains the expansion coefficients, any initial condition $\mathbf{x}_0$ is guaranteed to be smooth.

We now recognise that the model obtained by the Chebyshev collocation method is suitable for DNS, but not for Lyapunov analysis. On the contrary, the model generated by the Chebyshev Galerkin method is suitable for Lyapunov analysis, but less ideal for DNS. The primary goal of this chapter is to study the stability of the flow using Lyapunov theorems, thus the Chebyshev Galerkin method is an appropriate choice.

4.2.2 Forms of nonlinear terms

In Chapter 2, the nonlinear terms of the incompressible NSEs are given as

$$S_1 = u\frac{\partial u}{\partial x} + v\frac{\partial u}{\partial y} + w\frac{\partial u}{\partial z} \tag{4.10a}$$

$$S_2 = u\frac{\partial v}{\partial x} + v\frac{\partial v}{\partial y} + w\frac{\partial v}{\partial z} \tag{4.10b}$$

$$S_3 = u\frac{\partial w}{\partial x} + v\frac{\partial w}{\partial y} + w\frac{\partial w}{\partial z} \tag{4.10c}$$

This form is called the convective form in the literature. Due to the continuity equation (1.5d), the nonlinear terms can be written in many other equivalent forms. For example, the nonlinear terms in divergence form are

$$S_1 = \frac{\partial(u^2)}{\partial x} + \frac{\partial(uv)}{\partial y} + \frac{\partial(uw)}{\partial z} \tag{4.11a}$$
$$S_2 = \frac{\partial(uv)}{\partial x} + \frac{\partial(v^2)}{\partial y} + \frac{\partial(vw)}{\partial z} \tag{4.11b}$$
$$S_3 = \frac{\partial(uw)}{\partial x} + \frac{\partial(vw)}{\partial y} + \frac{\partial(w^2)}{\partial z} \tag{4.11c}$$

and the skew-symmetric form is the average of the convective form and the divergence form

$$S_1 = u\frac{\partial u}{\partial x} + v\frac{\partial u}{\partial y} + w\frac{\partial u}{\partial z} + \frac{1}{2}u(\frac{\partial u}{\partial x} + \frac{\partial v}{\partial y} + \frac{\partial w}{\partial z}) \tag{4.12a}$$
$$S_2 = u\frac{\partial v}{\partial x} + v\frac{\partial v}{\partial y} + w\frac{\partial v}{\partial z} + \frac{1}{2}v(\frac{\partial u}{\partial x} + \frac{\partial v}{\partial y} + \frac{\partial w}{\partial z}) \tag{4.12b}$$
$$S_3 = u\frac{\partial w}{\partial x} + v\frac{\partial w}{\partial y} + w\frac{\partial w}{\partial z} + \frac{1}{2}w(\frac{\partial u}{\partial x} + \frac{\partial v}{\partial y} + \frac{\partial w}{\partial z}) \tag{4.12c}$$

while the rotational form is

$$S_1 = (\frac{\partial u}{\partial z} - \frac{\partial w}{\partial x})w - (\frac{\partial v}{\partial x} - \frac{\partial u}{\partial y})v + \frac{1}{2}\frac{\partial(u^2+v^2+w^2)}{\partial x} \tag{4.13a}$$
$$S_2 = (\frac{\partial v}{\partial x} - \frac{\partial u}{\partial y})u - (\frac{\partial w}{\partial y} - \frac{\partial v}{\partial z})w + \frac{1}{2}\frac{\partial(u^2+v^2+w^2)}{\partial y} \tag{4.13b}$$
$$S_3 = (\frac{\partial w}{\partial y} - \frac{\partial v}{\partial z})v - (\frac{\partial u}{\partial z} - \frac{\partial w}{\partial x})u + \frac{1}{2}\frac{\partial(u^2+v^2+w^2)}{\partial z} \tag{4.13c}$$

While the equivalence of these forms in the continuous domain is straightforward to verify, it turns out that after discretisation they are generally no longer equivalent [25]. For example, all the four forms lead to different solutions in the collocation method [25]. As a result, choosing a suitable formulation of the nonlinear terms is an important step in simulations of the NSEs [91] [162] [25] [67]. Generally speaking, the factors that are taken into consideration when making the choice include accuracy and efficiency. The accuracy of the solution is no doubt the key issue of a simulation. It is known that some forms give more accurate numerical simulation results than others. For example, the skew-symmetric form is generally more accurate than the convective form in the collocation method [162]. The higher accuracy comes at the price of more computational efforts, which can be easily seen from a comparison of (4.10) and (4.12). Numerical stability sometimes also plays a role in choosing the form of the nonlinearity.

Now suppose that these four different forms of the nonlinear terms have been used and the NSEs are discretised using the Chebyshev Galerkin method, we arrive at four finite-dimensional models of the fluid flow system. If the four models are all different, how can one make any conclusions about the stability of the flow? If the stability result obtained by analysing the model with the convective form disagrees with that obtained from analysis of the model with skew-symmetric form, which result should one trust? Does the form that leads to more accurate numerical simulation also yields more accurate stability results?

These problems can be avoided if the four different forms of nonlinear terms after discretisation are equivalent. Furthermore, we have already recognised that the energy-preserving property of the nonlinearity is very important in our previous analysis of the stability of the flow. We now present a numerical discretisation of the NSEs in which the nonlinear terms in different forms are equivalent and remain passive in discrete forms. For simplicity, we only consider the 2-dimensional NSEs.

4.3 A numerical discretisation of the 2D Navier-Stokes equations

The equations governing the evolution of 2-dimensional plane Poiseuille flow in normal velocity formulation can be readily obtained in the way described in Chapter 2, but here a slightly different formulation is derived. As usual, let x and y be the streamwise and wall-normal directions, respectively. Consider a steady state flow with velocity field $(U, 0)$ and pressure P and a perturbed state with velocity field $(U + u, v)$ and pressure $P + p$. Suppose that there is no external force in both cases. Subtracting the NSEs for the steady state from the NSEs for the perturbed state gives

$$\frac{\partial u}{\partial t} + U\frac{\partial u}{\partial x} + vU' + S_1 = -\frac{\partial p}{\partial x} + \frac{1}{\mathrm{Re}}\nabla^2 u \tag{4.14a}$$

$$\frac{\partial v}{\partial t} + U\frac{\partial v}{\partial x} \qquad + S_2 = -\frac{\partial p}{\partial y} + \frac{1}{\mathrm{Re}}\nabla^2 v \tag{4.14b}$$

and

$$\frac{\partial u}{\partial x} + \frac{\partial v}{\partial y} = 0 \tag{4.14c}$$

where $U = 1 - y^2$, $U' = \frac{\mathrm{d}U}{\mathrm{dy}}$, the 2-dimensional Laplace operator ∇^2 takes the form

$$\nabla^2 = \frac{\partial^2}{\partial x^2} + \frac{\partial^2}{\partial y^2} \tag{4.15}$$

and the Reynolds number Re is defined in the same way as in 3-dimensional channel flow. The nonlinear terms in the convective form are

$$S_1 = u\frac{\partial u}{\partial x} + v\frac{\partial u}{\partial y} \tag{4.16a}$$

$$S_2 = u\frac{\partial v}{\partial x} + v\frac{\partial v}{\partial y} \tag{4.16b}$$

and it is straightforward to obtain the nonlinear terms in other forms in the way described in the previous section.

Taking $\frac{\partial}{\partial y}$ of (4.14a) and $\frac{\partial}{\partial x}$ of (4.14b)

$$\begin{aligned}
\frac{\partial^2 u}{\partial t \partial y} + U\frac{\partial^2 u}{\partial x \partial y} + U''v + \frac{\partial S_1}{\partial y} &= -\frac{\partial^2 p}{\partial x \partial y} + \frac{1}{\mathrm{Re}}\nabla^2 \frac{\partial u}{\partial y} && (4.17)\\
\frac{\partial^2 v}{\partial t \partial x} + U\frac{\partial^2 v}{\partial x^2} + \frac{\partial S_2}{\partial x} &= -\frac{\partial^2 p}{\partial x \partial y} + \frac{1}{\mathrm{Re}}\nabla^2 \frac{\partial v}{\partial x} && (4.18)
\end{aligned}$$

and then subtracting these equations eliminates the pressure term

$$\frac{\partial^2 u}{\partial t \partial y} - \frac{\partial^2 v}{\partial t \partial x} + U\frac{\partial^2 u}{\partial x \partial y} - U\frac{\partial^2 v}{\partial x^2} + U''v + \frac{\partial S_1}{\partial y} - \frac{\partial S_2}{\partial x} = \frac{1}{\mathrm{Re}}\nabla^2\frac{\partial u}{\partial y} - \frac{1}{\mathrm{Re}}\nabla^2\frac{\partial v}{\partial x} \quad (4.19)$$

The continuity equation (4.14c) guarantees that there exists a scalar function $\psi(x, y, t)$ such that

$$\begin{aligned}
u &= \frac{\partial \psi}{\partial y} && (4.20a)\\
v &= -\frac{\partial \psi}{\partial x} && (4.20b)
\end{aligned}$$

Substituting (4.20) to (4.19) yields the stream function formulation

$$\left(\frac{\partial}{\partial t} + U\frac{\partial}{\partial x}\right)\nabla^2\psi - U''\frac{\partial \psi}{\partial x} - \frac{1}{\mathrm{Re}}\nabla^4\psi = -\left(\frac{\partial S_1}{\partial y} - \frac{\partial S_2}{\partial x}\right) \quad (4.21)$$

and the nonlinearity can be written in terms of the stream function

$$\begin{aligned}
S_1 &= \frac{\partial \psi}{\partial y}\frac{\partial^2 \psi}{\partial x \partial y} - \frac{\partial \psi}{\partial x}\frac{\partial^2 \psi}{\partial y^2} && (4.22a)\\
S_2 &= -\frac{\partial \psi}{\partial y}\frac{\partial^2 \psi}{\partial x^2} + \frac{\partial \psi}{\partial x}\frac{\partial^2 \psi}{\partial x \partial y} && (4.22b)
\end{aligned}$$

The reason for employing the stream function formulation instead of the wall-normal velocity formulation is twofold. First of all, the divergence free condition is automatically imposed in the stream function formulation, making it easier to obtain an accurate semi-discrete nonlinear model of the 2-dimensional NSEs in which different forms of nonlinearity are equivalent. Secondly, the flow mode at zero streamwise wavenumber does not require extra assumptions and manipulation under this formulation.

The state equation (4.21) can be written in a more compact form

$$\dot{\mathbf{x}} = \mathcal{A}\mathbf{x} + \mathcal{B}\mathbf{S} \quad (4.23)$$

where $\dot{\mathbf{x}} = \psi$, $\mathbf{S} = \begin{bmatrix} S_1 & S_2 \end{bmatrix}^T$ and

$$\begin{aligned} \mathcal{A} &= (\nabla^2)^{-1}\left(-U\frac{\partial}{\partial x}\nabla^2 + U''\frac{\partial}{\partial x} + \frac{1}{\mathrm{Re}}\nabla^4\right) && (4.24) \\ \mathcal{B} &= (\nabla^2)^{-1}\left[-\frac{\partial}{\partial y} \quad \frac{\partial}{\partial x}\right] && (4.25) \end{aligned}$$

with $U'' = \frac{\mathrm{d}^2 U}{\mathrm{d}y^2}$.

As usual, the flow is assumed to be periodic in the streamwise direction and satisfy the no-slip boundary conditions in the wall-normal direction, i.e.,

$$u(y = \pm 1) = v(y = \pm 1) = 0 \tag{4.26}$$

and it follows from (4.14c) that

$$\frac{\partial v}{\partial y}(y = \pm 1) = 0 \tag{4.27}$$

Note that ψ is unique up to a constant, therefore there exists a ψ such that

$$\psi(y = \pm 1) = \frac{\partial \psi}{\partial y}(y = \pm 1) = 0 \tag{4.28}$$

Denoting L_x as the period of the flow in the streamwise direction, the nonlinearity is lossless in the sense that

$$\int_{y=-1}^{y=1}\int_{x=0}^{x=L_x} (uS_1 + vS_2)\, \mathrm{d}x\mathrm{d}y = 0 \tag{4.29}$$

and this can be proved by using integration by parts and the boundary conditions.

Since the flow is periodic, Fourier transform can be applied so that

$$\psi(x, y, t) = \sum_{m=-\infty}^{\infty} \tilde{\psi}_m(y, t)\, \mathrm{e}^{\mathrm{i}\alpha_m x} \tag{4.30}$$

and

$$S_i(x, y, t) = \sum_{m=-\infty}^{\infty} \tilde{S}_m^{(i)}(y, t)\, \mathrm{e}^{\mathrm{i}\alpha_m x} \tag{4.31}$$

where $\alpha_m = \frac{2\pi m}{L_x}$ and $i = 1, 2$. It follows from (4.22) that

$$\begin{aligned} \tilde{S}_m^{(1)} &= \sum_{m'=-\infty}^{\infty} \mathcal{D}\tilde{\psi}_{m-m'}\, \mathrm{i}\alpha_{m'}\mathcal{D}\tilde{\psi}_{m'} - \mathrm{i}\alpha_{m-m'}\tilde{\psi}_{m-m'}\, \mathcal{D}^2\tilde{\psi}_{m'} && (4.32a) \\ \tilde{S}_m^{(2)} &= \sum_{m'=-\infty}^{\infty} \mathcal{D}\tilde{\psi}_{m-m'}\alpha_{m'}^2\tilde{\psi}_{m'} - \alpha_{m-m'}\tilde{\psi}_{m-m'}\alpha_{m'}\, \mathcal{D}\tilde{\psi}_{m'} && (4.32b) \end{aligned}$$

Applying the Fourier transform, the state equation becomes

$$\begin{aligned}(\mathcal{D}^2-\alpha_m^2)\frac{\partial\tilde{\psi}_m}{\partial t} &= \left[-\mathrm{i}\alpha_m U(\mathcal{D}^2-\alpha_m^2)+\mathrm{i}\alpha_m U''+\frac{1}{\mathrm{Re}}(\mathcal{D}^2-\alpha_m^2)^2\right]\tilde{\psi}_m \\ &- \mathcal{D}\sum_{m'=-\infty}^{\infty}\mathcal{D}\tilde{\psi}_{m-m'}\,\mathrm{i}\alpha_{m'}\mathcal{D}\tilde{\psi}_{m'}-\,\mathrm{i}\alpha_{m-m'}\tilde{\psi}_{m-m'}\,\mathcal{D}^2\tilde{\psi}_{m'} \\ &+ \mathrm{i}\alpha_m\sum_{m'=-\infty}^{\infty}\mathcal{D}\tilde{\psi}_{m-m'}\alpha_{m'}^2\tilde{\psi}_{m'}-\alpha_{m-m'}\tilde{\psi}_{m-m'}\alpha_{m'}\,\mathcal{D}\tilde{\psi}_{m'} \qquad (4.33)\end{aligned}$$

Similarly, it can be written in a more compact form

$$\dot{\tilde{\mathbf{x}}}_m=\mathcal{A}_m\tilde{\mathbf{x}}_m+\mathcal{B}_m\tilde{\mathbf{S}}_m \qquad (4.34)$$

with $\tilde{\mathbf{x}}_m=\tilde{\psi}_m$, $\tilde{\mathbf{S}}_m=\begin{bmatrix}\tilde{S}_m^{(1)} & \tilde{S}_m^{(2)}\end{bmatrix}^T$, and

$$\begin{aligned}\mathcal{A}_m &= (\mathcal{D}^2-\alpha_m^2)^{-1}\left[-\mathrm{i}\alpha_m U(\mathcal{D}^2-\alpha_m^2)+\mathrm{i}\alpha_m U''+\frac{1}{\mathrm{Re}}(\mathcal{D}^2-\alpha_m^2)^2\right] \qquad (4.35) \\ \mathcal{B}_m &= (\mathcal{D}^2-\alpha_m^2)^{-1}\begin{bmatrix}\mathcal{D} & -\mathrm{i}\alpha_m\end{bmatrix} \qquad (4.36)\end{aligned}$$

where $\mathcal{D}$ denotes the partial differentiation in the y direction.

As ψ_m satisfies the homogeneous Dirichlet and Neumann boundary conditions, it can be approximated by the following polynomials

$$\tilde{\psi}_m=\sum_{n=0}^{N}a_{\psi_m,n}(1-y^2)^2T_n(y) \qquad (4.37)$$

where $T_n(y)$ is the n_{th} Chebyshev polynomial. Replacing the infinite series with finite sums by choosing $m,m',m-m'\in[-M,\ldots,0,\ldots,M]$, substituting (4.37) into the state equation (4.33) and using $(1-y^2)^2T_n(y)$ as the test functions, the following finite-dimensional model can be obtained

$$\dot{\check{\mathbf{x}}}=\mathbf{A}\check{\mathbf{x}}+\mathbf{B}\check{\mathbf{S}} \qquad (4.38)$$

where $\mathbf{A}\in\mathbb{C}^{L\times L}$ and $\mathbf{B}\in\mathbb{C}^{L\times L}$ are both block diagonal with $2M+1$ blocks of size $(N+1)\times(N+1)$ and $L=(2M+1)(N+1)$.

As $\check{\mathbf{S}}$ is a quadratic function of $\check{\mathbf{x}}$, it is always possible to find hermitian matrices $\mathbf{\Gamma}_l\in\mathbb{C}^{L\times L}, l=1,\cdots,L$ such that

$$\mathbf{B}(l,:)\check{\mathbf{S}}=\check{\mathbf{x}}^*\mathbf{\Gamma}_l\check{\mathbf{x}} \qquad (4.39)$$

where $\mathbf{B}(l,:)$ denotes the l_{th} row of the matrix $\mathbf{B}$. Therefore the model can be written as

$$\dot{\check{\mathbf{x}}} = \mathbf{A}\check{\mathbf{x}} + \begin{bmatrix} \check{\mathbf{x}}^*\mathbf{\Gamma}_1\check{\mathbf{x}} \\ \vdots \\ \check{\mathbf{x}}^*\mathbf{\Gamma}_L\check{\mathbf{x}} \end{bmatrix} \tag{4.40}$$

and note that here $\mathbf{\Gamma}_l \in \mathbb{C}^{L\times L}$ are all sparse matrices.

The flow system after discretisation is bilinear and its dimensionality is very high if M and N are large, which is usually the case when high accuracy needs to be achieved. As mentioned previously, this model is not ideal for DNS of 2-dimensional channel flow due to a lack of fast algorithms to compute the nonlinear terms. However, an important advantage of this model is that it does not depend on the form of the nonlinear terms. Moreover, the losslessness of the nonlinearity (4.29) is preserved by the discretisation.

The kinetic energy of the perturbation in the continuous form is

$$E = \frac{1}{2}\int_{y=-1}^{y=1}\int_{x=0}^{x=L_x} \left(u^2+v^2\right) \mathrm{d}x\mathrm{d}y = \frac{1}{2}\int_{y=-1}^{y=1}\int_{x=0}^{x=L_x} \left((\frac{\partial\tilde{\psi}}{\partial y})^2 + (\frac{\partial\tilde{\psi}}{\partial x})^2\right) \mathrm{d}x\mathrm{d}y \tag{4.41}$$

Performing a Fourier transform with truncation and substituting (4.37) yield

$$\begin{aligned} E &= \frac{1}{2}\sum_{m=-M}^{M}\int_{-1}^{1}\left((\mathcal{D}\tilde{\psi}_m)^*\mathcal{D}\tilde{\psi}_m + \alpha_m^2\tilde{\psi}_m^*\tilde{\psi}_m\right)\mathrm{d}y \\ &= \sum_{m=-M}^{M}\begin{bmatrix} a_{\psi_m,0} \\ \vdots \\ a_{\psi_m,N}\end{bmatrix}^* \begin{bmatrix} Q_{0,0}^{(m)} & \cdots & Q_{0,N}^{(m)} \\ \vdots & \ddots & \vdots \\ Q_{N,0}^{(m)} & \cdots & Q_{N,N}^{(m)} \end{bmatrix} \begin{bmatrix} a_{\psi_m,0} \\ \vdots \\ a_{\psi_m,N}\end{bmatrix} \\ &= \check{\mathbf{x}}^*\mathbf{Q}\check{\mathbf{x}} \end{aligned} \tag{4.42}$$

where

$$Q_{i,j}^{(m)} = \frac{1}{2}\int_{-1}^{1}\left(\alpha_m^2(1-y^2)^4T_i(y)T_j(y) + \frac{\mathrm{d}\left((1-y^2)^2T_i(y)\right)}{\mathrm{d}y}\frac{\mathrm{d}\left((1-y^2)^2T_j(y)\right)}{\mathrm{d}y}\right)\mathrm{d}y \tag{4.43}$$

and $\mathbf{Q} \in \mathbb{C}^{L\times L}$ is block diagonal with the m_{th} block being the matrix $Q^{(m)}, m = -M, \cdots, 0, \cdots, M$.

It is expected that if the kinetic energy $E = \check{\mathbf{x}}^*\mathbf{Q}\check{\mathbf{x}}$ is chosen as the Lyapunov function, system (4.40) can be proved globally asymptotically stable when the Reynolds number is smaller than the energy Reynolds number, which is $\mathrm{Re}_E \approx 87.7$ for 2-dimensional plane poiseuille flow. This means that at $\mathrm{Re} < \mathrm{Re}_E$

$$\dot{E} = \check{\mathbf{x}}^*(\mathbf{A}^*\mathbf{Q}+\mathbf{Q}\mathbf{A})\check{\mathbf{x}} + 2\check{\mathbf{x}}^*\mathbf{Q}\begin{bmatrix} \check{\mathbf{x}}^*\Gamma_1\check{\mathbf{x}} \\ \vdots \\ \check{\mathbf{x}}^*\Gamma_L\check{\mathbf{x}} \end{bmatrix} \tag{4.44}$$

should be negative definitive, which amounts to

$$\mathbf{A}^*\mathbf{Q} + \mathbf{Q}\mathbf{A} < 0 \tag{4.45}$$

and

$$\check{\mathbf{x}}^*\mathbf{Q}\begin{bmatrix}\check{\mathbf{x}}^*\Gamma_1\check{\mathbf{x}}\\ \vdots \\ \check{\mathbf{x}}^*\Gamma_L\check{\mathbf{x}}\end{bmatrix} = 0 \quad \forall\check{\mathbf{x}} \tag{4.46}$$

The first condition (4.45) has been discussed in the previous chapter, while the second condition (4.46) has been taken for granted so far and it is supposed to hold for any arbitrary Re. The model obtained by the discretisation described in this section meets these expectations, but it should be noted that it is generally not the case if different discretisation methods are used. The second condition (4.46) is particularly restrictive and only when the discretisation methods are carefully chosen does (4.46) hold true. To achieve expected stability results such as the flow is globally asymptotically stable at $\mathrm{Re} < \mathrm{Re}_E$ using finite-dimensional models turns out to be far trickier than it appears.

4.4 General Lyapunov functions

To find a higher Reynolds number below which the flow is globally asymptotically stable, we need to find more general Lyapunov functions other than the kinetic energy. Let us first consider a general quadratic function $V(\check{\mathbf{x}}) = \check{\mathbf{x}}^*\mathbf{P}\check{\mathbf{x}}$ where $\mathbf{P} = \mathbf{P}^*$. To make V a valid Lyapunov function in the entire state space, $\mathbf{P}$ has to satisfy the following two conditions

$$\mathbf{A}^*\mathbf{P} + \mathbf{P}\mathbf{A} < 0 \tag{4.47}$$

and

$$\check{\mathbf{x}}^*\mathbf{P}\begin{bmatrix}\check{\mathbf{x}}^*\Gamma_1\check{\mathbf{x}}\\ \vdots \\ \check{\mathbf{x}}^*\Gamma_L\check{\mathbf{x}}\end{bmatrix} = 0 \quad \forall\check{\mathbf{x}} \tag{4.48}$$

There is little hope of finding a $\mathbf{P} \neq \epsilon\mathbf{Q}$ with ϵ being a scalar such that the second condition (4.48) is satisfied and no such a $\mathbf{P}$ has been found so far. As a result, we should instead aim to search for higher order Lyapunov functions such as quartic functions.

Looking for a Lyapunov function for a general nonlinear dynamical system is usually very difficult. Fortunately, SOS programming can be used to construct Lyapunov functions for system (4.33). This approach is based on the fact that while proving the positivity of a general polynomial is a NP-hard problem, it is computationally tractable to determine whether there exists a SOS decomposition for the polynomial [116].

Definition 12. ***(Sum of squares)*** *A polynomial $g(z)$ is a SOS if there exists the following decomposition*

$$g(z) = \sum_{i=1}^{m} f_i^2(z) \tag{4.49}$$

where $z = [z_1, \cdots, z_n]^T \in \mathbb{R}^n$ and $f_i(z), i = 1, \cdots, m$ are polynomials of z.

It is immediately clear that if $g(z)$ is a SOS, it is positive semidefinite, i.e., $g(z) \geq 0$. However, the converse is not true. There exists some polynomials that are positive definite but cannot be written in the form of SOS. For example,

$$h(z_1, z_2, z_3) = z_1^4 z_2^2 + z_1^2 z_2^4 + z_3^6 - 3z_1^2 z_2^2 z_3^2 \tag{4.50}$$

is such a polynomial [116].

If there exists a function V such that both $V - \phi$ and $-\dot{V} - \varphi$ are SOS with ϕ and φ being some known positive definite functions, then V is a valid Lyapunov function. This condition is stricter than requiring V to be positive definite and $\dot{V}$ to be negative definite, but it is more computationally tractable. SOS decomposition problems can be formulated as semidefinite programming (SDP) problems and solved by the software toolbox SOSTOOLS [120] [121], which uses SeDuMi [144] or SDPT3 [149] as the SDP solver.

Constructing Lyapunov functions using SOS decomposition is especially suitable for systems with polynomial vector fields, as in our case, and has been discussed by Papachristodoulou and Prajna [115]. Examples can be found in the SOSTOOLS user's guide [121]. It has been shown that SOS programming is very efficient in searching for less conservative Lyapunov functions for systems of moderate size.

The difficulty lies in the fact that the dimensionality of the model (4.40) is too large and it requires a huge amount of computing resources to use SOS programming to look for general Lyapunov functions. This "curse of dimensionality" is common in the analysis of large-scale dynamical systems and it is the major difficulty in determining the stability of channel flow modelled by equation (4.40).

One possible way to circumvent this difficulty is proposed in [62]. The perturbation velocity $\mathbf{u} = (u, v, w)$ is regarded as the summation of a finite-dimensional part and an infinite-dimensional part

$$\mathbf{u} = \sum_{i=1}^{N} a_i \mathbf{u}_i + \mathbf{u}_s \tag{4.51}$$

where $\mathbf{u}_i, i = 1, \cdots, N$ are orthonormal basis functions and the infinite-dimensional part $\mathbf{u}_s$ is assumed to be orthogonal to $\mathbf{u}_i$. Both $\mathbf{u}_i$ and $\mathbf{u}_s$ satisfy the boundary conditions and are solenoidal, which means that they are divergence free. After substituting the partition (4.51) into the NSEs, $\mathbf{u}_i$ is used as the test functions. It is clear that in the case that $\mathbf{u}_s = 0$, this is a standard Galerkin projection and we are still faced with the dimensionality problem.

The purpose of including $\mathbf{u}_s$ is to capture the dynamics unmodelled by the finite-dimensional part $\mathbf{u}_i$. It is expected that increasing the number N can reduce the kinetic energy of the infinite-dimensional part $\mathbf{u}_s$ as larger N leads to more accurate finite-dimensional Galerkin projections. The effects of $\mathbf{u}_s$ may be neglected when N is sufficiently large. However, as pointed out previously, large N poses serious dimensionality problem. To avoid this problem, N has to be reasonably small, for example, 10. In this case, $\mathbf{u}_s$ certainly cannot be ignored. Unlike $\mathbf{u}_i$, $\mathbf{u}_s$ is unknown and as a result, it is not possible to obtain a model like (4.40). The key idea is that it is possible to derive bounds for the energy of the infinite-dimensional velocity component $\mathbf{u}_s$. Thus the fluid flow can be represented by a model with uncertainties characterised by some bounds. Strictly speaking, such a model characterises a set of nonlinear systems rather than a specific dynamical system and the fluid flow belongs to the set. Reducing the gap between the bounds as much as possible is crucial in order to reduce the conservativeness arising from the model.

After the model is derived, SOS programming can be used to search for higher order Lyapunov functions. This approach has been used to analyse the stability of the rotating Couette flow and Reynolds number higher than the one obtained by using the kinetic energy as the Lyapunov function is achieved [29] [30]. However, no similar results for plane channel flow have been obtained so far.

It should be pointed out that the existence of polynomial Lyapunov functions for a globally asymptotically stable system with a polynomial vector field is not guaranteed. It is shown in [2] that while the second order dynamical system

$$\begin{aligned} \dot{z}_1 &= -z_1 + z_1 z_2 && \text{(4.52a)} \\ \dot{z}_2 &= -z_2 && \text{(4.52b)} \end{aligned}$$

is globally asymptotically stable, there exists no polynomial Lyapunov function for the system. It means the existence of polynomial Lyapunov functions is not a necessary condition for a system with a polynomial vector field to be globally asymptotically stable. Furthermore, it is still not clear whether the existence of polynomial Lyapunov functions implies the existence of SOS Lyapunov functions [3]. As a result, it is possible that we would not be able to find less conservative Lyapunov functions for the fluid flow using SOS programming, even if there was sufficient computing power available.

As mentioned previously, the flow system is infinite-dimensional by nature and it is possible to study the stability of the flow directly without discretising the governing equations. A guideline to search for Lyapunov functionals for systems described by parabolic PDEs using SOS programming is given in [114]. It is crucial to use boundary conditions and functional inequalities such as Cauchy-Schwarz inequality and Poincaré inequality to reduce the conservativeness. Methods of constructing polynomial Lyapunov functionals for a class of systems described by PDEs with one spatial variable and one time variable are described in [158]. However, it is still far from straightforward to use these methods to analyse the stability of fluid flows [30], particularly due to the difficulties associated with the NSEs.

4.5 Region of attraction

An alternative way of studying the stability of the fluid flow is to look at how its ROA changes over Reynolds number. It is expected that the ROA becomes smaller when the Reynolds number is increasing and it would be of interest to measure the change quantitatively when $\mathrm{Re}_E < \mathrm{Re} < \mathrm{Re}_c$. Since ROA contains all the perturbations that the flow system can recover from, the size of ROA can be quantified by the lower bound on the energy of the perturbations at the ROA boundary.

Generally speaking, there are two types of methods to determine the ROA of a stable equilibrium of a given system, namely non-Lyapunov approach such as topological approach and Lyapunov approach. Based on the topological properties of the ROA, topological approach can sometimes find the exact ROA, but the method is not always feasible and it is generally very difficult to implement on higher dimensional systems. On the other hand, Lyapunov approach is based on the Lyapunov stability theorem and it can only find a subset of the exact ROA of the system.

Consider a nonlinear autonomous system

$$\dot{x} = f(x) \tag{4.53}$$

where $x \in \mathbb{R}^n$ and $f(x) : \mathbb{R}^n \rightarrow \mathbb{R}^n$ with $f(0) = 0$.

Definition 13. ***(Hyperbolic equilibrium point)*** *An equilibrium point x_0 is a hyperbolic equilibrium if the Jacobian matrix $\frac{\partial f}{\partial x}|_{x=x_0}$ has no eigenvalues with zero real parts.*

Definition 14. ***(Stable and unstable manifolds)*** *The stable manifold of a hyperbolic equilibrium x_0 is defined by*

$$W^s(x_0) = \{x \in \mathbb{R}^n : x(t) \rightarrow x_0 \quad as \quad t \rightarrow \infty\} \tag{4.54a}$$

and the unstable manifold of x_0 *is defined by*

$$W^u(x_0) = \{x \in \mathbb{R}^n : x(t) \to x_0 \quad as \quad t \to -\infty\} \tag{4.54b}$$

When the system satisfies the following assumptions

1. All the equilibrium points on the boundary of the ROA are hyperbolic.
2. Transversality condition [1] is satisfied by the stable and unstable manifolds of these equilibrium points.
3. As $t \to \infty$, every trajectory on the boundary of the ROA approaches one of the equilibrium points.

the ROA of the origin can be determined topologically using the algorithm proposed by Chiang *et al.* [32]. The algorithm consists of three steps

1. Find all the equilibrium points, i.e., find all the solutions to $f(x) = 0$.
2. Find all the equilibrium points whose unstable manifolds have trajectories approaching $x = 0$.
3. The union of the stable manifolds of the equilibria specified in the second step is the boundary of the ROA of $x = 0$.

When feasible, the method can be used to find the exact ROA of an equilibrium of a given nonlinear dynamical system and several examples are given in [32]. One problem with this method is that it is not easy to verify whether the assumptions are satisfied. Furthermore, there are no efficient computational methods to implement the algorithm for high dimensional systems. Finding all the equilibrium points may be straightforward for low dimensional systems, it becomes much harder when the dimensionality is high. Even more difficult is the second step of the algorithm. As a result, this method is not suitable for finding the ROA of a large scale system characterising plane channel flow.

While finding the exact ROA is usually very difficult or even not possible, it is always possible to find a subset of the ROA using Lyapunov approach. The basic idea is to construct a Lyapunov function $V(x)$ such that $V(x)$ is positive definite in a domain $D \in \mathbb{R}^n$ containing the origin $x = 0$ and $\dot{V}(x)$ is negative definite in the domain. If $\Omega_c = \{x \in \mathbb{R}^n : V(x) < c\}$ is contained in D for a scalar c, Ω_c is a subset of the ROA, which means that any trajectory starts within Ω_c cannot escape Ω_c and decays to

---

[1] See [69] for a precise definition.

zero eventually. This is a direct result of the Lyapunov stability theorem and Ω_c is an estimated ROA.

Our aim is to enlarge the estimated ROA as much as possible so that Ω_c is as close to the exact ROA as possible. This usually cannot be achieved by only one trial. Instead, Lyapunov functions are usually constructed iteratively in order to reduce the conservativeness. Before discussing this approach, it is necessary to address the existence of Lyapunov functions. It turns out that there always exist quadratic Lyapunov functions $V(x) = x^T P x$ such that $V(x)$ is positive definite in a neighbourhood of the origin and $\dot{V}(x)$ is negative definite in the neighbourhood as long as the origin is an exponentially stable equilibrium. This result is established by the following theorem [8].

Theorem 7. *Suppose that the origin is exponentially stable, i.e., all the eigenvalues of the Jacobian matrix* $A = \frac{\partial f}{\partial x}|_{x=0}$ *have negative real parts. Then there exists a differentiable function* $V(x)$ *in a neighbourhood of* 0 *such that for some positive constants* c_1, c_2, c_3, r *and* δ,

$$\|x\| < \delta \quad \Rightarrow \quad c_1\|x\|^r \le V(x) \le c_2\|x\|^r \tag{4.55a}$$

$$\|x\| < \delta \quad \Rightarrow \quad \dot{V}(x) \le -c_3\|x\|^r \tag{4.55b}$$

In addition, there exists a $P = P^T > 0$ *such that for some positive constants* c *and* δ

$$\|x\| < \delta \Rightarrow x^T P f(x) + f(x)^T P^T x \le -c\|x\|^2 \tag{4.56}$$

A solution to the following Lyapunov equation

$$PA + A^T P = -I \tag{4.57}$$

with A being the Jacobian matrix at the origin and I being the identity matrix of appropriate size gives a valid Lyapunov function $V(x) = x^T P x$ in a neighbourhood of the origin. With such a $V(x)$, we can always find a domain D such that $\dot{V}(x) < 0 \ \ \forall x \in D - \{0\}$. In practice, the estimated ROA obtained in this way is usually much smaller than the exact ROA and less conservative Lyapunov functions need to be constructed. Nevertheless, $V(x) = x^T P x$ can be used as the starting point of an iterative procedure.

A constructive methodology for estimating the ROA of a nonlinear dynamical system iteratively is proposed by Chiang and Thorp [33]. This methodology starts with a given Lyapunov function $V(x)$, which can be obtained in the way described above, and consists of the following three steps

1. Calculate the critical level value of $V(x)$. The lowest positive value of $V(x)$ at all the equilibrium points whose unstable manifolds converge to $x = 0$ is the critical level value.
2. Replace the current Lyapunov function $V(x)$ with a modified one.
3. Estimate the ROA of the origin from the modified Lyapunov function and the critical level value identified in step 1. Go to step 2.

The difficulty in applying this method to higher order systems lies in the fact that there are no efficient computational schemes to determine the critical level value of a given Lyapunov function [33].

Amato *et al.* [5] have proposed a method to determine whether a given polytope belongs to the ROA of a zero equilibrium of a nonlinear quadratic systems. In this method, it is necessary to list all the vertices in order to specify the polytope. As the number of vertices is an exponential function of the number of state variables, it is clear that the method is not suitable for the fluid system.

The ROA of a system with a polynomial vector field can also be studied within the framework of SOS programming [31]. Due to the existence of nonlinearity in the system, the computation of the invariant subsets of ROA using SOS relaxation leads to bilinear matrix inequality (BMI) problems. BMIs are nonconvex and in general NP-hard. As a result, there exist no efficient methods to solve BMIs. Nevertheless, BMIs of moderate size can be solved by the solver PENBMI [87]. One method that combines bilinear SOS programming and numerical simulations to search for ROA is proposed in [150]. In order to reduce the conservativeness, the Lyapunov function can be composite polynomial functions, as is discussed in [145].

Due to the limit of computational resources available, none of the methods discussed above is capable of dealing with large scale nonlinear dynamical systems with thousands or even more state variables.

DNS has been used to study how the ROA of channel flow changes as the Reynolds number is increasing in [102]. Appropriate initial conditions are chosen and the NSEs are simulated for a sufficiently long time to see whether transition occurs. This approach is straightforward, but very time-consuming. Denote ϵ as the minimum value of the energy of all the perturbations that can excite transition in channel flow. Using DNS, Lundbladh *et al.* [102] presented some examples where ϵ and Re is related by

$$\epsilon = \mathcal{O}(\mathrm{Re}^{-\frac{7}{4}}) \tag{4.58}$$

for plane Poiseuille flow with $1500 < \text{Re} < 5000$. Through formal asymptotical analysis, Chapman concluded that the threshold exponent is $-\frac{5}{4}$ instead of $-\frac{7}{4}$ [28].

4.6 Low order models

On the one hand, in order to characterise plane channel flow as accurately as possible, the order of finite-dimensional models in general have to be as high as possible so that the truncation error is reduced. On the other hand, as we have seen, high dimensionality places serious restrictions on computational resources and it is desirable to reduce the order of the finite-dimensional models so that they can be dealt with by contemporary computers.

There have been some efforts to devise low order models that capture the main dynamics and features of fluid flows. Stokes eigenfunctions are often used as the basis functions of low order Galerkin approximations [15] [132] [109]. In [132], the first 356 Stokes eigenfunctions are used for the Galerkin projections of plane Couette flow and plane Poiseuille flow. The models obtained are not particularly low order in this case. A nine-mode model for a fluid between two free-slip parallel plates subject to a sinusoidal force is proposed in [106]. The order of this model is fairly low and SOS programming has been used to search for general Lyapunov functions for this model in [62].

Eigenfunctions calculated using the method of proper orthogonal decomposition can also be used as the basis functions of Galerkin approximations [74], but it is pointed out in [126] that such models may exhibit unphysical stability properties. These models are suitable for qualitative study of the basic mechanisms of complex flows, but are not ideal for stability analysis.

In some sense, all the models generated by discretisation of the NSEs are low dimensional as plane channel flow is infinite-dimensional by nature. Truncation errors can only be reduced and cannot be completely removed in finite-dimensional models. When it is not possible to analyse the stability of the fluid flow quantitatively due to the dimensionality problem, it is still helpful to gain some insight through qualitative study.

A number of low order models of fluid flows are discussed in [10]. The orders of the models are substantially lower compared to those obtained by discretisting the full NSEs. In fact, most models covered in [10] have only two or three state variables. Of course, it is not expected that these models give quantitatively accurate descriptions of the fluid flows. Instead, they are devised to study the mechanisms of subcritical transition to turbulence qualitatively. They are sometimes called "toy" models as they are only used to shed some light on how the transition might be excited [28]. For example, one low order model proposed by Trefethen *et al.* [157][9] takes the form

$$\begin{bmatrix} \dot{u} \\ \dot{v} \end{bmatrix} = \begin{bmatrix} -\mathrm{Re}^{-1} & 1 \\ 0 & -2\mathrm{Re}^{-1} \end{bmatrix} \begin{bmatrix} u \\ v \end{bmatrix} + \left\| \begin{bmatrix} u \\ v \end{bmatrix} \right\|_2 \begin{bmatrix} 0 & -1 \\ 1 & 0 \end{bmatrix} \begin{bmatrix} u \\ v \end{bmatrix} \tag{4.59}$$

This model is to show that the linear part plays an important role in the subcritical transition when the disturbance is of finite magnitude, due to the nonnormality of the state operator. Another low order model, proposed by Henningson and Schmid [71], has three state variables

$$\begin{bmatrix} \dot{u} \\ \dot{v} \\ \dot{w} \end{bmatrix} = \begin{bmatrix} -\mathrm{Re}^{-1} & 1 & 0 \\ 0 & -\mathrm{Re}^{-1} & 0 \\ 0 & 0 & -1 \end{bmatrix} \begin{bmatrix} u \\ v \\ w \end{bmatrix} + \begin{bmatrix} 0 \\ w^2 \\ uw \end{bmatrix} \tag{4.60}$$

These (very) low order models are certainly not obtained through discretisation of the NSEs. They are in fact based on existing data on fluid flows gained from DNS [127]. Therefore in order to devise such models, it is important to have a good understanding of the instability mechanisms of the flows beforehand. The significance of these models is that they provide additional insight which would be very difficult to obtain through other means [127]. For example, it is found that the models discussed in [10] all demonstrate similar behaviours in the sense that

$$\epsilon = \mathcal{O}(\mathrm{Re}^r) \tag{4.61}$$

and $r < -1$ for all the models. It is identified that the interaction between the nonnormality of the linear operator and quadratic nonlinearity is the reason for this behaviour. While the threshold magnitude r is not accurate, the study of these models indeed offers insight on how the ROA of fluid flows changes as a function of the Reynolds number.

4.7 Conclusion

In this chapter, we have discussed issues arising from analysing stability of fluid flows via studying finite-dimensional models obtained by discretisation of the NSEs. It is shown that models suitable for numerical simulations may not be good choices for stability analysis using Lyapunov approach. On the other hand, models less ideal for simulations due to the lack of efficient algorithms to calculate the nonlinear terms, might be good for Lyapunov analysis. Spectral Galerkin methods are preferred to collocation methods when it comes to analysing the stability of the nonlinear dynamical systems governed by the NSEs. A Chebyshev Galerkin scheme is proposed to discretise the 2-dimensional NSEs so that the nonlinear terms of different forms are equivalent and energy-preserving after discretisation. After that, methods of searching for general Lyapunov functions and determining ROA are briefly discussed. It is recognised that the high order of the finite-dimensional models are still a difficulty that cannot be overcome. Finally, some low order models and their significance in stability analysis are discussed.

Chapter 5

Numerical Preliminaries of Channel Flow over Riblets

5.1 Introduction

In the previous chapters, we have studied the stability of channel flow between two flat plates. In the remainder of this thesis, we now consider the stability of channel flow between one flat plate and one plate fitted with riblets, which are small grooves that run parallel to one another and are aligned with the direction of the flow. The use of riblets has been regarded as one of the more promising drag reduction techniques and has attracted much research interest for several decades. Contrary to approaches such as blowing and suction, riblets are a passive drag reduction technique which does not require active control of the flow. Compared to other passive means, such as polymer additions and large eddy break up devices, riblets are more successful in reducing the skin friction of turbulent boundary layer [53]. As stated in Chapter 1, although the mechanism is still not fully understood, the drag reductions effects of riblets in turbulent flows have been confirmed by both experimental studies and numerical simulations [160] [40] [159] [78].

Less clear are the effects of riblets on laminar and transitional flows and as mentioned in Chapter 1, there have been some contradictory results in the literature. In this thesis, the effects of riblets on the stability of laminar channel flow are examined numerically. Specifically, the effects of the inclusion of riblets on the linear stability of channel flow will be studied in the next Chapter, and in Chapter 7, we investigate the impact of riblets on the energy amplification in channel flow. Some numerical issues arise due to the presence or riblets. The first one is that the computational domain is no longer a regular one and as a result, spectral methods cannot be directly used to discretise the governing equations of the flow. Secondly, the semi-discrete linearised NSEs are no longer decoupled in the spanwise direction as in the cases considered in the previous chapters. For this reason, the scale of the eigenvalue problem under consideration is significantly larger and eigenvalue algorithms should be carefully chosen to carry out the computation. This chapter presents some preliminary concepts that are useful to tackle these issues.

5.2 Spectral methods in irregular domains

To study the stability of a fluid flow numerically, we have to discretise the governing equations in space. As stated previously, the high-order accuracy makes spectral methods a preferred choice in CFD. However, one drawback of spectral methods is their lack of suitability for dealing with irregular domains, and as a result, we cannot use spectral methods directly to discretise the NSEs that describe the channel flow over riblets. Numerous methods have been developed to circumvent this difficulty and they can be roughly classified into the following three groups: change of coordinates, domain decomposition and embedded domain methods.

5.2.1 Change of coordinates

Change of coordinates is the most natural solution to the difficulty of irregular domains. It is in fact used extensively in spectral methods even for very simple problems, although often under the name of change of variables, mapping or normalisation. In spectral methods, a 1-dimensional spatial domain is almost always assumed to be either $x \in [0, 2\pi]$ or $x \in [-1, 1]$, depending whether the function $u(x)$ is periodic or not. When the domain is a bounded interval $\xi \in [a, b]$, it is straightforward to use the transformation $x = \frac{2\xi-b-a}{b-a}$ to map the interval to $x \in [-1, 1]$ or $x = 2\pi\frac{\xi-a}{b-a}$ to map the domain to $x \in [0, 2\pi]$. These transformations are so trivial that they are usually carried out without even being mentioned.

A less trivial scenario is that the domain is unbounded. For example, what if we want to approximate a function defined on $\xi \in [0, \infty)$ or $\xi \in (-\infty, \infty)$? There are three options. The first one is to expand the function in Laguerre or Hermite functions [20]. The second choice is to truncate the unbounded domain to a bounded one and then transform it into a standard domain. The last option is mapping the unbounded domain to the standard one directly. For example, the domain $\xi \in [0, \infty)$ can be mapped to $[-1, 1]$ by $x = \frac{\xi-L}{\xi+L}$ where L is a constant. Both the second and the third options involve mapping an irregular domain to a regular one. As we can see, changing the coordinate system such that the computational domains become the standard ones is intrinsic to spectral methods.

In 1-dimensional domains, the mapping is usually trivial and only under some special circumstances do we encounter unbounded domains, which need carefully chosen mappings. However, when the domain is 2-dimensional or 3-dimensional, the situation becomes much more involved. It is then rare that the domain can be transformed to a standard one by a trivial mapping. Nevertheless, when faced with a problem with irregular domain, change of coordinates is usually the first possibility we should explore. One example of mapping an irregular domain to a regular one was given in [113]. An annular region defined by

$$f_1(\theta) \le \xi \le f_2(\theta), \quad 0 \le \theta \le 2\pi$$

can be conveniently mapped to the rectangular domain $(x, \theta) \in [-1, 1] \times [0, 2\pi]$ by the transformation

$$x = 2\frac{\xi - f_1(\theta)}{f_2(\theta) - f_1(\theta)} - 1$$

In the reference, a heat equation on the annular region was solved by using such a transformation and high accuracy was achieved.

Figure 5.1 gives a 2-dimensional view of the geometry of a channel flow over riblets. The area of interest is defined by $(\tilde{y}, \tilde{z}) \in [-1+f(\tilde{z}), 1] \times [0, 2\pi]$. Analogous to the above example, through the change of coordinates

$$y = F = \frac{2\tilde{y} - f(\tilde{z})}{2 - f(\tilde{z})}, \quad z = \tilde{z} \tag{5.1}$$

the domain can be transformed to the rectangular one $(y, z) \in [-1, 1] \times [0, 2\pi]$. This transformation was used in [52] to study the linear stability of channel flow over riblets. Note that there are many other possible transformations which can achieve the effects of mapping the irregular domain to the standard one. For example,

$$y = F = \frac{2\tilde{y} - f(\tilde{z}) - \sigma(2 - f(\tilde{z}))}{2 - f(\tilde{z}) - \sigma(2\tilde{y} - f(\tilde{z}))}, \quad z = \tilde{z} \tag{5.2}$$

with $\sigma \in (-1, 1)$ is a more general (and more complicated) mapping. The presence of σ gives the flexibility to arrange grid density in the original domain, therefore it sometimes gives more accurate results. Karniadakis and Sherwin [85] give many useful transformations in 2-dimensional and 3-dimensional domains, for example, the transformation that maps a triangular area to a rectangular area and the transformation that maps a tetrahedron to a hexahedron.

One complication of using change of coordinates is that the differential equations have to be changed accordingly. For example, with the change of coordinates (5.1),

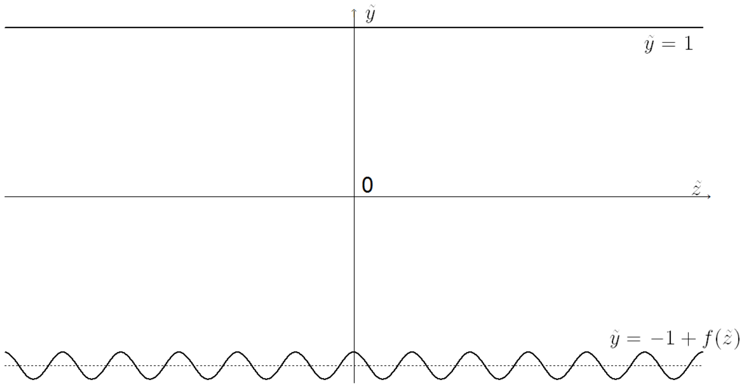

Figure 5.1: 2-dimensional view of the riblet geometry.

the differential operators in the original domain have the following forms in the new coordinate system

$$\frac{\partial}{\partial \tilde{y}} = \frac{\partial \tilde{x}}{\partial \tilde{y}}\frac{\partial}{\partial x} + \frac{\partial F}{\partial \tilde{y}}\frac{\partial}{\partial y} + \frac{\partial \tilde{z}}{\partial \tilde{y}}\frac{\partial}{\partial z} = \frac{\partial F}{\partial \tilde{y}}\frac{\partial}{\partial y} \tag{5.3}$$

$$\frac{\partial}{\partial \tilde{z}} = \frac{\partial \tilde{x}}{\partial \tilde{z}}\frac{\partial}{\partial x} + \frac{\partial F}{\partial \tilde{z}}\frac{\partial}{\partial y} + \frac{\partial \tilde{z}}{\partial \tilde{z}}\frac{\partial}{\partial z} = \frac{\partial}{\partial z} + \frac{\partial F}{\partial \tilde{z}}\frac{\partial}{\partial y} \tag{5.4}$$

$$\frac{\partial^2}{\partial \tilde{y}^2} = \left(\frac{\partial F}{\partial \tilde{y}}\frac{\partial}{\partial y}\right)\left(\frac{\partial F}{\partial \tilde{y}}\frac{\partial}{\partial y}\right) = \left(\frac{\partial F}{\partial \tilde{y}}\right)^2 \frac{\partial^2}{\partial y^2} + \frac{\partial F}{\partial \tilde{y}}\frac{\partial^2 F}{\partial y \partial \tilde{y}}\frac{\partial}{\partial y} \tag{5.5}$$

$$\frac{\partial^2}{\partial \tilde{z}^2} = \left(\frac{\partial^2 F}{\partial z \partial \tilde{z}} + \frac{\partial F}{\partial \tilde{z}}\frac{\partial^2 F}{\partial y \partial \tilde{z}}\right)\frac{\partial}{\partial y} + \left(\frac{\partial F}{\partial \tilde{z}}\right)^2 \frac{\partial^2}{\partial y^2} + \frac{\partial^2}{\partial z^2} + 2\frac{\partial F}{\partial \tilde{z}}\frac{\partial^2}{\partial y \partial z} \tag{5.6}$$

For higher order operators, the formulations in the new coordinate system will be even more complicated, although this causes no real difficulties.

There are two scenarios where the change of coordinates encounters serious difficulties. One is that the explicit formula of the transformation may not be achievable. For example, if the closed forms of the functions characterising the boundaries of the annular region are not known, we cannot have the analytical form of the transformation. To overcome this difficulty, the boundaries with functions $f_1(\theta)$ and $f_2(\theta)$ can be approximated using numerical methods introduced in Section 2.3. The other serious difficulty occurs when the boundary of the domain is time dependent, for example, the boundary of a beating heart changes all the time [119]. Even if we are able to find suitable mappings at any given time, the cost of using change of coordinates is simply too high, given that the form of the differential equations has to be recalculated at every time step. We note that change of coordinates sometimes introduces singularities, and the treatment of singularities in spectral methods is a topic that attracts much interest [85].

5.2.2 Domain decomposition

An alternative way to deal with irregular domains is to decompose the region into a set of simpler regions, so that a function can be expanded into spectral series in each subdomain and continuity conditions are imposed at the intersections of the subdomains. This idea is the foundation of the FEM, where each of the subdomains is called an element. In the literature of spectral methods, domain decomposition is sometimes called patching. In [113], Orszag showed how a Poisson's equation on a L shaped domain

$$\begin{aligned} 0 \le x \le 1, &\quad 0 \le y \le 1, \\ -1 \le x \le 0, &\quad 0 \le y \le 2. \end{aligned}$$

can be solved by domain decomposition. The domain can be simply divided into three subdomains, as illustrated in Figure 5.2. Each subdomain can be trivially transformed into the standard domain $(x, y) \in [-1, 1] \times [-1, 1]$.

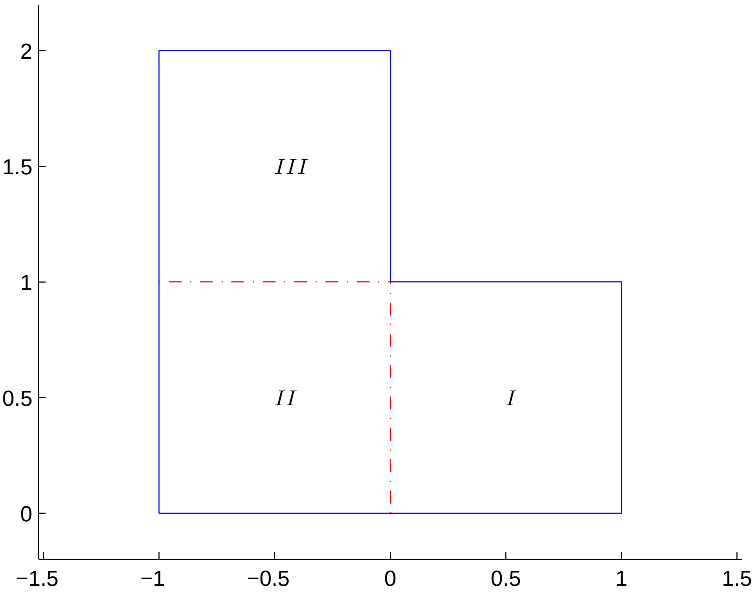

Figure 5.2: The L shape domain.

A function $u(x, y)$ can then be expanded as Chebyshev series in each of the subdomains

$$
\begin{aligned}
u_I(x,y) &= \sum_{i=0}^{N_x^I}\sum_{j=0}^{N_y^I} \hat{u}_{i,j}^I T_i(2x-1)T_j(2y-1) && (5.7)\\
u_{II}(x,y) &= \sum_{i=0}^{N_x^{II}}\sum_{j=0}^{N_y^{II}} \hat{u}_{i,j}^{II} T_i(2x+1)T_j(2y+1) && (5.8)\\
u_{III}(x,y) &= \sum_{i=0}^{N_x^{III}}\sum_{j=0}^{N_y^{III}} \hat{u}_{i,j}^{III} T_i(2x+1)T_j(2y-3) && (5.9)
\end{aligned}
$$

with $N_y^I = N_y^{II}$ and $N_x^{II} = N_x^{III}$ (where I, II, III denotes the subdomains), which means that the degrees of polynomials along the interface between two subdomains agree with each other. The neighbouring elements may be approximated by polynomials of different degrees, but in that case, the treatment of the interface is more complicated [25]. The function $u(x,y)$ is required to be continuous at the internal boundaries, for example, $u_I(0,y) = u_{II}(0,y)$ and $\frac{\partial u_I}{\partial x}(0,y) = \frac{\partial u_{II}}{\partial x}(0,y)$.

The L shape domain is simple in the sense that after first decomposition, each subdomains are square and can be trivially transformed to the standard domain. It is not the case for the domain illustrated in Figure 5.3. Now the subdomain III is a triangle, which has to be mapped to a standard square domain. This is what often happens in spectral methods with domain decomposition. Some of the subdomains have to been converted to standard domains by the methods discussed in the previous subsection.

Still, not all subdomains can be mapped to standard domains, so sometimes before approximating a function with spectral series, the domain itself may have to be approximated by subdomains. With increasing grid resolution, even most bizarre geometries can be approximated with high accuracy.

Domain decomposition is a fundamental concept in the FEM, whose main strength is its generality to complex geometries. The traditional FEM uses lower order polynomials as the trial functions and test functions, which makes the method suffer from lower accuracy. So why not use higher order trial functions such as the Chebyshev polynomials? In 1984, Patera combined the FEM and spectral methods to develop the spectral element method (SEM), which combines the strengths of both the FEM and spectral methods: the generality and the high-order accuracy [118]. Since then, the SEM has become a rapidly developing subject itself and a very useful reference for the SEM is [85]. In the FEM, higher accuracy is normally achieved by refining the element and this is called a h-type extension, while in spectral methods, higher accuracy is achieved by increasing the degree of the polynomials and this is called a p-type extension. As a consequence,

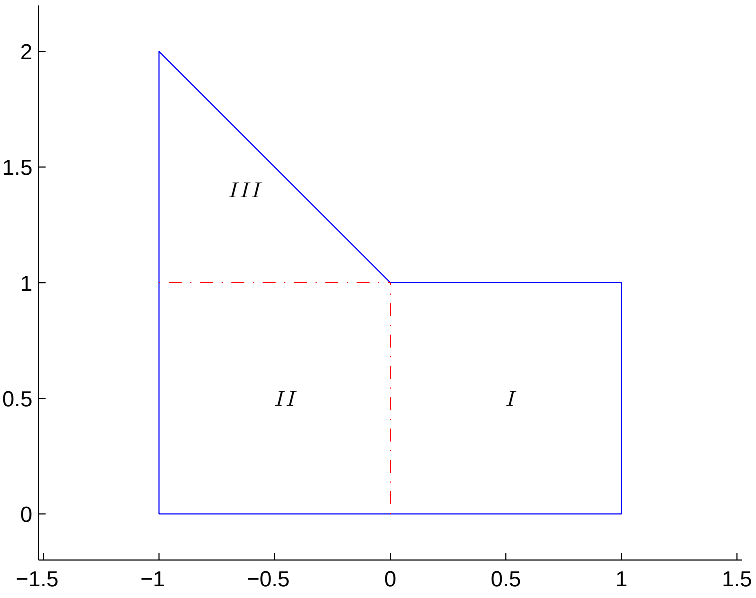

Figure 5.3: An irregular domain.

in the SEM, both refinements can be used to improve the accuracy and for this reason, the SEM is also called spectral/hp element method. Note that the implementation of the SEM is generally more difficult than that of the FEM because of the higher degrees of the basis functions.

Solving differential equations by decomposing the domain is sometimes called the multidomain approach. In a trivial case, the standard square domain $(x, y) \in [-1, 1] \times [-1, 1]$ can be divided into four squares, as shown in Figure 5.4. If the solution is infinitely smooth, then the multidomain approach leads to less accurate results than a single domain approach. This is due to the imposition of the continuity conditions at the internal boundaries. For example, in the multidomain approach, the approximation of a function $u(x, y)$ is only required to satisfy $u_I(x, 0) = u_{II}(x, 0)$ and $\frac{\partial u_I}{\partial y}(x, 0) = \frac{\partial u_{II}}{\partial y}(x, 0)$ at the interface between subdomains I and II. However, in a single domain approach, the continuity conditions hold true for derivatives of any order.

5.2.3 Embedded domain method

Domain decomposition method can solve the difficulty that some domains cannot be mapped to standard domains. However, it cannot resolve the difficulty associated with time dependent domains because mapping the domains at each time instant is simply too costly to be considered. Under this circumstance, a better idea is to embed the original

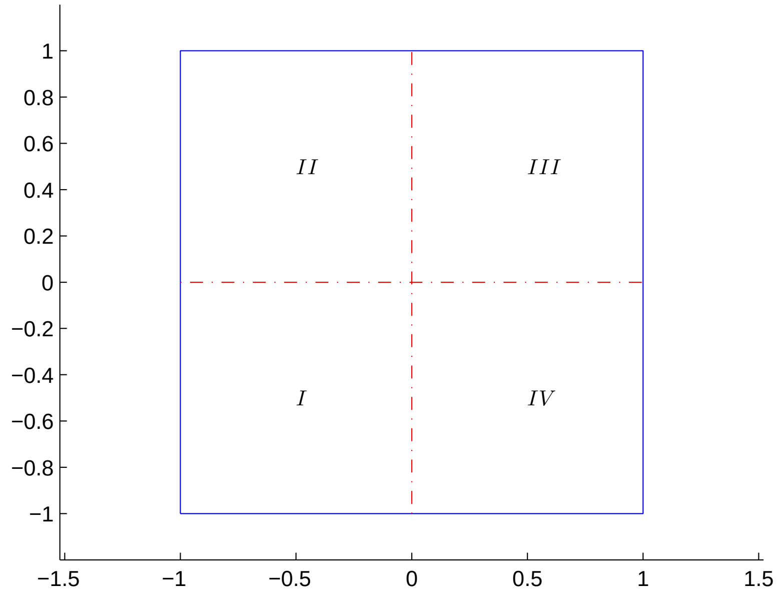

Figure 5.4: A decomposition of the standard domain.

domain in a larger, standard domain and then make sure that the boundary conditions are satisfied at the boundaries of the original domain. By doing this, the discretisation grids do not have to change. It is not difficult to see that the key part is to enforce the boundary conditions. This method is sometimes also called the fictitious domain method [56] and it should be noted that in practice the embedded domain method is frequently used, even if the domain does not change over time.

Consider a PDE of the form

$$\mathcal{L}(u(x,y)) = f(x,y) \tag{5.10}$$

on the domain $(x, y) \in \hat{\Omega}$, as illustrated in Figure 5.5. Instead of mapping the domain $\hat{\Omega}$ into a standard domain or decomposing $\hat{\Omega}$ into a set of subdomains, we can simply embed it into a larger, standard domain Ω. For ease of reference, we denote the boundary of $\hat{\Omega}$ as $\partial\hat{\Omega}$. The differential equation can now be discretised directly on the standard domain Ω with spectral methods.

One complication comes from function extension, i.e., the function $f(x, y)$ on $\hat{\Omega}$ has to be extended to a function $g(x, y)$ on Ω. The basic requirement is

$$g(x,y) = f(x,y) \quad \forall (x,y) \in \hat{\Omega} \tag{5.11}$$

The choice of $g(x, y)$ sometimes has a great influence on the accuracy. Boyd [21] gives a method to make the extended function $g(x, y)$ spatially periodic and infinitely differentiable on Ω. Under some circumstances, the extension is trivial, for example, when $f(x, y)$ is a constant in $\hat{\Omega}$.

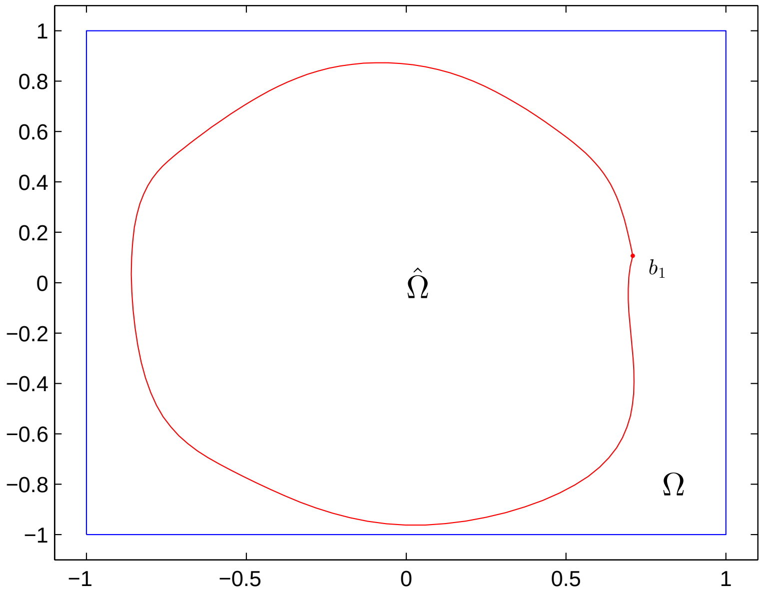

Figure 5.5: An embedded domain.

To solve the differential equation, the boundary conditions have to be imposed on the physical boundary $\partial\hat{\Omega}$. The differential equation can be discretised using the collocation method or the tau method, but it is generally impractical to apply the spectral Galerkin method because in the method, the basis functions are required to satisfy the boundary conditions.

In the case that the collocation method is used, the physical boundary Ω usually does not coincide with the collocation points. This is because the collocation points in spectral methods cannot be arranged arbitrarily, unlike in the FDM, where unstructured grids may be used. The remedy is interpolation, for example, the value of a function $u(x, y)$ at the point b_1 shown in Figure 5.6 can be represented through the interpolating polynomial of its neighbouring collocation points. Imposing the boundary conditions at point b_1 can be equivalently transformed to imposing suitable conditions on its neighbouring collocation points. Choosing an appropriate interpolation method is not always straightforward, see [142] for an example of interpolating the boundary in structured finite difference grids using second order Lagrange polynomials.

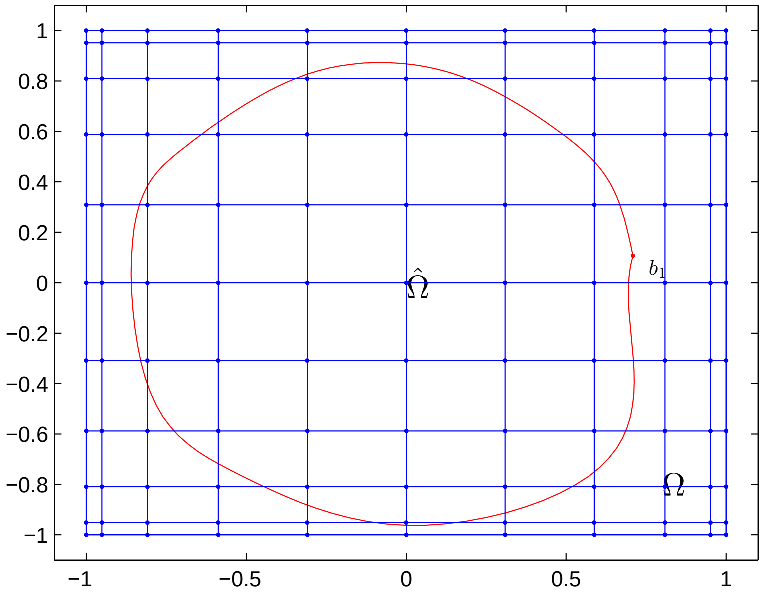

Figure 5.6: Collocation points and physical boundary.

As for the tau method, suppose that $\partial\hat{\Omega}$ has analytical form, the boundary conditions can be enforced in a different way. For example, suppose a segment of $\partial\hat{\Omega}$ takes the form

$$\Gamma = (x(s), y(s)), \quad s \in [-1, 1] \tag{5.12}$$

and the boundary condition at $\Gamma(x, y)$ is represented by

$$p(x, y) = p(x(s), y(s)) = \sum_{i=0}^{N} \hat{p}_i T_i(s) \tag{5.13}$$

then at the boundaries we have

$$u(x, y) = u(x(s), y(s)) = \sum_{i=0}^{N}\sum_{j=0}^{N} \hat{u}_{ij} T_i(x(s)) T_j(y(s)) = \sum_{i=0}^{N} \hat{p}_i T_i(s) = p(x, y) \tag{5.14}$$

which consists of $N + 1$ equations. This method has been used to solve Poisson-type equations in irregular domains in [88].

Another method based on domain embedding is the immersed boundary method (IBM). The actual domain is embedded in a larger, standard domain and the boundary conditions are imposed by exerting a virtual force to the system governed by PDEs. This method was first developed by Peskin to study the blood flow in a beating heart [119]. Since then, a large number of numerical methods based on the IBM have been developed. An interesting example is given in Goldstein *et al.* [57] where the virtual force is modelled by a proportional-integral feedback controller, and this numerical scheme was then used to simulate a turbulent channel flow over riblets [58]. It was pointed out in [57] and [58] that while quantitatively accurate turbulence statistics can be obtained, the method does not result in an exact simulation, because the boundary conditions generally cannot be satisfied exactly.

To impose the boundary conditions at the physical boundary, we once again encounter the problem that the boundary points usually do not coincide with the grid points of Ω. The virtual force that is used to impose the boundary conditions cannot be directly exerted on the boundary points. Instead, the force has to be distributed to the grid points close to the boundary points. One of the key issues in the IBM is to choose a suitable discrete delta function that imposes the distribution. One example of such a discrete delta function is

$$\delta_\epsilon = \begin{cases} \frac{1}{4\epsilon}(1+\cos(\frac{\pi x}{2\epsilon})), & -2\epsilon \leq x \leq 2\epsilon, \\ 0, & \text{otherwise.} \end{cases} \tag{5.15}$$

which has the shape illustrated in Figure 5.7. This means that the virtual force is acted on the grid points whose distances to the boundary points are less than 2ϵ.

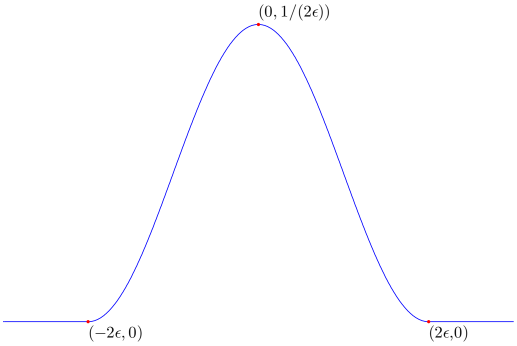

Figure 5.7: A discrete delta function.

After the boundary is embedded, the discretisation of the differential equations are usually carried out using the FDM, as is the case in [119], while in [57] the NSEs in the velocity-vorticity formulation were discretised by Fourier expansion in the periodic directions and Chebyshev expansion in the wall-normal direction. Inspired by the IBM, Leveque and Li developed the immersed interface method (IIM) [97]. The key idea of the method is to derive accurate jump conditions at the interfaces and then solve the differential equations with the FEM or the FDM. It seems that spectral methods have not been used in the IIM. Details on the IIM can be found in [98].

5.3 Matrix and matrix-free approaches

In the previous chapters, we have seen how to determine the linear stability and calculate the transient growth of plane channel flow using the matrix approach. For more complex flows, the matrix approach may not be an appropriate choice and the matrix-free approach often has to be used. We now briefly introduce how the matrix-free approach can be used to solve linear stability and transient growth problems.

5.3.1 Linear stability

In Chapter 2, the linear stability of plane channel flow is studied using the matrix approach. To be more precise, the linearised governing equations of the flow take the form

$$\frac{\partial}{\partial t}(\mathcal{B}q) = \mathcal{A}q \tag{5.16}$$

and the linear stability of the flow is determined by solving a generalised eigenvalue problem of the following form

$$\mathbf{Aq} = \lambda \mathbf{Bq} \tag{5.17}$$

where $\mathbf{A}$ and $\mathbf{B}$ are matrices obtained by discretising the operators $\mathcal{A}$ and $\mathcal{B}$. Eigenvalue problems of this form are very common in systems governed by PDEs. The matrix approach is straightforward and therefore preferred whenever possible. However, it is not always possible to formulate the linear stability problem into an explicit eigenvalue problem. Sometimes, especially when the flow has a complex geometry or the flow is 3-dimensional, the matrices may be so large that they exhaust the computer memory. In these cases, we can avoid forming the matrices explicitly and employ the so-called matrix-free approach.

To see how the matrix-free approach works, without loss of generality, we first simplify the discretised, linearised governing equations as

$$\dot{\mathbf{q}} = \mathbf{Aq} \tag{5.18}$$

where the solution to the above equation is

$$\mathbf{q}(\tau) = \mathrm{e}^{\mathbf{A}\tau}\mathbf{q}_0 \tag{5.19}$$

with $\mathbf{q}_0$ being the initial condition and $\tau > 0$ being a constant. Taking $\mathbf{q}(\tau)$ as the initial condition, after an evolution of time τ, the solution of the system is $\mathrm{e}^{\mathbf{A}\tau}\mathbf{q}(\tau) = (\mathrm{e}^{\mathbf{A}\tau})^2\mathbf{q}_0$. Continuing the process will give us a series of solutions in the form

$$\mathrm{e}^{\mathbf{A}\tau}\mathbf{q}_0, (\mathrm{e}^{\mathbf{A}\tau})^2\mathbf{q}_0, (\mathrm{e}^{\mathbf{A}\tau})^3\mathbf{q}_0, (\mathrm{e}^{\mathbf{A}\tau})^4\mathbf{q}_0, \ldots \tag{5.20}$$

The solutions are the bases of the Krylov subspaces generated by $\mathrm{e}^{\mathbf{A}\tau}$ and $\mathbf{q}_0$, and the eigenvalues of $\mathrm{e}^{\mathbf{A}\tau}$ can then be calculated using the Arnoldi algorithm [155], which will be discussed in the following section. As a consequence, the eigenvalues of the matrix $\mathbf{A}$ can also be calculated accordingly.

The matrices $\mathbf{A}$ and $\mathrm{e}^{\mathbf{A}\tau}$ do not have to be formulated explicitly in the process (in many cases it is impossible to do so). All the information we need is the solution series (5.20). DNS of the linearised governing equation has to be carried out to calculate the solutions. As a consequence, each iteration of simulation of (5.18) is equivalent to the multiplication of the matrix $\mathrm{e}^{\mathbf{A}\tau}$ and a given vector.

The matrix-free approach has a lower requirement for computer memory and it is applicable to any flows that can be numerically simulated. These advantages come at the cost of much longer CPU time because the simulation is generally very time-consuming. To improve the accuracy and convergence, usually the method described above has to be refined and the initial condition $\mathbf{q}_0$ has to be carefully chosen. The details are not pursued here and the reader is referred to [60].

5.3.2 Transient growth

Similarly, transient growth can also be calculated by using either the matrix approach or the matrix-free approach. The calculation of the transient growth in plane Poiseuille flow by using the matrix approach has been discussed in detail in Chapter 3. As in the calculation of linear stability, the explicit matrix form of the fluid flow system is not always available or desirable due to difficulties such as demanding requirements for memory storage. For fluid flows with complex geometries, it is usually not possible to use the matrix approach to calculate the transient growth. We now discuss how the matrix-free approach works and the details can be found in [12].

Without loss of generality, the linearised NSEs in a domain Ω are assumed to take the form

$$\dot{q} = \mathcal{A}q \tag{5.21}$$

and the kinetic energy of the perturbation is given by the inner product

$$E = \langle q, q\rangle = \int_{\Omega} q^* q \mathrm{d}\Omega \tag{5.22}$$

An adjoint system is assumed to have the form

$$\dot{q}^\dagger = \mathcal{A}^\dagger q^\dagger \tag{5.23}$$

where $\mathcal{A}^\dagger$ is the adjoint of the operator $\mathcal{A}$ with respect to the inner product (5.22) and $q^\dagger$ is the adjoint velocity and pressure field.

For a given initial condition q_0 with unit energy, the solution of the system at time τ is

$$q(\tau) = \mathcal{A}(\tau) q_0 \tag{5.24}$$

and the energy is

$$E(\tau) = \langle \mathcal{A}(\tau) q_0, \mathcal{A}(\tau) q_0 \rangle = \left\langle q_0, \mathcal{A}^\dagger(\tau)\mathcal{A}(\tau) q_0 \right\rangle \tag{5.25}$$

Therefore the energy amplification factor is dictated by the largest eigenvalue of the operator $\mathcal{A}^\dagger(\tau)\mathcal{A}(\tau)$.

The numerical solution of the original system (5.21) at time τ with initial condition $\mathbf{q}_0$ is

$$\mathbf{q}(\tau) = \mathrm{e}^{\mathbf{A}\tau}\mathbf{q}_0 \tag{5.26}$$

where the matrix $\mathbf{A}$ is obtained by discretising the operator $\mathcal{A}$. The next step is to use $\mathbf{q}(\tau)$ as the initial condition of the adjoint system (5.23) and after an evolution of time τ, the solution is

$$\mathbf{q}^\dagger(\tau) = \mathrm{e}^{\mathbf{A}^\dagger\tau}\mathbf{q}(\tau) = \mathrm{e}^{\mathbf{A}^\dagger\tau}\mathrm{e}^{\mathbf{A}\tau}\mathbf{q}_0 \tag{5.27}$$

where $\mathbf{A}^\dagger$ is obtained by discretising the operator $\mathcal{A}^\dagger$. This completes one iteration.

Now taking $\mathbf{q}^\dagger(\tau)$ as the initial condition, a second iteration gives the solution

$$\mathrm{e}^{\mathbf{A}^\dagger\tau}\mathrm{e}^{\mathbf{A}\tau}\mathbf{q}^\dagger(\tau) = \left(\mathrm{e}^{\mathbf{A}^\dagger\tau}\mathrm{e}^{\mathbf{A}\tau}\right)^2\mathbf{q}_0 \tag{5.28}$$

It is clear that continuing the process gives us a series of vectors

$$\mathrm{e}^{\mathbf{A}^\dagger\tau}\mathrm{e}^{\mathbf{A}\tau}\mathbf{q}_0, \left(\mathrm{e}^{\mathbf{A}^\dagger\tau}\mathrm{e}^{\mathbf{A}\tau}\right)^2\mathbf{q}_0, \left(\mathrm{e}^{\mathbf{A}^\dagger\tau}\mathrm{e}^{\mathbf{A}\tau}\right)^3\mathbf{q}_0, \dots \tag{5.29}$$

These vectors form the bases of the Krylov subspaces generated by $\mathrm{e}^{\mathbf{A}^\dagger\tau}\mathrm{e}^{\mathbf{A}\tau}$ and $\mathbf{q}_0$. Similar to how linear stability is calculated using the matrix-free approach, the matrices $\mathbf{A}$ and $\mathbf{A}^\dagger$ do not have to be formulated explicitly. To calculate the largest eigenvalue of the matrix $\mathrm{e}^{\mathbf{A}^\dagger\tau}\mathrm{e}^{\mathbf{A}\tau}$ using the Arnoldi algorithm, we only need the solution series (5.29). This can be achieved by carrying out DNS of the original and the adjoint systems. Each iteration of the simulation has the effect of calculating the product of $\mathrm{e}^{\mathbf{A}^\dagger\tau}\mathrm{e}^{\mathbf{A}\tau}$ and a certain vector which is the initial condition of the iteration.

The idea of the approach described above is very similar to that used to calculate the linear stability of the flow. The difference is that now an adjoint system has to be derived and at each iteration, the adjoint system also has to be simulated numerically. Therefore it is expected to be even more time-consuming. The benefit is that the requirement for computer memory is much lower than the matrix approach. An example of using this method to calculate the transient growth of a flow past a cylinder is given in [1].

5.4 Eigenvalue algorithms

Intuitively, it seems rather wasteful to calculate all the eigenvalues to determine the linear stability since only the eigenvalue with the largest real part is of interest, especially when the matrix is very large. Why do we calculate the other eigenvalues at all if we are only interested in one? Unfortunately, in practice and more importantly in theory, it is impossible to calculate only one eigenvalue and make sure that it is the most unstable one without knowing its location in advance.

5.4.1 Power iteration and inverse iteration

A seemingly similar but in fact entirely different problem is to calculate the eigenvalue with largest magnitude. This problem can be solved very straightforward using the power iteration method [155]. With a slight abuse of terminology, we call the eigenvalue with largest magnitude simply the largest eigenvalue. The convergence rate of power iteration depends on the ratio of the second largest eigenvalue to the largest one.

Algorithm 1 Power iteration

```
start with a normalised vector $q_0$ with $\|q_0\| = 1$
for $k = 1, 2, 3, \ldots$ do
    $p = Aq_{k-1}$
    $q_k = \frac{p}{\|p\|}$
    $\lambda_k = q_k^* A q_k$
end for
```

Suppose that the eigenvalues of A are λ_j. One observation is that the eigenvectors of A are the same as those of $(A - \sigma I)^{-1}$ provided that $A - \sigma I$ is nonsingular (which is equivalent to the requirement that σ is not an eigenvalue of A) where σ is a constant. The eigenvalues of $(A-\sigma I)^{-1}$ are $(\lambda_j - \sigma)^{-1}$, and for a particular σ, the largest magnitude of $(\lambda_j - \sigma)^{-1}$ is achieved for λ_J which is closest to σ. This observation means that the power iteration method applied on $(A - \sigma I)^{-1}$ can be used to calculate the eigenvalue λ_J of A. This idea is called inverse iteration and the matrix $(A - \sigma I)^{-1}$ does not have to be formed explicitly. It is also called "shift and invert" strategy in the literature and

σ is referred to as the shift. Although simple, this idea forms the bases of many of the most powerful eigenvalue algorithms. The choice of the shift is particularly important when we want to calculate the most unstable eigenvalue of a given large scale matrix.

Algorithm 2 Inverse iteration

```
start with a normalised vector $q_0$ with $\|q_0\| = 1$ and a constant $\sigma$
for $k = 1, 2, 3, \dots$ do
    solve $(A - \sigma I)p = q_{k-1}$ for $p$
    $q_k = \frac{p}{\|p\|}$
    $\lambda_k = q_k^* A q_k$
end for
```

5.4.2 QR and QZ algorithms

In plane Poiseuille flow studied in Chapter 2, due to the decoupling of the flow modes after Fourier transformation in the streamwise and spanwise directions, the Orr-Sommerfeld /Squire operator is in essence 1-dimensional. After discretisation using spectral methods in the wall-normal direction, the most unstable eigenvalue of the operator converges when the size of the state matrix A is as small as 80×80 (which means the number of discretisation nodes in the wall-normal direction is 40). Other eigenvalues and eigenvectors of interest will converge fairly well when A is of size 200×200, as shown previously. Since the size of the matrix is small, it is straightforward to use the QZ algorithm to solve the generalised eigenvalue problem $Ax = \lambda Bx$ or use the QR algorithm to calculate the eigenvalues of the matrix $B^{-1}A$ (note that B is nonsingular in the velocity-vorticity form). In other words, we can always calculate all the eigenvalues of the matrices generated by discretisation.

The QR algorithm has been the standard algorithm to calculate all the eigenvalues of a matrix A since the 1960s. The algorithm derives its name from the fact that it iteratively carries out QR factorizations in the process. The basic idea is to apply similarity transformations to triangularize the matrix A, and the overall effect is equivalent to a Schur factorization of A. The QR algorithm without shift is extremely simple in form.

Algorithm 3 QR without shift

```
$A^{(0)} = A$
for $k = 1, 2, 3, \dots$ do
    $Q^{(k)}R^{(k)} = A^{(k-1)}$ (The QR decomposition of $A^{(k-1)}$, $Q^{(k)}$ is orthogonal and $R^{(k)}$ is upper triangular.)
    $A^{(k)} = R^{(k)}Q^{(k)}$
end for
```

Verifying the fact that $A^{(k)}$ is similar to A and therefore has the same eigenvalues is trivial. To improve the convergence, the "shift and invert" strategy is used at each step and the matrix $A^{(k)}$ is broken to smaller submatrices whenever possible. The details of the practical QR algorithm can be found in [59].

Not every generalised eigenvalue problem $Ax = \lambda Bx$ can be converted to the eigenvalue problem $B^{-1}Ax = \lambda x$ because B is not always invertible. For example, when the primitive variable form is used, the matrix B is singular. Therefore the QR algorithm cannot be used to solve such a generalised eigenvalue problem. Instead, the QZ algorithm should be used. Developed by Moler and Stewart [107], the QZ algorithm can be regarded as a generalisation of the QR algorithm and it derives its name from the fact that the algorithm is designed to find the unitary matrices Q and Z such that both QAZ and QBZ are upper triangular. The first step is to use Householder reflectors to reduce A to upper Hessenberg form while reducing B to upper triangular form. The second step is to reduce A to upper triangular form iteratively, while simultaneously maintaining the upper triangular form of B. This is called explicit QZ step, which is potentially unstable. To get around this difficulty, the implicit shift method has to be used. The details can be found in the original paper [107] or the textbook [59]. It should also be noted that it is not always desirable to invert B even when it is invertible. For example, in the case that both A and B are Hermitian, the inversion of B may destroy the symmetry of the matrices.

When the purpose is to calculate the eigenvalues of plane Poiseuille flow, understanding the eigenvalue algorithms does not seem particularly important considering that there are many existing software packages such as LAPACK that can solve the eigenvalue problems very quickly. This is the reason that we did not discuss the eigenvalue algorithms in previous chapters despite the fact that we frequently carry out eigenvalue and eigenvector calculations. The situation is more complicated in the case of channel flow over riblets, because the flow is no longer decoupled in the spanwise direction due to the presence of riblets. As a result, we are now faced with a 2-dimensional eigenvalue problem. After discretisation, the size of the matrix can be as large as 20000×20000 in order to achieve convergence and it is usually impossible to use the QZ or QR algorithm to calculate all the eigenvalues.

5.4.3 Arnoldi algorithm

Now that we are not able to calculate all the eigenvalues, we are left with no choice but to compute only some of the eigenvalues. One of the possible choices is the Arnoldi algorithm. We note that the matrices under study are not Hermitian, which means that the

Lanczos algorithm [89] is not an option. For the moment let us only consider eigenvalue problem $Ax = \lambda x$ where $A \in \mathbb{C}^{m\times m}$. The general idea of the Arnoldi algorithm is to construct orthonormal bases for successive Krylov subspaces. The algorithm starts with an arbitrary vector b, which becomes q_1 after normalisation. At each iteration, a new normalised vector q_i which is orthogonal to $[q_1, \ldots, q_{i-1}]$ is formed. Define $Q_n \in \mathbb{C}^{m\times n}$ as the matrix containing the first n vectors q_i and $Q_{n+1} \in \mathbb{C}^{m\times(n+1)}$ as the matrix that contains Q_n and an additional vector q_{n+1}. The iteration gives the relationship

$$AQ_n = Q_{n+1}\tilde{H}_n \tag{5.30}$$

where $\tilde{H}_n \in \mathbb{C}^{(n+1)\times n}$ is a upper Hessenberg matrix. The vectors of Q_n are the orthonormal bases of the Krylov subspace generated by A and b. It can be easily verified that

$$H_n = Q_n^* A Q_n \tag{5.31}$$

where $H_n = \tilde{H}_n(1 : n, :)$. Loosely speaking, this indicates that H_n can in some sense be regarded similar to A. The eigenvalues of H_n can be seen as approximations of the eigenvalues of A. By doing this, the size of the eigenvalue problem is reduced from $m \times m$ to $n \times n$ and when $n \ll m$, the reduction of computation time is significant. On the other hand, many eigenvalues of A are lost in the process. The connection between the Arnoldi algorithm and power iteration method is evident. Thus it is also the largest eigenvalues that first converge in the iterations.

Algorithm 4 Arnoldi iteration

```
start with a random vector $b$, normalisation gives $q_1 = \frac{b}{\|b\|}$.
for $n = 1, 2, 3, \ldots$ do
    $v = Aq_n$
    for $j = 1, \ldots, n$ do
        $h_{jn} = q_j^* v$
        $v = v - h_{jn} q_j$
    end for
    $h_{n+1,n} = \|v\|$
    $q_{n+1} = \frac{v}{h_{n+1,n}}$
end for
```

In practice, the orthogonality of the vectors q_i is usually lost in the iterations due to rounding errors. The remedy is the implicitly restarted Arnoldi algorithm (IRAM). As for the generalised eigenvalue problem, a simple “shift and invert” strategy is used, such that an equivalent problem is solved

$$(A - \sigma B)^{-1} B x = \mu x \tag{5.32}$$

where $\mu = \frac{1}{\lambda - \sigma}$. The details can be found in the ARPACK users' guide [95].

We now return to the problem that there is no easy way to calculate the most unstable eigenvalue. We either calculate all the eigenvalues using the QR/QZ algorithm, or only a subset of the eigenvalues using the Arnoldi algorithm. When the QR/QZ algorithm is out of the question because of the size of the matrices, it is crucial to determine suitable shifts to find the most unstable eigenvalue using the Arnoldi algorithm. The importance of suitable shifts cannot be over-emphasised. It is not surprising that in [44], the most unstable eigenvalues of the lid-driven cavity flow are missing in the calculation [148]. In [110], the most unstable eigenvalues are calculated by choosing zero as the shift and then computing 500 eigenvalues that are closest to zero. We will later show in the next chapter that this is not always reliable.

5.5 Channel flow over riblets

We consider channel flow between two stationary plates, over a 3-dimensional computational domain, as shown in Figure 5.8, where $\tilde{x}$, $\tilde{y}$ and $\tilde{z}$ are the coordinates of the streamwise, wall-normal and spanwise directions, respectively. The upper wall is a flat plate, while the lower wall is a plate with riblets aligned with the streamwise direction. The dimensions of the problem are normalised, so that the upper boundary of the flow occurs at the plate positioned at $\tilde{y} = 1$, while the lower boundary is at $\tilde{y} = -1 + f(\tilde{z})$ where $f(\tilde{z})$ describes the "shape" of the riblets.

5.5.1 Equations of motion

The streamwise, wall-normal and spanwise components of the flow in the coordinate system $(\tilde{x}, \tilde{y}, \tilde{z})$ are denoted by $u(\tilde{x}, \tilde{y}, \tilde{z}, t)$, $v(\tilde{x}, \tilde{y}, \tilde{z}, t)$ and $w(\tilde{x}, \tilde{y}, \tilde{z}, t)$ respectively, and the dimensionless NSEs in this coordinate system are given by

$$\left(\frac{\partial}{\partial t} + u\frac{\partial}{\partial \tilde{x}} + v\frac{\partial}{\partial \tilde{y}} + w\frac{\partial}{\partial \tilde{z}}\right) u = -\frac{\partial p}{\partial \tilde{x}} + \frac{1}{\mathrm{Re}}\tilde{\Delta} u \tag{5.33a}$$

$$\left(\frac{\partial}{\partial t} + u\frac{\partial}{\partial \tilde{x}} + v\frac{\partial}{\partial \tilde{y}} + w\frac{\partial}{\partial \tilde{z}}\right) v = -\frac{\partial p}{\partial \tilde{y}} + \frac{1}{\mathrm{Re}}\tilde{\Delta} v \tag{5.33b}$$

$$\left(\frac{\partial}{\partial t} + u\frac{\partial}{\partial \tilde{x}} + v\frac{\partial}{\partial \tilde{y}} + w\frac{\partial}{\partial \tilde{z}}\right) w = -\frac{\partial p}{\partial \tilde{z}} + \frac{1}{\mathrm{Re}}\tilde{\Delta} w \tag{5.33c}$$

$$\frac{\partial u}{\partial \tilde{x}} + \frac{\partial v}{\partial \tilde{y}} + \frac{\partial w}{\partial \tilde{z}} = 0 \tag{5.33d}$$

where

$$\tilde{\Delta} = \frac{\partial^2}{\partial \tilde{x}^2} + \frac{\partial^2}{\partial \tilde{y}^2} + \frac{\partial^2}{\partial \tilde{z}^2} \tag{5.34}$$

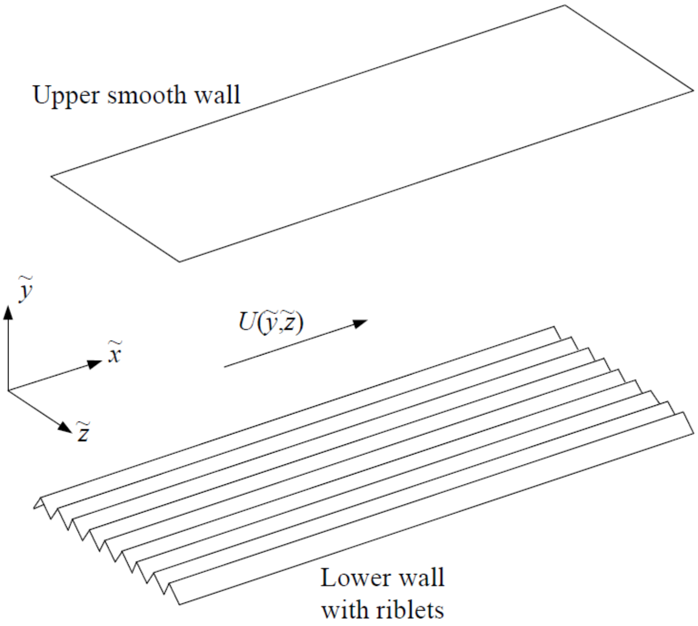

Figure 5.8: 3-dimensional view of computational domain showing riblet structure on lower wall of channel. $U(\tilde{y}, \tilde{z})$ denotes the direction of the steady, streamwise flow.

and as in [52], the Reynolds number Re is defined by

$$\mathrm{Re} = \frac{\rho^\star U_c^\star L_c^\star}{\mu^\star} \tag{5.35}$$

with $\rho^\star$ and $\mu^\star$ being the density and dynamic viscosity of the fluid, $L_c^\star$ is the characteristic length by which the wall-normal domain is normalised to $[-1+f(\tilde{z}), 1]$, and $U_c^\star$ is the characteristic velocity, which is related to a constant steady state streamwise pressure gradient $P_{\tilde{x}}^\star$ by

$$U_c^\star = -\frac{L_c^{\star 2} P_{\tilde{x}}^\star}{4\mu^\star} \tag{5.36}$$

Note that the superscript $\star$ is used to denote dimensional variables.

We now make some remarks about the definition of the Reynolds number. In (5.35), $U_c^\star$ is induced by the streamwise pressure gradient $P_{\tilde{x}}^\star$, which is assumed to be constant and is not changed by the presence of riblets. This assumption is believed to be reasonable [159] and has been used in some numerical studies in the literature, for example, [52] and [34]. Alternatively, in some other studies, the flow rate is assumed to be constant [37]. There are also some different ways of defining the characteristic length $L_c^\star$. In [34], the mean channel height is defined as $2L_c^\star$, while in [37], the mean channel height is $1.9L_c^\star$ with the height of the riblet being $0.2L_c^\star$. The distance between the smooth wall and the upper tip of the riblets is defined as $2L_c^\star$ in [52]. It is hard to tell which definition is the best, and in this thesis, we define the characteristic length as half of the mean channel height, as is done in [34].

By plugging the (dimensionless) steady state velocity $(U(\tilde{y},\tilde{z}),0,0)$ into (5.33), it can be shown that U is independent of the streamwise direction, i.e.,

$$\frac{\partial U}{\partial \tilde{x}} = 0 \tag{5.37}$$

and satisfies the Poisson's equation

$$\tilde{\Delta} U = -2 \tag{5.38}$$

Denote the streamwise, wall-normal and spanwise components of the perturbation velocity field as $u(\tilde{x},\tilde{y},\tilde{z}), v(\tilde{x},\tilde{y},\tilde{z})$ and $w(\tilde{x},\tilde{y},\tilde{z})$ and the perturbation pressure as $p(\tilde{x},\tilde{y},\tilde{z})$. Linearising about the steady state gives

$$\begin{aligned}
\frac{\partial u}{\partial t} + U\frac{\partial u}{\partial \tilde{x}} + v\frac{\partial U}{\partial \tilde{y}} + w\frac{\partial U}{\partial \tilde{z}} &= -\frac{\partial p}{\partial \tilde{x}} + \frac{1}{\mathrm{Re}}\tilde{\Delta} u && \text{(5.39a)}\\
\frac{\partial v}{\partial t} + U\frac{\partial v}{\partial \tilde{x}} &= -\frac{\partial p}{\partial \tilde{y}} + \frac{1}{\mathrm{Re}}\tilde{\Delta} v && \text{(5.39b)}\\
\frac{\partial w}{\partial t} + U\frac{\partial w}{\partial \tilde{x}} &= -\frac{\partial p}{\partial \tilde{z}} + \frac{1}{\mathrm{Re}}\tilde{\Delta} w && \text{(5.39c)}\\
\frac{\partial u}{\partial \tilde{x}} + \frac{\partial v}{\partial \tilde{y}} + \frac{\partial w}{\partial \tilde{z}} &= 0 && \text{(5.39d)}
\end{aligned}$$

As in plane Poiseuille flow, it is assumed that the perturbation velocity field is periodic in the spanwise direction and no-slip conditions are satisfied at solid boundaries, so that at $\tilde{y} = 1$,

$$u(\tilde{x},1,\tilde{z},t) = v(\tilde{x},1,\tilde{z},t) = w(\tilde{x},1,\tilde{z},t) = 0 \tag{5.40}$$

while for the riblet wall at $\tilde{y} = -1 + f(\tilde{z})$,

$$u(\tilde{x},-1+f(\tilde{z}),\tilde{z},t) = v(\tilde{x},-1+f(\tilde{z}),\tilde{z},t) = w(\tilde{x},-1+f(\tilde{z}),\tilde{z},t) = 0 \tag{5.41}$$

Similarly, the steady state velocity U satisfies

$$U(\tilde{x},1,\tilde{z},t) = U(\tilde{x},-1+f(\tilde{z}),\tilde{z},t) = 0 \tag{5.42}$$

5.5.2 Change of coordinates

As stated in Section 5.2, a change of coordinates is the preferred way to deal with the riblet geometry, compared to domain decomposition and embedded domain methods. The computational domain can be transformed by the following change of coordinates

$$x = \tilde{x}, \quad y = F(\tilde{y},\tilde{z}) = \frac{2\tilde{y} - f(\tilde{z})}{2 - f(\tilde{z})}, \quad z = \tilde{z} \tag{5.43}$$

which has the effect of mapping $\tilde{y} \in [-1+f(\tilde{z}),1]$ to $y \in [-1,1]$. For ease of reference, we note that

$$\frac{\partial}{\partial \tilde{x}} = \frac{\partial}{\partial x}, \quad \frac{\partial}{\partial \tilde{y}} = \frac{\partial F}{\partial \tilde{y}} \frac{\partial}{\partial y}, \quad \frac{\partial}{\partial \tilde{z}} = \frac{\partial}{\partial z} + \frac{\partial F}{\partial \tilde{z}} \frac{\partial}{\partial y} \tag{5.44}$$

where

$$\frac{\partial F}{\partial \tilde{y}} = \frac{2}{2-f(z)}, \quad \frac{\partial F}{\partial \tilde{z}} = \frac{(y-1)\, f'(z)}{2-f(z)} \tag{5.45}$$

with $f'(z) = \frac{\mathrm{d}}{\mathrm{d}z} f(z)$. Operators involving higher order derivatives can be readily transformed into the new coordinates in the same manner, although the expressions are rather cumbersome.

After the change of coordinates, the boundary conditions can also be transformed, so that for the smooth wall at $y = \tilde{y} = 1$, equation (5.40) becomes

$$u(x,1,z,t) = v(x,1,z,t) = w(x,1,z,t) = 0 \tag{5.46}$$

and for the riblet wall at $\tilde{y} = -1 + f(\tilde{z})$, equation (5.41) transforms to

$$u(x,-1,z,t) = v(x,-1,z,t) = w(x,-1,z,t) = 0 \tag{5.47}$$

Similarly, we have

$$U(x,1,z,t) = U(x,-1,z,t) = 0 \tag{5.48}$$

5.5.3 Steady state solution

Since the geometry is homogenous in the streamwise direction, the velocity components and the pressure in the transformed coordinate system can be expressed as Fourier series such as

$$v = \hat{v}(y,z,t)\mathrm{e}^{\mathrm{i}\alpha x} \tag{5.49}$$

$$p = \hat{p}(y,z,t)\mathrm{e}^{\mathrm{i}\alpha x} \tag{5.50}$$

where α is the streamwise wavenumber. The riblet structure is taken to be periodic in the z direction with period $2\pi/\gamma$. As in plane Poiseuille flow, the perturbation velocity field is also assumed to be periodic in the z direction with wavenumber β. Since the period of the velocity field must be an exact multiple of that of the riblets, $\zeta = \gamma/\beta$ is a whole number. This assumption is more general than assuming the perturbation has the same period as the riblets in the spanwise direction, which is equivalent to assuming that $\zeta = 1$.

Due to the periodicity of the flow in the spanwise direction, the variables can be further expressed as

$$\begin{aligned} \hat{v}(y,z,t) &= \sum_{n=-\infty}^{\infty} \hat{v}_n(y,t)\mathrm{e}^{\mathrm{i}n\beta z} && (5.51) \\ f(z) &= \sum_{n=-\infty}^{\infty} \hat{f}_n \mathrm{e}^{\mathrm{i}n\beta z} && (5.52) \\ U(y,z) &= \sum_{n=-\infty}^{\infty} \hat{U}_n(y)\mathrm{e}^{\mathrm{i}n\beta z} && (5.53) \end{aligned}$$

and $\hat{f}_n = 0$ for all $n \neq m\zeta$ where m is an integer. This sparsity is exploited in the solution of the problem when $\zeta > 1$.

We are now ready to solve the steady state using spectral methods. The discretisation in the y direction is implemented using the Chebyshev collocation method and either the Fourier collocation method or the Fourier Galerkin method can be used to discretise the equations in the z direction. When $\gamma = \beta$, these two methods do not make much difference in terms of the computational efforts to solve the eigenvalue problem. However, in the case that ζ is a relatively large number, the Fourier Galerkin method has decisive advantages over the collocation method. To see this, we show how the computational load of solving the steady state flow $U(y,z)$ is greatly reduced using the Fourier Galerkin method.

The steady state flow velocity $U(y,z)$ is described by the Poisson's equation (5.38). In the new coordinate system, the Laplace operator $\tilde{\Delta}$ is given by

$$\tilde{\Delta} = K_1(y,z)\frac{\partial}{\partial y} + K_2(y,z)\frac{\partial^2}{\partial y \partial z} + K_3(y,z)\frac{\partial^2}{\partial y^2} + K_4(y,z)\frac{\partial^2}{\partial z^2} \qquad (5.54)$$

where the expressions $K_i, i \in \{1,2,3,4\}$ are known and can be expressed in terms of Fourier series

$$K_i(y,z) = \sum_{n=-\infty}^{\infty} \hat{k}_n^{(i)}(y)\,\mathrm{e}^{\mathrm{i}n\beta z} \qquad (5.55)$$

Moreover, it can be shown that $\hat{k}_n^{(i)}(y)$ is nonzero only when n is an exact multiple of ζ.

Using these expansions in (5.38), applying the convolution theorem for Fourier series and rearranging leads to

$$\begin{aligned} \sum_{n=-\infty}^{\infty} \mathrm{e}^{\mathrm{i}n\beta z} \sum_{m=-\infty}^{\infty} \left[\hat{k}_{n-m}^{(1)}(y) + \mathrm{i}m\,\hat{k}_{n-m}^{(2)}(y)\right]\frac{\mathrm{d}\hat{U}_m(y)}{\mathrm{d}y} + \hat{k}_{n-m}^{(3)}(y)\,\frac{\mathrm{d}^2\hat{U}_m(y)}{\mathrm{d}y^2} \\ -m^2\hat{k}_{n-m}^{(4)}(y)\,\hat{U}_m(y) = -2 \qquad (5.56) \end{aligned}$$

Defining an inner product as

$$\langle p(y,z), q(y,z)\rangle = \int_0^{2\pi/\beta} p^*(y,z)\, q(y,z) dz \tag{5.57}$$

and taking the inner product of the expression in (5.56) with a test function $\mathrm{e}^{\mathrm{i}\ell\beta z}$, then

$$\sum_{m=-\infty}^{\infty} \left[\hat{k}^{(1)}_{\ell-m}(y) + \mathrm{i}m\, \hat{k}^{(2)}_{\ell-m}(y)\right] \frac{\mathrm{d}\hat{U}_m(y)}{\mathrm{d}y} + \hat{k}^{(3)}_{\ell-m}(y)\, \frac{\mathrm{d}^2\hat{U}_m(y)}{\mathrm{d}y^2} - m^2 \hat{k}^{(4)}_{\ell-m}(y)\, \hat{U}_m(y) = b_\ell, \;\; \ell \in \mathbb{Z} \tag{5.58}$$

where

$$b_\ell = \begin{cases} -2, & \ell = 0, \\ 0, & \ell \neq 0. \end{cases} \tag{5.59}$$

Approximating $U(y,z)$ by limiting the summation to $2M+1$ terms, we have

$$\sum_{m=-M}^{M} \left[\hat{k}^{(1)}_{\ell-m}(y) + \mathrm{i}m\, \hat{k}^{(2)}_{\ell-m}(y)\right] \frac{\mathrm{d}\hat{U}_m(y)}{\mathrm{d}y} + \hat{k}^{(3)}_{\ell-m}(y)\, \frac{\mathrm{d}^2\hat{U}_m(y)}{\mathrm{d}y^2} - m^2 \hat{k}^{(4)}_{\ell-m}(y)\, \hat{U}_m(y) = b_\ell \tag{5.60}$$

for $\ell \in \{-M, \ldots, 0, \ldots, M\}$. Stacking the values of $\hat{U}_m(y)$ at N Chebyshev Gauss-Lobatto points into a vector $\hat{\mathbf{U}} \in \mathbb{C}^{(2M+1)N}$, so that

$$\hat{\mathbf{U}} = \begin{bmatrix} \hat{\mathbf{U}}_{-M} \; \ldots \; \hat{\mathbf{U}}_{-1} \; \hat{\mathbf{U}}_0 \; \hat{\mathbf{U}}_1 \; \ldots \hat{\mathbf{U}}_M \end{bmatrix}^{\mathrm{T}} \tag{5.61}$$

where $\hat{\mathbf{U}}_m \in \mathbb{C}^N$ are the samples of $\hat{U}_m(y)$ at the N collocation points. The discretised version of the equation (5.58) takes the form

$$\tilde{\mathbf{\Delta}}\hat{\mathbf{U}} = \mathbf{b} \tag{5.62}$$

where $\mathbf{b} \in \mathbb{C}^{(2M+1)N}$ contains the values of b_ℓ at the sample points. The matrix $\tilde{\mathbf{\Delta}} \in \mathbb{C}^{(2M+1)N\times(2M+1)N}$ consists of a series of blocks $[\tilde{\mathbf{\Delta}}]_{\ell,m} \in \mathbb{C}^{N\times N}$, that satisfy

$$[\tilde{\mathbf{\Delta}}]_{\ell,m} = \mathtt{diag}\left\{\hat{\mathbf{k}}^{(1)}_{\ell-m} + \mathrm{i}m\,\hat{\mathbf{k}}^{(2)}_{\ell-m}\right\}\mathbf{D} + \mathtt{diag}\left\{\hat{\mathbf{k}}^{(3)}_{\ell-m}\right\}\mathbf{D}_2 - \mathtt{diag}\left\{m^2\hat{\mathbf{k}}^{(4)}_{\ell-m}\right\} \tag{5.63}$$

where $\mathbf{D} \in \mathbb{R}^{N\times N}$ and $\mathbf{D}_2 \in \mathbb{R}^{N\times N}$ are the first and second order Chebyshev differentiation matrices with the homogeneous Dirichlet boundary conditions imposed on, respectively, and $\hat{\mathbf{k}}^{(i)}_{\ell-m} \in \mathbb{C}^N$ are vectors obtained by sampling $\hat{k}^{(i)}_{\ell-m}(y)$ at the N collocation points.

The key point is that because $\hat{k}^{(i)}_{\ell-m}(y)$ is only nonzero when $\ell - m$ is an exact multiple of ζ, the matrix $\tilde{\mathbf{\Delta}}$ has the structure shown in Figure 5.9(a), where each of the individual blocks has dimension $N \times N$. By rearranging the order of the terms in $\hat{\mathbf{U}}$, which is equivalent to premultiplying a permutation matrix, the structure of $\tilde{\mathbf{\Delta}}$ can be arranged

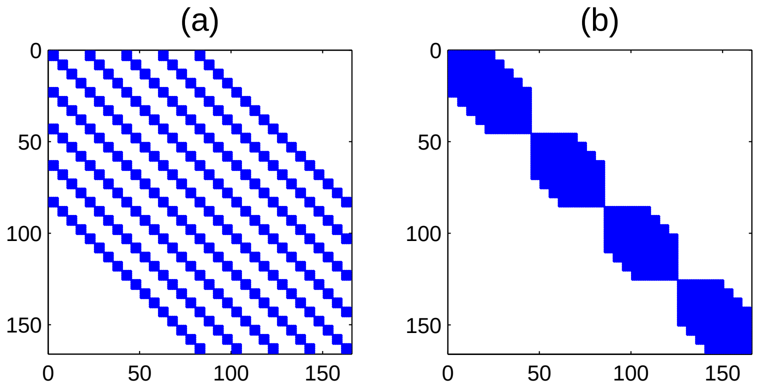

Figure 5.9: Structure of the matrix $\tilde{\boldsymbol{\Delta}}$: (a) before rearranging, (b) after rearranging.

into the block diagonal form shown in Figure 5.9(b), which consists of ζ blocks. Such a structure breaks the problem into ζ independent subproblems and the eigenvalue problem for this structure reduces the computational load by roughly a factor of ζ^2 in terms of CPU time, which is significant when ζ is large. Furthermore, the subproblems can be solved in parallel due to the fact that they are independent. The parallelisation further reduces the wall-clock time of the computation by a factor of ζ. In terms of space complexity, using the Fourier Galerkin method is also more efficient because of the block diagonal structure of the matrices.

By contrast, the differentiation matrices produced using the Fourier collocation method do not have the block diagonal structure, so that the Fourier Galerkin method is preferable when ζ is greater than 1. Only in the case that $\zeta = 1$ do these two methods have comparable performances.

We note that numerical computation reveals that the base flow U has the same period as the riblets, even under the assumption that its period is an exact multiple of that of the riblets. Figure 5.10 depicts the profile $U(\tilde{y}, \tilde{z})$ when the riblet shape function is $f(\tilde{z}) = 0.04 \times \cos(20\tilde{z})$. The steady state of channel flow over riblets has a similar velocity profile to that of the flow over flat plates. The velocity gradient in the spanwise direction decreases with $\tilde{y}$ and almost vanishes at $\tilde{y} \approx -0.8$.

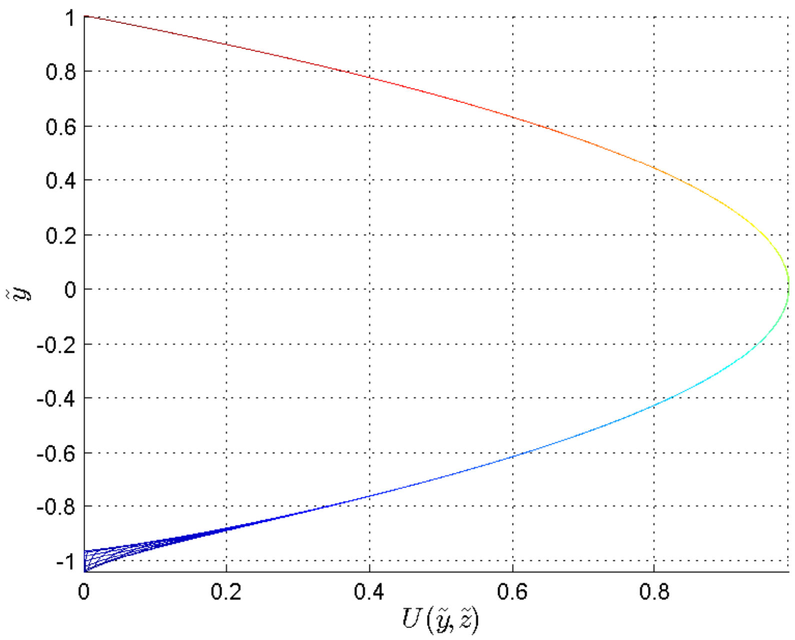

Figure 5.10: Steady state velocity profile of channel flow over riblets with shape function $f(\tilde{z}) = 0.04 \times \cos(20\tilde{z})$.

5.6 Conclusion

This chapter presents some preliminaries as a preparation for the numerical study of the stability of channel flow over riblet. We have introduced three kinds of methods that enable spectral methods to be used in irregular computational domains: change of coordinates, domain decomposition and embedded domain methods. We also briefly introduce how to use the matrix-free approach to determine the linear stability and calculate transient growth in a complex flow. Some commonly used eigenvalue algorithms are then discussed and it is recognised that choosing appropriate shifts is of great importance to solve large scale eigenvalue problems using the Arnoldi algorithm. After that, we give the linearised NSEs that govern the motion of the flow and the riblet geometry is transformed into a smooth one by a change of coordinates. Finally, the steady state of the flow is solved numerically. It is shown that using the Fourier Galerkin method to discretise the NSEs in the spanwise direction can greatly reduce the computational load, as the matrices generated by discretisation can be made block diagonal by rearranging their structures.

Chapter 6

Effects of Riblets on Linear Stability

6.1 Introduction

This chapter focuses on the effects of riblets on the linear stability of channel flow. Although linear instability is an unlikely path to transition, if riblets significantly change the linear stability of the flow, it is expected that the transition will also be influenced. If the flow is made more linearly unstable, riblets could trigger the transition from laminar flow to turbulence. Whereas if the flow is more linearly stable in the presence of riblets, the transition could be delayed.

The linear stability of channel flow over semi-circular riblets has been previously studied by Ehrenstein [52], who concluded that the linearised flow is more unstable in the presence of riblets. The most important difference between our work and Ehrenstein's [52] is that here only no-slip boundary conditions and periodic conditions are assumed. We do not assume the perturbation is invariant by reflection in the spanwise direction. Furthermore, in [52], the perturbation velocity field is assumed to have the same period as the riblets, here instead a more general assumption is made where the period of the velocity components is an exact multiple of that of the riblets. To avoid making assumptions about the pressure gradient, a "velocity-velocity" formulation in which the pressure terms are eliminated is derived. Since the flow equations in this velocity-velocity form consist of two fourth-order differential equations, to ensure that the eigenvalue problem is well-posed, sufficient boundary conditions are derived directly from the no-slip boundary conditions and the NSEs. Because the eigenvalues of the linearised operator are sensitive to assumptions that are made, in order to make comparisons between the channel flow over riblets and the flow over flat plates, consistent assumptions about the boundary conditions in the two cases are considered. The results obtained using the velocity-velocity formulation are then compared with those obtained by using the primitive variable formulation.

6.2 Formulations of the governing equations

The linearised NSEs that govern the motion of channel flow over riblets are given by (5.39). The equations are repeated here for convenience

$$\begin{aligned}
\frac{\partial u}{\partial t}+U\frac{\partial u}{\partial \tilde{x}}+v\frac{\partial U}{\partial \tilde{y}}+w\frac{\partial U}{\partial \tilde{z}} &= -\frac{\partial p}{\partial \tilde{x}}+\frac{1}{\mathrm{Re}}\tilde{\Delta}u && \text{(6.1a)}\\
\frac{\partial v}{\partial t}+U\frac{\partial v}{\partial \tilde{x}} &= -\frac{\partial p}{\partial \tilde{y}}+\frac{1}{\mathrm{Re}}\tilde{\Delta}v && \text{(6.1b)}\\
\frac{\partial w}{\partial t}+U\frac{\partial w}{\partial \tilde{x}} &= -\frac{\partial p}{\partial \tilde{z}}+\frac{1}{\mathrm{Re}}\tilde{\Delta}w && \text{(6.1c)}\\
\frac{\partial u}{\partial \tilde{x}}+\frac{\partial v}{\partial \tilde{y}}+\frac{\partial w}{\partial \tilde{z}} &= 0 && \text{(6.1d)}
\end{aligned}$$

The linear stability of the flow can be determined by using the matrix approach, and the next question is what formulation of the governing equations we should use in the calculation. Although mathematically equivalent, different formulations of the linearised NSEs have different numerical behaviours. The first formulation that one would think of is the velocity-vorticity formulation, which is used to calculate the eigenvalues of linearised plane Poiseuille flow. Unfortunately, such a formulation is not appropriate for channel flow over riblets since the steady state flow is now also dependent on the spanwise direction.

The advantage of the velocity-vorticity formulation is that it reduces four equations to two equations, and in particular, the elimination of the pressure term from the equations is desirable. The pressure term p is a source of the difficulties attached to the NSEs, because unlike the velocity components u, v, w, the pressure p does not have a time-dependent equation that governs its evolution. For this reason, the treatment of pressure is one of the major difficulties in numerical simulations of fluid flows [26].

The primitive variable form of the NSEs can be used to calculate the eigenvalues. The disadvantage is that the matrix $\mathbf{B}$ in the generalised eigenvalue problem $\mathbf{Aq} = \lambda\mathbf{Bq}$ is singular, which is a direct result of the presence of the pressure term. There are a number of ways in the literature to circumvent this difficulty. For example, Ramanan and Homsy use two potential equations to formulate a nonsingular eigenvalue problem [122], while in [44] slight compressibility is introduced such that there is a time-dependent governing equation for pressure.

Although the singularity in the primitive variable form is not desirable, the eigenvalue problem can still be solved as long as the compatibility conditions for the pressure term are imposed. This form has been used to check the linear stability of a range of flows such as the flow in a duct and the lid-driven cavity flow [148].

In this chapter, a velocity-velocity formulation for the channel flow over riblets is derived. The pressure term is eliminated and the four equations are reduced to two fourth-order equations. We then derive enough boundary conditions without making additional assumptions.

6.2.1 Primitive variable form

The primitive variable form in matrix form is straightforward to obtain

$$\frac{\partial}{\partial t}(\mathcal{B}_p q_p) = \mathcal{A}_p q_p \tag{6.2}$$

where

$$q_p = \begin{bmatrix} u & v & w & p \end{bmatrix}^T \tag{6.3}$$

$$\mathcal{B}_p = \begin{bmatrix} 1 & 0 & 0 & 0 \\ 0 & 1 & 0 & 0 \\ 0 & 0 & 1 & 0 \\ 0 & 0 & 0 & 0 \end{bmatrix} \tag{6.4}$$

$$\mathcal{A}_p = \begin{bmatrix} \frac{1}{\mathrm{Re}}\tilde{\Delta} - U\frac{\partial}{\partial \tilde{x}} & -\frac{\partial U}{\partial \tilde{y}} & -\frac{\partial U}{\partial \tilde{z}} & -\frac{\partial}{\partial \tilde{x}} \\ 0 & \frac{1}{\mathrm{Re}}\tilde{\Delta} - U\frac{\partial}{\partial \tilde{x}} & 0 & -\frac{\partial}{\partial \tilde{y}} \\ 0 & 0 & \frac{1}{\mathrm{Re}}\tilde{\Delta} - U\frac{\partial}{\partial \tilde{x}} & -\frac{\partial}{\partial \tilde{z}} \\ \frac{\partial}{\partial \tilde{x}} & \frac{\partial}{\partial \tilde{y}} & \frac{\partial}{\partial \tilde{z}} & 0 \end{bmatrix} \tag{6.5}$$

with the subscripts in $\mathcal{B}_p, \mathcal{A}_p$ and q_p denoting the primitive variable form. It is clear that the operator $\mathcal{B}_p$ is singular, therefore the governing equations are partial differential-algebraic equations.

6.2.2 Velocity-velocity form

The derivation of the velocity-velocity form is similar to that of the velocity-vorticity form. Taking the divergence of the momentum equations (6.1a)-(6.1c) leads to

$$2\frac{\partial v}{\partial \tilde{x}}\frac{\partial U}{\partial \tilde{y}} + 2\frac{\partial w}{\partial \tilde{x}}\frac{\partial U}{\partial \tilde{z}} = -\tilde{\Delta} p \tag{6.6}$$

which can be used with equation (6.1b) to eliminate the pressure p

$$\left(\frac{\partial}{\partial t} + U\frac{\partial}{\partial \tilde{x}}\right)\tilde{\Delta} v + 2\frac{\partial U}{\partial \tilde{z}}\frac{\partial^2 v}{\partial \tilde{x}\partial \tilde{z}} + \frac{\partial^2 U}{\partial \tilde{z}^2}\frac{\partial v}{\partial \tilde{x}} - \frac{\partial v}{\partial \tilde{x}}\frac{\partial^2 U}{\partial \tilde{y}^2} - \frac{1}{\mathrm{Re}}\tilde{\Delta}^2 v = 2\frac{\partial^2 w}{\partial \tilde{x}\partial \tilde{y}}\frac{\partial U}{\partial \tilde{z}} + 2\frac{\partial w}{\partial \tilde{x}}\frac{\partial^2 U}{\partial \tilde{y}\partial \tilde{z}} \tag{6.7}$$

Similarly, taking the Laplacian of equation (6.1c) and eliminating the pressure term gives

$$\left(\frac{\partial}{\partial t} + U\frac{\partial}{\partial \tilde{x}}\right)\tilde{\Delta} w + 2\frac{\partial U}{\partial \tilde{y}}\frac{\partial^2 w}{\partial \tilde{x}\partial \tilde{y}} - \frac{\partial^2 U}{\partial \tilde{z}^2}\frac{\partial w}{\partial \tilde{x}} + \frac{\partial^2 U}{\partial \tilde{y}^2}\frac{\partial w}{\partial \tilde{x}} - \frac{1}{\mathrm{Re}}\tilde{\Delta}^2 w = 2\frac{\partial^2 v}{\partial \tilde{x}\partial \tilde{z}}\frac{\partial U}{\partial \tilde{y}} + 2\frac{\partial v}{\partial \tilde{x}}\frac{\partial^2 U}{\partial \tilde{y}\partial \tilde{z}} \tag{6.8}$$

The flow equations (6.7) and (6.8) can be combined to give

$$\frac{\partial}{\partial t}(\mathcal{B}_v q_v) = \mathcal{A}_v q_v \tag{6.9}$$

where $q_v, \mathcal{A}_v$ and $\mathcal{B}_v$ are

$$\begin{aligned} q_v &= \begin{bmatrix} v & w \end{bmatrix}^T && (6.10)\\ \mathcal{B}_v &= \begin{bmatrix} \tilde{\Delta} & 0 \\ 0 & \tilde{\Delta} \end{bmatrix} && (6.11)\\ \mathcal{A}_v &= \begin{bmatrix} A_{11} & A_{12} \\ A_{21} & A_{22} \end{bmatrix} && (6.12) \end{aligned}$$

with

$$\begin{aligned} A_{11} &= -U\frac{\partial}{\partial \tilde{x}}\tilde{\Delta} - 2\frac{\partial U}{\partial \tilde{z}}\frac{\partial^2}{\partial \tilde{x}\partial \tilde{z}} - \frac{\partial^2 U}{\partial \tilde{z}^2}\frac{\partial}{\partial \tilde{x}} + \frac{\partial^2 U}{\partial \tilde{y}^2}\frac{\partial}{\partial \tilde{x}} + \frac{1}{\mathrm{Re}}\tilde{\Delta}^2 && (6.13)\\ A_{12} &= 2\frac{\partial U}{\partial \tilde{z}}\frac{\partial^2}{\partial \tilde{x}\partial \tilde{y}} + 2\frac{\partial^2 U}{\partial \tilde{y}\partial \tilde{z}}\frac{\partial}{\partial \tilde{x}} && (6.14)\\ A_{21} &= 2\frac{\partial U}{\partial \tilde{y}}\frac{\partial^2}{\partial \tilde{x}\partial \tilde{z}} + 2\frac{\partial^2 U}{\partial \tilde{y}\partial \tilde{z}}\frac{\partial}{\partial \tilde{x}} && (6.15)\\ A_{22} &= -U\frac{\partial}{\partial \tilde{x}}\tilde{\Delta} - 2\frac{\partial U}{\partial \tilde{y}}\frac{\partial^2}{\partial \tilde{x}\partial \tilde{y}} + \frac{\partial^2 U}{\partial \tilde{z}^2}\frac{\partial}{\partial \tilde{x}} - \frac{\partial^2 U}{\partial \tilde{y}^2}\frac{\partial}{\partial \tilde{x}} + \frac{1}{\mathrm{Re}}\tilde{\Delta}^2 && (6.16) \end{aligned}$$

Note that the subscripts in $\mathcal{B}_v, \mathcal{A}_v$ and q_v are used to denote the velocity-velocity formulation.

This formulation is different from the velocity-vorticity form that is used to analyse plane Poiseuille flow where both walls are smooth [133]. The reason for making this change is that due to the presence of the riblet, the differential equations in the velocity-vorticity form will be of sixth order, but the velocity-velocity formulation is only of fourth order.

The velocity-velocity formulation has several advantages over the primitive variable form. First of all, it reduces four equations to two equations, which means that with the same discretisation resolution, the matrix size is halved. Equivalently, with the same computational resources, the velocity-velocity formulation can achieve higher resolution. This is especially important when we are interested in calculating the eigenfunctions. Secondly, the matrix $\mathbf{B}$ obtained by discretising the operator $\mathcal{B}_v$ is nonsingular, which means that the generalised eigenvalue problem can be transformed to a simpler eigenvalue problem by inverting $\mathbf{B}$.

One disadvantage of the velocity-velocity formulation is that fourth derivatives of the flow have to been calculated, as opposed to second derivatives in the primitive variable form. When the solutions are smooth, this causes no real problem. However, when the solutions are not sufficiently smooth, more collocation points may be needed to achieve convergent results. In addition, the primitive variable form is more general in the sense that it is applicable to all incompressible flows, while the velocity-velocity form can only be derived when the linearised flow is periodic and decoupled in one spatial direction. Finally, we will see that the derivation of the boundary conditions in the velocity-velocity form is more difficult.

Irrespective of what formulation is used, the governing equations have to be transformed into the new coordinate system after the change of coordinate (5.43) is applied.

6.3 Boundary conditions

The derivation and imposition of the boundary conditions are essential to solve the eigenvalue problem numerically, and we now derive the boundary conditions for both the primitive variable form and the velocity-velocity form.

6.3.1 Primitive variable form

The homogeneous Dirichlet boundary conditions (5.46) and (5.47) are not sufficient to produce convergent eigenvalue results in the primitive variable form. Because we have no physical boundary conditions for the pressure p, it is the so-called compatibility conditions that come into play [148]. Evaluating the momentum equations (6.1a) at the boundaries $\tilde{y} = 1$ and $\tilde{y} = -1 + f(\tilde{z})$, we have

$$\left[\frac{1}{\mathrm{Re}}\tilde{\Delta} u - \frac{\partial p}{\partial \tilde{x}}\right]\bigg|_{\tilde{y}=1} = \left[\frac{1}{\mathrm{Re}}\tilde{\Delta} u - \frac{\partial p}{\partial \tilde{x}}\right]\bigg|_{\tilde{y}=-1+f(\tilde{z})} = 0 \tag{6.17}$$

In the same manner, evaluating the momentum equatons (6.1b) and (6.1c) at the boundaries gives the following compatibility conditions

$$\left[\frac{1}{\mathrm{Re}}\tilde{\Delta} v - \frac{\partial p}{\partial \tilde{y}}\right]\bigg|_{\tilde{y}=1} = \left[\frac{1}{\mathrm{Re}}\tilde{\Delta} u - \frac{\partial p}{\partial \tilde{y}}\right]\bigg|_{\tilde{y}=-1+f(\tilde{z})} = 0 \tag{6.18}$$

$$\left[\frac{1}{\mathrm{Re}}\tilde{\Delta} w - \frac{\partial p}{\partial \tilde{z}}\right]\bigg|_{\tilde{y}=1} = \left[\frac{1}{\mathrm{Re}}\tilde{\Delta} u - \frac{\partial p}{\partial \tilde{z}}\right]\bigg|_{\tilde{y}=-1+f(\tilde{z})} = 0 \tag{6.19}$$

Equations (6.17)-(6.19) can then be transformed into the new coordinate system.

6.3.2 Velocity-velocity form

In the velocity-velocity formulation, the pressure term is eliminated and the eignvalue problem is now characterised by two fourth-order differential equations. Apart from the four homogeneous Dirichlet conditions for v and w at the solid boundaries, four more boundary conditions are needed. After the transformation of coordinates, the continuity equation (6.1d) becomes

$$\frac{\partial u}{\partial x} + \frac{\partial F}{\partial \tilde{y}}\frac{\partial v}{\partial y} + \frac{\partial w}{\partial z} + \frac{\partial F}{\partial \tilde{z}}\frac{\partial w}{\partial y} = 0 \tag{6.20}$$

Since

$$\left.\frac{\partial u}{\partial x}\right|_{y=\pm 1} = \left.\frac{\partial w}{\partial z}\right|_{y=\pm 1} = 0 \tag{6.21}$$

substituting (5.45) into (6.20) yields

$$\left.\left[2\frac{\partial v}{\partial y} + (y-1)f'(z)\frac{\partial w}{\partial y}\right]\right|_{y=\pm 1} = 0 \tag{6.22}$$

The derivation of the remaining two boundary equations that are required to make the eigenvalue problem well posed is not intuitive. Taking $\frac{\partial^2}{\partial \tilde{x}\partial \tilde{z}}$ of (6.1a), $\frac{\partial^2}{\partial \tilde{x}^2}$ of (6.1c) and eliminating the pressure term gives

$$\begin{aligned} &\frac{\partial^3 u}{\partial t\partial \tilde{x}\partial \tilde{z}} - \frac{\partial^3 w}{\partial t\partial \tilde{x}^2} + \frac{\partial U}{\partial \tilde{z}}\frac{\partial u}{\partial \tilde{x}^2} + U\frac{\partial^3 u}{\partial \tilde{x}^2\partial \tilde{z}} + \frac{\partial U}{\partial \tilde{y}}\frac{\partial^2 v}{\partial \tilde{x}\partial \tilde{z}} + \frac{\partial^2 U}{\partial \tilde{y}\partial \tilde{z}}\frac{\partial v}{\partial \tilde{x}} \\ &+ \frac{\partial U}{\partial \tilde{z}}\frac{\partial^2 w}{\partial \tilde{x}\partial \tilde{z}} + \frac{\partial^2 U}{\partial \tilde{z}^2}\frac{\partial w}{\partial \tilde{x}} - U\frac{\partial^3 w}{\partial \tilde{x}^3} = \frac{1}{\mathrm{Re}}\tilde{\Delta}\left(\frac{\partial^2 u}{\partial \tilde{x}\partial \tilde{z}} - \frac{\partial^2 w}{\partial \tilde{x}^2}\right) \end{aligned} \tag{6.23}$$

Evaluating equation (6.23) at $\tilde{y} = 1$ and substituting the continuity equation, we have

$$\left.\left[\tilde{\Delta}\left(\frac{\partial^2 v}{\partial \tilde{y}\partial \tilde{z}} + \frac{\partial^2 w}{\partial \tilde{x}^2} + \frac{\partial^2 w}{\partial \tilde{z}^2}\right)\right]\right|_{\tilde{y}=1} = 0 \tag{6.24}$$

Similarly, evaluating at $\tilde{y} = -1 + f(\tilde{z})$ leads to

$$\left.\left[\frac{\partial^3 u}{\partial t\partial \tilde{x}\partial \tilde{z}} + \frac{\partial U}{\partial \tilde{y}}\frac{\partial^2 v}{\partial \tilde{x}\partial \tilde{z}} + \frac{\partial U}{\partial \tilde{z}}\frac{\partial^2 w}{\partial \tilde{x}\partial \tilde{z}}\right]\right|_{\tilde{y}=-1+f(\tilde{z})} = \left.\left[\frac{1}{\mathrm{Re}}\tilde{\Delta}\left(\frac{\partial^2 u}{\partial \tilde{x}\partial \tilde{z}} - \frac{\partial^2 w}{\partial \tilde{x}^2}\right)\right]\right|_{\tilde{y}=-1+f(\tilde{z})} \tag{6.25}$$

However, this expression involves a time derivative, so we need another equation to eliminate the time derivative. Taking $\frac{\partial^2}{\partial \tilde{x}\partial \tilde{y}}$ of (6.1a), $\frac{\partial^2}{\partial \tilde{x}^2}$ of (6.1b) and subtracting the resulting equations yields

$$\begin{aligned} &\frac{\partial^3 u}{\partial t\partial \tilde{x}\partial \tilde{y}} - \frac{\partial^3 v}{\partial t\partial \tilde{x}^2} + \frac{\partial U}{\partial \tilde{y}}\frac{\partial^2 u}{\partial \tilde{x}^2} + U\frac{\partial^3 u}{\partial \tilde{x}^2\partial \tilde{y}} + \frac{\partial U}{\partial \tilde{y}}\frac{\partial^2 v}{\partial \tilde{x}\partial \tilde{y}} + \frac{\partial^2 U}{\partial \tilde{y}^2}\frac{\partial v}{\partial \tilde{x}} \\ &+ \frac{\partial U}{\partial \tilde{z}}\frac{\partial^2 w}{\partial \tilde{x}\partial \tilde{y}} + \frac{\partial^2 U}{\partial \tilde{y}\partial \tilde{z}}\frac{\partial w}{\partial \tilde{x}} - U\frac{\partial^3 v}{\partial \tilde{x}^3} = \frac{1}{\mathrm{Re}}\tilde{\Delta}\left(\frac{\partial^2 u}{\partial \tilde{x}\partial \tilde{y}} - \frac{\partial^2 v}{\partial \tilde{x}^2}\right) \end{aligned} \tag{6.26}$$

Evaluating at $\tilde{y} = -1 + f(\tilde{z})$ gives

$$\left.\left[\frac{\partial^3 u}{\partial t\partial \tilde{x}\partial \tilde{y}} + \frac{\partial U}{\partial \tilde{y}}\frac{\partial^2 v}{\partial \tilde{x}\partial \tilde{y}} + \frac{\partial U}{\partial \tilde{z}}\frac{\partial^2 w}{\partial \tilde{x}\partial \tilde{y}}\right]\right|_{\tilde{y}=-1+f(\tilde{z})} = \left.\left[\frac{1}{\mathrm{Re}}\tilde{\Delta}\left(\frac{\partial^2 u}{\partial \tilde{x}\partial \tilde{y}} - \frac{\partial^2 v}{\partial \tilde{x}^2}\right)\right]\right|_{\tilde{y}=-1+f(\tilde{z})} \tag{6.27}$$

After transformation of coordinates, evaluating the left-hand side of (6.25) at $y = -1$ gives

$$\left[\frac{\partial F}{\partial \tilde{z}}\frac{\partial^3 u}{\partial t\partial x\partial y} + \frac{\partial F}{\partial \tilde{y}}\frac{\partial F}{\partial \tilde{z}}\frac{\partial U}{\partial y}\frac{\partial^2 v}{\partial x\partial y} + \left(\frac{\partial F}{\partial \tilde{z}}\right)^2\frac{\partial U}{\partial y}\frac{\partial^2 w}{\partial x\partial y}\right]\Bigg|_{y=-1} \tag{6.28}$$

Similarly, the left-hand side of (6.27) becomes

$$\left[\frac{\partial F}{\partial \tilde{y}}\frac{\partial^3 u}{\partial t\partial x\partial y} + \left(\frac{\partial F}{\partial \tilde{y}}\right)^2\frac{\partial U}{\partial y}\frac{\partial^2 v}{\partial x\partial y} + \frac{\partial F}{\partial \tilde{y}}\frac{\partial F}{\partial \tilde{z}}\frac{\partial U}{\partial y}\frac{\partial^2 w}{\partial x\partial y}\right]\Bigg|_{y=-1} \tag{6.29}$$

We note that the left-hand side of (6.25) multiplying $\frac{\partial F}{\partial \tilde{y}}$ equals the left-hand side of (6.27) multiplying $\frac{\partial F}{\partial \tilde{z}}$. As a result,

$$\left[\frac{\partial F}{\partial \tilde{y}}\tilde{\Delta}\left(\frac{\partial^2 v}{\partial \tilde{y}\partial \tilde{z}} + \frac{\partial^2 w}{\partial \tilde{x}^2} + \frac{\partial^2 w}{\partial \tilde{z}^2}\right) - \frac{\partial F}{\partial \tilde{z}}\tilde{\Delta}\left(\frac{\partial^2 v}{\partial \tilde{x}^2} + \frac{\partial^2 v}{\partial \tilde{y}^2} + \frac{\partial^2 w}{\partial \tilde{y}\partial \tilde{z}}\right)\right]\Bigg|_{\tilde{y}=-1+f(\tilde{z})} = 0 \tag{6.30}$$

After transforming to the new coordinate system, (6.24) and (6.30) give the two additional boundary conditions needed.

6.4 Numerical results

The governing equations in the primitive variable form (6.2) or in the velocity-velocity form (6.9) can be discretised in the same manner as the way the steady state flow is solved in Section 5.5.3, although the implementation is more laborious. The matrices generated by discretising the operators $\mathcal{B}_p, \mathcal{A}_p, \mathcal{B}_v$ and $\mathcal{A}_v$ are all block diagonal when the Fourier Galerkin method is used in the spanwise direction. As mentioned previously, the disadvantage of the Galerkin method compared to the collocation method is that it is more difficult to implement. Regardless of whether the Fourier Galerkin method or the Fourier collocation method is used, the boundary conditions are implemented using the boundary-bordering method [20]. As usual, the differentiation matrices given by Weideman and Reddy [161] are used in the wall-normal direction.

We are now in a position to present the numerical results on the linear stability of channel flow over riblets. In this section, the results under different assumptions on ζ are described. Three types of riblets are considered: sinusoidal, triangular and semi-circular ones. The results reported here are calculated on the computer cluster ARCUS at Oxford Advanced Research Computing (ARC) centre.

	$\alpha = 0.1, \beta = 2$	$\alpha = 1, \beta = 1$
$N = 44, M = 24$	-0.00245676 - 0.09706185i	0.00025187 - 0.25944754i
$N = 50, M = 32$	-0.00245676 - 0.09706184i	0.00025194 - 0.25944989i

Table 6.1: Eigenvalues with largest real parts for different resolutions and different α, β at $\text{Re} = 6000, h = 0.03$.

6.4.1 Assumption 1: $\zeta = 1$

It is assumed in [52] that the flow has the same period as the riblets, which means that $\beta = \gamma$, or equivalently $\zeta = 1$. Under this assumption, there is no need to use the Fourier Galerkin method to discretise the governing equations in the spanwise direction. We therefore use the Chebyshev collocation and the Fourier collocation methods for discretisation.

6.4.1.1 Sinusoidal riblets

The effects of sinusoidal riblets on the linear stability of channel flow are first investigated. Specifically, we consider how the linear stability of the fluid flow is affected by the spacing and height of the riblets. The shape of riblets under consideration takes the form

$$f(z) = h\cos(\gamma z) \tag{6.31}$$

Note that since the system model is based on the assumption that the presence of riblets does not change the pressure gradient, the riblet height h should not be too large, otherwise the assumption may not be valid. In this work we restrict to our attention to $h \in [0, 0.04]$ to ensure that the model is within its range of validity, although in both [52] and [34], h is as large as 0.1.

The velocity-velocity form is used in the computation and the discretisation resolutions used to obtain the results reported here are confirmed to be sufficiently high so that the relative errors are less than 10^{-3}. Denoting N as the number of collocation points between $y \in [-1, 1]$ and M as the number of collocation points between $z \in [0, 2\pi/\beta]$, Table 6.1 lists the eigenvalues with the largest real parts for different resolutions, α and β at $\text{Re} = 6000, h = 0.03$. Finer resolution has to be used for larger β and h to achieve the same level of accuracy. Given that the matrices are of moderate sizes and in order to avoid the omission of some of the eigenvalues we are most interested in, the QR algorithm rather than the Arnoldi algorithm is used.

When $\alpha = 0$, the eigenvalues cannot be calculated accurately due to ill-conditioning of the matrices. The calculation at this particular streamwise wavenumber has little effect on the analysis. We will come back to this point in the next chapter.

It is expected that by setting $h = 0$, the eigenvalues of the linearised plane Poiseuille flow between two flat walls can be recovered and the results should agree with those calculated by the classical methods. The numerical solution of the steady state velocity U at $h = 0$ is in good agreement with the analytical solution and the absolute error is smaller than 10^{-10}. In addition, at $h = 0$ the critical Reynolds number above which the flow loses its linear stability is $\mathrm{Re} = 5772.22$, which agrees with the value obtained by Orszag [112].

Figure 6.1 depicts the real part of the most unstable eigenvalue as a function of streamwise wavenumber α and riblet height h at $\mathrm{Re} = 6000, \beta = 1$. As can be seen, for $\alpha < 0.8$, the linear stability reduces with increasing height of riblets. In other words, the higher the riblets, the less stable the flow. However, as shown in Figure 6.2, a closer examination reveals that for α close to 1, increasing the height of the riblet has the effect of increasing the stability of the flow.

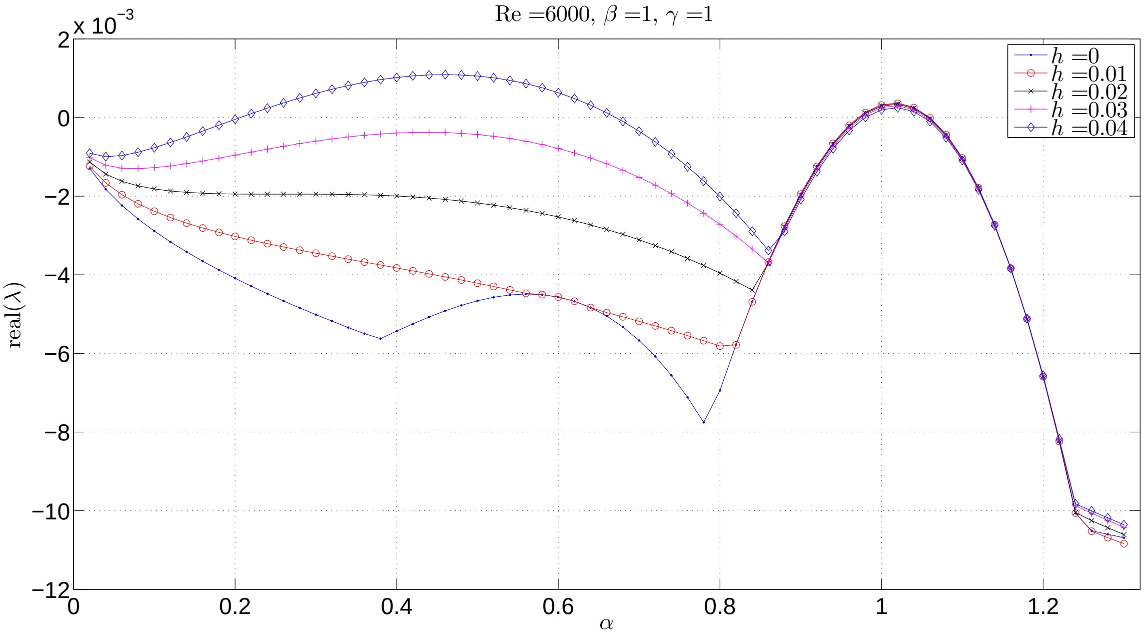

Figure 6.1: Real part of the most unstable eigenvalue for different α and h at $\mathrm{Re} = 6000, \beta = 1$. h are shown in the legend. (Sinusoidal riblets)

The critical Reynolds number at $h = 0.04, \beta = 1$ is 4012.4, which is obtained at $\alpha \approx 0.44$, suggesting that the flow is more unstable than plane Poiseuille flow. By contrast, the critical Reynolds numbers for $\beta = 1$ at $h = 0.01, h = 0.02$ and $h = 0.03$ are $5776.8, 5790.7$ and 5813.6, respectively. As in plane Poiseuille flow, the streamwise wavenumber of the most unstable flow mode is $\alpha \approx 1.02$. Although the real part of

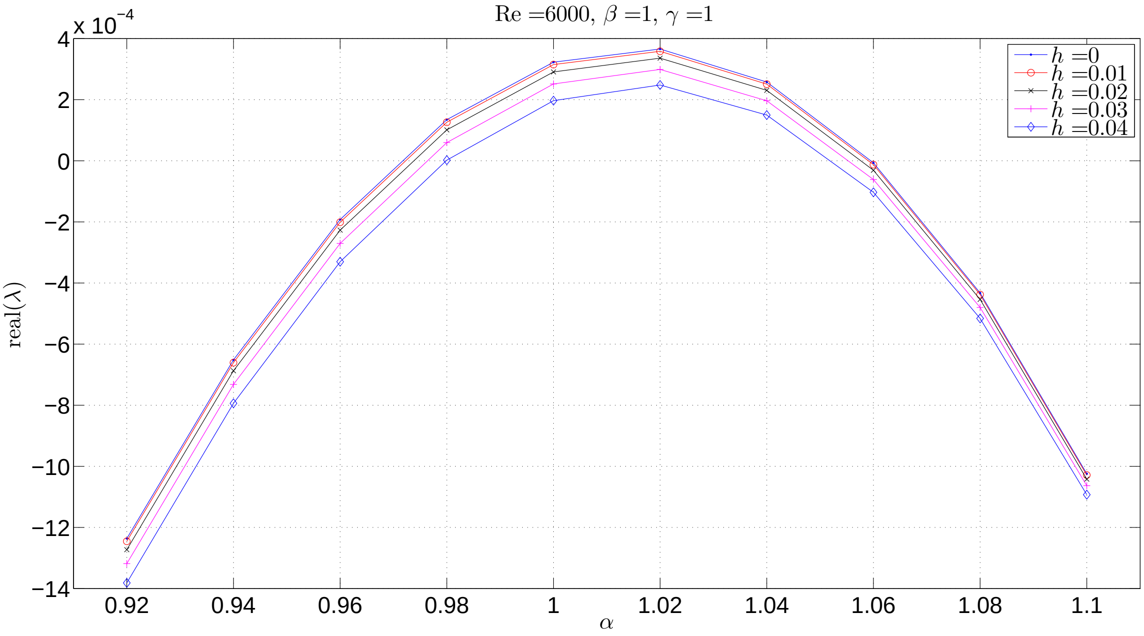

Figure 6.2: Real part of the most unstable eigenvalue for different α and h at $\text{Re} = 6000, \beta = 1$. (Amplification of Figure 6.1)

the rightmost eigenvalue is increased by the presence of riblets for most streamwise wavenumbers in these cases, it can be said that the flow is more stable due to the increase of the critical Reynolds number.

We stress that the eigenvalues are calculated using the QR algorithm. If the Arnoldi algorithm is used to calculate the 500 eigenvalues closest to zero, then the most unstable eigenvalues cannot be found. This can be seen by comparing Figure 6.1 and Figure 6.3. Although the results in the two figures match well when α is close to 1, there is considerable discrepancy for $\alpha < 0.9$, and we would not be able to reach the conclusion that the critical Reynolds number is significantly lower than 5772.22 at $h = 0.04, \beta = 1$. It should be noted that this does not mean that the eigenvalues calculated by the Arnoldi algorithm are not accurate. The problem is that the most unstable eigenvalue of the linearised flow at certain α, β and h does not always belong to the 500 eigenvalues closest to zero. The importance of appropriate shifts therefore becomes clear.

The eigenvalues are also calculated using the QR algorithm at $\text{Re} = 6000$ for $\beta \in \{2, 4, 10, 20, 50, 100\}$ and the results for $\beta = 10$ and $\beta = 50$ are illustrated in Figure 6.4 and Figure 6.5, respectively. It can be seen that in these cases, the higher the riblets, the less stable the flow. The critical Reynolds number at $h = 0.04, \beta = 50$ is 4790.4, which is obtained at $\alpha \approx 1.06$. Figure 6.6 depicts the real part of the most unstable eigenvalue at $\text{Re} = 6000, h = 0.03$ as a function of β. It shows that for a fixed riblet

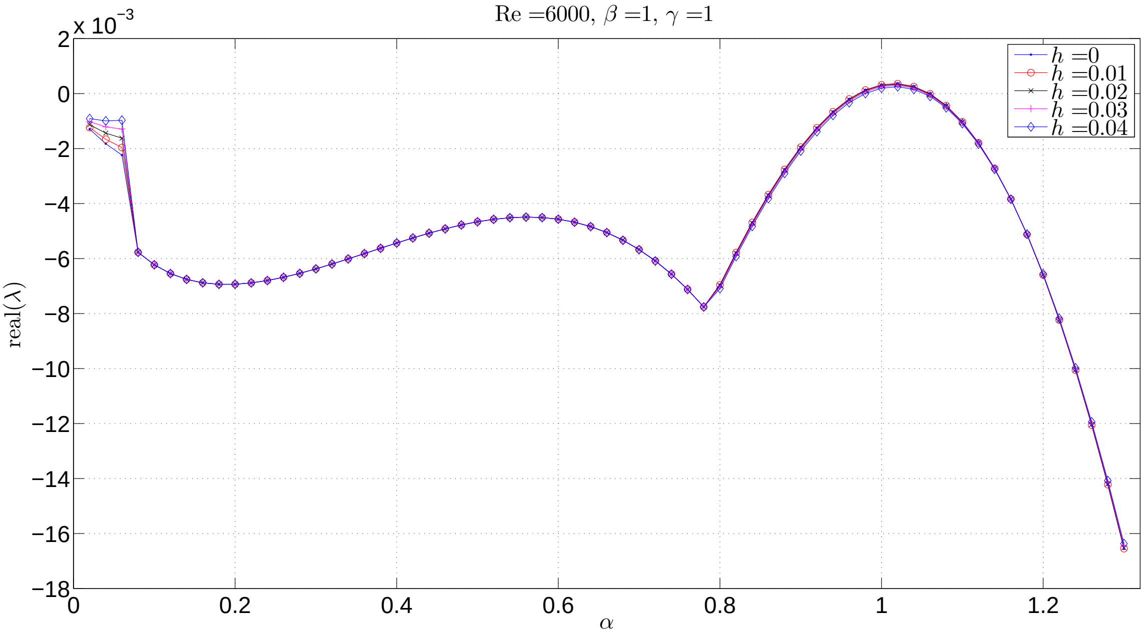

Figure 6.3: Real part of the rightmost eigenvalue for different α and h at Re $= 6000, \beta = 1$ in the 500 eigenvalues calculated by the Arnoldi algorithm with 0 as the shift. (Sinusoidal riblets)

height, reducing the spacing of the riblets has the effect of making the flow less linearly stable when $\beta \leq 50$. However, reducing the riblet spacing even further does not make the flow more unstable, as shown by the results at $\beta = 100$.

The magnitude of the eigenfunction corresponding to the most unstable eigenvalue at $\tilde{x} = 0$ with Re $= 4014, \alpha = 0.44, \beta = 1, h = 0.04$ is shown in the first row of Figure 6.7, where the second row gives the eigenfunction in the absence of riblets. ω_x, v and w are the streamwise vorticity, wall-normal velocity and spanwise velocity, respectively. ω_x and w have noticeable changes with the presence of riblets. Surprisingly, the change mainly occurs in the vicinity of $\tilde{y} = 0$ instead of the region close to the riblets. Eigenfunctions are also calculated at Re $= 6000, \alpha = 1.02, \beta = 50$ for $h = 0.04$ and $h = 0$. The result is illustrated in Figure 6.8 and the change mainly occurs on the riblet wall.

In the case that the shape function of the riblets is $f(z) = h\sin(\gamma z)$, which in essence means a shift of the origin of the coordinate system, it is expected that the same results should be obtained. This is confirmed by our numerical computation. To the best of our knowledge, there is no existing data on the linear stability of channel flow over sinusoidal riblets in the literature. It is therefore not possible to directly check the accuracy of our results by comparing them with benchmark data. The same problem in the primitive variable form is then solved using the QZ algorithm. The results calculated

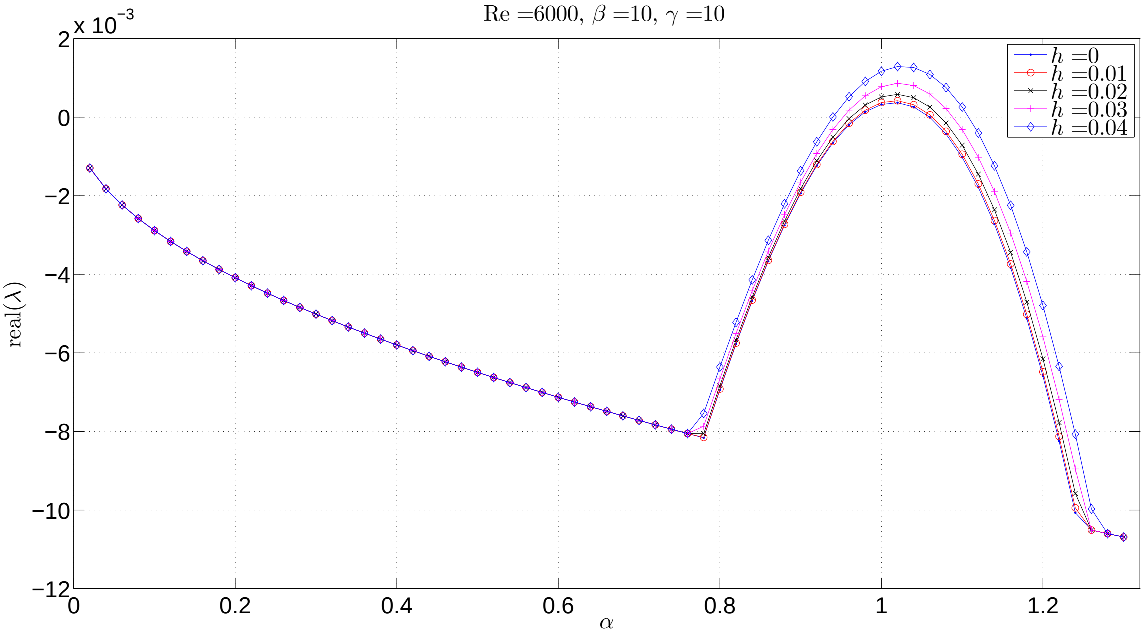

Figure 6.4: Real part of the most unstable eigenvalue for different α and h at Re $=$ $6000, \beta = 10$. (Sinusoidal riblets)

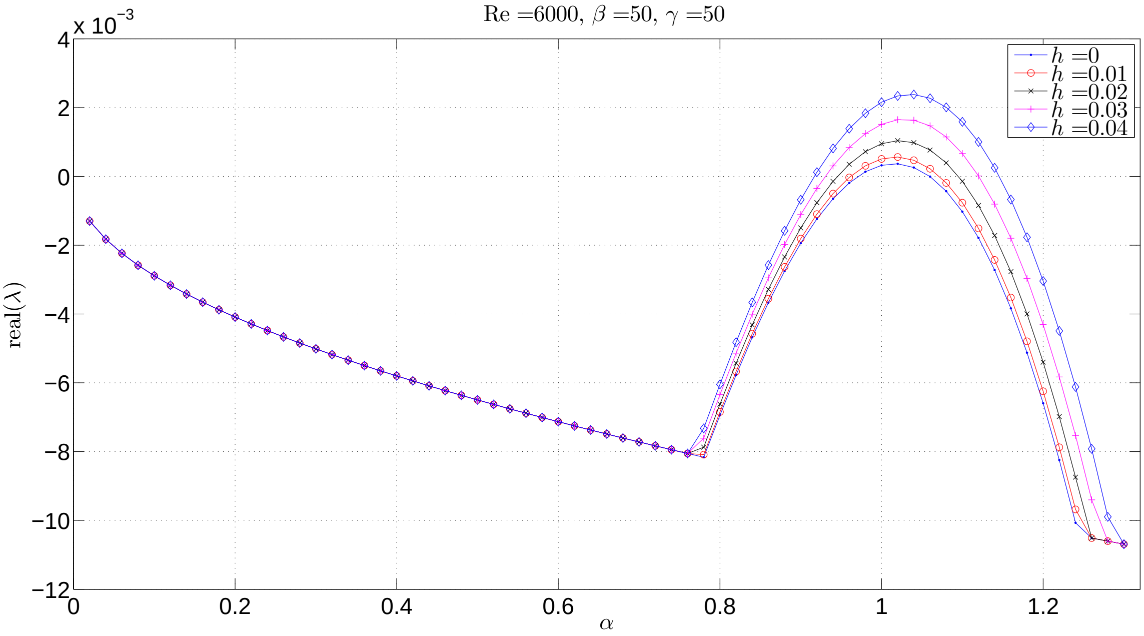

Figure 6.5: Real part of the most unstable eigenvalue for different α and h at Re $=$ $6000, \beta = 50$. (Sinusoidal riblets)

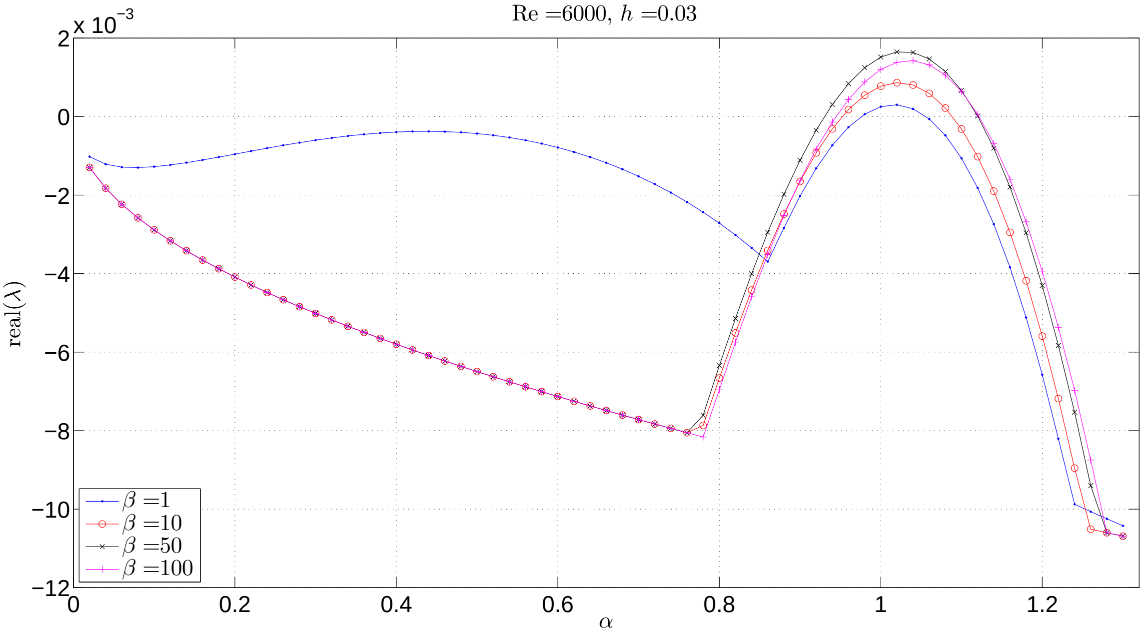

Figure 6.6: Real part of the most unstable eigenvalue for different α and β at Re $=6000, h=0.03$. β are shown in the legend. $\gamma=\beta$. (Sinusoidal riblets)

using the primitive variable form are in very good agreement with those obtained using the velocity-velocity formulation in the sense that the absolute error is typically smaller than 10^{-6}, suggesting the results reported here are accurate.

6.4.1.2 Triangular riblets

Triangular riblets are the most extensively studied riblets in the literature [37] [45] [35] [58]. While sinusoidal functions are smooth in the sense that they are infinitely differentiable, this is not the case for periodic triangular waves, which are continuous but not differentiable. The fact that the shape function $f(z)$ of triangular riblets is not differentiable causes a difficulty when the original, irregular domain is converted to a regular one through a change of coordinates. Second derivatives of $f(z)$ have to be calculated in the primitive variable form, while fourth derivatives are needed in the velocity-velocity form. Since the derivatives can be computed numerically, this difficulty is not as severe as it seems. The cost is that much higher discretisation resolution may be needed to achieve convergent numerical results. As stated before, the spatial domain itself sometimes needs to be approximated. Here the shape function of triangular riblets is approximated by the following Fourier series

$$f(z)=\frac{8h}{\pi^2}\sum_{k=0}^{k=10}(-1)^k\frac{\sin((2k+1)\gamma z)}{(2k+1)^2} \tag{6.32}$$

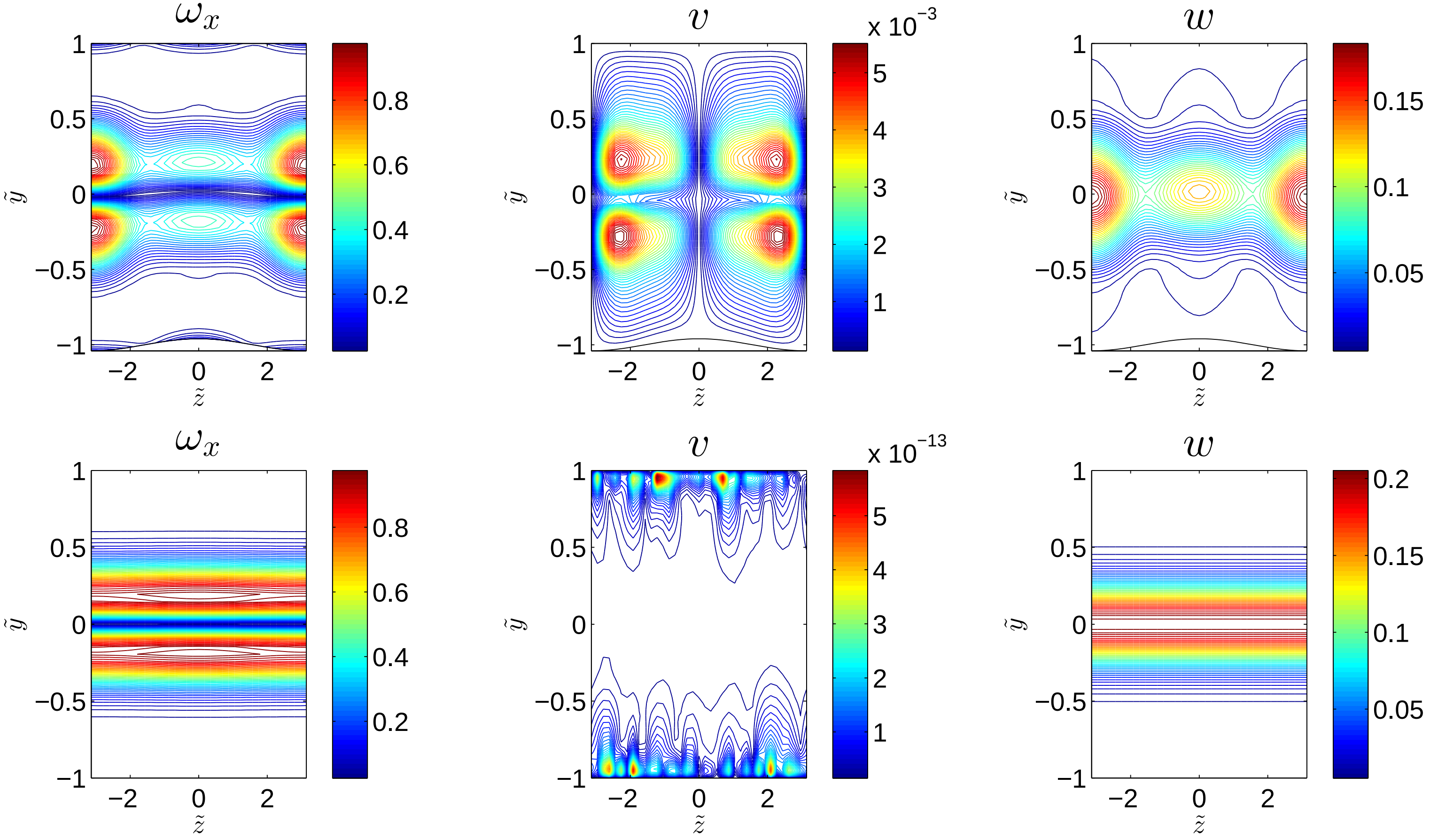

Figure 6.7: Eigenfunction corresponding to the most unstable eigenvalue at $\mathrm{Re} = 4014, \alpha = 0.44, \beta = 1$. First row: $h = 0.04$; second row: $h = 0$. (Sinusoidal riblets)

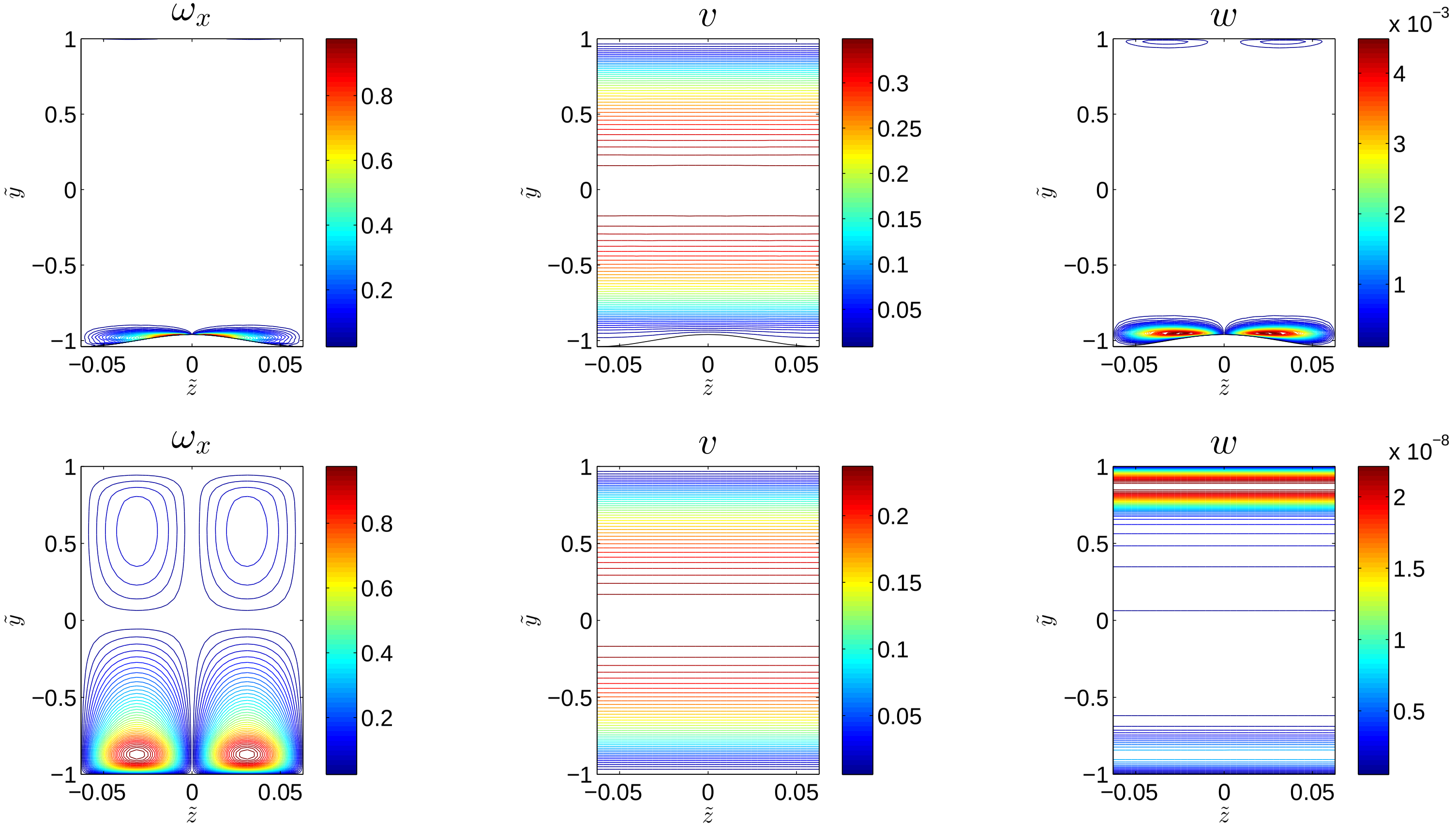

Figure 6.8: Eigenfunction corresponding to the most unstable eigenvalue at $\mathrm{Re} = 6000, \alpha = 1.02, \beta = 50$. First row: $h = 0.04$; second row: $h = 0$. (Sinusoidal riblets)

and the function at $h = 0.04, \gamma = 1$ is illustrated in Figure 6.9. As can be seen, $f(z)$ defined by (6.32) closely approximates a periodic triangular function.

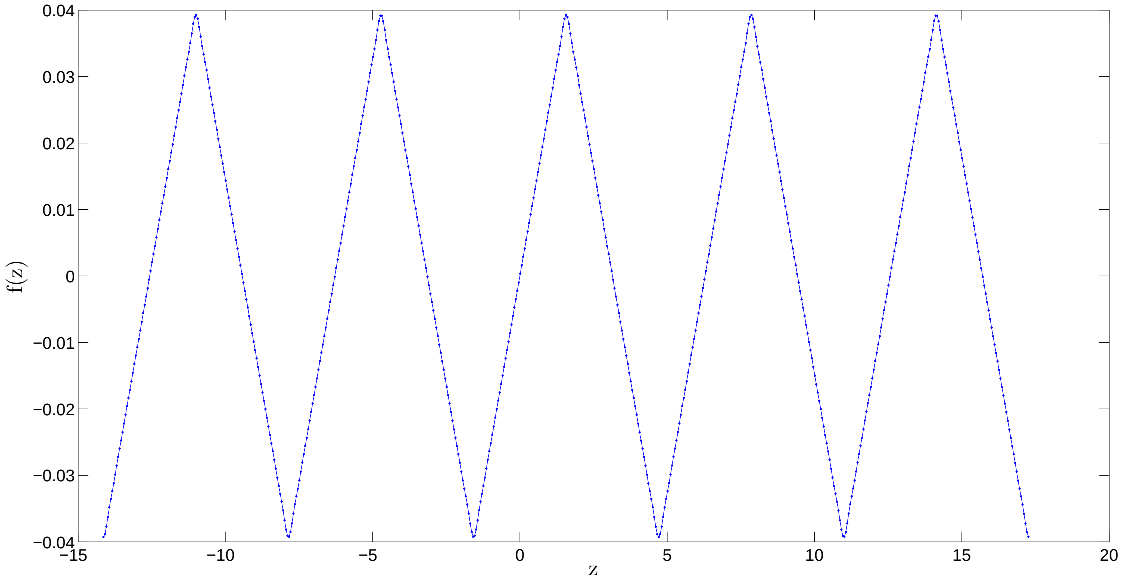

Figure 6.9: Triangular riblets approximated by Fourier series

Because finer resolution has to be used in the discretisation in order to accommodate the lack of smoothness, the matrices generated by numerical differentiation are larger than those in the case of sinusoidal riblets. As a consequence, it is no longer practical to calculate all the eigenvalues using the QR/QZ algorithm. The Arnoldi algorithm is then the only remaining option. We now discuss how to choose the shifts.

We have shown that computing the 500 eigenvalues closest to zero is sometimes not enough to find the most unstable eigenvalue. Nevertheless, zero is still a shift we should consider. To calculate the most unstable eigenvalue problem using the Arnoldi algorithm, more than one shift is usually needed in order to reduce the chance of missing the eigenvalue we are looking for. Another possible shift is the rightmost eigenvalue of the flow in the absence of riblets. This is to say that we consider the flow over triangular riblets as a slight perturbation of the flow over flat plates. The rightmost eigenvalue calculated in the case of sinusoidal riblets is a third reasonably good shift to compute the most unstable eigenvalue when the riblets are triangular. Similarly, this amounts to regarding the flow over triangular riblets as a slight perturbation of the flow over sinusoidal riblets. The most unstable eigenvalues in these two scenarios are not expected to be the same, but they should not be far away in the complex plane.

The computation is carried out in the following way. First of all, for each given shift, 500 eigenvalues closest to it are calculated. All these eigenvalues are stacked and then sorted in descending order in terms of their real parts. The first element of the resulting vector is the one we are seeking.

In the presence of triangular riblets whose shape function is given by (6.32), the real part of the most unstable eigenvalue as a function of α and h at $\mathrm{Re} = 6000, \beta = 1$ is plotted in Figure 6.10, which is similar to Figure 6.1. The key difference is that at $h = 0.04$, the streamwise wavenumber of the most unstable flow mode is now $\alpha \approx 1.02$ instead of $\alpha \approx 0.46$. As shown in Figure 6.11, for α close to 1, the higher the riblet, the more linearly stable the flow. Therefore the critical Reynolds number of channel flow over triangular riblets at $\beta = 1$ is higher than 5772.22.

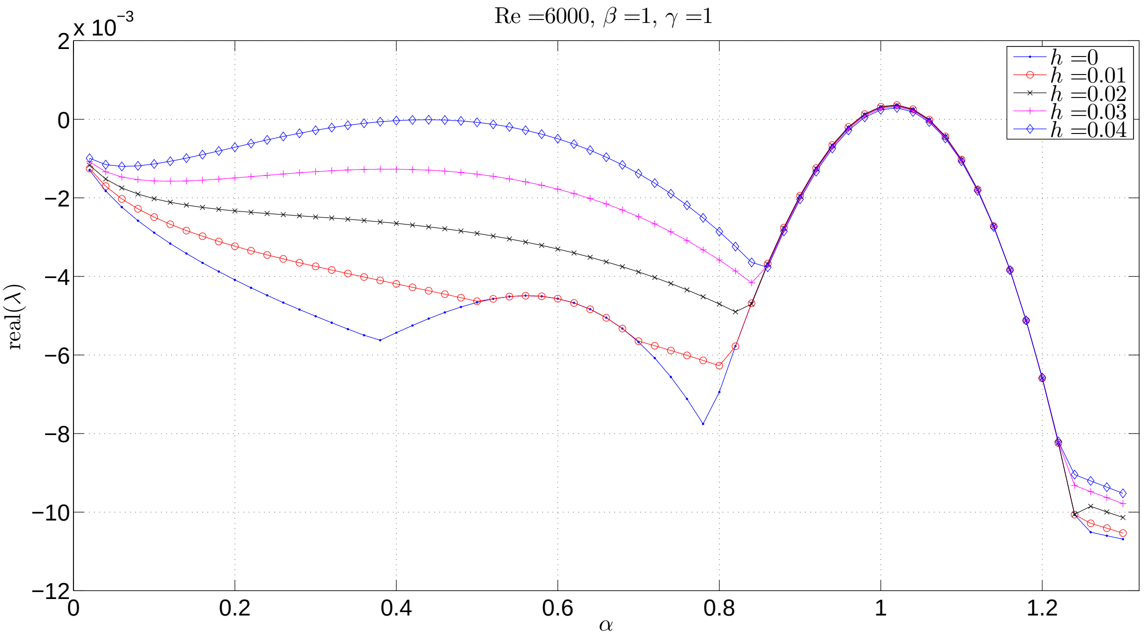

Figure 6.10: Real part of the most unstable eigenvalue for different α and h at $\mathrm{Re} = 6000, \beta = 1$. (Triangular riblets)

The effects of triangular riblets at $\mathrm{Re} = 6000, \beta = 50$ are similar to those of sinusoidal riblets under the same condition, as can be seen from Figure 6.12. Increasing the height of the riblets has the effects of making the flow more linearly unstable. This is also true when $\beta = 10$ or $\beta = 100$. The real part of the rightmost eigenvalue as a function of α and β is plotted in Figure 6.13. Once again, we arrive at the conclusion that the smaller the riblet spacing, the less stable the flow.

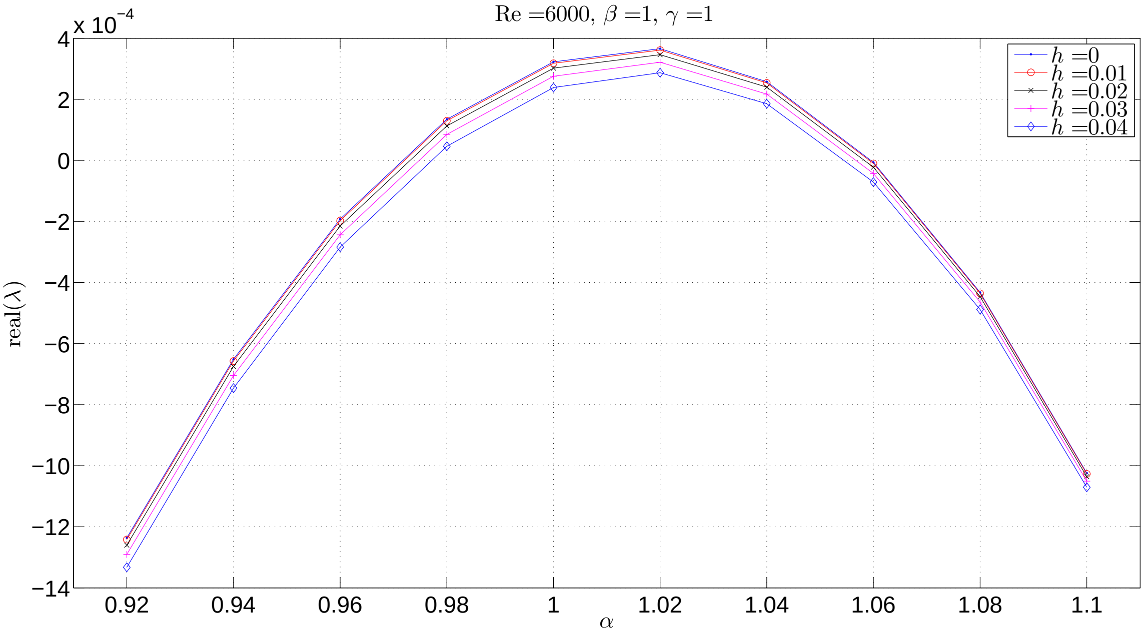

Figure 6.11: Real part of the most unstable eigenvalue for different α and h at Re = 6000, $\beta = 1$. (Amplification of Figure 6.10)

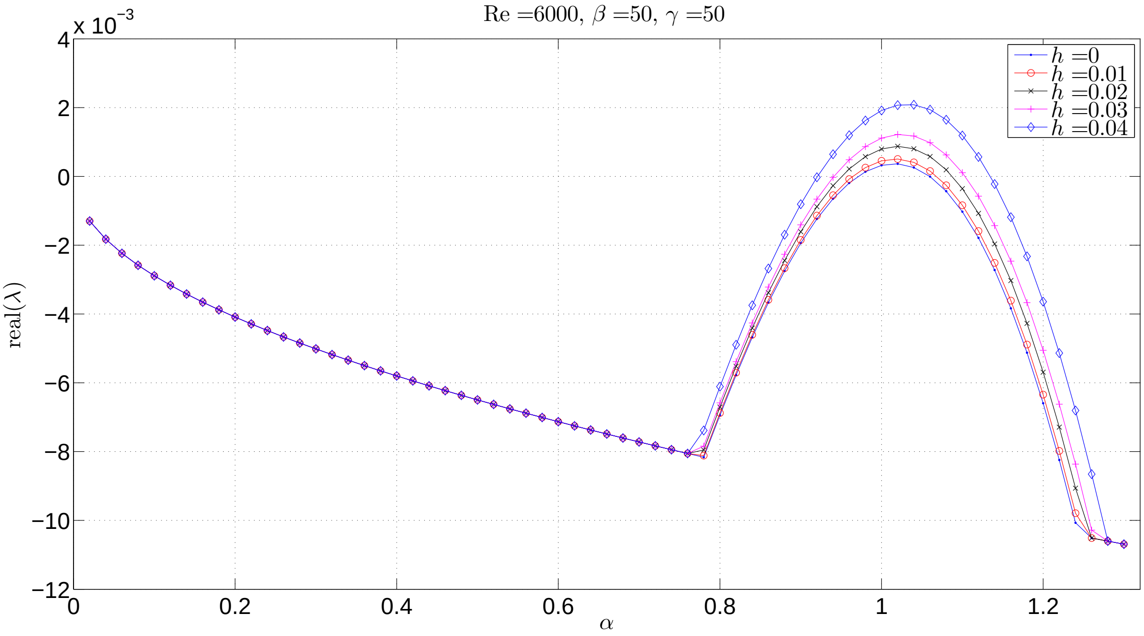

Figure 6.12: Real part of the most unstable eigenvalue for different α and h at Re = 6000, $\beta = 50$. (Triangular riblets)

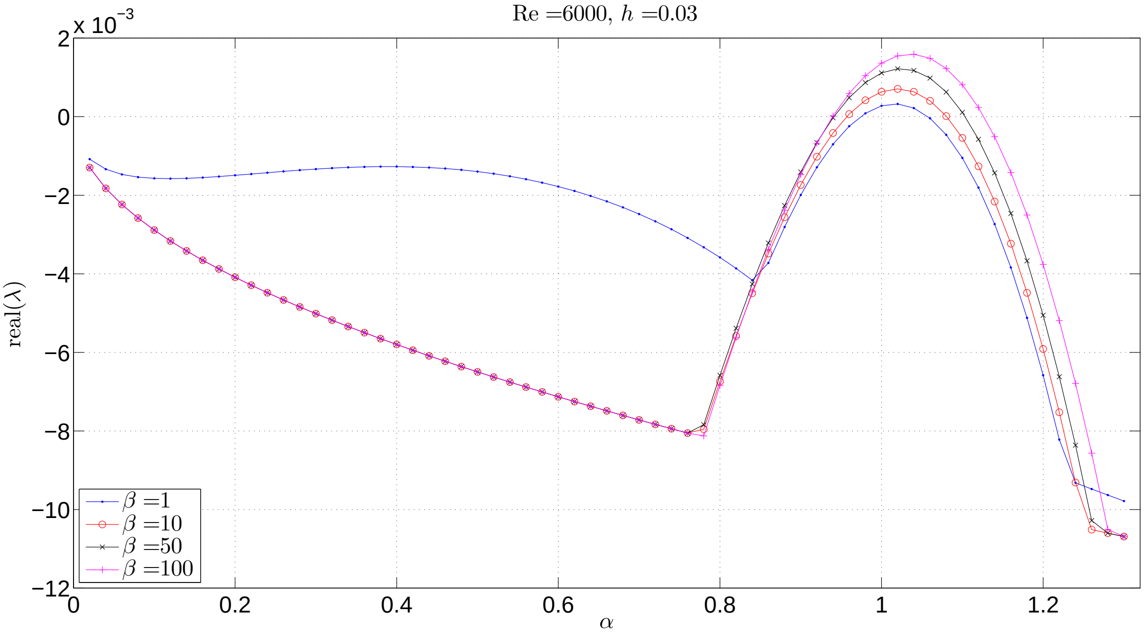

Figure 6.13: Real part of the most unstable eigenvalue for different α and β at Re $=$ $6000, h = 0.03$. $\gamma = \beta$. (Triangular riblets)

6.4.1.3 Semi-circular riblets

We now study the effects of semi-circular riblets whose shape function is given by

$$f(z) = h - \frac{4h}{\pi} + \frac{8h}{\pi}\sum_{k=1}^{k=15}(-1)^{(k)}\frac{\cos(k\gamma z)}{4k^2-1} \tag{6.33}$$

The riblet shape at $h = 0.04, \gamma = 1$ is plotted in Figure 6.14.

The same shifts as in the study of triangular riblets are chosen to calculate the eigenvalues using the Arnoldi algorithm. The analysis and calculation are very similar except that the shape function is changed. The real part of the rightmost eigenvalue as a function of α and h at Re $= 6000, \beta = 1$ is plotted in Figure 6.15. The most unstable eigenvalue for $h = 0.04$ is obtained at $\alpha \approx 1$, as opposed to $\alpha \approx 0.46$ in the case of sinusoidal riblets and $\alpha \approx 1.02$ in the case of triangular riblets. A more important difference is that when $h \leq 0.03$, increasing the riblet height has the effects of reducing the linear stability of the flow. In the case of $h = 0.04$, the flow is more linearly stable than that at $h = 0.03$, but still more unstable than the flow at $h \leq 0.02$.

A similar trend is observed at Re $= 6000, \beta = 50$ from Figure 6.17. The flow becomes more unstable when the height of the riblets is increasing from $h = 0$ to $h = 0.03$. At $h = 0.04$, the real part of the rightmost eigenvalue is decreased compared to that at

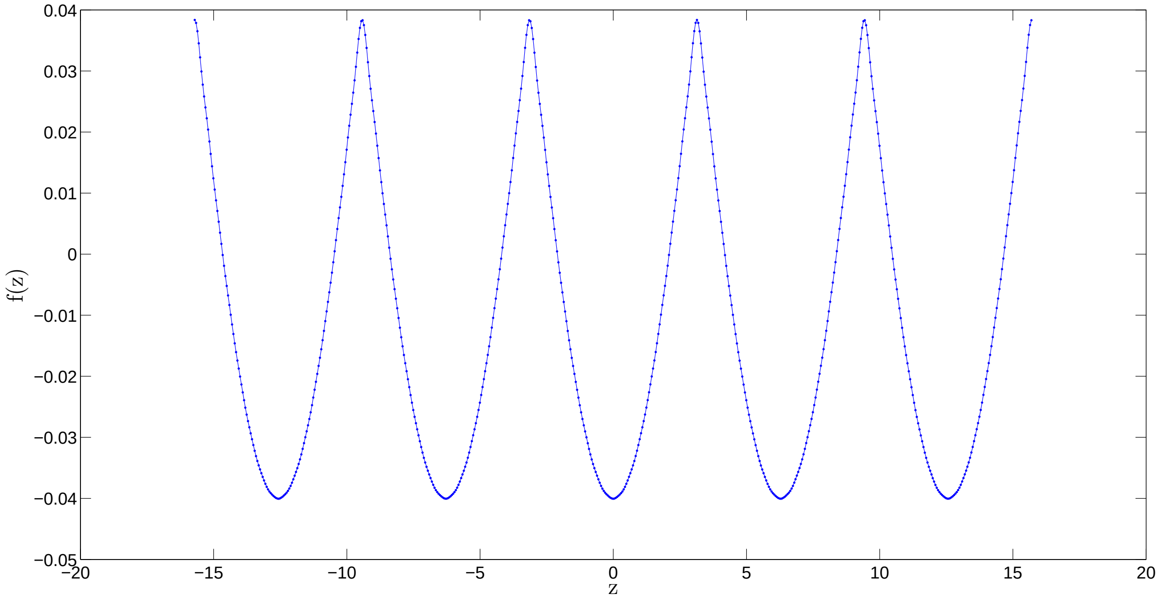

Figure 6.14: Semi-circular riblets approximated by Fourier series

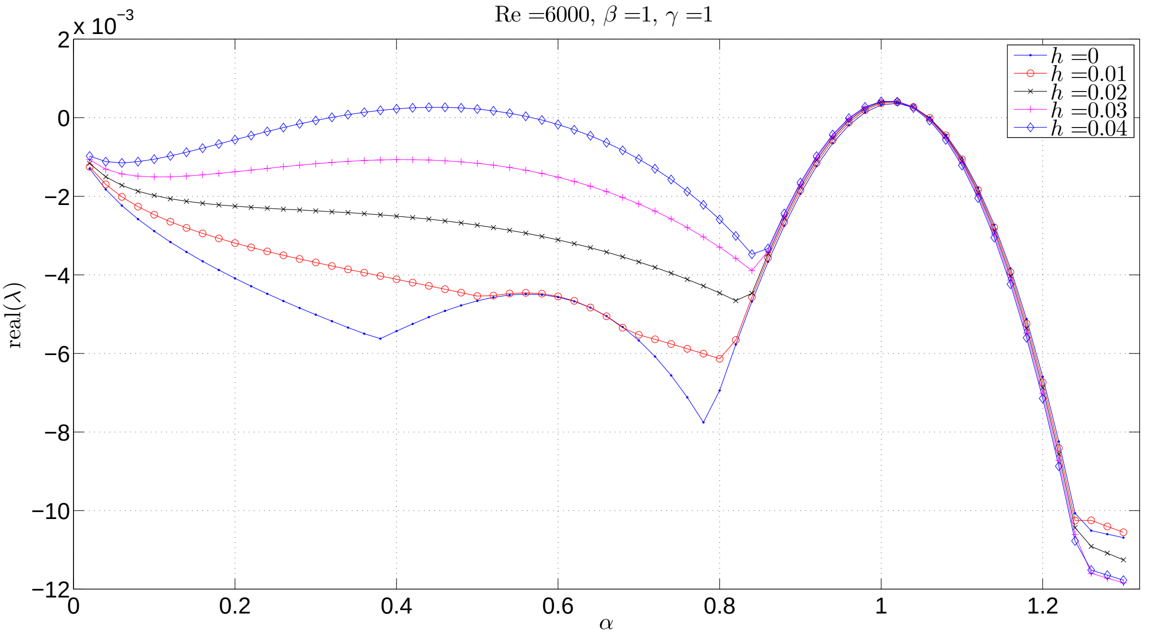

Figure 6.15: Real part of the most unstable eigenvalue for different α and h at $\mathrm{Re} = 6000, \beta = 1$. (Semi-circular riblets)

$h = 0.03$. Nevertheless, the flow is still more unstable in the presence of semi-circular riblets, regardless of the riblet height.

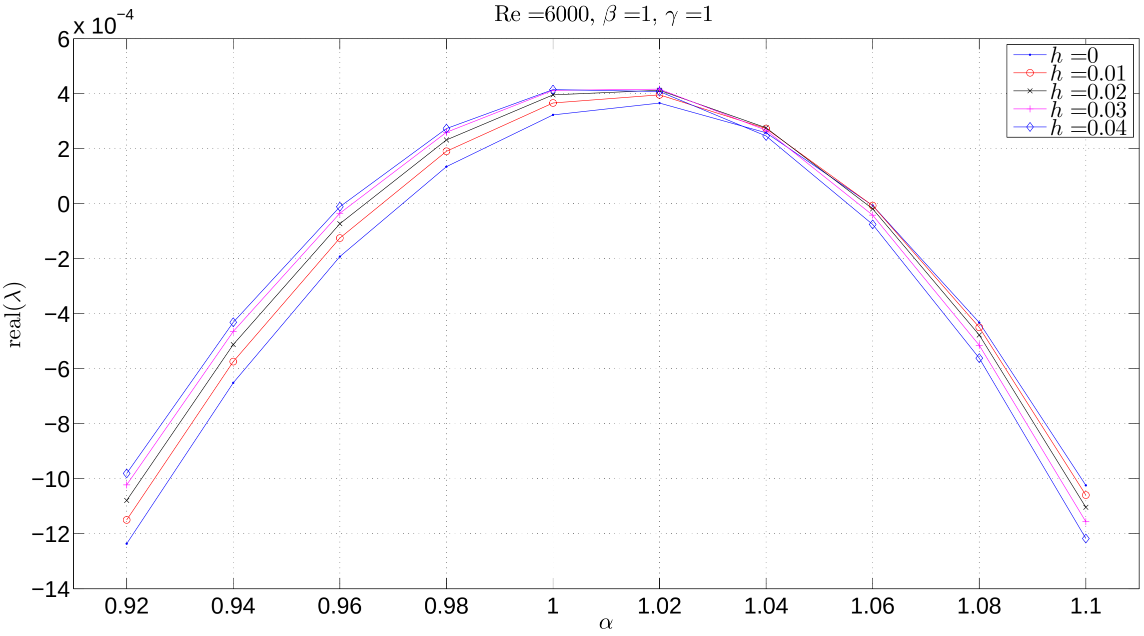

Figure 6.16: Real part of the most unstable eigenvalue for different α and h at Re $= 6000, \beta = 1$. (Amplification of Figure 6.15)

Figure 6.18 shows how the linear stability changes with the riblet spacing. The real part of the most unstable eigenvalue increases with β in the cases of $\beta = \{1, 10, 50\}$. However, when $\beta = 100$, the flow is more linearly stable compared to that at $\beta = 50$.

6.4.2 Assumption 2: $\zeta > 1$

A more general assumption is that the period of the velocity field is an exact multiple of that of the riblets, which means that $\zeta = \gamma/\beta$ is a whole number. It is clear that $\zeta = 1$ is merely a special case of this assumption. For a fixed β, ζ stands for the number of riblets fitted in $[0, 2\pi/\beta]$, which is one period of the velocity field. Therefore larger ζ means more riblets are present in $[0, 2\pi/\beta]$, which amounts to smaller riblet spacing. Even when the Reynolds number is fixed, there are an infinite number of different combinations of α, β, γ, h and it is impossible to exhaust all these combinations. In this section, we investigate how the linear stability is influenced by sinusoidal, triangular and semi-circular riblets for a fixed $\beta = 1$.

The computational load under the assumption $\zeta > 1$ is much higher since the size of the matrices generated by numerical discretisation of the governing equations is proportional to ζ. Large ζ places more severe requirements for the storage of the matrices and

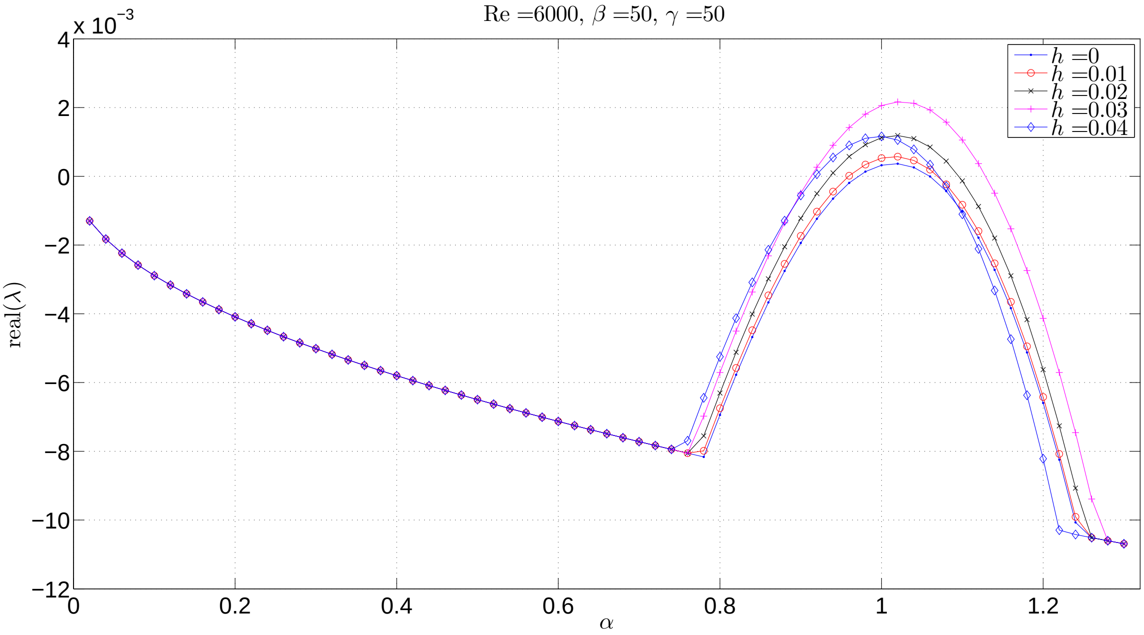

Figure 6.17: Real part of the most unstable eigenvalue for different α and h at Re = 6000, $\beta = 50$. (Semi-circular riblets)

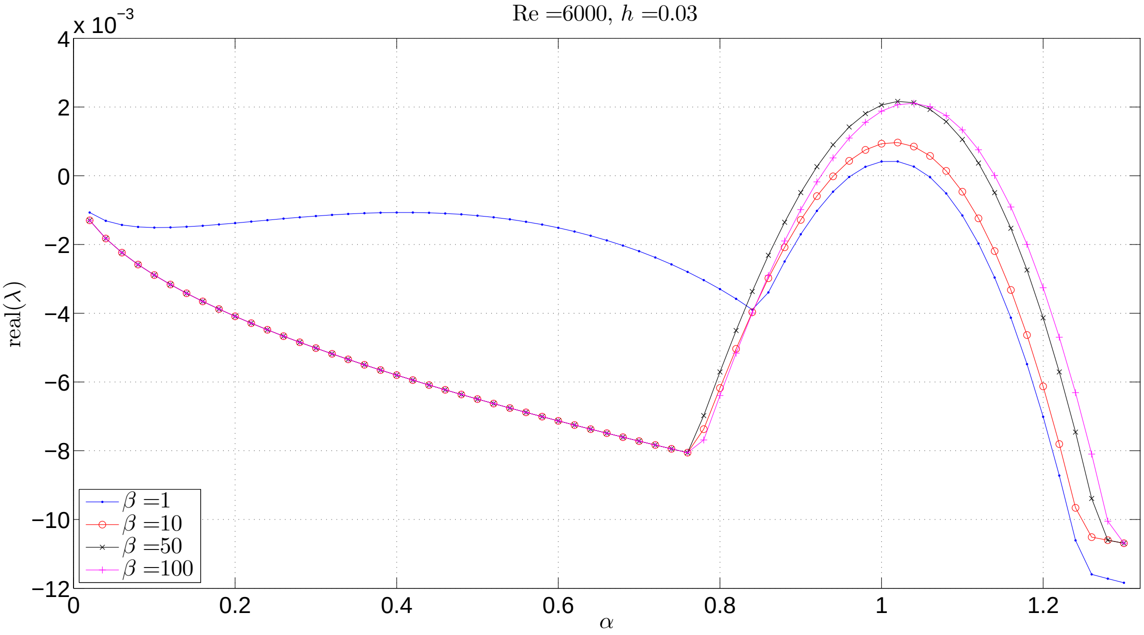

Figure 6.18: Real part of the most unstable eigenvalue for different α and β at Re = 6000, $h = 0.03$. $\gamma = \beta$. (Semi-circular riblets)

the calculations of the riblets, but by using the block diagonal structure of the matrices, the difficulty can be partially resolved. However, we are still unable to carry out the computation when $\zeta = 50$ because of memory shortage.

As mentioned in Chapter 5, numerical computation confirms that the base flow U is independent of the assumptions on ζ. Therefore the calculation of the steady state flow remains the same.

6.4.2.1 Sinusoidal riblets

We now consider the effects of riblets whose shape function is given by (6.31) under the assumption that $\zeta > 1$. The real part of the most unstable eigenvalue at $\mathrm{Re} = 6000, \beta = 1, \gamma = 10$ is plotted against α and h in Figure 6.19. It is clear that increasing the riblet height makes the flow more unstable. This is a result of the change taking place at α close to 1. For $0.4 < \alpha < 0.8$, it is observed the real part of the rightmost eigenvalue is decreasing with h. This is different from what is shown in Figure 6.4. In these two figures, the effects of riblets with the same height and spacing are not the same due to different assumptions on ζ. Nevertheless, the overall effect of riblets under both assumptions is that the flow is more unstable than that over flat plates.

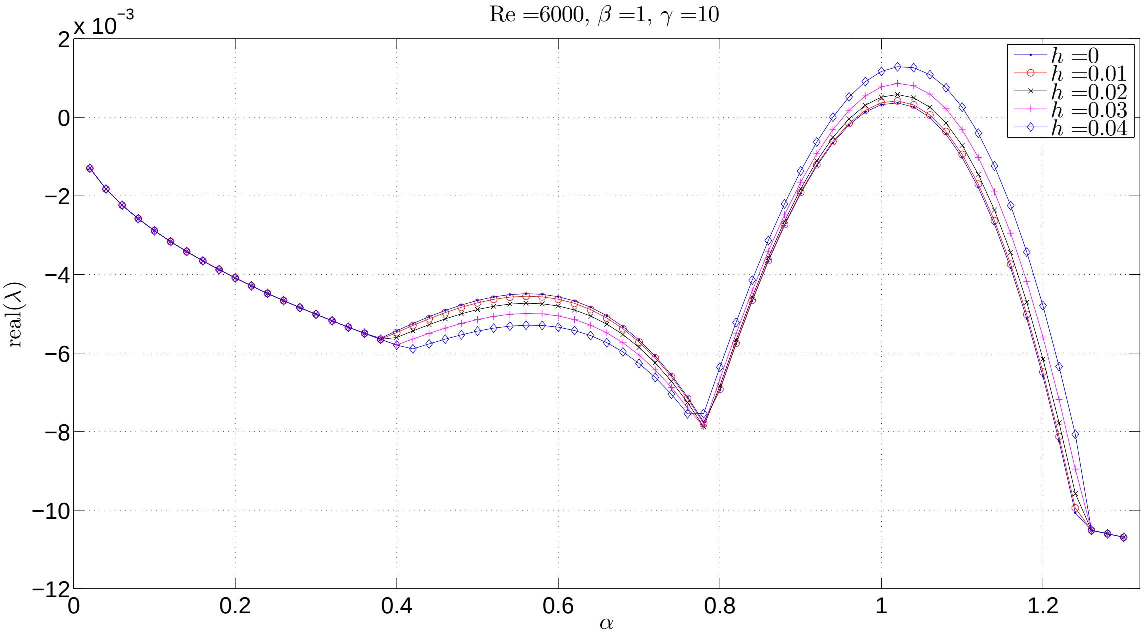

Figure 6.19: Real part of the most unstable eigenvalue for different α and h at $\mathrm{Re} = 6000, \beta = 1, \gamma = 10$. (Sinusoidal riblets)

How the linear stability changes with γ is depicted in Figure 6.20. For the cases considered, fitting more riblets in $[0, 2\pi]$ makes the flow more linearly unstable.

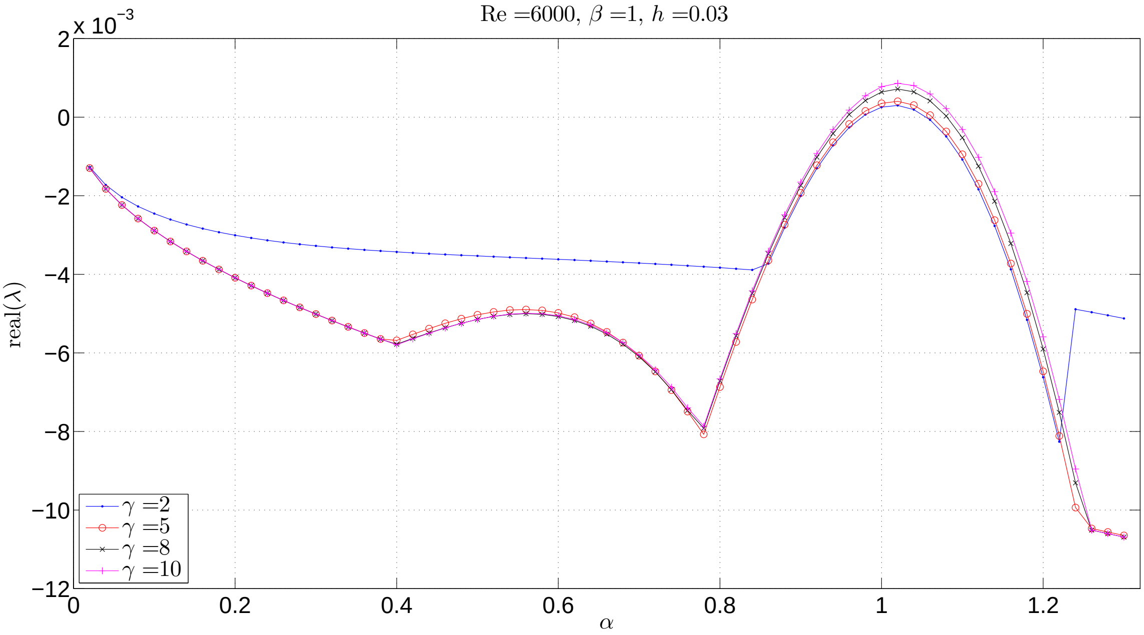

Figure 6.20: Real part of the most unstable eigenvalue for different α and γ at Re $=$ $6000, \beta = 1, h = 0.03$. γ are shown in the legend. (Sinusoidal riblets)

6.4.2.2 Triangular riblets

The shape of the triangular riblets under consideration is defined by (6.32). Due to the roughness of the riblets, higher discretisation resolution is needed. This together with the fact that the size of the matrices is proportional to ζ makes the computational load even higher. It takes more than 1000 CPU hours to calculate the data that generate Figure 6.21 and Figure 6.22. As can be seen, triangular riblets have similar effects to sinusoidal ones.

6.4.2.3 Semi-circular riblets

The effects of semi-circular riblets described by (6.33) under the assumption that $\zeta > 1$ are also studied. As can be seen, the resemblance between Figure 6.23 and Figure 6.19 is striking, although the changes of the eigenvalues brought by semi-circular riblets and sinusoidal riblets are not identical. In addition, Figure 6.24 is also very similar to Figure 6.20. These results show that effects of semi-circular and sinusoidal riblets on the linear stability of channel flow are comparable, despite that sinusoidal ones are smoother.

6.4.2.4 Comparison

In Figure 6.25, a comparison of the effects of the three types of riblets on the linear stability of channel flow at Re $= 6000, h = 0.04, \beta = 1, \gamma = 10$ is made. It is shown

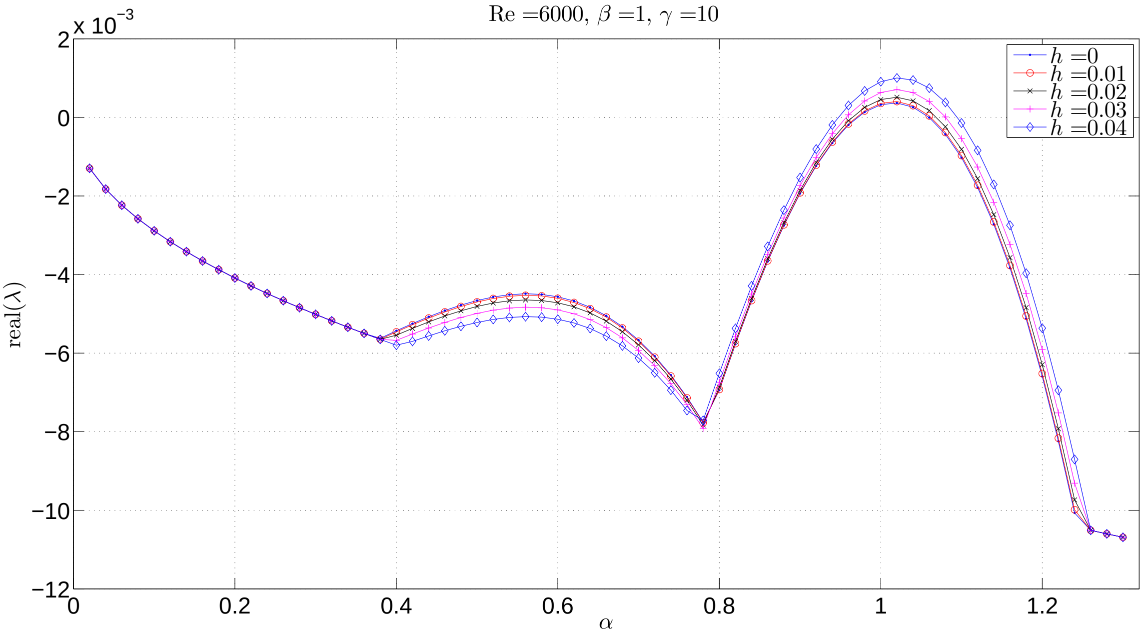

Figure 6.21: Real part of the most unstable eigenvalue for different α and h at Re = 6000, $\beta = 1, \gamma = 10$. (Triangular riblets)

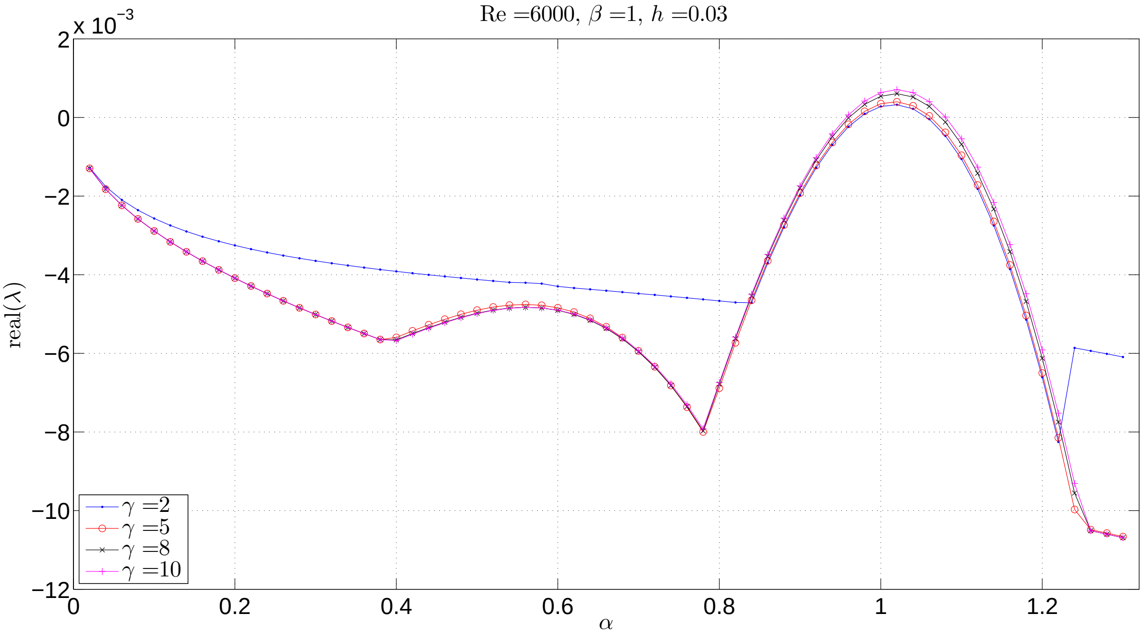

Figure 6.22: Real part of the most unstable eigenvalue for different α and γ at Re = 6000, $\beta = 1, h = 0.03$. (Triangular riblets)

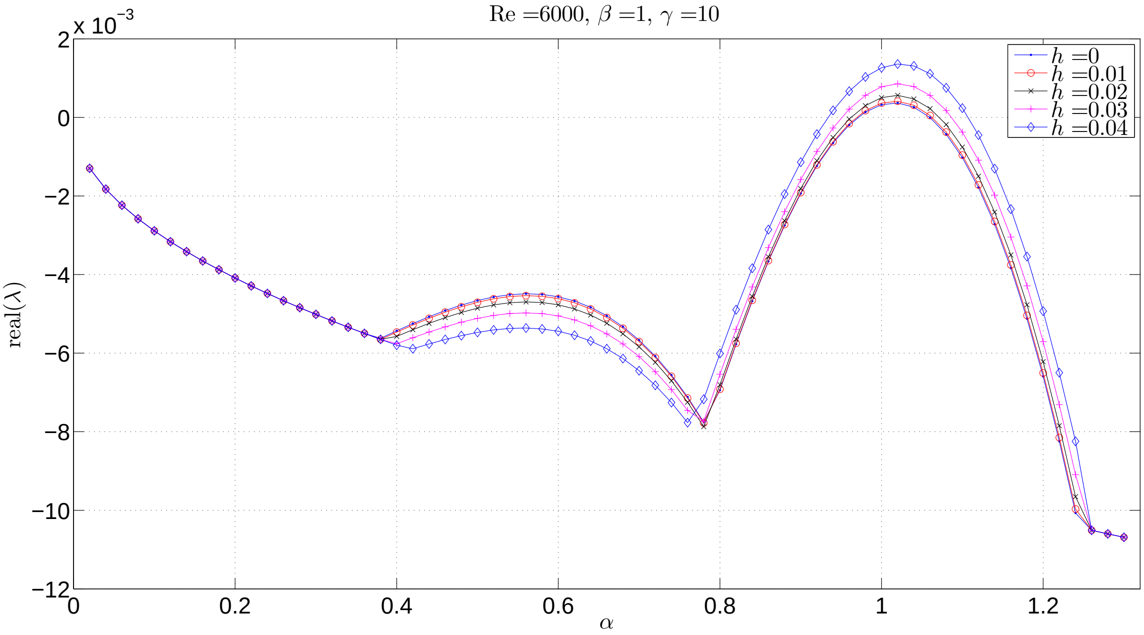

Figure 6.23: Real part of the most unstable eigenvalue for different α and h at Re = 6000, $\beta = 1, \gamma = 10$. (Semi-circular riblets)

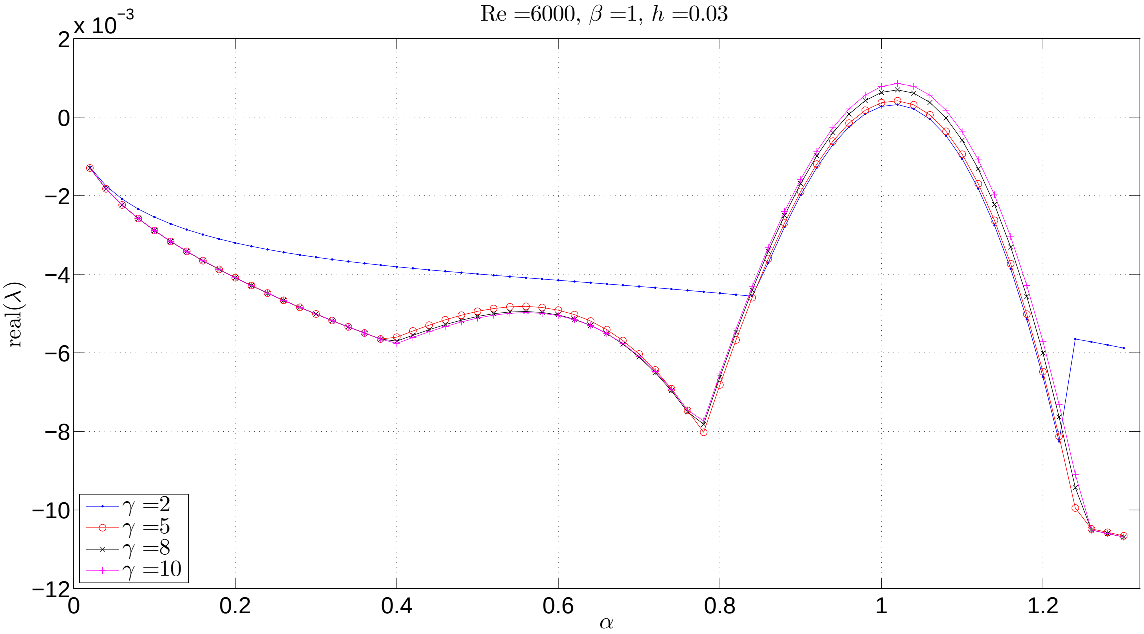

Figure 6.24: Real part of the most unstable eigenvalue for different α and γ at Re = 6000, $\beta = 1, h = 0.03$. (Semi-circular riblets)

that the instability is increased the least by triangular ones, this might to some extent explain the popularity of this kind of riblets.

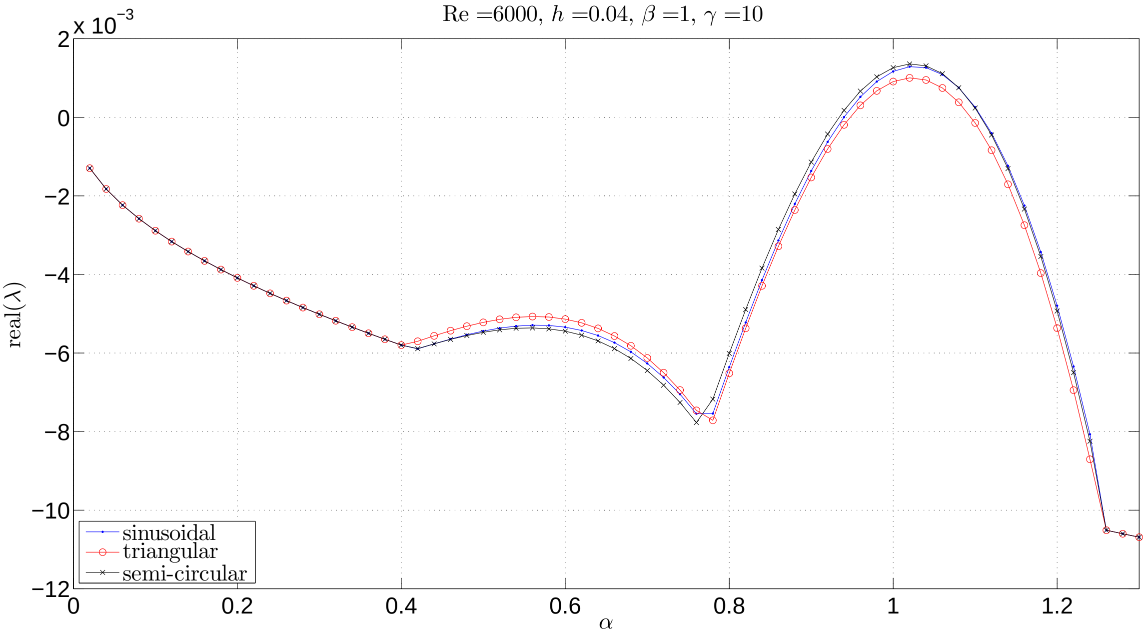

Figure 6.25: Real part of the most unstable eigenvalue for different α and riblets at $\mathrm{Re} = 6000, \beta = 1, \gamma = 10, h = 0.04$.

6.5 Conclusion

In this chapter we have conducted a systematic study of the effects of riblets on the linear stability of channel flow. Three types of riblets, namely sinusoidal, triangular and semi-circular ones, are considered. The NSEs in the velocity-velocity form are used in the study and the results are confirmed by the calculation using the primitive variable form. Boundary conditions are derived directly from the no-slip conditions on the solid walls and periodic conditions in the spanwise directions, without making additional assumptions. In addition to the assumption that the flow has the same period as the riblets, we also study the effects of riblets under the more general assumption that the period of the flow is an exact multiple of the riblet period.

Numerical computations show that the effects on the linear stability of the flow vary with the shape, height and spacing of the riblets. Under most circumstances the flow is made more unstable by the presence of riblets. The stability of the flow usually decreases when the riblet height is increased or when the riblet spacing is decreased.

Chapter 7

Effects of Riblets on Energy Amplification

7.1 Introduction

Although it is shown in the last chapter that in practice, the linear stability of channel flow is likely to be decreased by the inclusion of riblets on the lower plate, the investigation of the effects of riblets on the stability of channel flow is not yet conclusive, especially considering that linear instability, which is characterised by Tollmien-Schlichting waves, is an unlikely path to transition. As stated in Chapter 3, transient growth has been recognised as one explanation for the subcritical transition in plane Poiseuille flow. Furthermore, amplification of the energy of background noise can also possibly lead to the onset of transition [83]. It is shown that the energy amplification factor can be as high as $\mathcal{O}(\mathrm{Re}^3)$ when the noise is modelled by stochastic forcing [11]. For simplicity, we use the term "energy amplification" to refer to both the amplification of the kinetic energy of perturbation and the growth of background noise. It is recognised that energy amplification is the mechanism responsible for the creation of streamwise vortices and streaks [83], which are a path to transition.

This chapter considers the effects of riblets on energy amplification in channel flow. If the presence of the riblets suppresses the amplification of the disturbance and/or the background noise, the transition from laminar flow to turbulent flow could be delayed. By contrast, the subcritical transition may be triggered by the inclusion of riblets if the energy amplification in the flow is increased.

The calculation of energy amplification is more demanding in terms of memory storage and CPU time than calculating the linear stability. The linear stability can be determined when the most unstable eigenvalue is found, although in practice it is not possible to calculate only one eigenvalue, as discussed in Chapter 5. By contrast, in order to calculate the energy amplification, a large number of the eigenvalues and eigenvectors have to be computed. SVD also needs to be carried out in the process. Moreover, to determine the largest possible energy amplification factor, transient growth has to be calculated at a series of time instants. As a result, it is not possible to calculate the energy amplification in the flow over riblets as comprehensively as the study of linear stability in the last chapter. We instead restrict our attention to streamwise-constant channel flow, which is the flow with the streamwise wavenumber $\alpha = 0$. This choice is justified by the fact that the largest possible transient growth of the perturbation energy and amplification of the background noise in plane Poiseuille flow both occur at streamwise-constant flow modes [134]. Once again, sinusoidal, triangular and semi-circular riblets are investigated in the study.

7.2 Energy amplification and $\mathcal{H}_2$ norm

In this section, we give a brief review of the $\mathcal{H}_2$ norm, which can be used to quantify the energy amplification of stochastic noise in a system. The details can be found in many standard textbooks on robust control, for example, [169] [65]. Consider a finite-dimensional, stable system with a state space representation

$$\begin{aligned} \dot{x} &= Ax + Bu && (7.1)\\ y &= Cx && (7.2) \end{aligned}$$

where for simplicity, all the matrices and vectors are assumed to be real-valued. The transfer function of the system is

$$G(s) = C(sI - A)^{-1}B \tag{7.3}$$

Denoting each entry of $G(s)$ as $G_{i,j}(s)$, then the $\mathcal{H}_2$ norm is defined by

$$\|G\|_2 = \left(\frac{1}{2\pi} \int_{-\infty}^{\infty} \sum_{i,j} |G_{i,j}(j\omega)|^2 \mathrm{d}\omega \right)^{\frac{1}{2}} \tag{7.4}$$

By using the identities of matrix trace, we have

$$\|G\|_2 = \left(\frac{1}{2\pi} \int_{-\infty}^{\infty} \mathtt{trace}[G^T(-j\omega)G(j\omega)] \mathrm{d}\omega \right)^{\frac{1}{2}} \tag{7.5}$$

In the time domain, the following relationship is obtained using Parseval's theorem

$$\|G\|_2^2 = \mathtt{trace} \left(C \left[\int_0^{\infty} \mathrm{e}^{At} BB^T \mathrm{e}^{A^T t} \mathrm{d}t \right] C^T \right) \tag{7.6}$$

For notational convenience, denote

$$\Omega = \int_0^\infty \mathrm{e}^{At} B B^T \mathrm{e}^{A^T t} \mathrm{d}t \tag{7.7}$$

It is a standard result that Ω is the unique solution to the Lyapunov equation [51]

$$A\Omega + \Omega A^T = -BB^T \tag{7.8}$$

which can be solved by using the algorithm given in [13]. The algorithm is implemented by the MATLAB built-in function `lyap`. We now arrive at the conclusion that the $\mathcal{H}_2$ norm of the system can be calculated by

$$\|G\|_2 = \sqrt{\texttt{trace}(C\Omega C^T)} \tag{7.9}$$

In the case that the input of the system is white noise with unit variance matrix, $\|G\|_2^2$ is the sum of the stationary variances of the outputs.

7.3 2D/3C Formulation

Choosing a suitable formulation of the linearised NSEs is an important step in using the matrix approach to compute energy amplification. As we have explained in the previous chapter, the velocity-vorticity form is not appropriate for channel flow over riblets. By contrast, the primitive variable form can be applied to almost any fluid flows. However, this generality comes at the cost that the size of the matrices obtained by discretisation is large, as we have seen in the last chapter. When the aim is to determine linear stability, the increase in the computational load resulting from the large size of matrices can sometimes be minimised by using the Arnoldi algorithm with carefully chosen shifts. This is no longer the case when the goal is to calculate the energy amplification in a flow, since the majority of the eigenvalues and eigenvectors have to be computed. The velocity-velocity formulation derived in the previous chapter avoids the problem posed by the size of the matrices. However, in the case that the streamwise wavenumber of the flow is zero, it is found that the formulation is also not applicable, due to the poor conditioning of the state matrix.

As our attention in this chapter is restricted to streamwise-constant flow, it is useful to apply this condition at the beginning of the derivation. The 2-dimensional/3-component (2D/3C) formulation then emerges as a good choice. Since the flow is streamwise-constant, we have

$$\frac{\partial u}{\partial \tilde{x}} = \frac{\partial v}{\partial \tilde{x}} = \frac{\partial w}{\partial \tilde{x}} = \frac{\partial p}{\partial \tilde{x}} = 0 \tag{7.10}$$

and as a result, the linearised NSEs (5.39) become

$$\begin{aligned}
\frac{\partial u}{\partial t} + v\frac{\partial U}{\partial \tilde{y}} + w\frac{\partial U}{\partial \tilde{z}} &= \frac{1}{\mathrm{Re}}\tilde{\Delta} u && (7.11\text{a})\\
\frac{\partial v}{\partial t} &= -\frac{\partial p}{\partial \tilde{y}} + \frac{1}{\mathrm{Re}}\tilde{\Delta} v && (7.11\text{b})\\
\frac{\partial w}{\partial t} &= -\frac{\partial p}{\partial \tilde{z}} + \frac{1}{\mathrm{Re}}\tilde{\Delta} w && (7.11\text{c})\\
\frac{\partial v}{\partial \tilde{y}} + \frac{\partial w}{\partial \tilde{z}} &= 0 && (7.11\text{d})
\end{aligned}$$

Taking $\frac{\partial}{\partial \tilde{z}}$ of (7.11b), $\frac{\partial}{\partial \tilde{y}}$ of (7.11c) and eliminating the pressure terms gives

$$\frac{\partial}{\partial t}\left(\frac{\partial v}{\partial \tilde{z}} - \frac{\partial w}{\partial \tilde{y}}\right) = \frac{1}{\mathrm{Re}}\tilde{\Delta}\left(\frac{\partial v}{\partial \tilde{z}} - \frac{\partial w}{\partial \tilde{y}}\right) \tag{7.12}$$

Since v and w are related by the continuity equation (7.11d), we can define a stream function $\psi(\tilde{y}, \tilde{z}, t)$ such that

$$\begin{aligned}
\frac{\partial \psi}{\partial \tilde{z}}(\tilde{y}, \tilde{z}, t) &= v(\tilde{y}, \tilde{z}, t) && (7.13)\\
\frac{\partial \psi}{\partial \tilde{y}}(\tilde{y}, \tilde{z}, t) &= -w(\tilde{y}, \tilde{z}, t) && (7.14)
\end{aligned}$$

and (7.12) can be rewritten as

$$\frac{\partial}{\partial t}\tilde{\Delta}\psi = \frac{1}{\mathrm{Re}}\tilde{\Delta}^2\psi \tag{7.15}$$

Equations (7.11a) and (7.13)-(7.15) can be combined to give

$$\begin{aligned}
\mathcal{B}\dot{\mathbf{x}} &= \mathcal{A}\mathbf{x} && (7.16\text{a})\\
\mathbf{y} &= \mathcal{C}\mathbf{x} && (7.16\text{b})
\end{aligned}$$

where $\mathbf{x} = \begin{bmatrix} u & \psi \end{bmatrix}^T$, $\mathbf{y} = \begin{bmatrix} u & v & w \end{bmatrix}^T$, and

$$\begin{aligned}
\mathcal{B} &= \begin{bmatrix} 1 & 0 \\ 0 & \tilde{\Delta} \end{bmatrix} && (7.17)\\
\mathcal{A} &= \begin{bmatrix} \frac{1}{\mathrm{Re}}\tilde{\Delta} & \frac{\partial U}{\partial \tilde{z}}\frac{\partial}{\partial \tilde{y}} - \frac{\partial U}{\partial \tilde{y}}\frac{\partial}{\partial \tilde{z}} \\ 0 & \frac{1}{\mathrm{Re}}\tilde{\Delta}^2 \end{bmatrix} && (7.18)\\
\mathcal{C} &= \begin{bmatrix} 1 & 0 \\ 0 & \frac{\partial}{\partial \tilde{z}} \\ 0 & -\frac{\partial}{\partial \tilde{y}} \end{bmatrix} && (7.19)
\end{aligned}$$

The kinetic energy of the perturbation is defined by

$$E = \frac{1}{2}\int_{\tilde{z}=0}^{\tilde{z}=2\pi/\beta}\int_{\tilde{y}=-1+f(\tilde{z})}^{\tilde{y}=1}\left(u^2+v^2+w^2\right)\mathrm{d}\tilde{y}\mathrm{d}\tilde{z} \tag{7.20}$$

where β is the spanwise wavenumber of the flow.

As in previous chapters, the governing equations have to be transformed after the change of coordinates (5.43) is applied. In addition, it is now also necessary to convert the perturbation energy equivalently to the new coordinate system

$$E = \frac{1}{2}\int_{z=0}^{z=2\pi/\beta}\int_{y=-1}^{y=1}\left(u^2+v^2+w^2\right)\left(\frac{1}{\frac{\partial F}{\partial \tilde{y}}}\right)\mathrm{d}y\mathrm{d}z \tag{7.21}$$

7.4 Boundary conditions

As stated in Section 5.5.2, after the change of coordinates, the no-slip boundary conditions take the form

$$u(1,z,t) = v(1,z,t) = w(1,z,t) = 0 \tag{7.22}$$

$$u(-1,z,t) = v(-1,z,t) = w(-1,z,t) = 0 \tag{7.23}$$

We now need to derive the boundary conditions for the stream function ψ.

From the boundary conditions of w, we have

$$\left.\frac{\partial \psi}{\partial \tilde{y}}\right|_{y=\pm 1} = \left.\frac{\partial F}{\partial \tilde{y}}\frac{\partial \psi}{\partial y}\right|_{y=\pm 1} = 0 \tag{7.24}$$

which means that

$$\left.\frac{\partial \psi}{\partial y}\right|_{y=\pm 1} = 0 \tag{7.25}$$

Similarly, from the boundary conditions of v,

$$\left.\frac{\partial \psi}{\partial \tilde{z}}\right|_{y=\pm 1} = \left.\left[\frac{\partial \psi}{\partial z} + \frac{\partial F}{\partial \tilde{z}}\frac{\partial \psi}{\partial y}\right]\right|_{y=\pm 1} = 0 \tag{7.26}$$

which together with (7.25) yields

$$\left.\frac{\partial \psi}{\partial z}\right|_{y=\pm 1} = 0 \tag{7.27}$$

Due to the assumption that the velocity field is periodic in the spanwise direction, this condition leads to

$$\psi|_{y=\pm 1} = 0 \tag{7.28}$$

To sum up, in the new coordinate system, both u and ψ satisfy homogeneous Dirichlet boundary conditions, while ψ also satisfies homogeneous Neumann boundary conditions.

7.5 Numerical discretisation

The discretisation of the governing equations in 2D/3C form can be implemented in the same manner as in the study of the linear stability of channel flow over riblets. The Chebyshev collocation method is used in the wall-normal direction and the Fourier Galerkin method is used in the spanwise direction. Since the boundary conditions are much simpler in the 2-dimensional case, the implementation of the Fourier Galerkin methods becomes less awkward.

Ideally the Chebyshev Galerkin method should be used rather than the Chebyshev collocation method since the purpose is to calculate energy amplification. However, the presence of riblets makes the implementation of the Chebyshev Galerkin method far more difficult. Although the collocation method is not sufficiently accurate when the Reynolds number is low, it is reasonably reliable at moderately high Reynolds number, as concluded in Chapter 3. This fact justifies our choice of numerical discretisation methods.

The assumption that the streamwise wavenumber of the perturbation velocity field is zero does not have any effects on the steady state flow. Since all the other assumptions are the same as in the previous study, the method of solving the the base flow U remains unchanged.

A finite-dimensional state space model of the linearised flow can then be expressed as

$$\mathbf{B}\dot{\hat{\mathbf{x}}} = \mathbf{A}\hat{\mathbf{x}} \tag{7.29a}$$

$$\hat{\mathbf{y}} = \mathbf{C}\hat{\mathbf{x}} \tag{7.29b}$$

where $\mathbf{B}, \mathbf{A}$ and $\mathbf{C}$ are the discretised versions of the operators $\mathcal{B}, \mathcal{A}$ and $\mathcal{C}$, respectively. $\hat{\mathbf{x}}$ and $\hat{\mathbf{y}}$ are vectors obtained by stacking the values of Fourier coefficients of $\mathbf{x}$ and $\mathbf{y}$ at the sample points, respectively. These matrices can also be made block diagonal by rearranging the structures.

Since $\mathbf{B}$ is relatively well-conditioned (the condition number is 8.613×10^4 when there are 42 collocation points in the wall-normal direction), it is possible to invert the matrix without introducing non-negligible errors, so that we are able to describe the system with a standard state space representation

$$\dot{\hat{\mathbf{x}}} = \hat{\mathbf{A}}\hat{\mathbf{x}} \tag{7.30a}$$

$$\hat{\mathbf{y}} = \hat{\mathbf{C}}\hat{\mathbf{x}} \tag{7.30b}$$

with $\hat{\mathbf{A}} = \mathbf{B}^{-1}\mathbf{A}$ and $\hat{\mathbf{C}} = \mathbf{C}$.

The kinetic energy of the perturbation in the discrete formulation becomes

$$E = \hat{\mathbf{y}}^* \hat{\mathbf{W}}_y \hat{\mathbf{y}} = \hat{\mathbf{x}}^* \hat{\mathbf{C}}^* \hat{\mathbf{W}}_y \hat{\mathbf{C}} \hat{\mathbf{x}} \tag{7.31}$$

where the energy weight matrix $\hat{\mathbf{W}}_y$ is block diagonal after reordering. The integration (7.21) in the y and z directions can be dealt with separately. The complication arises from the integration in the z direction. For ease of reference, define

$$g(z) = \frac{1}{\frac{\partial F}{\partial \tilde{y}}} = 1 - \frac{1}{2} f(z) \tag{7.32}$$

which can be written as

$$g(z) = \sum_{n=-\infty}^{\infty} \hat{g}_n \mathrm{e}^{\mathrm{i}n\beta z} \tag{7.33}$$

Since

$$[u(y,z)]^2 g(z) \quad = \quad \sum_{\ell=-\infty}^{\infty} \sum_{m=-\infty}^{\infty} \sum_{n=-\infty}^{\infty} \hat{u}_m(y) \hat{u}_{\ell-n}(y) \hat{g}_{n-m} \mathrm{e}^{\mathrm{i}\ell\beta z} \tag{7.34}$$

by limiting the summation to $2M+1$ terms, we have

$$\frac{1}{2} \int_{y=-1}^{y=1} \int_{z=0}^{z=2\pi/\beta} \left([u(y,z)]^2 g(z) \right) \mathrm{d}z \mathrm{d}y = \frac{\pi}{\beta} \int_{y=-1}^{y=1} \left(\sum_{m=-M}^{M} \sum_{n=-M}^{M} \hat{u}_m(y) \hat{u}_{-n}(y) \hat{g}_{n-m} \right) \mathrm{d}y \tag{7.35}$$

and the integration can be approximated by $\hat{\mathbf{u}}^* \hat{\mathbf{W}}_u \hat{\mathbf{u}}$ where

$$\hat{\mathbf{u}} = [\ \hat{\mathbf{u}}_{-M}\ \ldots\ \hat{\mathbf{u}}_{-1}\ \hat{\mathbf{u}}_0\ \hat{\mathbf{u}}_1\ \ldots \hat{\mathbf{u}}_M\ ]^{\mathrm{T}} \tag{7.36}$$

with $\hat{\mathbf{u}}_m \in \mathbb{C}^N$ being the vector containing the values of $\hat{u}_m(y)$ at the N collocation points. The matrix $\hat{\mathbf{W}}_u \in \mathbb{C}^{(2M+1)N \times (2M+1)N}$ consists of a series of blocks $[\hat{\mathbf{W}}_u]_{n,m} \in \mathbb{C}^{N \times N}$ satisfying

$$[\hat{\mathbf{W}}_u]_{n,m} = \frac{\pi}{\beta} \hat{g}_{n-m} \mathtt{diag}\{\mathbf{q}\} \tag{7.37}$$

where $\mathbf{q} \in \mathbb{R}^N$ is the Clenshaw-Curtis quadrature weights [153]. It is easy to see that

$$\hat{\mathbf{W}}_y = \begin{bmatrix} \hat{\mathbf{W}}_u & & \\ & \hat{\mathbf{W}}_u & \\ & & \hat{\mathbf{W}}_u \end{bmatrix} \tag{7.38}$$

Defining

$$\hat{\mathbf{W}}_x = \hat{\mathbf{C}}^* \hat{\mathbf{W}}_y \hat{\mathbf{C}} \tag{7.39}$$

and

$$\hat{\mathbf{F}}_x = \mathtt{chol}(\hat{\mathbf{W}}_x) \tag{7.40}$$

where `chol` denotes the Cholesky decomposition, then the energy norm and the standard Euclidean norm of vector $\hat{\mathbf{x}}$ are related by

$$\|\hat{\mathbf{x}}\|_E = \|\hat{\mathbf{F}}_x\hat{\mathbf{x}}\|_2 \tag{7.41}$$

Similarly, denoting

$$\hat{\mathbf{F}}_y = \texttt{chol}(\hat{\mathbf{W}}_y) \tag{7.42}$$

then we have

$$\|\hat{\mathbf{y}}\|_E = \|\hat{\mathbf{F}}_y\hat{\mathbf{y}}\|_2 \tag{7.43}$$

By a change of variables

$$\check{\mathbf{x}} = \hat{\mathbf{F}}_x\hat{\mathbf{x}} \tag{7.44}$$

$$\check{\mathbf{y}} = \hat{\mathbf{F}}_y\hat{\mathbf{y}} \tag{7.45}$$

the representation of the system can be equivalently transformed to

$$\dot{\check{\mathbf{x}}} = \check{\mathbf{A}}\check{\mathbf{x}} \tag{7.46a}$$

$$\check{\mathbf{y}} = \check{\mathbf{C}}\check{\mathbf{x}} \tag{7.46b}$$

where

$$\check{\mathbf{A}} = \hat{\mathbf{F}}_x\hat{\mathbf{A}}\hat{\mathbf{F}}_x^{-1} \tag{7.47}$$

$$\check{\mathbf{C}} = \hat{\mathbf{F}}_y\hat{\mathbf{C}}\hat{\mathbf{F}}_x^{-1} \tag{7.48}$$

7.6 Numerical results

The effects of sinusoidal, triangular and semi-circular riblets on the energy amplification in channel flow under the general assumption that the period of the perturbed flow is an exact multiple of the riblet period are studied.

The Reynolds number considered in the study of the linear stability of the flow is $\mathrm{Re} = 6000$, because it is in the area that the flow loses its linear stability. When the goal is to study the energy amplification, it is more appropriate to consider a lower Reynolds number at which the flow is not yet linearly unstable. However, for the reasons pointed out in Chapter 3, the Reynolds number should also be high enough so that the transient growth can be calculated accurately by using spectral collocation methods.

7.6.1 Sinusoidal riblets

In what follows, how the riblets with the shape function

$$f(z) = h\cos(\gamma z) \tag{7.49}$$

alter the linear stability, transient growth and $\mathcal{H}_2$ norm of the system is investigated

7.6.1.1 Most unstable eigenvalue

Before addressing energy amplification in streamwise-constant flow, we start with linear stability analysis using the 2D/3C model. In the previous chapter, the effects of riblets on the linear stability of streamwise-constant channel flow are not studied due to the ill-conditioning of the matrix $\mathbf{B}$ in the velocity-velocity formulation at $\alpha = 0$. Nevertheless, it still can be seen from the figures in the last chapter that the change of the most unstable eigenvalue of the flow brought by riblets at $\alpha \to 0$ is almost negligible. It is expected that the effects should also be very small at $\alpha = 0$.

The use of the 2D/3C formulation avoids the ill-conditioning of the matrix $\mathbf{B}$, and the linear stability of the flow system can be determined by calculating the eigenvalues of $\hat{\mathbf{A}}$. Due to the structure of operator $\mathcal{A}$ given in equation (7.18), a change of Reynolds number Re only scales the eigenvalues. Therefore it suffices to compute the eigenvalues at one Reynolds number. Note that the size of the matrix, which is a reflection of discretisation resolution, is proportional to ζ in order to produce convergent numerical results. The CPU time of calculating the eigenvalues and eigenvectors of $\hat{\mathbf{A}}$ is reduced by a factor of roughly ζ^2 due to the block diagonal structure of the matrix. We stress that the eigenvalues and eigenvectors are calculated by using the QR algorithm.

Figure 7.1 plots the eigenvalue with largest real part against ζ and h at $\mathrm{Re} = 600$, $\beta = 2$. It is interesting to see that the real part of the rightmost eigenvalue decreases when ζ is increasing. The effect of sinusoidal riblets with a certain height on the linear stability of the flow is almost a linear function of ζ. Note that $\zeta = \gamma/\beta$ stands for the number of riblets within one period of perturbation velocity field, it therefore means that in the case considered, the smaller the riblet spacing, the more linearly stable the streamwise-constant flow. On the other hand, the decrease of the real part of the most unstable eigenvalue is enhanced by the increase in the riblet height h. For the cases considered, the higher the riblets, the more linearly stable the streamwise-constant flow.

The change of the most unstable eigenvalue brought by riblets is small, as expected. The differences between the most unstable eigenvalues of the flow over sinusoidal riblets and flat plates are between 10^{-4} and 10^{-6}. We stress that such differences are not a result of rounding errors. We note that the most unstable eigenvalue in the absence of riblet is calculated at each different ζ with the resolution proportional to ζ. As can be seen, the increasing resolution almost has no effects on the results, suggesting that the convergence is very good. The real parts of the most unstable eigenvalues at $h = 0.02$ for some different discretisation resolutions are listed in Table 7.1. The absolute error is of order 10^{-14}, suggesting that the eigenvalues converge very well. In practice, a resolution with $M = 8\zeta$ and $N = 40$ provides sufficiently convergent results.

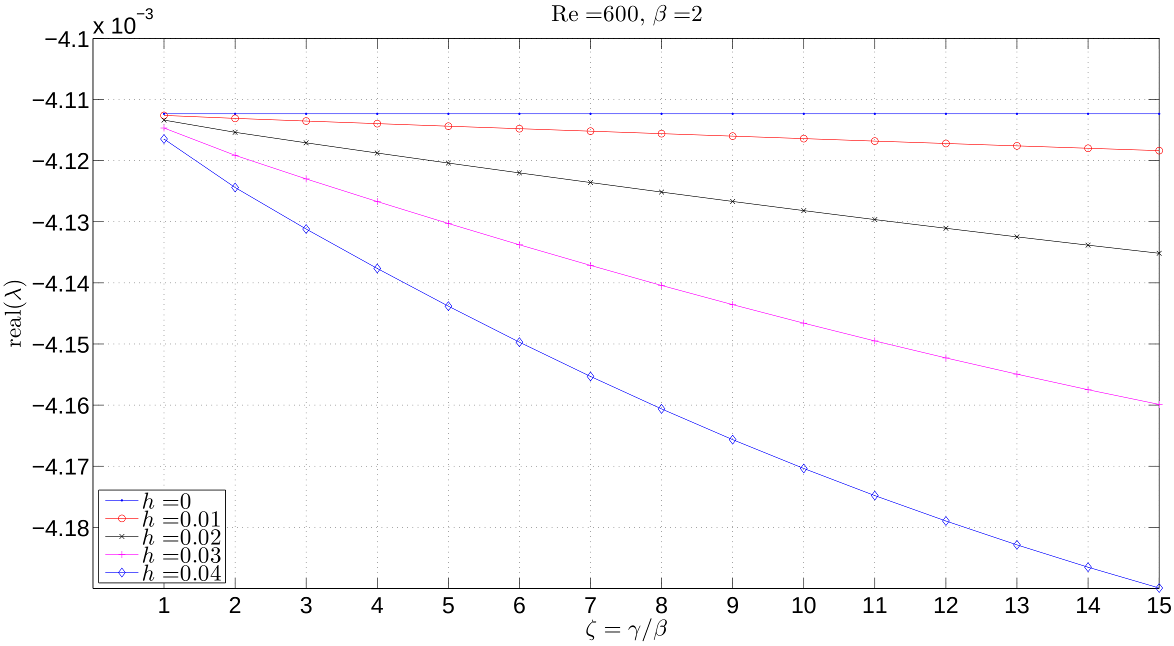

Figure 7.1: Real part of the most unstable eigenvalue for different ζ and h at Re $=$ $600, \beta = 2$. h are shown in the legend. (Sinusoidal riblets)

	$\zeta = 1$	$\zeta = 4$
$N = 40, M = 16$	-4.113367613551272e-003	-4.118754476625063e-003
$N = 50, M = 30$	-4.113367613559341e-003	-4.118754476618415e-003

Table 7.1: Real part of rightmost eigenvalue at different resolutions, Re $= 600, h = 0.02$

7.6.1.2 Transient growth

In this subsection, the effects of sinusoidal riblets on the transient energy growth of the linearised flow are investigated. The maximal energy amplification factor at time t is defined by

$$G(t) = \sup_{\check{\mathbf{x}}_0 \neq 0} \frac{\|\check{\mathbf{x}}(t)\|_2^2}{\|\check{\mathbf{x}}_0\|_2^2} = \|\mathrm{e}^{\check{\mathbf{A}}t}\|_2^2 = \|\hat{\mathbf{F}}_x \mathrm{e}^{\hat{\mathbf{A}}t} \hat{\mathbf{F}}_x^{-1}\|_2^2 \tag{7.50}$$

and it is essentially an optimisation over all initial conditions, as stated in Chapter 3. For ease of reference, we define

$$G = \sup_t G(t) \tag{7.51}$$

which is an optimisation over time t.

Denoting G_c as the maximal amplification factor G for streamwise-constant plane Poiseuille flow at $\mathrm{Re} = 600, \beta = 2$, it is straightforward to use the methods discussed in Chapter 3 to obtain $G_c \approx 70.772$, which occurs at $t \approx 46$. Note that this value can also be obtained by setting $h = 0$ and carrying out the computation described above. The relative error is of order 10^{-7}. We use G_c as a benchmark to check how G is changed by the presence of riblets with the amplitude of the riblets being $h = \{0.01, 0.02, 0.03, 0.04\}$. To reduce the computation time, a number of the most stable eigenmodes of $\hat{\mathbf{A}}$ are discarded in the calculation. This strategy was employed in [125] and the details can be found in [133]. As pointed out in Chapter 3, this approach can generate accurate results when the Reynolds number is moderately high. The accuracy can be confirmed by the convergence of the results when the discretisation resolution is increased. In fact, this approach is necessary in order to reduce the CPU time so that the calculation can be completed in a reasonable amount of time, given that the size of the matrices is proportional to ζ.

The results are illustrated in Figure 7.2, where the change of the maximal energy amplification factor $(G/G_c - 1) \times 100$ is plotted against ζ and h. Note that the amplification factor at $h = 0$ is recalculated at each ζ with different resolution and the results are well convergent.

As can be seen, the presence of sinusoidal riblets can indeed reduce G with the exception at $\zeta = 2$. The percentage of reduction is monotonically increasing with ζ between 2 and 15, suggesting that the smaller the spacing of riblet, the smaller the transient growth. The calculation for larger ζ is very expensive even for a supercomputer and therefore is not carried out here.

What is interesting is that at $\zeta = 2$, although the most unstable eigenvalue is decreased by riblets, G is larger than G_c. As shown in Figure 7.3, a closer examination reveals that the second rightmost eigenvalue of $\hat{\mathbf{A}}$ at $\zeta = 2$ is increased by riblets. While

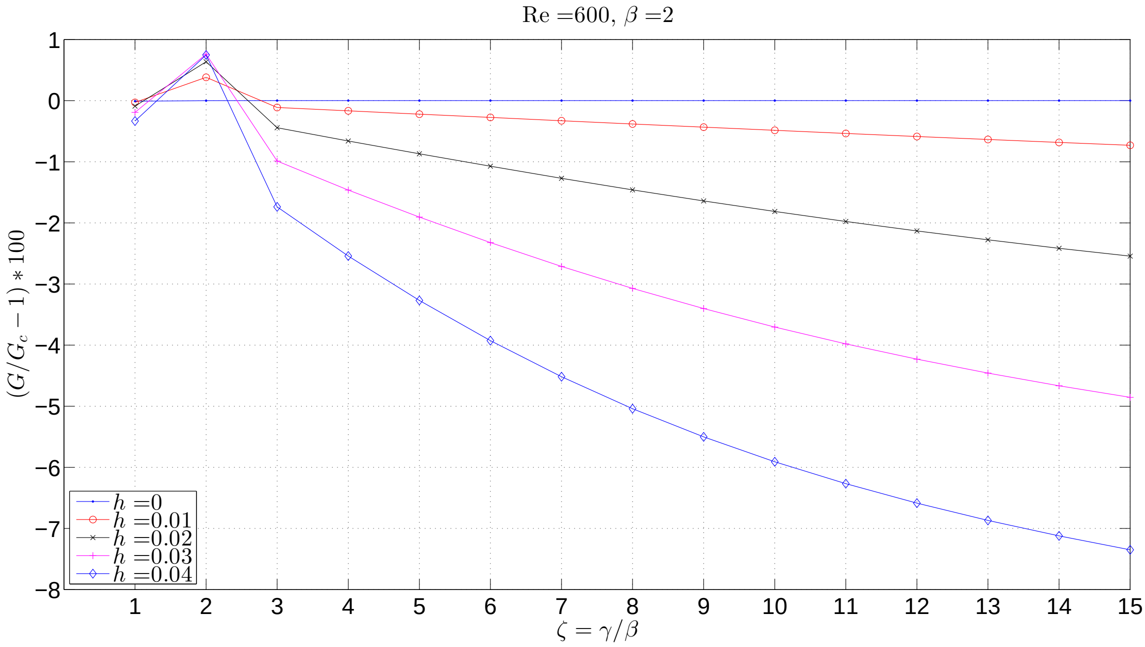

Figure 7.2: $(G/G_c-1)\times 100$ for different ζ and h at $\mathrm{Re}=600, \beta=2$. (Sinusoidal riblets)

for other ζ, this particular eigenvalue is decreased. This might be the reason that G is increased at $\zeta=2$.

Apart from at $\zeta=2$, the percentage of reduction is monotonically increasing with h. At $\zeta=15, h=0.04$, the maximal energy amplification factor is reduced by roughly 7.35%, suggesting that the transient growth in the flow is significantly suppressed by the riblets. In practice, ζ can be as high as $\mathcal{O}(100)$ and the riblets' effects on transient growth are probably more significant.

The behaviour of G at $\mathrm{Re}=1000$ is very similar to that at $\mathrm{Re}=600$, although the exact percentages of reduction are not identical. This is probably because the change of eigenvalues by riblets has a dominant effect on G.

7.6.1.3 $\mathcal{H}_2$ norm

This subsection is concerned with the energy amplification of the fluid flow system subject to stochastic forcing which models background noise. For simplicity, the covariance matrix of the stochastic forcing is assumed to be an identity matrix. Studies of energy amplification of stochastic forcing in plane channel flow were conducted in [24] and [11], and it has been shown analytically that the energy amplification of streamwise-constant channel flow with stochastic excitation can be as high as $\mathcal{O}(\mathrm{Re}^3)$. The situation is more involved with the presence of riblets and the analysis here is carried out numerically.

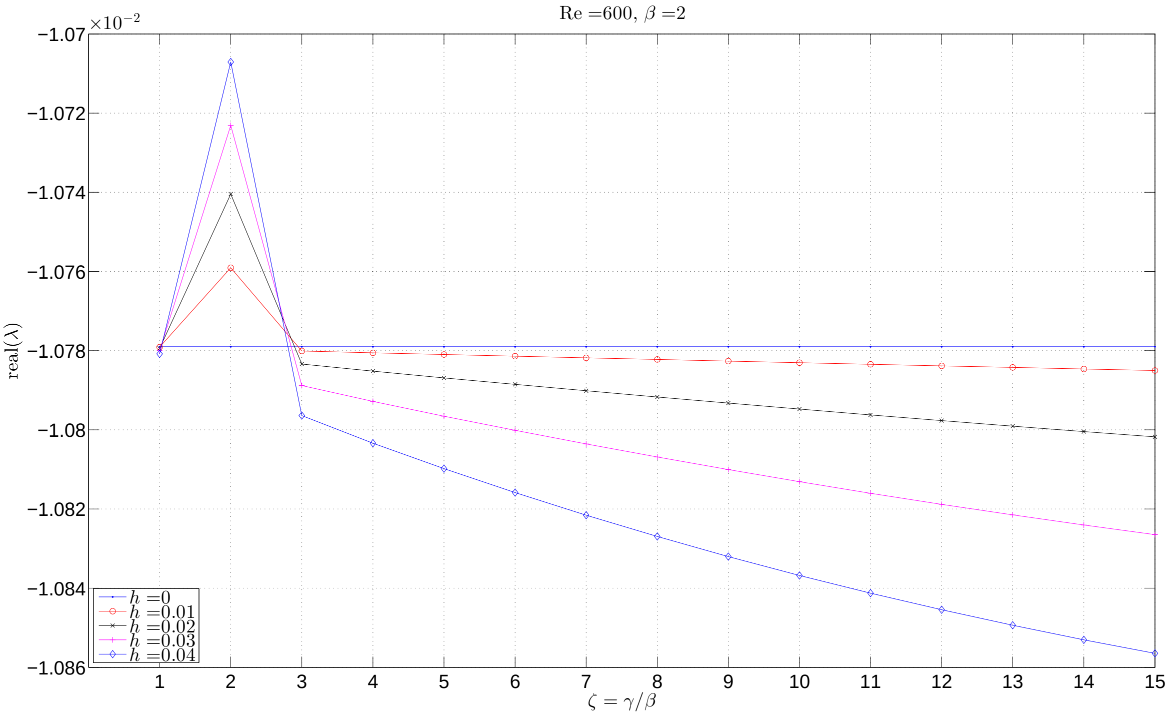

Figure 7.3: Real part of the second most unstable eigenvalue for different ζ and h at $\mathrm{Re} = 600, \beta = 2$. (Sinusoidal riblets)

Since we assume that the stochastic forcing has unit energy (the covariance matrix of the stochastic forcing is an identity matrix), the model of system (7.30) becomes

$$\begin{aligned} \dot{\check{\mathbf{x}}} &= \check{\mathbf{A}}\check{\mathbf{x}} + \check{\mathbf{d}}_{\mathbf{w}} && (7.52\text{a}) \\ \check{\mathbf{y}} &= \check{\mathbf{C}}\check{\mathbf{x}} && (7.52\text{b}) \end{aligned}$$

where $\check{\mathbf{d}}_{\mathbf{w}}$ denotes the stochastic forcing. As stated in Section 7.2, the energy amplification factor of the system is given by $\texttt{trace}(\check{\mathbf{C}}\check{\mathbf{\Omega}}\check{\mathbf{C}}^*)$ with $\check{\mathbf{\Omega}}$ being the controllability grammian, which is the solution of the Lyapunov equation

$$\check{\mathbf{A}}\check{\mathbf{\Omega}} + \check{\mathbf{\Omega}}\check{\mathbf{A}}^* = -\mathbf{I} \tag{7.53}$$

where $\mathbf{I}$ is an identity matrix.

From the identities of matrix trace and the definition of the matrices, we have

$$\begin{aligned} \texttt{trace}(\check{\mathbf{C}}\check{\mathbf{\Omega}}\check{\mathbf{C}}^*) &= \texttt{trace}(\check{\mathbf{\Omega}}\check{\mathbf{C}}^*\check{\mathbf{C}}) \\ &= \texttt{trace}[\check{\mathbf{\Omega}}(\hat{\mathbf{F}}_x^{-1})^*\hat{\mathbf{C}}^*\hat{\mathbf{F}}_y^*\hat{\mathbf{F}}_y\hat{\mathbf{C}}\hat{\mathbf{F}}_x^{-1}] \\ &= \texttt{trace}[\check{\mathbf{\Omega}}(\hat{\mathbf{F}}_x^{-1})^*\hat{\mathbf{C}}^*\hat{\mathbf{W}}_y\hat{\mathbf{C}}\hat{\mathbf{F}}_x^{-1}] \\ &= \texttt{trace}[\check{\mathbf{\Omega}}(\hat{\mathbf{F}}_x^{-1})^*\hat{\mathbf{W}}_x\hat{\mathbf{F}}_x^{-1}] \\ &= \texttt{trace}(\check{\mathbf{\Omega}}) && (7.54) \end{aligned}$$

The square root of $\texttt{trace}(\check{\mathbf{\Omega}})$ is the $\mathcal{H}_2$ norm of the system. By comparing the $\mathcal{H}_2$ norms of channel flow over riblets and over flat plates, we can see how the riblets affect the energy amplification.

Denote T as $\sqrt{\texttt{trace}(\check{\mathbf{\Omega}})}$ at $\text{Re} = 600, \beta = 2$ and T_c as the value without riblets. Figure 7.4 shows that riblets have the effect of suppressing the $\mathcal{H}_2$ norm of the system. Unlike the transient growth, the $\mathcal{H}_2$ norm is reduced for all ζ considered.

7.6.2 Triangular riblets

The triangular riblets under consideration are the same as in the last chapter. The shape function is defined by

$$f(z) = \frac{8h}{\pi^2}\sum_{k=0}^{k=10}(-1)^k\frac{\sin((2k+1)\gamma z)}{(2k+1)^2} \tag{7.55}$$

7.6.2.1 Most unstable eigenvalue

Figure 7.5 plots the real part of the most unstable eigenvalue against ζ and h at $\text{Re} = 600, \beta = 2$ in the presence of triangular riblets. A comparison of this figure with Figure 7.1 reveals that triangular riblets have very similar impact on the linear stability of the flow as sinusoidal riblets.

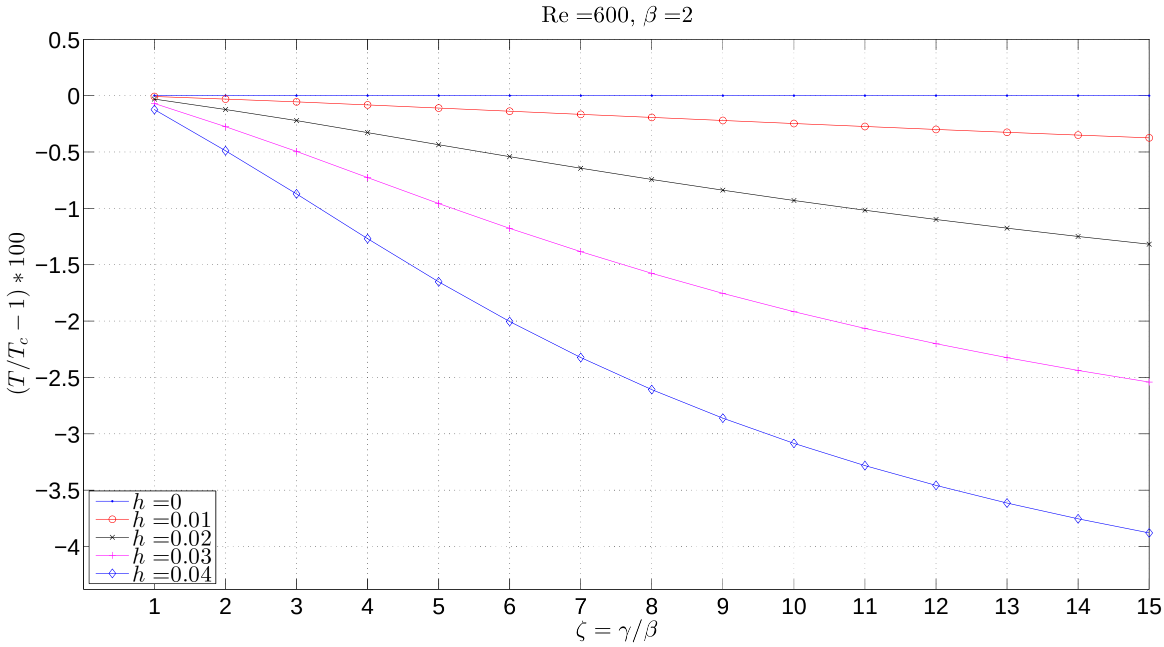

Figure 7.4: Change in $\mathcal{H}_2$ norm of the system for different ζ and h at Re $= 600, \beta = 2$. (Sinusoidal riblets)

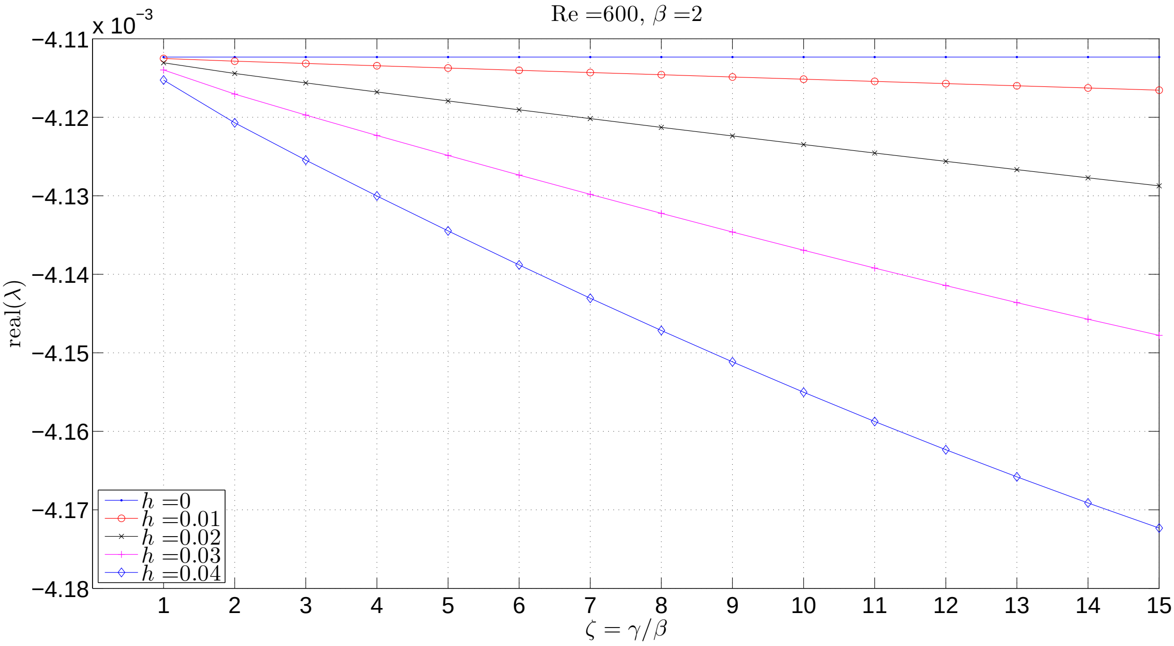

Figure 7.5: Real part of the most unstable eigenvalue for different ζ and h at Re $=$ $600, \beta = 2$. (Triangular riblets)

7.6.2.2 Transient growth

How the transient growth is changed by the triangular riblets is depicted in Figure 7.6. The similarity of triangular riblets and sinusoidal riblets is once again confirmed by a comparison between Figure 7.2 and Figure 7.6. Larger height h and smaller spacing $2\pi/\gamma$ lead to more reduction in transient growth except at $\zeta = 2$. This exception can again be explained by an increase in the second most unstable eigenvalues due to the presence of riblets, as shown in Figure 7.7.

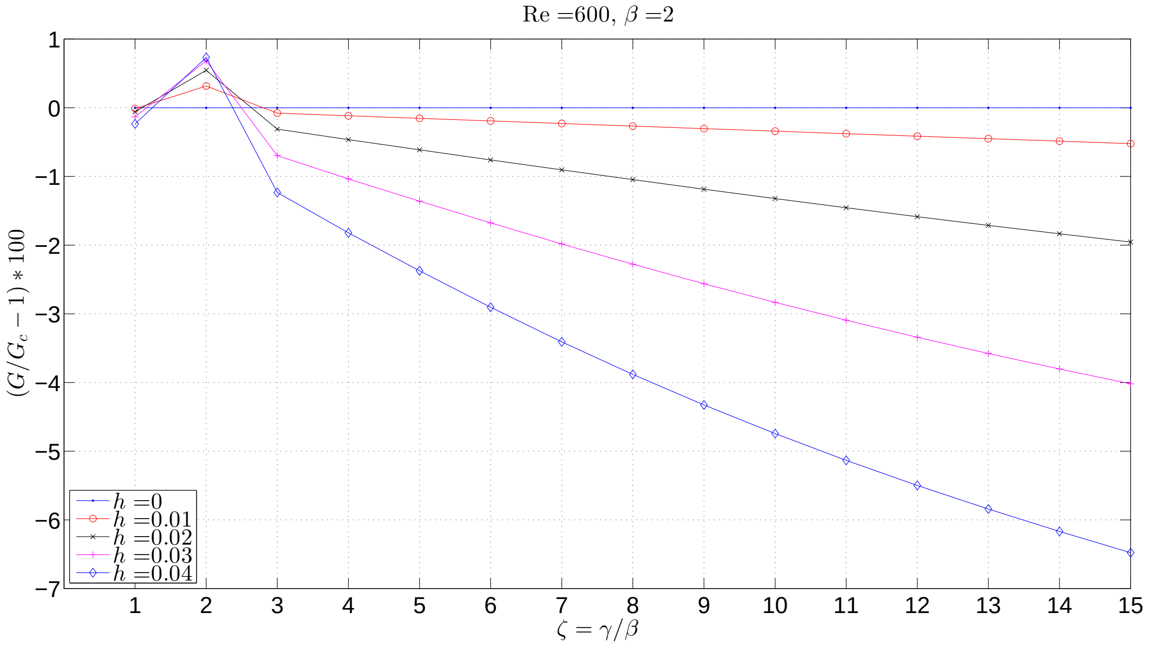

Figure 7.6: $(G/G_c - 1) \times 100$ for different ζ and h at Re $= 600, \beta = 2$. (Triangular riblets)

7.6.2.3 $\mathcal{H}_2$ norm

The reduction in $\mathcal{H}_2$ norm caused by the triangular riblets is illustrated in Figure 7.8. Note that triangular riblets are less effective than sinusoidal ones at reducing the energy amplification in channel flow. This somehow comes as a surprise since triangular riblets are far more popular in applications. We stress that here the flow under study is in laminar regime and it is expected that the impact of riblets on laminar flow and turbulent flow may be quite different.

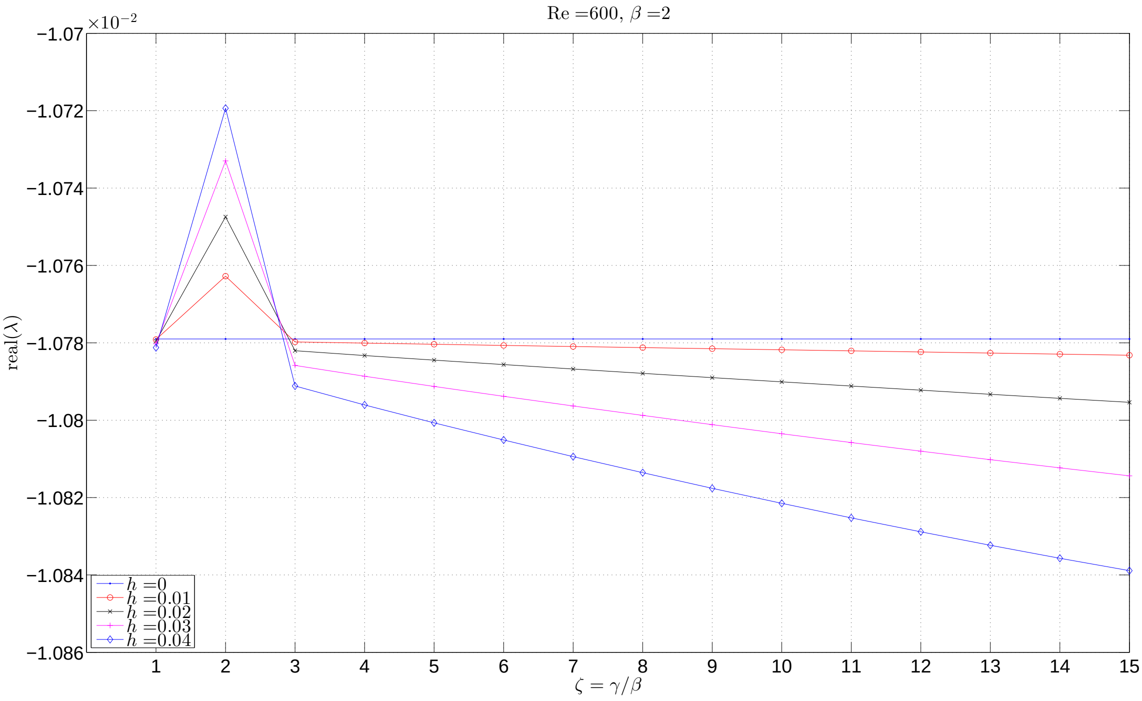

Figure 7.7: Real part of the second most unstable eigenvalue for different ζ and h at $\mathrm{Re} = 600, \beta = 2$. (Triangular riblets)

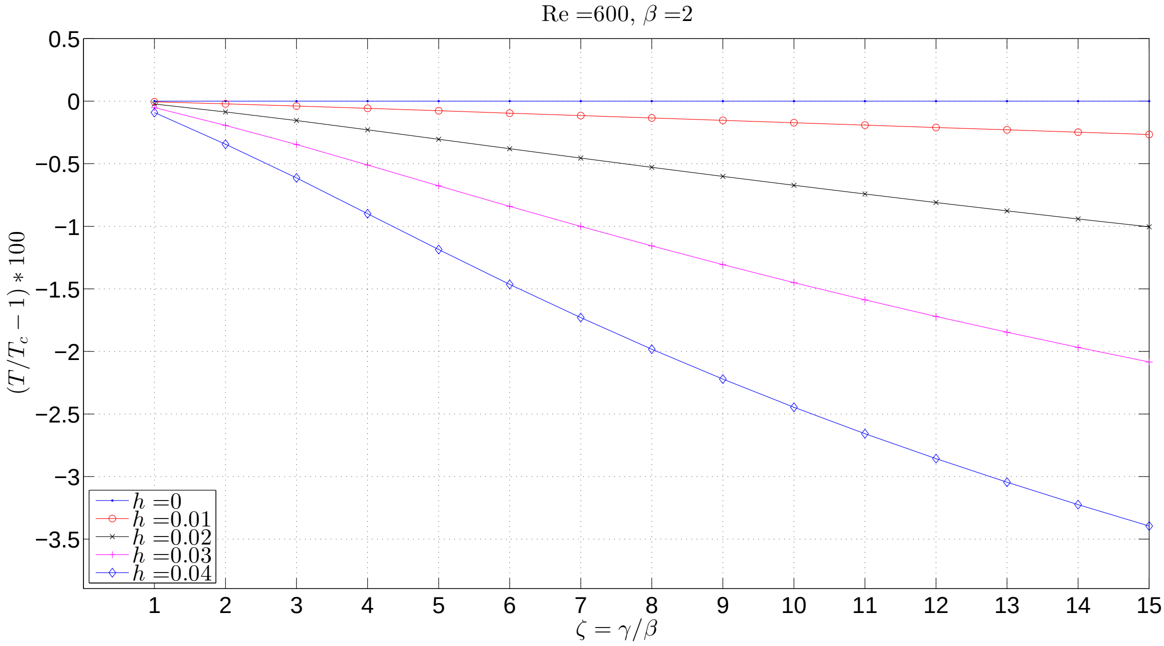

Figure 7.8: Change in $\mathcal{H}_2$ norm of the system for different ζ and h at $\mathrm{Re} = 600, \beta = 2$. (Triangular riblets)

7.6.3 Semi-circular riblets

We now study the effects of semi-circular riblets on the energy amplification on streamwise-constant flow. The semi-circular riblets are described by

$$f(z) = h - \frac{4h}{\pi} + \frac{8h}{\pi} \sum_{k=1}^{k=15} (-1)^k \frac{\cos(k\gamma z)}{4k^2 - 1} \tag{7.56}$$

which is the same as the function given in (6.33).

7.6.3.1 Most unstable eigenvalue

Similar to Figures 7.1 and 7.5, Figure 7.9 shows that the linear stability of the streamwise-constant flow can be enhanced by the presence of riblets. Note that the decrease in the real part of the most unstable eigenvalue is larger than in the other two cases. As we have speculated that the change in the most unstable eigenvalue has a dominant effect on transient growth, we expect that among the three types of riblets considered, semi-circular riblets are the most effective ones at reducing the energy amplification.

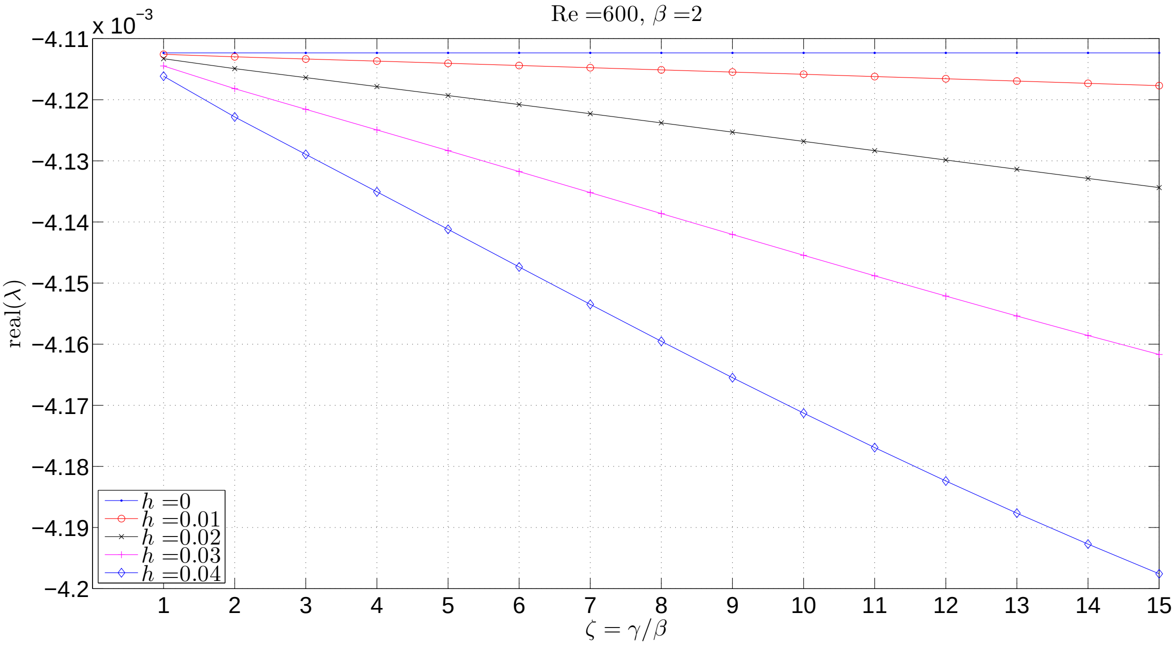

Figure 7.9: Real part of the most unstable eigenvalue for different ζ and h at $\mathrm{Re} = 600, \beta = 2$. (Semi-circular riblets)

7.6.3.2 Transient growth

As can be seen form Figure 7.10, at $\zeta = 15, h = 0.04$, the reduction in transient growth by semi-circular riblets is about 15.87%, as opposed to 7.35% by sinusoidal riblets and

6.48% by triangular riblets. Given that in practice, ζ can be a much larger number, the reduction can probably be made even more significant. At $\zeta = 2$, the transient growth is again enhanced and the real part of the second largest eigenvalue is increased, as shown in Figure 7.11.

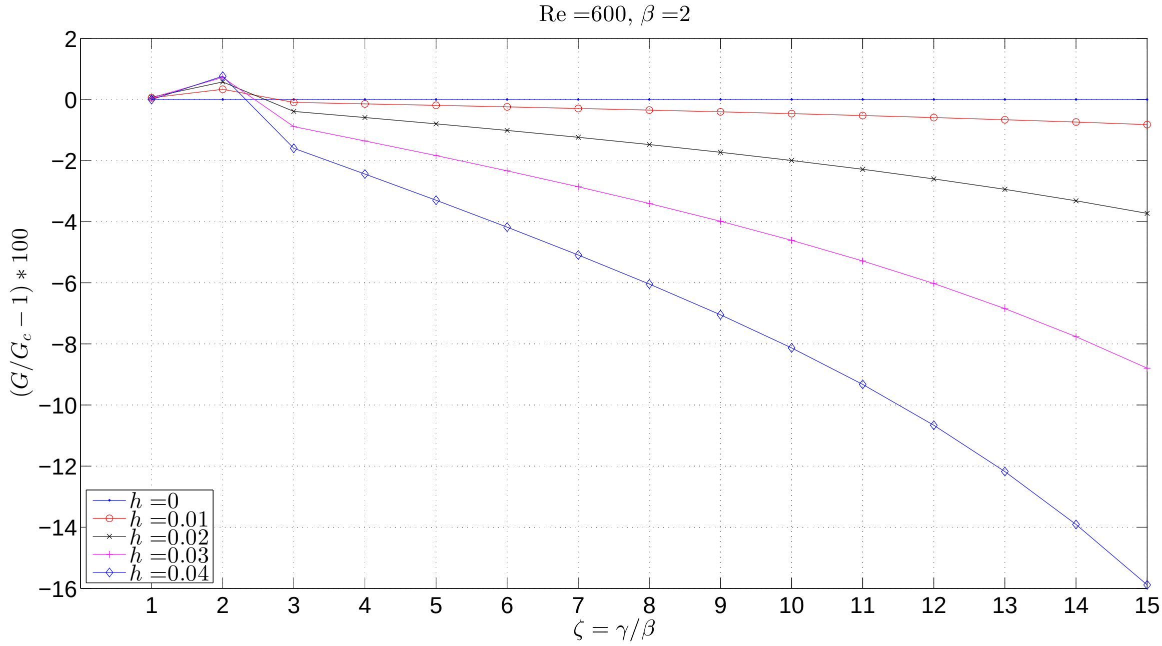

Figure 7.10: $(G/G_c - 1) \times 100$ for different ζ and h at Re $= 600, \beta = 2$. (Semi-circular riblets)

7.6.3.3 $\mathcal{H}_2$ norm

Figure 7.12 shows that semi-circular riblets also cause the most reduction in the $\mathcal{H}_2$ norm of the flow system. The reduction is found for all ζ considered, similar to Figures 7.4 and 7.8.

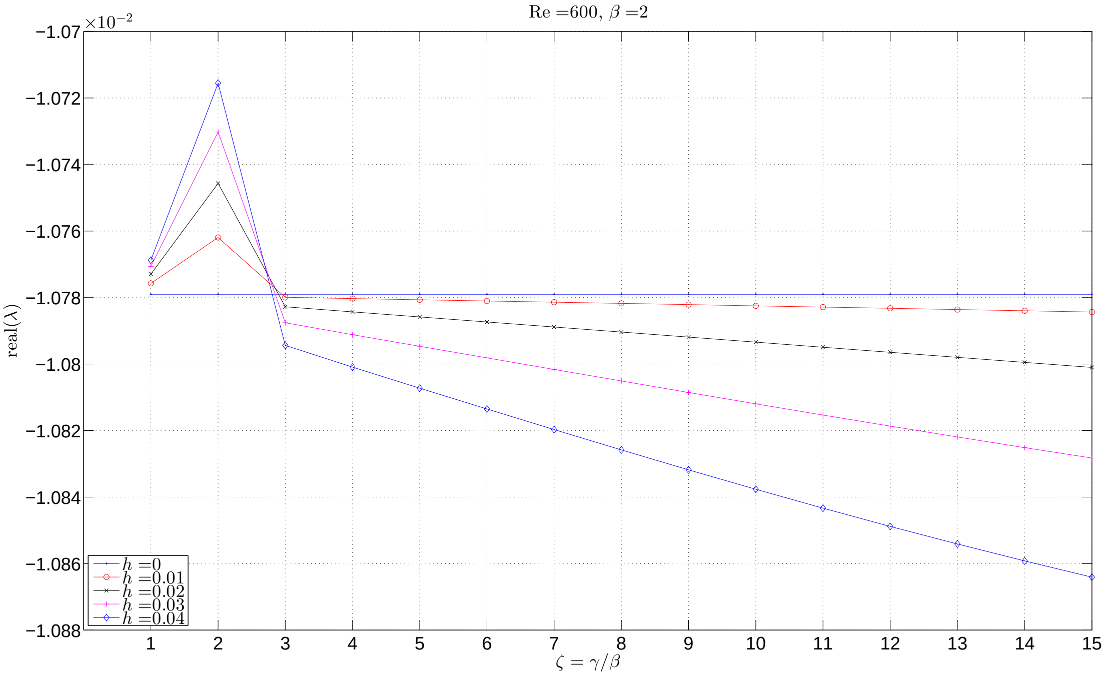

Figure 7.11: Real part of the second most unstable eigenvalue for different ζ and h at $\text{Re} = 600, \beta = 2$. (Semi-circular riblets)

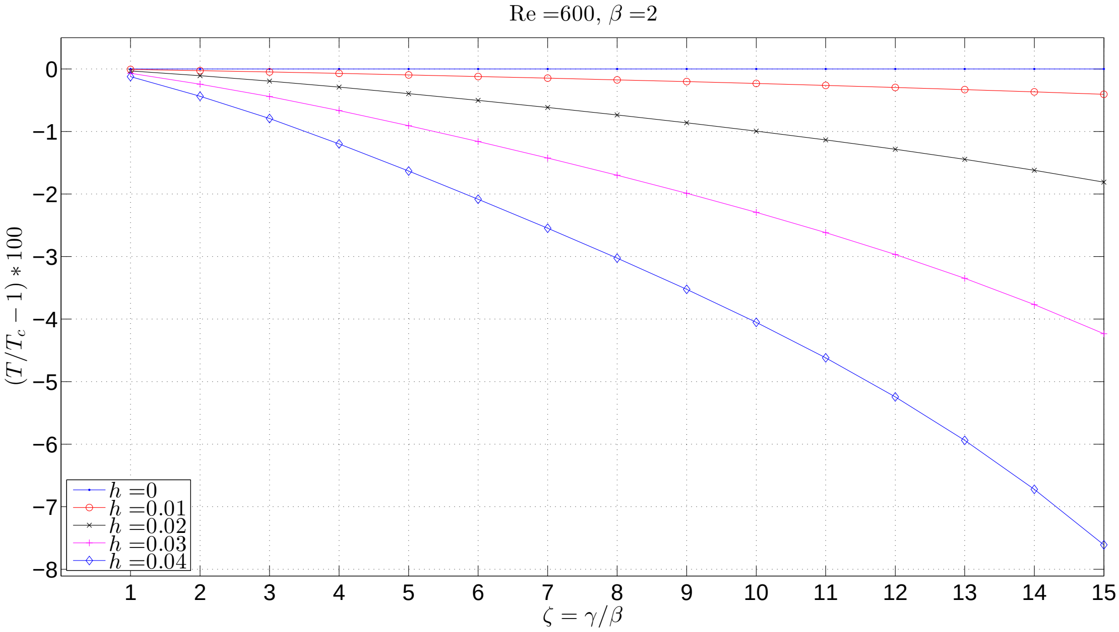

Figure 7.12: Change in $\mathcal{H}_2$ norm of the system for different ζ and h at $\text{Re} = 600, \beta = 2$. (Semi-circular riblets)

7.7 Conclusion

This chapter shows that the introduction of riblets can suppress the transient growth of the most sensitive initial conditions and amplification of stochastic noise in linearised channel flow. Three types of riblets are considered and among them, semi-circular riblets are most effective at reducing the energy amplification. Since energy amplification has been identified as the possible reason for subcritical transition of channel flow, its suppression could be the reason for the delay of laminar-turbulent transition of the flow over riblets.

From the numerical computations, we conclude that in order to reduce the energy amplification as much as possible, semi-circular riblets with larger height and smaller spacing should be used. Riblets with $h > 0.1$ may have entirely different effects as the assumption that the pressure gradient is not changed by riblets may no longer hold. By contrast, reducing the riblet spacing is likely to be beneficial in a wide range, although in practice it is subject to manufacturing limitations.

Chapter 8

Summary and Future Work

8.1 Summary

This thesis is composed of two parts. In the first part, we have used systems theory to study the stability of plane channel flow and in the second part, the effects of riblets on the stability of channel flow are investigated. Throughout the thesis, fluid flow systems, which are described by the NSEs and are infinite-dimensional by nature, are approximated by finite-dimensional models by applying spatial discretisations.

In Chapter 2, passivity theorems from systems theory are used to analyse the global stability of plane channel flow, which is modelled as a closed-loop system consisting of a linear dynamical system and a memoryless nonlinear feedback. Since the standard passive definitions and theorems cannot be directly applied to the flow system, they are extended from finite-dimensional Euclidean spaces to finite-dimensional Hilbert spaces. Using this generalised passivity approach, plane Poiseuille flow is found to be globally asymptotically stable when the Reynolds number is lower than $\mathrm{Re}_E \approx 49.6$, which agrees with the result obtained by the classical energy approach. Therefore the passivity approach can be considered as an alternative to the classical energy approach to analyse the stability of some fluid flows. We then show that if a finite-dimensional system can be proved stable using the generalised passivity approach on a Hilbert space, its stability can also be proved by applying the standard passivity theorems on a Euclidean space after a unique loop transformation is made.

Above the energy Reynolds number Re_E, it is now understood that channel flow may experience transient energy growth due to the nonnormality of the Orr-Sommerfeld/ Squire operator [157] and the calculation of transient growth is often of interest. Numerical experiments are carried out in Chapter 3 to illustrate that the Chebyshev collocation method, which is commonly used in the literature, is not sufficiently accurate to calculate the transient growth in channel flow. Numerical integration errors, spurious eigenvalues with negative real parts of large magnitudes and the corresponding eigenfunctions, are identified as the sources of inaccuracy. We further show that a Chebyshev Galerkin method in which the boundary conditions are satisfied by the basis functions can be used and the transient growth can be calculated very accurately.

The different performances of the collocation method and the Galerkin method in calculating the transient growth indicate that the result of stability analysis of finite-dimensional approximations may vary with the choice of spatial discretisation method. It is explained in Chapter 4 that the collocation method is more suitable for DNS, while the Galerkin method is a better choice for stability analysis using Lyapunov theorems. We then present a numerical discretisation of the 2-dimensional NSEs such that the nonlinear terms of different forms are equivalent and remain lossless or energy-preserving after discretisation. The key idea is to choose a formulation in which the continuity equations is automatically satisfied in discrete form. After obtaining a finite-dimensional model, we briefly discuss existing methods of searching for general Lyapunov functions and estimated ROA. Our conclusion is that for the moment, it is impractical to obtain a higher Reynolds number below which channel flow is globally asymptotically stable by using finite-dimensional models, due to the restrictive requirement for computing resources.

The second part of the thesis starts from Chapter 5, which presents some numerical preliminaries for the study of the stability of channel flow over riblets in the following two chapters. The presence of riblets on the lower wall of the channel makes the computational domain irregular and as a result, spectral methods cannot be directly applied to discretise the NSEs. Three kinds of methods that are able to deal with this difficulty are introduced and we conclude that for the geometry under study, a change of coordinates is the most appropriate way to achieve accurate results. We also give a short introduction to the matrix-free approach for determining the linear stability and calculating the transient growth in complex flows. Some commonly used eigenvalue algorithms are then introduced and we recognise that to study the linear stability of channel flow, it is very important to choose suitable shifts in the Arnoldi algorithm so that the eigenvalues of interest are not lost. After giving the governing equations for the flow under study, we show that the Fourier Galerkin method can be used to discretise the NSEs in the spanwise direction so that the resulting matrices can be made block diagonal, which means that the computational load can be significantly reduced.

The effects of riblets on the linear stability of channel flow are studied in Chapter 6. A novel velocity-velocity formulation in which the pressure term is eliminated and the corresponding boundary conditions are derived. As a comparison, the primitive variable formulation is also used in the study. Sinusoidal, triangular and semi-circular riblets are considered, and numerical computations in these two forms give very close results, suggesting that high accuracy is achieved. It is found that under most circumstances, the flow is made more linearly unstable by the riblets. The linear stability of the flow is usually reduced when the riblet height is increased or the riblet spacing is decreased.

Chapter 7 investigates the impact of riblets on the energy amplification in channel flow. The attention is restricted to streamwise-constant modes, which are identified to have the largest energy amplification factors and as the flow under consideration is independent of the the streamwise direction, a 2D/3C formulation of the NSEs is used. Two scenarios of energy amplification are considered. The first one is that the kinetic energy of the perturbation experiences transient growth after the flow is subject to an initial disturbance, while the other one is that the flow is subject to white noise as an external forcing and the energy of the noise is amplified by the system. The amplification factor in the later scenario can be quantified by the $\mathcal{H}_2$ norm of the system. It is found that the energy amplification can be greatly suppressed by the use of riblets. Energy amplification is reduced further when the riblet height is increased or the riblet spacing is decreased. Among the three types of riblets, semi-circular ones are found to be most effective at suppressing energy amplification. By contrast, sinusoidal and triangular riblets have very similar performances.

The Reynolds numbers considered in Chapter 6 and Chapter 7 are $\mathrm{Re} = 6000$ and $\mathrm{Re} = 600$, respectively. Our results show that at lower Reynolds number, energy amplification is reduced by the riblets. As a result, the transition from laminar flow to turbulent flow could be delayed. At higher Reynolds number, the riblets make the flow more linearly unstable. It is not surprising that the effects of riblets are not uniform, because the flow is in different regimes in these two cases.

8.2 Future Work

As we concluded in the first part of the thesis, it is impractical to find a Reynolds number higher than Re_E below which plane channel flow is globally asymptotically stable by searching for general Lyapunov functions for finite-dimensional models, because the dimensionality of the models obtained by spatial discretisations is beyond the capability of modern computers. Therefore, it is more likely to achieve the goal by searching for Lyapunov functionals for the PDEs that govern the motion of the flow. Alternatively, the system can be divided into a low order finite-dimensional part and an infinite-dimensional part that capture the dynamics unmodelled by the finite-dimensional part. In both cases, SOS programming plays an important role in the search.

Considering that we have studied the effects of riblets on the $\mathcal{H}_2$ norm, it would also be interesting to investigate how the $\mathcal{H}_\infty$ norm of the flow system is changed by the inclusion of riblets,

Using eigenvalue analysis, we have shown that riblets make channel flow more linearly unstable. In plane Poiseuille flow, linear instability is characterised by Tollmien-Schlichting waves and it would be interesting to see how the dynamics of channel flow evolve over time in the presence of riblets when the eigenfunction corresponding to the most unstable eigenvalue is used as an initial condition. DNS of channel flow over riblets with this initial condition could provide physical insight on how the stability of the flow is changed by riblets.

Similarly, SVD is used in the study of effects of riblets on the energy amplification in channel flow. Since we are able to find the initial condition which leads to the largest possible transient growth, as discussed in Chapter 3, this initial condition can be used in DNS of channel flow over riblets. A comparison with DNS of plane Poiseuille flow will provide a more direct answer to the question whether riblets can delay laminar-turbulent transition.

In summary, the work in this thesis can be used as a starting point of DNS of channel flow over riblets and several interesting initial conditions can be obtained from our study.

References

[1] N. Abdessemed, A. S. Sharma, S. Sherwin, and V. Theofilis. Transient growth analysis of the flow past a circular cylinder. *Physics of Fluids*, 21(4):044103, 2009.

[2] A. A. Ahmadi, M. Krstic, and P. A. Parrilo. A globally asymptotically stable polynomial vector field with no polynomial Lyapunov function. In *50th IEEE Conference on Decision and Control and European Control Conference (CDC-ECC)*, pages 7579–7580, Orlando, FL, 2011.

[3] A. A. Ahmadi and P. A. Parrilo. Converse results on existence of sum of squares Lyapunov functions. In *50th IEEE Conference on Decision and Control and European Control Conference (CDC-ECC)*, pages 6516–6521, Orlando, FL, 2011.

[4] A. Alving and P. Freeberg. The effect of riblets on sails. *Experiments in Fluids*, 19(6):397–404, 1995.

[5] F. Amato, C. Cosentino, and A. Merola. On the region of attraction of nonlinear quadratic systems. *Automatica*, 43(12):2119–2123, 2007.

[6] B. D. O. Anderson. A system criterion for positive real matrices. *SIAM Journal on Control*, 5(2):171–182, 1967.

[7] E. J. Anderson, P. S. MacGillivray, and M. E. DeMont. Scallop shells exhibit optimization of riblet dimensions for drag reduction. *The Biological Bulletin*, 192(3):341–344, 1997.

[8] A. Bacciotti and L. Rosier. *Liapunov Functions and Stability in Control Theory.* Springer, Netherlands, 2005.

[9] J. S. Baggett, T. A. Driscoll, and L. N. Trefethen. A mostly linear model of transition to turbulence. *Physics of Fluids*, 7(4):833–838, 1995.

[10] J. S. Baggett and L. N. Trefethen. Low-dimensional models of subcritical transition to turbulence. *Physics of Fluids*, 9(4):1043–1053, 1997.

[11] B. Bamieh and M. Dahleh. Energy amplification in channel flows with stochastic excitation. *Physics of Fluids*, 13(11):3258–3269, 2001.

[12] D. Barkley, H. Blackburn, and S. J. Sherwin. Direct optimal growth analysis for timesteppers. *International Journal for Numerical Methods in Fluids*, 57(9):1435–1458, 2008.

[13] R. H. Bartels and G. Stewart. Solution of the matrix equation AX + XB = C. *Communications of the ACM*, 15(9):820–826, 1972.

[14] G. K. Batchelor. *An Introduction to Fluid Dynamics.* Cambridge University Press, Cambridge, United Kingdom, 2000.

[15] P. F. Batcho and G. E. Karniadakis. Generalized Stokes eigenfunctions: a new trial basis for the solution of incompressible Navier-Stokes equations. *Journal of Computational Physics*, 115(1):121–146, 1994.

[16] D. Bechert, M. Bruse, and W. Hage. Experiments with three-dimensional riblets as an idealized model of shark skin. *Experiments in Fluids*, 28(5):403–412, 2000.

[17] D. Bechert, G. Hoppe, and W. Reif. On the drag reduction of the shark skin. In *23rd Aerospace Sciences Meeting*, Reno, NV, 1985.

[18] T. R. Bewley and S. Liu. Optimal and robust control and estimation of linear paths to transition. *Journal of Fluid Mechanics*, 365:305–349, 1998.

[19] T. R. Bewley, P. Moin, and R. Temam. DNS-based predictive control of turbulence: an optimal benchmark for feedback algorithms. *Journal of Fluid Mechanics*, 447:179–225, 2001.

[20] J. P. Boyd. *Chebyshev and Fourier Spectral Methods.* Dover Publications, New York, NY, second edition, 2001.

[21] J. P. Boyd. Fourier embedded domain methods: extending a function defined on an irregular region to a rectangle so that the extension is spatially periodic and $\mathbf{C}^\infty$. *Applied Mathematics and Computation*, 161(2):591–597, 2005.

[22] S. Boyd, L. E. Ghaoui, E. Feron, and V. Balakrishnan. *Linear Matrix Inequalities in System and Control Theory.* SIAM, Philadelphia,PA, 1994.

[23] F. H. Busse. Bounds on the transport of mass and momentum by turbulent flow between parallel plates. *Zeitschrift für Angewandte Mathematik und Physik*, 20(1):1–14, 1969.

[24] K. M. Butler and B. F. Farrell. Three-dimensional optimal perturbations in viscous shear flow. *Physics of Fluids A*, 4(8):1637–1650, 1992.

[25] C. Canuto, M. Y. Hussaini, A. Quarteroni, and T. A. Zang. *Spectral Methods: Fundamentals in Single Domains*. Springer, Germany, 2006.

[26] C. Canuto, M. Y. Hussaini, A. Quarteroni, and T. A. Zang. *Spectral Methods: Evolution to Complex Geometries and Applications to Fluid Dynamics*. Springer, Germany, 2007.

[27] D. R. Carlson, S. E. Widnall, and M. F. Peeters. Flow-visualization study of transition in plane Poiseuille flow. *Journal of Fluid Mechanics*, 121:487–505, 1982.

[28] S. J. Chapman. Subcritical transition in channel flows. *Journal of Fluid Mechanics*, 451:35–97, 2002.

[29] S. Chernyshenko, D. Huang, P. Goulart, D. Lasagna, and O. Tutty. Nonlinear stability analysis of fluid flow using sum of squares of polynomials. In *11th International Conference of Numerical Analysis and Applied Mathematics*, pages 265–268, Rhodes, Greece, 2013.

[30] S. Chernyshenko, P. Goulart, D. Huang, and A. Papachristodoulou. Polynomial sum of squares in fluid dynamics: a review with a look ahead. *Philosophical Transactions of the Royal Society A: Mathematical, Physical and Engineering Sciences*, 372(2020):20130350, 2014.

[31] G. Chesi. *Domain of Attraction: Analysis and Control via SOS Programming*. Springer, London, United Kingdom, 2011.

[32] H.-D. Chiang, M. W. Hirsch, and F. F. Wu. Stability region of nonlinear automous dynamical systems. *IEEE Transactions on Automatic Control*, 33(1):16–26, 1988.

[33] H.-D. Chiang and J. S. Thorp. Stability regions of nonlinear dynamical systems: A constructive methodology. *IEEE Transactions on Automatic Control*, 34(12):1229–1241, 1989.

[34] H. Choi, P. Moin, and J. Kim. On the effects of riblets in fully developed laminar channel flows. *Physics of Fluids*, 3(8):1892–1896, 1991.

[35] H. Choi, P. Moin, and J. Kim. Direct numerical simulation of turbulent flow over riblets. *Journal of Fluid Mechanics*, 255:503–539, 1993.

[36] H. Choi, P. Moin, and J. Kim. Active turbulence control for drag reduction in wall-bounded flows. *Journal of Fluid Mechanics*, 262:75–110, 1994.

[37] D. C. Chu and G. E. Karniadakis. A direct numerical simulation of laminar and turbulent flow over riblet-mounted surfaces. *Journal of Fluid Mechanics*, 250:1–42, 1993.

[38] J. W. Cooley and J. W. Tukey. An algorithm for the machine calculation of complex Fourier series. *Mathematics of Computation*, 19(90):297–301, 1965.

[39] L. Cortelezzi, J. Speyer, K. Lee, and J. Kim. Robust reduced-order control of turbulent channel flows via distributed sensors and actuators. In *37th IEEE Conference on Decision and Control (CDC)*, pages 1906–1911, Tampa, FL, 1998.

[40] E. Coustols and A. Savill. Turbulent skin-friction drag reduction by active and passive means. Part 1. Everything you wanted to know about riblets, LEBUs and other devices. Technical report, DTIC Document, Toulouse, France, 1992.

[41] R. F. Curtain and H. Zwart. *An Introduction to Infinite-Dimensional Linear Systems Theory.* Springer-Verlag, New York, NY, 1995.

[42] P. Dawkins, S. R. Dunbar, and R. W. Douglass. The origin and nature of spurious eigenvalues in the spectral tau method. *Journal of Computational Physics*, 147:441–462, 1998.

[43] L. Debnath and P. Mikusiński. *Introduction to Hilbert Spaces with Applications.* Elsevier Academic Press, Burlington, MA, third edition, 2005.

[44] Y. Ding and M. Kawahara. Linear stability of incompressible flow using a mixed finite element method. *Journal of Computational Physics*, 139(2):243–273, 1998.

[45] L. Djenidi, F. Anselmet, J. Liandrat, and L. Fulachier. Laminar boundary layer over riblets. *Physics of Fluids*, 6(9):2993–2999, 1994.

[46] J. J. Dongarra, B. Straughanb, and D. W. Walker. Chebyshev tau-QZ algorithm methods for calculating spectra of hydrodynamic stability problems. *Applied Numerical Mathematics*, 22:399–434, 1996.

[47] R. C. Dorf and R. H. Bishop. *Modern Control Systems.* Pearson, Upper Saddle River, NJ, 2011.

[48] J. F. Douglas, J. M. Gasiorek, J. A. Swaffield, and L. B. Jack. *Fluid Mechanics.* Pearson, Essex, United Kingdom, 2005.

[49] P. G. Drazin. *Introduction to Hydrodynamic Stability.* Cambridge University Press, Cambridge, United Kingdom, 2002.

[50] P. G. Drazin and W. H. Reid. *Hydrodynamic Stability.* Cambridge University Press, Cambridge, United Kingdom, second edition, 2004.

[51] G. E. Dullerud and F. Paganini. *A Course in Robust Control Theory.* Springer, New York, NY, 2000.

[52] U. Ehrenstein. On the linear stability of channel flow over riblets. *Physics of Fluids*, 8(11):3194–3196, 1996.

[53] R. García-Mayoral and J. Jiménez. Drag reduction by riblets. *Philosophical Transactions of the Royal Society A: Mathematical, Physical and Engineering Sciences*, 369(1940):1412–1427, 2011.

[54] R. Garcia-Mayoral and J. Jimenez. Hydrodynamic stability and breakdown of the viscous regime over riblets. *Journal of Fluid Mechanics*, 678:317–347, 2011.

[55] D. R. Gardner, S. A. Trogdon, and R. W. Douglass. A modified tau spectral method that eliminates spurious eigenvalues. *Journal of Computational Physics*, 80:137–167, 1989.

[56] R. Glowinski, T.-W. Pan, and J. Periaux. A fictitious domain method for Dirichlet problem and applications. *Computer Methods in Applied Mechanics and Engineering*, 111(3):283–303, 1994.

[57] D. Goldstein, R. Handler, and L. Sirovich. Modeling a no-slip flow boundary with an external force field. *Journal of Computational Physics*, 105(2):354–366, 1993.

[58] D. Goldstein, R. Handler, and L. Sirovich. Direct numerical simulation of turbulent flow over a modeled riblet covered surface. *Journal of Fluid Mechanics*, 302:333–376, 1995.

[59] G. H. Golub and C. F. Van Loan. *Matrix Computations.* JHU Press, Baltimore, MD, 2012.

[60] F. Gómez, R. Gómez, and V. Theofilis. On three-dimensional global linear instability analysis of flows with standard aerodynamics codes. *Aerospace Science and Technology*, 32(1):223–234, 2014.

[61] D. Gottlieb and S. A. Orszag. *Numerical Analysis of Spectral Methods: Theory and Applications.* SIAM, Philadelphia, PA, 1977.

[62] P. J. Goulart and S. Chernyshenko. Global stability analysis of fluid flows using sum-of-squares. *Physica D*, 241:692–704, 2011.

[63] P. J. Goulart and S. I. Chernyshenko. Stability analysis of fluid flows using sum-of-squares. In *American Control Conference (ACC)*, pages 2971–2976, Baltimore, MD, 2010.

[64] R. A. Granger. *Fluid Mechanics.* Dover Publications, Mineola, NY, 1995.

[65] M. Green and D. J. Limebeer. *Linear Robust Control.* Dover Publications, Englewood Cliffs, NJ, 2012.

[66] G. Grek, V. Kozlov, and S. Titarenko. An experimental study of the influence of riblets on transition. *Journal of Fluid Mechanics*, 315:31–50, 1996.

[67] P. M. Gresho. Incompressible fluid dynamics: some fundamental formulation issues. *Annual Review of Fluid Mechanics*, 23(1):413–453, 1991.

[68] C. E. Grosch and H. Salwen. The continuous spectrum of the Orr-Sommerfeld equation. Part 1. The spectrum and the eigenfunctions. *Journal of Fluid Mechanics*, 87(01):33–54, 1978.

[69] V. Guillemin and A. Pollack. *Differential Topology.* American Mathematical Society, Englewood Cliffs, NJ, 2010.

[70] S. V. Gusev and A. Likhtarnikov. Kalman-Popov-Yakubovich lemma and the S-procedure: A historical essay. *Automation and Remote Control*, 67(11):1768–1810, 2006.

[71] D. S. Henningson and P. J. Schmid. Vector eigenfunction expansions for plane channel flows. *Studies in Applied Mathematics*, 87(1):15–43, 1992.

[72] M. Högberg, T. Bewley, and D. S. Henningson. Relaminarization of $\mathrm{Re}_\tau = 100$ turbulence using gain scheduling and linear state-feedback control. *Physics of Fluids*, 15(11):3572–3575, 2003.

[73] M. Högberg, T. R. Bewley, and D. S. Henningson. Linear feedback control and estimation of transition in plane channel flow. *Journal of Fluid Mechanics*, 481:149–175, 2003.

[74] P. J. Holmes, J. L. Lumley, G. Berkooz, J. C. Mattingly, and R. W. Wittenberg. Low-dimensional models of coherent structures in turbulence. *Physics Reports*, 287(4):337–384, 1997.

[75] W. Huang and D. M. Sloan. The pseudospectral method for solving differential eigenvalue problems. *Journal of Computational Physics*, 111:399–409, 1994.

[76] D. Huybrechs. On the Fourier extension of nonperiodic functions. *SIAM Journal on Numerical Analysis*, 47(6):4326–4355, 2010.

[77] M. Itoh, S. Tamano, R. Iguchi, K. Yokota, N. Akino, R. Hino, and S. Kubo. Turbulent drag reduction by the seal fur surface. *Physics of Fluids*, 18(6):065102, 2006.

[78] J. Jiménez. Turbulent flows over rough walls. *Annual Review of Fluid Mechanics*, 36:173–196, 2004.

[79] D. D. Joseph and S. Carmi. Stability of Poiseuille flow in pipes, annuli, and channels. *Quarterly of Applied Mathmatics*, 26(1):575–599, 1969.

[80] D. D. Joseph. *Stability of Fluid Motions I.* Springer-Verlag, Berlin Heidelberg, Germany, 1976.

[81] S. S. Joshi. *A Systems Theory Approach to the Control of Plane Poiseuille Flow.* PhD thesis, University of California, Los Angeles, Los Angeles, CA, 1996.

[82] S. S. Joshi, J. L. Speyer, and J. Kim. A systems theory approach to the feedback stabilization of infinitesimal and finite-amplitude disturbances in plane Poiseuille flow. *Journal of Fluid Mechanics*, 332:157–184, 1997.

[83] M. R. Jovanovic and B. Bamieh. Componentwise energy amplification in channel flows. *Journal of Fluid Mechanics*, 534:145–183, 2005.

[84] G. Karniadakis and K.-S. Choi. Mechanisms on transverse motions in turbulent wall flows. *Annual Review of Fluid Mechanics*, 35(1):45–62, 2003.

[85] G. Karniadakis and S. Sherwin. *Spectral/hp Element Methods for Computational Fluid Dynamics.* Oxford University Press, New York, NY, 2004.

[86] H. K. Khalil. *Nonlinear Systems.* Pearson Education, New York, NY, 2000.

[87] M. Kocvara and M. Stingl. *PENBMI user's guide (version 2.0)*, 2005 (accessed November 7, 2014). `http://tomopt.com/docs/penbmi.pdf`.

[88] W. Kong and X. Wu. Chebyshev tau matrix method for Poisson-type equations in irregular domain. *Journal of Computational and Applied Mathematics*, 228(1):158–167, 2009.

[89] C. Lanczos. An iteration method for the solution of the eigenvalue problem of linear differential and integral operators. *Journal of Research of the National Bureau of Standards*, 45(4), 1950.

[90] B. E. Launder and S. Li. A numerical study of riblet effects on laminar flow through a plane channel. *Applied Scientific Research*, 46(3):271–279, 1989.

[91] W. Layton, C. C. Manica, M. Neda, M. Olshanskii, and L. G. Rebholz. On the accuracy of the rotation form in simulations of the Navier-Stokes equations. *Journal of Computational Physics*, 228:3433–3447, 2009.

[92] K. H. Lee. *A Systems Theory Approach to Control of Transitional and Turbulent Flows.* PhD thesis, University of California, Los Angeles, Los Angeles, CA, 1999.

[93] K. H. Lee, L. Cortelezzi, J. Kim, and J. Speyer. Application of reduced-order controller to turbulent flows for drag reduction. *Physics of Fluids*, 13(5):1321–1330, 2001.

[94] M. Lee, N. Malaya, and R. D. Moser. Petascale direct numerical simulation of turbulent channel flow on up to 786k cores. In *Proceedings of SC13: International Conference for High Performance Computing, Networking, Storage and Analysis*, page 61, Denver, CO, 2013.

[95] R. B. Lehoucq, D. C. Sorensen, and C. Yang. *ARPACK Users' Guide: Solution of Large-scale Eigenvalue Problems with Implicitly Restarted Arnoldi Methods.* SIAM, Philadelphia, PA, 1998.

[96] R. J. LeVeque. *Finite Difference Methods for Ordinary and Partial Differential Equations: Steady-state and Time-dependent Problems.* SIAM, Philadelphia, PA, 2007.

[97] R. J. Leveque and Z. Li. The immersed interface method for elliptic equations with discontinuous coefficients and singular sources. *SIAM Journal on Numerical Analysis*, 31(4):1019–1044, 1994.

[98] Z. Li and K. Ito. *The immersed interface method: numerical solutions of PDEs involving interfaces and irregular domains.* SIAM, Philadelphia, PA, 2006.

[99] J. Lim. *Control of wall-bounded turbulent shear flows using modern control theory.* PhD thesis, University of California, Los Angeles, Los Angeles, CA, 2003.

[100] C. C. Lin. *The Theory of Hydrodynamic Stability.* Cambridge University Press, Cambridge, United Kingdom, 1955.

[101] A. Lundbladh and A. V. Johansson. Direct simulation of turbulent spots in plane Couette flow. *Journal of Fluid Mechanics*, 229:499–516, 1991.

[102] A. Lundbladh, D. S. Henningson, and S. C. Reddy. Threshold amplitudes for transition in channel flows. In *Transition, Turbulence and Combustion*, pages 309–318. Springer, 1994.

[103] F. Martinelli, M. Quadrio, J. McKernan, and J. F. Whidborne. Linear feedback control of transient energy growth and control performance limitations in subcritical plane Poiseuille flow. *Physics of Fluids*, 23:014103–1–014103–9, 2011.

[104] G. B. McFadden, B. T. Murray, and R. F. Boisvert. Elimination of spurious eigenvalues in the Chebyshev tau spectral method. *Journal of Computational Physics*, 91:228–239, 1990.

[105] J. McKernan. *Control of plane Poiseuille flow: a theoretical and computational investigation.* PhD thesis, Cranfield University, United Kingdom, 2006.

[106] J. Moehlis, H. Faisst, and B. Eckhardt. A low-dimensional model for turbulent shear flows. *New Journal of Physics*, 6(1):56, 2004.

[107] C. B. Moler and G. W. Stewart. An algorithm for generalized matrix eigenvalue problems. *SIAM Journal on Numerical Analysis*, 10(2):241–256, 1973.

[108] R. Moser, P. Moin, and A. Leonard. A spectral numerical method for the Navier-Stokes equations with applications to Taylor-Couette flow. *Journal of Computational Physics*, 52(3):524–544, 1983.

[109] A. Nerli and S. Camarri. Stokes eigenfunctions and Galerkin projection of the disturbance equations in plane Poiseuille flow: a systematic analytical approach. *Meccanica*, 41(6):671–680, 2006.

[110] E. Non, R. Pierre, and J.-J. Gervais. Linear stability of the three-dimensional lid-driven cavity. *Physics of Fluids*, 18(8):084103, 2006.

[111] W. Orr. The stability or instability of the steady motions of a perfect liquid and of a viscous liquid. Part II: A viscous liquid. *Proceedings of the Royal Irish Academy. Section A: Mathematical and Physical Sciences*, 27:69–138, 1907.

[112] S. A. Orszag. Accurate solution of the Orr-Sommerfeld stability equation. *Journal of Fluid Mechanics*, 50:689–703, 1971.

[113] S. A. Orszag. Spectral methods for problems in complex geometries. *Journal of Computational Physics*, 37(1):70–92, 1980.

[114] A. Papachristodoulou and M. M. Peet. On the analysis of systems described by classes of partial differential equations. In *American Control Conference (ACC)*, pages 747–752, San Diego, CA, 2006.

[115] A. Papachristodoulou and S. Prajna. On the construction of Lyapunov functions using the sum of squares decomposition. In *41st IEEE Conference on Decision and Control (CDC)*, pages 3482–3487, Las Vegas, NV, 2002.

[116] P. A. Parrilo. *Structured Semidefinite Programs and Semialgebraic Gemometry Methods in Robustness and Optimization.* PhD thesis, California Institute of Technology, Pasadena, CA, 2000.

[117] V. C. Patel and M. R. Head. Some observations on skin friction and velocity profiles in fully developed pipe and channel flows. *Journal of Fluid Mechanics*, 38:181–201, 1969.

[118] A. T. Patera. A spectral element method for fluid dynamics: laminar flow in a channel expansion. *Journal of Computational Physics*, 54(3):468–488, 1984.

[119] C. S. Peskin. Flow patterns around heart valves: a numerical method. *Journal of Computational Physics*, 10(2):252–271, 1972.

[120] S. Prajna, A. Papachristodoulou, and P. A. Parrilo. Introducing SOSTOOLS: A general purpose sum of squares programming solver. In *American Control Conference (ACC)*, pages 741–746, Las Vegas, NV, 2002.

[121] S. Prajna, A. Papachristodoulou, and P. A. Parrilo. SOSTOOLS: sum of squares optimization toolbox for MATLAB–user's guide. *Control and Dynamical Systems, California Institute of Technology, Pasadena, CA*, 91125, 2004.

[122] N. Ramanan and G. M. Homsy. Linear stability of lid-driven cavity flow. *Physics of Fluids*, 6(8):2690–2701, 1994.

[123] C. Reddy, P. J. Schmid, and D. S. Henningson. Pseudospectra of the Orr-Sommerfeld operator. *SIAM Journal on Applied Mathematics*, 53(1):15–47, 1993.

[124] J. N. Reddy. *An Introduction to the Finite Element Method*. McGraw-Hill, New York, NY, 1993.

[125] S. C. Reddy and D. S. Henningson. Energy growth in viscous channel flows. *Journal of Fluid Mechanics*, 252:209–238, 1993.

[126] D. Rempfer. On low-dimensional Galerkin models for fluid flow. *Theoretical and Computational Fluid Dynamics*, 14(2):75–88, 2000.

[127] D. Rempfer. Low-dimensional modeling and numerical simulation of transition in simple shear flows. *Annual Review of Fluid Mechanics*, 35(1):229–265, 2003.

[128] J. Reneaux. Overview on drag reduction technologies for civil transport aircraft. In *European Congress on Computational Methods in Applied Sciences and Engineering*, pages 1–18, Jyväskylä, Finland, 2004.

[129] E. Reshotko. Transient growth: A factor in bypass transition. *Physics of Fluids*, 13(5):1067–1075, 2001.

[130] O. Reynolds. An experimental investigation of the circumstances which determine whether the motion of water shall be direct or sinuous, and of the law of resistance in parallel channels. *Proceedings of the Royal Society of London*, 35(224-226):84–99, 1883.

[131] O. Reynolds. On the dynamical theory of incompressible viscous fluids and the determination of the criterion. *Philosophical Transactions of the Royal Society of London. A*, pages 123–164, 1895.

[132] B. Rummler and A. Noske. Direct Galerkin approximation of plane-parallel-Couette and channel flows by stokes eigenfunctions. *Notes on Numerical Fluid Mechanics*, 64:3–19, 1998.

[133] P. J. Schmid and D. S. Henningson. *Stability and Transition in Shear Flows.* Springer-Verlag, New York, NY, 2001.

[134] P. J. Schmid. Nonmodal stability theory. *Annual Review of Fluid Mechanics*, 39:139–162, 2007.

[135] J. Serrin. On the stability of viscous fluid motions. *Archive for Rational Mechanics and Analysis*, 3(1):1–13, 1959.

[136] A. S. Sharma. Model reduction of turbulent fluid flows. *International Journal of Bifurcation and Chaos*, 19(4):1267–1278, 2009.

[137] A. S. Sharma, D. J. N. Limebeer, B. J. Mckeon, and J. F. Morrison. Stabilising control laws for the incompressible Navier-Stokes equations using sector stability theory. In *3rd AIAA Flow Control Conference*, San Francisco, CA, 2006.

[138] A. S. Sharma, J. F. Morrison, B. J. Mckeon, D. J. N. Limebeer, and W. H. Koberg. Relaminarisation of $\mathrm{Re}_\tau = 100$ channel flow with globally stabilising linear feedback control. *Physics of Fluids*, 23:125105–1–125105–23, 2011.

[139] J. Shen. Efficient spectral-Galerkin method. I. Direct solvers of second-and fourth-order equations using Legendre polynomials. *SIAM Journal on Scientific Computing*, 15(6):1489–1505, 1994.

[140] J. Shen. Efficient spectral-Galerkin method. II. Direct solvers of second-and fourth-order equations using Chebyshev polynomials. *SIAM Journal on Scientific Computing*, 16(1):74–87, 1995.

[141] J. Shen, T. Tang, and L.-L. Wang. *Spectral Methods: Algorithms, Analysis and Applications*. Springer, Germany, 2011.

[142] L. E. Silva, A. Silveira-Neto, and J. Damasceno. Numerical simulation of two-dimensional flows over a circular cylinder using the immersed boundary method. *Journal of Computational Physics*, 189(2):351–370, 2003.

[143] O. J. Staffans. Passive and conservative continuous-time impedance and scattering systems. Part I: Well-posed systems. *Mathematics of Control, Signals, and Signals*, 15(4):291–315, 2002.

[144] J. F. Sturm. Using SeDuMi: a MATLAB toolbox for optimization over symmetric cones. *Optimization Methods and Software*, 11(1-4):625–653, 1999.

[145] W. Tan and A. Packard. Stability region analysis using polynomial and composite polynomial Lyapunov functions and sum-of-squares programming. *IEEE Transactions on Automatic Control*, 53(2):565–570, 2008.

[146] T. Tatsumi and T. Yoshimura. Stability of the laminar flow in a rectangular duct. *Journal of Fluid Mechanics*, 212:437–449, 1990.

[147] G. I. Taylor. Stability of a viscous liquid contained between two rotating cylinders. *Philosophical Transactions of the Royal Society of London*, pages 289–343, 1923.

[148] V. Theofilis, P. Duck, and J. Owen. Viscous linear stability analysis of rectangular duct and cavity flows. *Journal of Fluid Mechanics*, 505:249–286, 2004.

[149] K.-C. Toh, M. J. Todd, and R. H. Tütüncü. SDPT3: a MATLAB software package for semidefinite programming, version 1.3. *Optimization Methods and Software*, 11(1-4):545–581, 1999.

[150] U. Topcu, A. Packard, and P. Seiler. Local stability analysis using simulations and sum-of-squares programming. *Automatica*, 44(10):2669–2675, 2008.

[151] L. N. Trefethen. Pseudospectra of matrices. In D. F. Griffiths and G. A. Watson, editors, *Numerical Analysis*, pages 234–265. Longman Scientific & Technical, Essex, United Kingdom, 1991.

[152] L. N. Trefethen. Pseudospectra of linear operators. *SIAM Review*, 39(3):383–406, 1997.

[153] L. N. Trefethen. *Spectral Methods in MATLAB*. SIAM, Philadelphia, PA, 2000.

[154] L. N. Trefethen. *Approximation Theory and Approximation Practice.* SIAM, Philadelphia, PA, 2013.

[155] L. N. Trefethen and D. Bau III. *Numerical Linear Algebra.* SIAM, Philadelphia, PA, 1997.

[156] L. N. Trefethen and M. Embree. *Spectra and Pseudospectra: The Behavior of Nonnormal Matrices and Operators.* Princeton University Press, Princeton, NJ, 2005.

[157] L. N. Trefethen, A. E. Trefethen, S. C. Reddy, and T. A. Driscoll. Hydrodynamic stability without eigenvalues. *Science*, 261(5121):578–584, 1993.

[158] G. Valmorbida, M. Ahmadi, and A. Papachristodoulou. Semi-definite programming and functional inequalities for distributed parameter systems. *preprint arXiv:1403.6882*, 2014.

[159] P. Viswanath. Aircraft viscous drag reduction using riblets. *Progress in Aerospace Sciences*, 38(6):571–600, 2002.

[160] M. J. Walsh. Riblets as a viscous drag reduction technique. *AIAA Journal*, 21(4):485–486, 1983.

[161] J. A. Weideman and S. C. Reddy. A MATLAB differentiation matrix suite. *ACM Transactions on Mathematical Software*, 26:465–519, 2000.

[162] T. A. Zang. On the rotation and skew-symmetric forms for incompressible flow simulations. *Applied Numerical Mathematics*, pages 27–40, 1991.

[163] T. A. Zang, C. L. Streett, and M. Y. Hussaini. Spectral methods for CFD. Contractor Report NAS1-18605, NASA, Hampton, VA, 1989.

[164] A. Zebib. Removal of spurious modes encountered in solving stability problems by spectral methods. *Journal of Computational Physics*, 70:521–525, 1987.

[165] S. Zhao and S. Duncan. Passivity of plane Poiseuille flow. In *12th European Control Conference (ECC)*, pages 1077–1082, Zürich, Switzerland, 2013.

[166] S. Zhao and S. Duncan. Energy amplification of Poiseuille flow in a pipe lined with riblets. In *10th UKACC International Conference on Control*, pages 232–237, Loughborough, United Kingdom, 2014.

[167] S. Zhao and S. Duncan. Energy amplification of streamwise constant channel flow over riblets. In *19th IFAC World Congress*, pages 857–862, Cape Town, South Africa, 2014.

[168] S. Zhao and S. Duncan. On the accuracy of the calculation of transient growth in plane Poiseuille flow. *International Journal for Numerical Methods in Fluids*, 74(12):857–871, 2014.

[169] K. Zhou, J. C. Doyle, and K. Glover. *Robust and Optimal Control*. Prentice Hall, Englewood Cliffs, NJ, 1996.